UNSTEADY THRUST MEASUREMENT TECHNIQUES FOR PULSE DETONATION ENGINES

by

DIBESH DHOJ JOSHI

Presented to the Faculty of the Graduate School of
The University of Texas at Arlington in Partial Fulfillment
of the Requirements
for the Degree of

DOCTOR OF PHILOSOPHY

THE UNIVERSITY OF TEXAS AT ARLINGTON

May 2014

Acknowledgements

I would like to thank Prof. Frank Lu for his help and support throughout the period of my study at the University of Texas at Arlington. I am grateful to him for providing me with the opportunity to work as an Undergraduate Research Assistant at the Aerodynamics Research Center and motivating me to pursue higher education. I also thank him for choosing me to work on externally funded projects which have helped me gain a lot of research experience. I express my gratitude towards Prof. Donald Wilson for awarding me with an Enhanced Graduate Teaching Assistantship which helped to support and finance my graduate studies. I would also like to thank him for his recommendations which have helped to vastly improve my research project. I would like to thank Prof. Luca Maddalena for all his guidance and helpful suggestions to make my research project more focused and informative. I would like to thank him for selecting me to work as a Graduate Teaching Assistant for the Aerodynamics and Fluids Laboratory course and all those informal lectures which have helped me to understand basic underlying concepts and theories. I would like to thank Prof. Kent Lawrence for his valuable suggestions and helping me out with the finite element analysis part of my research project. I would like to thank Prof. Ali Abolmaali for serving to be a part of my dissertation committee and for being very supportive. I gratefully acknowledge the help from Prof. David Mee of the University of Queensland and Prof. Herbert Olivier of RWTH in providing detailed information on dynamic calibration techniques.

I would like to thank James Peace and Steven Tester who helped me and invested countless hours to build the experimental setup used in this research project. I am thankful to have such motivated individuals as a part of my research team. I would like to

thank our technician Mr. David Carter for all this help and practical advice. I would also like to thank the entire ARC family including alumni who have been very understanding and supportive and helped me reach my goal.

Finally, I would like to thank my caring family who have been my source of encouragement. I would like to thank my fiancée, Trija Joshi, for being patient and understanding. I would like to thank all my friends who have made me feel at home in this beautiful part of the world which is thousands of miles away from my native soil.

April 25, 2014

Abstract

UNSTEADY THRUST MEASUREMENT TECHNIQUES FOR PULSE DETONATION ENGINES

Dibesh D. Joshi, PhD

The University of Texas at Arlington, 2014

Supervising Professor: Frank Lu

Thrust is a critical performance parameter and its correct determination is necessary to characterize an engine. Many conventional thrust measurement techniques prevail. However, further developments are required for correct measurement of thrust for pulse detonation engines (PDEs), since the entire thrust generation process is intermittent. The significant effect of system dynamics in the form of inertial forces, stress wave propagation and reflections initiated in the structure due to detonations and pulse-to-pulse interaction in a fast operating PDE further complicates the thrust measurement process. These complications call for a detailed study of unsteady thrust characteristics.

A general approach was first developed to recover actual thrust from the measured thrust generated by the PDE. The developed approach consisted of two steps. The first step incorporated a deconvolution procedure using a pre-established system transfer function and measured input to reconstruct the output yielding the deconvolved thrust. The second step accounted for inertial forces through an acceleration compensation procedure. These two steps allowed the actual thrust to be determined.

A PDE operating at 10 and 20 Hz with oxygen and hydrogen at different filling fractions and mixture equivalence ratios was used for the experimental application of the general approach. A semi-empirical approach utilizing the measured pressure histories at the exit of the engine together with gas dynamics theory was able to estimate the generated thrust during a cycle. The semi-empirical thrust values were compared against actual experimental data. Further, a dynamical model of the PDE was created for studying the unsteady thrust characteristics using finite element analysis. The results from finite element analysis were compared against the semi-empirical and experimental results. In addition, finite element analysis enabled thrust estimates to be made numerically at higher operating frequencies of 50 and 100 Hz. The thrust estimated experimentally, semi-empirically and numerically was expressed in the form of specific impulse for comparison. The results obtained via the semi-empirical method and finite element analysis were found to be in good agreement with each other. However, the results obtained experimentally were slightly lower than the other two. Finally, the results obtained in this research work were also compared against the findings reported in literature. The comparison was satisfactory.

The developed general approach used to recover actual thrust generated by a PDE was also used to recover actual aerodynamic drag experienced by a blunt nose cone model in a nominal Mach 8–9 flow. The limited validation against modified Newtonian theory was provided as the results obtained after applying the developed approach matched the predicted values.

Table of Contents

List of Illustrations

List of Tables

Nomenclature

a	acceleration; also, speed of sound
A	area of cross section
AFS	Alternate Fuel Systems Inc., Calgary, Canada
c	damping coefficient
$\boldsymbol{C}$	damping coefficient matrix
C_d	discharge coefficient
C_D	drag coefficient
CJ	Chapman–Jouguet state
c_p	specific heat at constant pressure
D	amplitude
D_{CJ}	Chapman–Jouguet detonation speed
DAQ	data acquisition system
DFT	discrete Fourier transform
EMI	electromagnetic interference
f	frequency
ff	filling fraction
FEA	finite element analysis
FT	Fourier transform
FFT	fast Fourier transform
$F(t)$	unsteady force
g	standard gravitational acceleration

$g(t)$	system transfer function
$G(f)$	$\mathrm{FT}\big(g(t)\big)$, frequency response function
h	specific enthalpy
h^0	heat of formation in standard state per unit mass
$h(t)$	system transfer function
I_p	impulse per pulse per unit area
I_{sp}	specific impulse
J	rms of the response registered by piezoelectric film
k	spring stiffness coefficient
$\boldsymbol{K}$	stiffness coefficient matrix
LT	Linear Technology, Milpitas, California
m	mass
$\dot{m}$	mass flow rate
M	Mach number
M_{CJ}	propagation Mach number of Chapman–Jouguet detonation wave
NI	National Instruments Corporation, Austin, Texas
p_w	pressure at the closed end of PDE during decay portion
PDE	pulse detonation engine
$p(t)$	pressure
q	energy released from chemical reaction
R	gas constant
rms	root-mean-square value

s	specific entropy
t	time
T	temperature
TR	transmissibility ratio
t_{CJ}	time at which detonation wave reached open end of PDE tube
t_{exh}	time at which PDE tube returns to relaxed state of 1 atm
t_{plt}	time at which plateau in pressure history at thrust wall ends
t_{ir}	time at which reflected rarefaction wave reached the open end
u	flow velocity
v	specific volume
V	volume
$x(t), \dot{x}(t), \ddot{x}(t)$	displacement, velocity and acceleration
$z(t), \dot{z}(t), \ddot{z}(t)$	displacement, velocity and acceleration
ZND	Zel'dovich-von Neumann-Doering
α	alpha damping value; also, dimensionless heat release value
β	beta damping value
γ	specific heat ratio
$\delta(t), \dot{\delta}(t), \ddot{\delta}(t)$	displacement, velocity, and acceleration
ζ	damping factor
θ	phase angle
κ	user defined constant
ρ	density

τ	time; also, time constant
ϕ	equivalence ratio
$\chi(t), \dot{\chi}(t), \ddot{\chi}(t)$	displacement, velocity and acceleration
ψ	user-defined constant
ω	forcing frequency, rad/s
ω_n	undamped natural frequency, rad/s
$\mathcal{F}(f)$	FT$\big(F(t)\big)$
$\mathscr{h}(f)$	FT$\big(h(t)\big)$- frequency response function
$\mathscr{p}(f)$	FT$\big(p(t)\big)$

Subscripts

0,1	initial state
2	final state
act	actual value
$comp$	acceleration compensated
$filt$	Filtered
$meas$	measured value
t	stagnation property

Accents

$(\tilde{\ })$	measured value
$(\hat{\ })$	deconvolved value

Chapter 1

Introduction

1.1 Motivation

The prospect of utilizing repeated pulses of detonations as a jet propulsion device or for power production has seen much interest over the past twenty plus years [1, 2]. Amongst some of the advantages of pulse detonation engines (PDEs) are higher theoretical efficiencies, ease of manufacture and maintenance, and reduced moving parts. With continued development, a major impediment in implementing PDEs, which is sustained and reliable detonations, appears to be addressed with sufficient confidence, at least for gaseous fuels and oxygen operation. One of the challenges in developing PDEs which has not been well addressed is the accurate measurement of unsteady thrust. The unsteady nature of the PDE means that conventional force measuring techniques that can be labeled as “quasi-static” may not be proper. The effective thrust generation period for a single pulse of detonation is in the order of milliseconds. Hence, load cells proposed to be used for unsteady thrust measurement need to have a sufficiently fast response time to record the thrust generated intermittently. Moreover, the acceleration of the structure due to impulsive excitation via detonations is also expected to yield an additive error. For longer test durations, the propagation and reflections of stress waves and pulse-to-pulse interaction between two consecutive pulses of thrust can affect the thrust measurement process.

There have been attempts to measure the maximum thrust generated by a PDE using the “ballistic pendulum” arrangement which is probably suitable only for a single-shot type of test [3, 4]. In such an arrangement, a detonation tube is hung by wires and the maximum displacement is related to the thrust. A more refined approach is to record the entire swing and thus the thrust history can be related to the displacement. An average thrust value can then be obtained from the detailed, single-pulse history.

While the single-shot ballistic pendulum approach may be acceptable for fundamental studies, engine development requires sustained test times to study various performance aspects such as cooling, throttling, etc. Thus, to satisfy engine development needs, another approach to thrust measurement makes use of a load cell which, without modification, is similar to that used in conventional aero-engine tests. Such an arrangement allows a long time record of a repetitive pulse loading to be acquired to yield an average thrust value [5–9].

A force measurement method which requires identification of the system's dynamic parameters has been well-established in thrust and drag measurements in shock tunnels [10–26] and appears feasible for application to PDEs. In fact, as an intermediate step, these force measurement techniques can be directly applied to a single-shot detonation tube. However, loading in the form of a pulse train of repeated detonations in case of PDEs complicates the measurement and analysis. There are at least two consequences of the repeated detonations on force measurements, namely, dynamic excitation of the system and the effect of interference between the pulses. For a fast operating PDE, the structural response due to consecutive detonations can also have a severe effect on the thrust measurement process. The superposition of the structural response with the generated thrust can overestimate or underestimate the thrust measured by the load cell depending upon the phase. Moreover, the sudden dynamic excitation induces inertial load due to the acceleration of the engine structure [27, 28]. The dynamic excitation also initiates stress waves within the structure. These stress waves propagate and reflect within the engine structure including the thrust measurement rig. The inertial load due to cyclic acceleration experienced by the system and the propagation and reflection of high-frequency stress waves are expected to affect the measured thrust which can cause an error even to the time-averaged value. Hence, conventional thrust measurement techniques need to be reconsidered to account for the pulse-to-pulse interaction, cyclic acceleration of the structure and the interference of stress waves which are the subject of this research.

1.2 Background

The subject matter of this dissertation focuses on the development of unsteady force measurement techniques for PDEs. Therefore, a general understanding of the detonation phenomenon and unsteady force measurement is useful before the detailed methodology is described. Consequently, a discussion on detonation and its thermodynamics, pulse detonation engines and a literature review on unsteady thrust measurements in hypervelocity facilities is presented in this section.

1.2.1 Detonation

Detonation is a supersonic combustion process involving a reacting shock wave where reactants transform into products accompanied by a rapid energy release. Since the detonation phenomenon is supersonic in nature, the reactants ahead are not disturbed prior to its arrival and remain in their initial state. As this strong shock wave passes, it compresses, heats and ignites the reactants resulting in a combustion zone propagating with the velocity of the shock. The shock wave and the combustion zone following it can be regarded as single surface of discontinuity separating the burned and unburned gases.

This surface of discontinuity is called the detonation wave. Across the detonation wave, thermodynamic properties such as pressure, temperature, etc. increase sharply. Detonations are a rare class of combustion.

On the other hand, deflagrations represent the common class of combustion. It is also referred to as slow combustion as the flame propagates with a velocity of less than O(10) m/s. Simultaneous heat conduction and diffusion of radicals ensure that the combustion speed is low and this slow reaction allows for the pressure to nearly remain constant during the process. Table 1.1 shows the qualitative differences between detonations and deflagrations. The subscript 1 for the parameters represents initial state for the reactants and subscript 2 represents the final state for the products.

Table 1.1: Qualitative differences between detonations and deflagrations in gases [29].

Parameter	Detonation	Deflagration
u_1/c_1	5–10	0.0001–0.03
u_2/u_1	0.4–0.7	4–16
p_2/p_1	13–55	0.98–0.976
T_2/T_1	8–21	4–16
ρ_2/ρ_1	1.4–2.6	0.06–0.25

Another phenomenon capable of rapid heat release and pressure rise is an explosion. It is a common to confuse an explosion with a detonation. An explosion does not essentially require the propagation of combustion wave through the exploding medium, whereas the presence of an explosive gas mixture is needed in order to have either a deflagration or a detonation [29]. In short, all three phenomena—detonations, deflagrations and explosions—exhibit energy release but deflagrations and detonations require a presence of a self-sustained waveform.

Detonations can be initiated by various methods. For instance, a detonation can be initiated in a long tube closed at one end and filled with a detonable mixture in the presence of a prominent ignition source. In such a scenario, the flame that travels along the tube towards the open end will have products expanding behind it. This expansion of products emits disturbances which coalesce to form fast travelling compression waves. These compression waves coalesce to form a shock wave which is supported by heat addition provided by the rapid heat release. This method of initiating a detonation is known as deflagration-to-detonation transition (DDT). Certain DDT enhancement devices can also be used to facilitate the transition from deflagration to detonation, such as a Shchelkin spiral, grooves, dimples, etc. The DDT method of initiation is actively applied in detonation-based engines such as PDEs. Alternatively, a shock wave or a detonation wave from another device could be transmitted to the detonable mixture to instantly form the detonation wave. This method of detonation initiation is known as shock- or detonation-induced detonation. More specifically, the pilot detonation wave used to initiate another detonation wave is called an initiator. Shock- or detonation-induced detonation is a new area of research and could be used for firing a multi-tube PDE as the detonation wave from one tube can be transferred to other tube to initiate detonation. Shock-induced detonations have been utilized in hypervelocity facilities to establish high-enthalpy flows [30].

1.2.2 On the Thermodynamics of Detonation

Detonations were systematically studied in the last quarter of the 19th century by various scholars including Berthelot, Vieille, Mallard and Le Chatelier [31]. Currently, two well-known theories can be used to model detonation waves. The first is called the

Chapman–Jouguet (CJ) theory, which was proposed separately by Chapman (1899) [32] and Jouguet (1905) [33]. The second theory which, was proposed much later, was the result of individual work in the early 1940s by Zel'dovich [34] , von Neumann [35] and Doering [36], and thus known as the *Zel'dovich–von Neumann–Doering* (ZND) theory that describes the leading shock wave driven by heat addition. A simplified study of detonation waves utilizing CJ theory is discussed in this section. This study will help to provide insight on the dynamics of detonation products and understand the potential of detonations for thrust generation.

Figure 1.1 shows a schematic of detonation wave propagation with the wave fixed in laboratory frame where subscripts 1 and 2 denote the states of the reactants and products respectively.

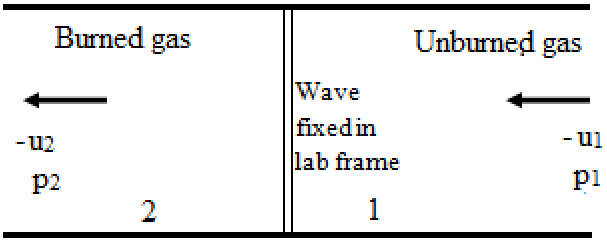

Figure 1.1: Schematic of detonation wave propagation with wave fixed in laboratory frame.

It is assumed that the flow is steady, planar and one dimensional. Hence, the conservation equations along with the equation of state for the reactants and products assuming these are perfect gases, neglecting heat transfer and friction, can be written as

$$\rho_1 u_1 = \rho_2 u_2 \tag{1.1}$$

$$p_1 + \rho_1 u_1^2 = p_2 + \rho_2 u_2^2 \tag{1.2}$$

$$c_{p,1}T_1 + \frac{1}{2}u_1^2 + q = c_{p,2}T_2 + \frac{1}{2}u_2^2 \tag{1.3}$$

$$p_1 = \rho_1 R_1 T_1 \tag{1.4}$$

$$p_2 = \rho_2 R_2 T_2 \tag{1.5}$$

It is assumed that all combustion events are collapsed into a discontinuity. The initial state of the gas is assumed to be known and q in equation (1.3) represents the heat added via release of chemical energy. Hence, the unknowns u_1, u_2, ρ_2, p_2 and T_2 can be obtained using the above equations.

The total enthalpy, sensible plus chemical, in a mixture is defined such that $h = c_p T + h^0$ with h^0 being the specific heat of formation in the standard state. The heat added via energy release shown in equation (1.3) can be represented as $q = {h_1}^0 - {h_2}^0$. Using equation (1.1) or the mass conservation equation, the expression for u_2 obtained can be substituted into equation (1.2) or the momentum equation to get a generic expression for u_1 as a function of pressure and density

$$u_1^2 = \frac{1}{\rho_1^2}\left[(p_2 - p_1)\Big/\left(\frac{1}{\rho_1} - \frac{1}{\rho_2}\right)\right] \tag{1.6}$$

Equation (1.6) can be substituted back into the mass conservation equation to obtain

$$u_2^2 = \frac{1}{\rho_2^2}\left[(p_2 - p_1)\Big/\left(\frac{1}{\rho_1} - \frac{1}{\rho_2}\right)\right] \tag{1.7}$$

Subtracting equation (1.7) from (1.6),

$$u_1^2 - u_2^2 = \left[(p_2 - p_1)\left(\frac{1}{\rho_1} + \frac{1}{\rho_2}\right)\right] \tag{1.8}$$

Equation (1.8) can be substituted into the energy equation to yield

$$c_{p,2}T_2 - c_{p,1}T_1 = q + \frac{1}{2}\left[(p_2 - p_1)\left(\frac{1}{\rho_1} + \frac{1}{\rho_2}\right)\right] \tag{1.9}$$

For constant specific heats, equation (1.9) reduces to the Hugoniot equation for a perfect gas with heat release

$$q = \frac{\gamma}{(\gamma - 1)}\left(\frac{p_2}{\rho_2} - \frac{p_1}{\rho_1}\right) - \frac{1}{2}\left[(p_2 - p_1)\left(\frac{1}{\rho_1} + \frac{1}{\rho_2}\right)\right] \tag{1.10}$$

Equation (1.10) holds for a shock wave when $q = 0$. For an inert gas with constant specific heat, equations (1.8) and (1.10) can be used to obtain the inert Hugoniots, also known as shock adiabats. Similarly, equations (1.8) and (1.9), and for chemical equilibrium, can be used to iteratively solve for all possible combinations of pressure and specific volume to yield the Hugoniot curve. For a reactive mixture, two curves can be obtained representing states of before and after heat release.

Figure 1.2 shows the real gas Hugoniot curves for a stoichiometric H_2–air combustion with initial conditions of $T = 300$ K $(27°\text{C})$ and $p = 0.1013$ MPa. The inert or shock Hugoniot represents all possible values of pressure and specific volume that can be achieved via shock compression without combustion.

For combustion, the heat added q pushes the Hugoniot curve to the right. However, any possible solution for the reactive Hugoniot still depends on the initial state of the mixture. Figure 1.2 also defines an angle α such that

$$\tan\alpha = \frac{p_2 - p_1}{(1/\rho_1) - (1/\rho_2)} \tag{1.11}$$

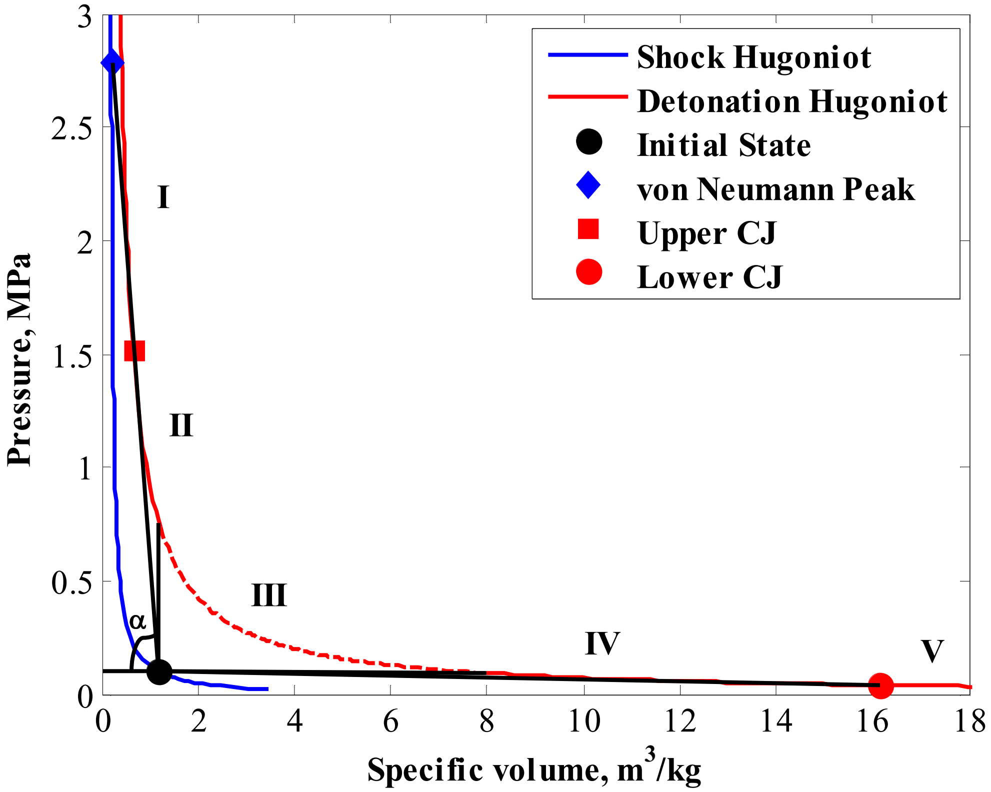

Figure 1.2: Real gas Hugoniot curves for stoichiometric H_2–air combustion.

Equation (1.11) along with equation (1.6) can be used to yield

$$u_1 = \frac{1}{\rho_1}\sqrt{\tan\alpha} \tag{1.12}$$

It can be noted that the form of the Hugoniot equation is a rectangular hyperbola and there are two tangents to the curve through the initial state point. These tangency points are known as upper and lower CJ points. The upper CJ point corresponds to combustion supported by a high-speed compression wave and the lower CJ point is a low-speed expansion wave [29]. The tangents, horizontal and vertical lines through the initial state point divide the Hugoniot into five regions, as shown by Roman numerals I–V in Fig. 1.2. Regions I corresponds to strong detonation region with supersonic gas velocities before and subsonic after the wave. Region II is the weak detonation region with supersonic gas velocities before and after the wave. In region III, equation (1.12) shows a negative wave velocity, which is not physically possible and plotted as a dashed line. Region IV gives solutions which correspond to weak deflagration and the gas flow stays subsonic across the wave. Region V gives strong deflagration with gas speed increasing from subsonic to supersonic across the wave which is physically impossible.

Although this thermodynamic study is based on CJ detonation theory, for providing better insight of the phenomenon, Fig. 1.2 also shows a von Neumann peak which corresponds to the state of the gas after compression via a shock wave but before heat addition. A tangent drawn from this point to a point in region II will intersect region I at the ZND point. This depicts that all of the chemical enthalpy is added to the gas before region II is reached. For detonation waves, if a subsonic flow occurs behind the detonation wave, the trailing expansion waves can penetrate the reaction zone and attenuate the detonation [37]. Hence, a freely propagating detonation must have either a sonic or supersonic condition behind it. Moreover, a stable detonation is realized only when the final conditions of the products correspond to the upper CJ point. This implies that the velocity of the wave is equal to the sound speed of the combustion products plus their mass velocity such that the detonation wave is self-sustained [29]. The discussion on the thermodynamics of detonation wave from the detonation wave propagation point of view is further continued in Chapter 2, where CJ detonation properties are calculated using the initial conditions to determine the state of the products behind the detonation wave.

With the fundamental knowledge of the thermodynamics of detonation waves and following detailed explanation in [29, 38], a $p{-}v$ and a $T{-}s$ diagram representing a pulse detonation engine cycle are constructed and shown in Figs. 1.3 and 1.4 respectively. The detonation of a stoichiometric hydrogen–air mixture at an initial state of 0.1013 MPa and 300 K is considered and which is represented by the initial state point 0 in Fig. 1.3. The equilibrium conditions were obtained using the NASA CEA code [39]. Figure 1.3 shows the inert Hugoniot by a dashed blue line and the reactive Hugoniot by a dashed red line. The corresponding von Neumann and upper CJ point for this case are also shown in Fig. 1.3.

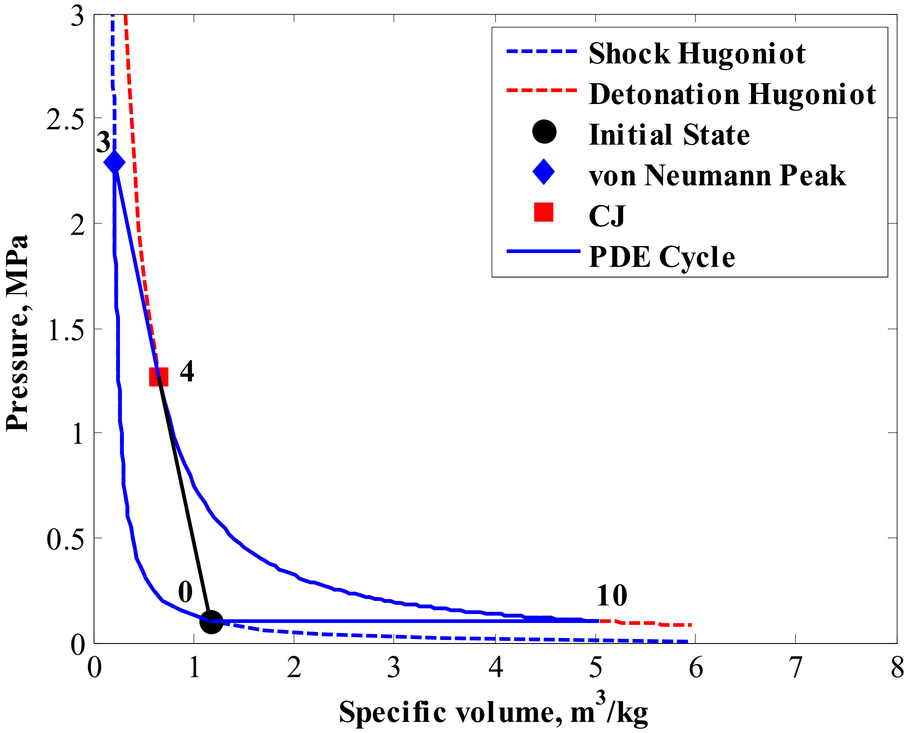

Figure 1.3: A $p{-}\ v$ diagram of the pulse detonation engine cycle operating with a stoichiometric hydrogen–air mixture initially at STP.

The solid blue line depicts the ideal PDE cycle. In the cycle, the path 0 to 3 represents compression via a shock, followed by state 3 to 4 representing heat addition due to release of chemical energy from combustion. Path 4 to 10 represents the isentropic expansion which is followed by path 10 to 0 representing heat rejection. The area enclosed by the PDE cycle in the $p-v$ diagram represents the work output of the engine and the area enclosed in the $T-s$ diagram represents the heat release of the engine.

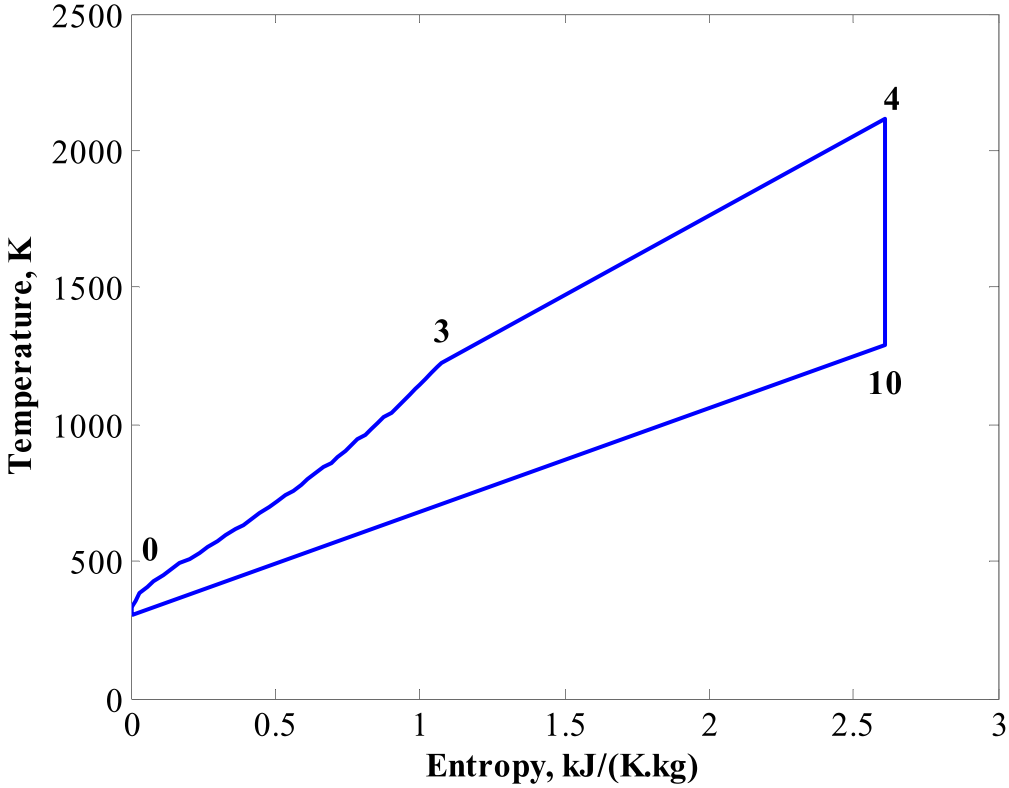

Figure 1.4: A $T-s$ diagram of the pulse detonation engine cycle.

It is important to note that the procedure described above considers the equilibrium states of the gases at each point in the non-reactive and reactive Hugoniot. This signifies that the states of gases depicted in Figs. 1.2–1.4 are independent of time.

However, the entire detonation phenomenon is unsteady. This property of detonation calls for an in-depth study of thermodynamics considering characteristics time of the process. A study of nonequilibrium thermodynamics can provide confidence in results obtained via classical thermodynamics and better estimate the performance of PDEs.

1.2.3 The Pulse Detonation Engine

Pulse detonation engines utilize detonation waves to compress and combust the fuel–oxidizer mixture. This application of detonations for propulsion applications have been explored for the past 50 years or so [40]. Since detonation waves are an extremely efficient means of combustion, the temperatures and pressures achieved and the available power levels are much higher than other combustion engines such as gas turbines, pulsejets or rockets. The major benefit of the PDE is the increase in power or thrust density as the rapid burning or material conversion occurs at a rate thousands of times faster than in a flame [1]. Hence, all these advantages call for building of practical PDEs for use in propulsion and power generations applications.

Interestingly, a PDE can be as simple as a straight tube with constant cross-sectional area and with one end closed and other end open. Incorporating control valves to supply fuel and oxidizer and an ignition system makes up a working model. A nozzle can be used to further accelerate the flow at the exit. A practical PDE may also have one or more devices to facilitate the DDT process such as a Shchelkin spiral. In the present study, a simple PDE is used for the development of unsteady thrust measurement techniques. A detailed description of the experimental setup utilizing a simple PDE is further described in Chapter 3.

A basic PDE cycle has four stages, namely, purge, fill, combustion and blow down or exhaust. Figure 1.5 shows the different stages of a PDE cycle. The process is started with the purging phase during which fresh air or inert gas is blown through the tube. The purge phase is followed by the filling phase. During the filling phase, a detonable mixture of fuel and oxidizer is delivered into detonation chamber to the required volume. Near the end of the filling phase, the combustion phase commences when a spark from an ignition source is fired. This facilitates the development of a detonation wave which travels through the mixture and causes the pressure and temperature to increase behind it. Rapid heat release due to the combustion of mixture occurs. Due to the closed boundary condition, a so-called Taylor rarefaction follows the detonation wave. The combustion phase is followed by a blow down phase. During this phase, first the detonation wave exits which is followed by the burned gases. The exit of detonation wave forms a rarefaction wave at the open end which travels towards the closed end of the tube and exhausts any remaining burned gas left in the tube. A PDE cycle is completed after the blow down phase and the next cycle is then started with a new purging phase. The purging process aids in cooling the tube and prevents the fresh detonable mixture from igniting due to high temperature or residual combustion products from the previous cycle. An important parameter which characterizes a PDE is its operating frequency. The operating frequency signifies how many times the above four phases occur in a second. The operating frequency of a PDE is controlled by valves and the igniter. A high operating frequency implies high thrust or specific impulse per cycle. Practically, a high-frequency PDE system can be obtained either by timing the supply valves such that they deliver the detonable mixture at a very high frequency or by using multiple tubes with phased operation to increase the effective frequency of the system.

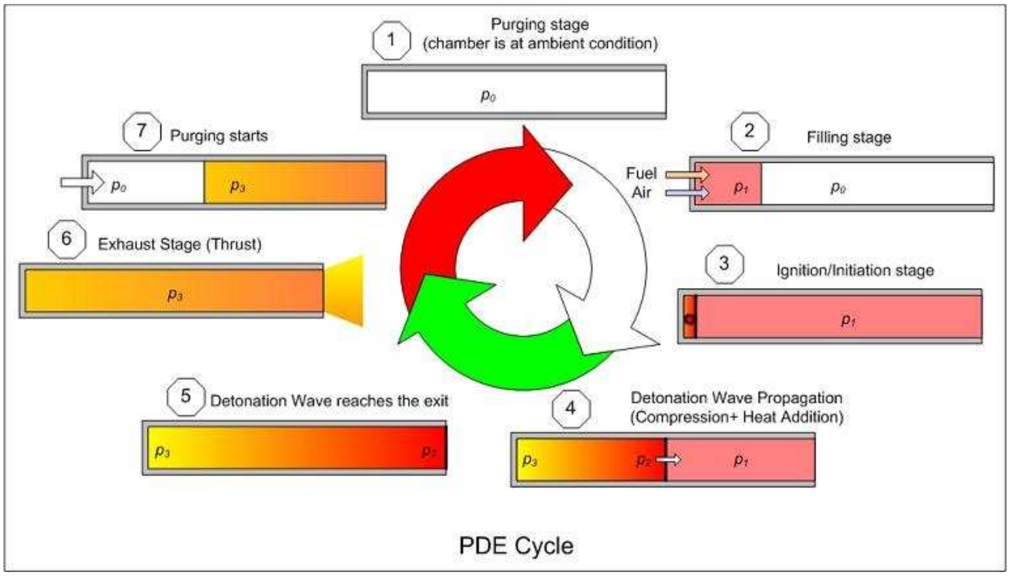

Figure 1.5: Stages of a PDE cycle [31].

1.2.4 Literature Review of Unsteady Force Measurements in Hypervelocity Facilities

Unsteady force measurements techniques in hypervelocity facilities provide the basis for the development of unsteady force measurement techniques for PDEs. Hypervelocity facilities offer a relatively short time whereby there is a distinct possibility that the model-balance structure will not achieve equilibrium. This dynamic state requires dynamic calibration of the entire model-balance system to account for the effects of system dynamics or any inertial effects.

Unsteady force measurements in impulse facilities such as shock and gun tunnels have been developed. Researchers have addressed this problem in different ways [11–26]. Bernstein [11] gave a most comprehensive but dated review of this topic. In addition to this, much progress has been made in recent years through better instrumentation and computer-aided techniques. Tanno et al. [13] proposed acceleration-based techniques to estimate the correct aerodynamic force in a short-duration test facility. They described a way to experimentally identify the modes of vibration of a relatively long model. Determining the modes of vibrations established the nodes of each mode. This allowed the determination of the spot where accelerometers could be placed such that averaging the measured acceleration signals in the corresponding nodes cancelled out the natural vibration response of the system, leaving behind the actual acceleration experienced by the structure. This method effectively cancelled out the oscillations associated with the lower modes of natural vibration after the oscillations from higher modes of natural vibration were filtered out.

Tanno et al. [14] also described a force measurement technique for an extremely short test time. The technique utilized a deconvolution method for signal recovery. The experimental apparatus was a vertical shock tube and the test article was a sphere, 80 mm in diameter. The main aspect of this work was the signal recovery method used to remove the oscillations caused by mechanical vibrations of the test article. This method involved obtaining a system function through calibration. An impact test was performed to facilitate calibration where the output from the accelerometer mounted inside the test sphere was divided by the output of the impact hammer leading to the determination of the transfer function when the calculations were carried out in the frequency domain. The input signal was recovered by using this transfer function. Tanno et al. [14] included an interesting discussion on the frequency response function of the system obtained with the impact test. As presented in the paper, the transfer function of the system is given by,

$$TF(f) = \frac{O(f)}{I(f)} \tag{1.13}$$

where $I(f)$ was the input to the system in the form of an impulsive force. Tanno et al. stated that the impact hammer could not fully initiate the high-frequency components; hence $O(f)$ was low for higher values of frequencies. In other words, the high-frequency component of $TF(f)$ would be amplified when used to reconstruct the input. This amplification of high-frequency component in $TF(f)$ brought about high-frequency noise on the deconvoluted signals.

The effects of forces that are applied for very short periods of time, or are changing rapidly, must be considered in terms of the propagation of stress waves [10]. Stress waves are mechanical waves and travel in elastic medium with a velocity equal to $\sqrt{E/\rho}$, where E is the modulus of elasticity and ρ is the density of the medium. The elasticity of the material provides the restoring force of the wave. The study of the decay rates of such waves to measure material damping was reported by Nowick [41].

A method known as the stress wave force measurement technique (SWFM) [17] was also developed to address the complications from the short test duration which is also based on the study of stress waves. This method measures the stress waves propagating within the force balance. The SWFB principle utilizes the stress waves initiated in a model-balance structure due to aerodynamic loading. This method requires instruments that can capture the high-frequency stress waves.

Mee et al. [15] analyzed different techniques for the calibration of force balances for use in short-duration impulse hypersonic facilities. The authors discussed four calibration techniques applied to a single-component stress wave force balance. In addition to this, these authors also discussed the use of the deconvolution technique to infer aerodynamic forces on models in impulse tunnels through an established system transfer function. A step load, an impulse and an arbitrary input were used as calibration inputs to the system and the corresponding outputs were measured to establish the system transfer function which was later used to facilitate the deconvolution procedure and reconstruct inputs for different other cases.

Joarder et al. [16] carried out dynamic calibration based on the procedure developed in [15]. Force recovery was carried out through an iterative procedure. Initially a force variation for a typical free stream condition in the shock tunnel was assumed based on modified Newtonian theory. Then the assumed force signal was convolved using the system response function obtained from dynamic calibration to arrive at an acceleration history. The iteration process was terminated when the experimentally obtained acceleration history matched well with that estimated from a system dynamic approach.

Another force measurement approach is internal and accelerometer based [18–20], requiring the model to be free floating. This type of internal balance requires springs and rubber flexures mounted in a model suspension system. The measured acceleration-time history can then be related to obtain the force history.

As with conventional aerodynamic facilities, force balances for impulse facilities are either internal where the sensing elements are placed within the test model or external otherwise. Robinson et al. [22] showed that high accuracy of the recovered force and moment loads was attained using an external force balance. Also, for a blunt body, these authors found that the interaction of an external balance on the model forces was less than that of an internal balance. Moreover, [24, 25] discussed the possibilities of using finite element methods for developing aerodynamic force measurement devices.

References [27, 28] discussed the effect of inertial forces brought about by oscillation of the model–balance structure under aerodynamic loading. In both works, the authors discussed a procedure which required measuring the acceleration during a test. This measured acceleration is multiplied by a value called the "oscillating mass" which is the active oscillating mass of the model–balance structure. The product of the two yields the effective inertial force from which the measured force is subtracted to get the actual aerodynamic force. Reference [27] describes the vibrating mass to be a part of the entire model-balance structure and considers only the forward half of the balance and the model. In [28], a procedure is developed to estimate the "oscillating mass" of the model–balance structure which incorporates measuring the acceleration of the model–balance structure due to known impulsive forces. The subsequent division of the applied force by the measured acceleration within a restricted time interval window gave the value of the effective oscillating mass.

Based on the study of the force measurement techniques developed for hypervelocity wind tunnels, an unsteady force measurement technique for PDEs is developed accounting for the influence of dynamics of the system under repeated loading and inertial effects due to the inherent unsteadiness of the system brought about by repetitive acceleration.

1.3 Objectives and Contributions

1.3.1 Objectives of the Research

The primary objective is to develop a methodology to measure the thrust generated by a pulse detonation engine which is complicated by the inherent unsteadiness of the entire system. The approach is experimental, numerical and analytical. For this purpose, a small PDE rig is built. In addition to this, finite element analysis is performed to evaluate the method. Analytical methods are also be applied to check the obtained results. Since the entire methodology is developed based on force measurement techniques in hypervelocity facilities, the developed methods for PDEs is also tested to recover drag force on a blunt nose cone model in a nominal Mach 8−9 flow. The research objectives are listed below.

I. Develop a general approach to recover actual thrust generated by a pulse detonation engine accounting for the influence of pulse-to-pulse interaction under repeated loading, inertial effects due to cyclic acceleration and interference due to stress waves.

II. Develop a pulse detonation engine including all the essential systems required for its operation in order to study unsteady thrust characteristics by applying the developed general approach. Calibrate the setup to identify its practicability and determine other essential parameters to facilitate data analysis.

III. Perform a finite element analysis of the unsteady thrust characteristics of a PDE via dynamical model to evaluate the effectiveness of the developed approach.

IV. Estimate thrust generated by a PDE using semi-empirical methods. Also, revisit the analytical model to estimate the pressure gain at the thrust wall for thrust estimation.

V. Apply the same general approach developed to recover actual thrust generated by a PDE to estimate true aerodynamic drag experienced by a blunt nose cone model in a nominal Mach 8–9 hypersonic wind tunnel and check for its viability.

1.3.2 Literature Contributions

The objectives of the research are accomplished and the results have been presented in the form of conference papers with corresponding journal articles, some still being prepared. The following is the list of publications:

I. Lu, F.K., Awasthi, M. and Joshi, D.D., "Influence of Unsteadiness on Thrust Measurements of Pulse Detonation Engines," *AIAA Paper 2010–755,* 2010.

II. Joshi, D.D. and Lu, F.K., "On the Unsteady Thrust Measurements for Pulse Detonation Engines," *AIAA Paper 2012–0324*, 2012.

III. Joshi, D.D., Vadassery, P. and Lu, F.K., "Acceleration Compensation for Force Measurements in Hypersonic Shock Tunnel," *AIAA Paper 2013–1020*, 2013.

IV. Joshi, D.D. and Lu, F.K., "Unsteady Force Measurements for Hypersonic Shock Tunnel," *29th International Symposium on Shock Waves,* Paper 131, July 17–22, Madison, Wisconsin, 2013.

V. Vadassery, P., Joshi, D.D., Rolim, T.C. and Lu, F.K., "Design and Testing of an External Drag Balance for a Hypersonic Shock Tunnel," *Measurement*, Vol. 46, No. 7, 2013, pp. 2110–2117.

VI. Peace, J., Joshi, D.D. and Lu, F.K., “Experimental Study of High Frequency Valve Injectors with Variable Cavity Lengths,” *AIAA Paper 2014–1318*, 2014.

VII. Joshi, D.D. and Lu, F.K., “Unsteady Force Measurement Techniques for Pulse Detonation Engines,” *50th AIAA/ASME/SAE/ASEE Joint Propulsion Conference*, July 28–30, 2014, Cleveland, Ohio. Accepted.

VIII. Joshi, D.D. and Lu, F.K., “Unsteady Force Measurements for Hypersonic Shock Tunnel,” *Measurement*. Submitted.

Papers being prepared:

I. *Unsteady Thrust Measurement Techniques for Pulse Detonation Engines*.

II. *Study of Unsteady Thrust Characteristics of Pulse Detonation Engines using Finite Element Analysis.*

III. *A New Method to Predict Flow Rates of Gaseous Fuels Injected Intermittently for Pulse Detonation Engines.*

IV. *Cycle Analysis for Pulse Detonation Engines*

V. *A Comparison of the Performance of Pulse Detonation Engines, Gas Generators and Diesel Generators*

VI. *Prospects for Detonation-Based Propulsion and Power*

VII. *Wave Processes in Fluidic Valves for Detonation Engines*

Chapter 2

General Approach

This chapter describes in detail the methodology adopted to recover true thrust from the measured thrust of a PDE. The first section of this chapter introduces the problem, outlines the deconvolution procedure, discusses the calibration procedure used to establish the system transfer function and finally presents the acceleration compensation technique developed to account for the inertial forces. In addition, this chapter also discusses the method of determining impulse of a PDE using semi-empirical methods and dynamical modeling of the PDE using finite element analysis.

2.1 Methodology

2.1.1 Introduction to the Problem

A PDE generates thrust from intermittent pulses of detonations. This nature of loading excites the system impulsively and makes the thrust generation process unsteady, unlike regular gas turbine engines which generate steady thrust. The inherent unsteadiness in the system affects the measured thrust. In addition, there are other aspects related to this unsteadiness which can induce errors in the measurement. Hence, it is important to identify the factors that can affect the unsteady thrust measurement process.

One of the important factors that have a large impact on the unsteady thrust measurement process is the damping factor of the system. In general, engine systems used for fundamental studies are underdamped. Underdamping is not a problem for low-frequency operation, say, at less than 1 Hz, since the entire structure will have enough time to return to steady state before the occurrence of the next pulse. However, there is consensus, based on system studies and from numerical simulation, that pulse detonation engines must operate with higher frequencies in the 20−100 Hz range to be considered as part of a viable propulsion system. At higher operating frequencies, the structural response of an undamped system may not necessarily damp out before the advent of the following pulse. This situation causes pulse-to-pulse interaction of the unsteady thrust. One way to dampen out the system in a relatively short time is to make the system overdamped which might not be practical for a system intended to be utilized for fundamental studies. Moreover, for research purposes, engines are usually mounted on a nearly frictionless slide to facilitate direct measurement of thrust. The only significant force restraining its motion is usually the preload applied to the load cell. Hence, for research implications, an overdamped test rig is not a viable option for studying unsteady thrust characteristics. Therefore, research requirements dictate the system dynamics of the experimental setup. Nonetheless, the system can be assumed to be linear and characterized by a system transfer function. The system transfer function can be established by measuring the response due to a known input. This system transfer function can provide a complete description of the dynamic characteristics of the system. A deconvolution procedure can then be carried out using an established transfer function to alleviate the effects of convolution arising due to pulse-to-pulse interaction of the unsteady thrust into the measured thrust values. The procedure is further described later in this chapter.

In addition to pulse-to-pulse interaction, the thrust signals can also include high-frequency components. Some of the sources of these high-frequency contents are as follows. The occurrence of a transient but powerful phenomenon such as detonation inside a detonation tube propagates stress waves within the structure. The propagation and reflection of stress waves are prominent during the phase when thrust is being generated. The frequencies of the associated stress waves depend on the property of the material used, dimensions of the engine and reflecting surfaces. These propagated and reflected stress waves are convolved with the thrust signals. Hence, this superposition of stress waves introduces errors in the thrust measurement. The velocity of stress waves traveling in steel is in the order of 7800 m/s. For the developed setup with a length of 0.66 m, the lowest frequency of the stress waves is O(12,000) Hz. These stress waves get reflected multiple times within the structure, appearing in the thrust data as weak waves with high frequency.

Another source of high-frequency content in the measurement process is brought about by the addition of resonance responses of the instrumentation such as load cell and accelerometers. However, the resonant frequencies of the instruments are usually very high and in the order of several thousand hertz. The high-frequency content brought about by the combined effects of propagation and reflection of stress waves and the resonant responses of the instruments can be removed by filtering techniques. The chosen filtering techniques for this research include Butterworth filters and moving averages of the measured signals.

Finally, another complexity in unsteady thrust measurement of a PDE is the effect of inertial forces. The generation of thrust causes the entire underdamped engine and the thrust measurement rig to vibrate. These vibrations arise from the transient response of the system. The induced acceleration of the thrust measurement rig along with the vibrating/oscillating mass generates inertial forces which get added to the measured force. The aggregate inertial force is the contribution of instantaneous acceleration and an *effective oscillating mass* of the system, which has to be deducted from the measured thrust. Therefore, a separate procedure is developed to account for the inertial forces added in the measured thrust signal and is further discussed later in this chapter.

A general approach is developed to obtain correct thrust values from the measured thrust accounting for the effects of pulse-to-pulse interaction, stress wave interference, added inertial forces and other high frequency contents. The developed approach will be first applied to recover actual thrust from the measured thrust for a PDE operating at 10 and 20 Hz. The recovered actual thrust is further used to calculate the specific impulse of the PDE. This calculated value of specific impulse is compared against values determined using semi-empirical methods. The semi-empirical method involves a control volume analysis of the PDE. Moreover, the experimentally calculated and semi-empirically determined specific impulse values are compared against the specific impulse estimated using an analytical models developed by other researchers in [1, 42, 43]. The analytical methods incorporate the determination of specific impulse via estimation of pressure history at the closed end of the PDE, also referred to as the thrust wall.

Finally, the effectiveness of the general approach for cases when the operating frequency is higher such as 50 and 100 Hz is determined by finite element analysis of a PDE dynamical model using ANSYS Workbench 13.0. Force input with a frequency of 50 and 100 Hz is applied to the dynamical model and the calculated output is further processed to check the validity of the general approach.

A detailed description of the general approach is provided in Section 2.1.4 of this chapter. In short, the general approach developed has two primary steps. The first is the deconvolution procedure carried out using the established transfer function. The second is the acceleration compensation procedure. The general approach from hereafter will be referred to as the "experimental approach" to avoid any confusion with chapter heading itself.

2.1.2 Deconvolution

Convolution is mathematically an operation that involves superposition, multiplication and shifting of two functions resulting in a new function. An inverse procedure can be applied to recover the original function; this inverse procedure is called deconvolution. This reverse operation can be utilized to calculate the input to the system, knowing the system's impulse response and its output signal. For a linear system, the convolution of any function can be written as,

$$\mathrm{y} = \int_0^t h(t-\tau)x(t)d\tau \tag{2.1}$$

$$= x(t)\otimes h(t) \tag{2.2}$$

where $y(t)$ is the output of the system, $x(\tau)$ is the input to the system and $h(t)$ is the system transfer function.

The above equations can be applied for both continuous and discrete signals. The output of the system, $y(t)$, can be determined using any arbitrary input, $x(\tau)$, and established system transfer function, $h(t)$. However, performing the integration in the time domain can be complicated. The convolution process is easier to perform in the frequency domain. The convolution of two functions in the frequency domain is given by

$$Y(f) = X(f)\, H(f) \tag{2.3}$$

where $Y(f)$ is the Fourier transform of the measured output, $X(f)$ is the Fourier transform of the input and $H(f)$ is the Fourier transformed transfer function of the system. The mathematical operations become much simpler in the frequency domain. Simple multiplication or division can facilitate the procedure of deconvolution [44].

A block diagram showing the input–output relation in the time and frequency domains is depicted in Fig. 2.1. Fast Fourier transform (FFT) algorithms in Matlab are used for data processing. Mathematical operations are carried out in the frequency domain and deconvolution by an inverse FFT reverted the data to the time domain.

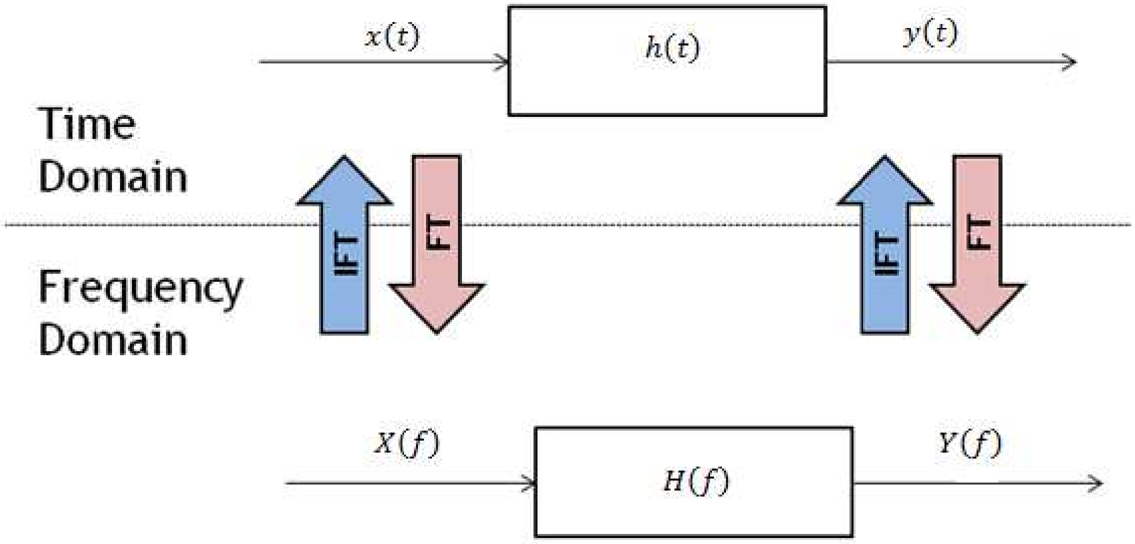

Figure 2.1: Block diagram showing the relation between the input, output and the transfer function in both time and frequency domain [45].

2.1.3 Fast Fourier Transform

As mentioned in Section 2.1.2, the fast Fourier transform (FFT) is one of the vital mathematical tools used in this work. The FFT is simply a very efficient scheme for computing the discrete Fourier transform, namely, the digital implementation [46]. The Fourier transform comprises of sinusoidal basis functions that are used to decompose the function into an infinite set of sinusoidal functions [47]. This set of infinite sinusoidal functions is used to generate the spectral contents for the given function. The spectral contents of the function are also called the frequency response which is a complex function of frequency that can be expressed by a magnitude and a phase spectrum. The continuous Fourier transform (CFT) of a function can be defined as

$$X(f) = \mathcal{F}\{x(t)\} = \int_{-\infty}^{\infty} x(t)\, e^{-j2\pi ft} dt \tag{2.4}$$

where

$$e^{-j2\pi ft} = \cos(2\pi ft) - j\sin(2\pi ft) \tag{2.5}$$

As mentioned earlier, for digital signal processing, the DFT is used which utilizes a finite dataset that is physically realizable and expressed as,

$$X(k) = \sum_{n=0}^{N-1} x(n)\, e^{-j2\pi kn/N}, \quad k = 0,1,2,\dots\dots,N-1 \tag{2.6}$$

The DFT is usually computed with the FFT algorithm which is a computationally efficient method for determining the DFT. The FFT outputs $(N+2)$ values for a given data record size of N which has to be a number represented by a power of two. Half of the dataset contains the real, cosine component and the other half contains the imaginary, sine component. The real component represents the symmetric portion of the signal while the imaginary components represent the asymmetric portion. In order to fulfill this requirement, all the measured datasets are sampled at the same rate for the same duration with appropriate discretization ensuring that the sample size is a power of two. Prior knowledge of desired sample size and sampling rate helps to prevent any trimming and padding of the data record. Trimming the data reduces the spectral resolution and hence reduces the likelihood of capturing the periodic component of a signal. Trimming can also cause the signal to be nonstationary when a higher frequency component has to be analyzed. Similarly, padding introduced by adding zeros or interpolation may be misleading as it can set up unstructured resolution in the signal. It is also important to note that FFT produces two-sided spectra that contain both positive and negative frequencies. Usually the negative spectrum of the frequency is ignored due to symmetry.

2.1.4 Experimental Approach

The experimental approach is in fact the general approach developed as a part of this research project to recover actual thrust generated by the PDE from measured thrust. The general approach or the experimental approach has two main steps. The first is the reconstruction of generated thrust using a system transfer function. The second is acceleration compensation to account for the additional inertial force due to the vibration of the system. Both of these steps are further discussed in the following subsections.

2.1.4.1 System Transfer Function

The first step of the experimental approach involves deconvolution through a previously established system transfer function. The approach assumes that the PDE and its thrust stand are a linear, time-invariant system. Thus, as shown by the block diagram of Fig. 2.2, an input of $p(\tau)$ can be related to an output of $f(t)$ where the system's transfer function is $h(t-\tau)$ with the relationship between the three given by a convolution integral similar to equation (2.1) in the time domain [15]. This relationship is given by

$$F(t) = \int_0^t p(\tau)h(t-\tau)d\tau \;\equiv\; p(\tau)\otimes h(t-\tau) \underset{IFT}{\overset{FT}{\leftrightharpoons}} \mathscr{p}(f)\mathscr{h}(f) = \mathcal{F}(f) \tag{2.7}$$

Equation (2.7) relates the input and the output via the system's transfer function which can be determined as follows. If $p(\tau)$ and $F(t)$ are known or, equivalently, if $\mathcal{F}(f)$ and $\mathscr{p}(f)$ are known, then $h(t-\tau)$ or $\mathscr{h}(f)$ can be found, the former by a deconvolution procedure. Once the system transfer function is known and kept unchanged, then any arbitrary output can be determined from a measurement of the input and vice versa. As will be elaborated further, it was found to be convenient to relate a pressure measurement as the input with the desired output, namely, the force.

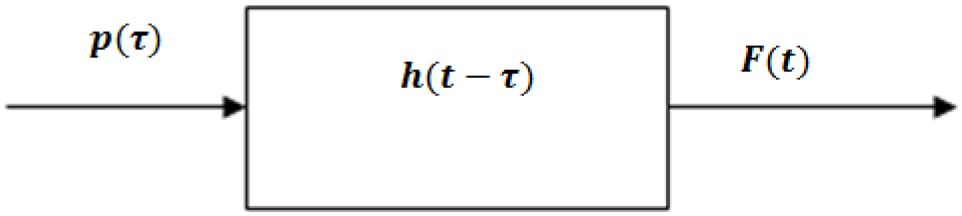

Figure 2.2: Block diagram for the system under consideration.

It is standard procedure for the dynamics of a linear, time-invariant system to be conveniently determined by applying an impulse say from an instrumented impulse hammer. In the present study, it is convenient to relate pressure measured at the exit of the PDE to the input. Hence, an input in the form of a single shot of detonation is used instead of a hammer strike,

$$p_{det}(\tau) = p(\tau) \tag{2.8}$$

which yields a response

$$F(t) = \int_{0}^{t} p(\tau)h(t-\tau)d\tau \tag{2.9}$$

so that

$$\mathcal{h}(f) = \frac{\mathcal{F}(f)}{\mathcal{p}(f)} \tag{2.10}$$

With this established transfer function and a subsequent measured input, one can then determine the output in the Fourier domain or, by a deconvolution procedure, in the time domain.

2.1.4.2 Acceleration Compensation

The exit of the detonation wave and that of the subsequent burned products apply an impulsive force to the system and excites it dynamically. In addition, this process occurs in a cyclic manner resulting in a cyclic acceleration of the system. Hence, the mode of operation of a PDE prevents a steady force from developing. The measured force is an oscillatory one which is interfered with by the oscillatory acceleration of the entire structure. Ideally, the true unsteady thrust generated by a PDE can be described as the product of the mass of PDE and the acceleration through which it undergoes due to the exit of the detonation wave and the following burned gas. This generated force in principle can be measured without compensation by a load cell mounted on a *completely rigid* thrust measurement rig. However, in reality, the reaction of the thrust measurement rig to this dynamic excitation is not ideal, that is, the entire system, including the thrust measurement rig and the PDE, vibrates. Although the displacement of the thrust measurement rig might not be detected by eye, the acceleration can still be significant. In fact, this induced acceleration is responsible for the inertial forces. Hence, the measured thrust for a PDE operation includes both the force generated via detonations and any inertial forces added by the vibration of the thrust measurement rig. The added inertial force needs to be accounted for separately in addition to the deconvolution procedure above to get the actual thrust generated. In this section, a description of structural dynamics of the PDE system in the form of a single degree-of-freedom (SDOF) is presented followed by the description of the acceleration compensation technique adopted.

The simplest approach to model the PDE along with its thrust measurement rig is by using a SDOF system as shown in Fig. 2.3. The basic elements are a mass m, comparable to a PDE and a spring-dashpot unit attached to the mass at one end and the thrust measurement rig at other end. This spring-dashpot represents the load cell. The displacement of the thrust measurement rig is $z(t)$ and the force applied to the entire system is given by $F(t)$. The displacement of the mass is given by $x(t)$ and the relative displacement of the mass with respect to the thrust measurement rig is given by

$$\delta(t) = x(t) - z(t) \tag{2.11}$$

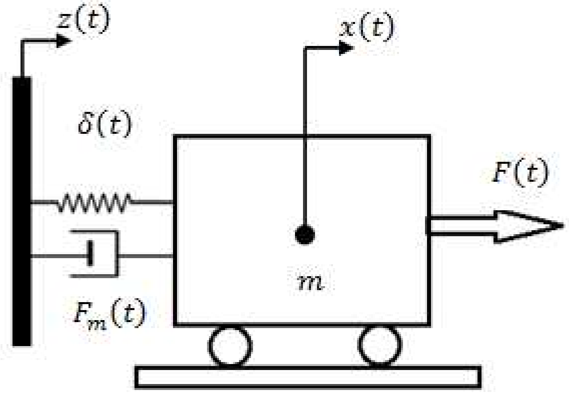

Figure 2.3: SDOF model for PDE with thrust measurement rig.

The equation of motion for the system can then be written as

$$m[\ddot{\delta}(t)] + c[\dot{x}(t) - \dot{z}(t)] + k[x(t) - z(t)] = -m\ddot{z}(t) + F(t) \tag{2.12}$$

where k is the equivalent stiffness and c is the equivalent damping of the system. The parameter $F_m(t)$ represents the total force transmitted to the load cell. This force can also be expressed as

$$F_m(t) = -c[\dot{x}(t) - \dot{z}(t)] - k[x(t) - z(t)] - m\ddot{z}(t) \tag{2.13}$$

Equation (2.12) can also be written as

$$\ddot{\delta}(t) + 2\zeta\omega_n\dot{\delta}(t) + \omega_n{}^2\delta(t) = \ddot{\chi} \tag{2.14}$$

where $\omega_n = \sqrt{k/m}$ such that $k = m\omega_n{}^2$ and $c = 2\zeta\sqrt{km}$. And, $\ddot{\chi}$ signifies the acceleration which is proportional to the forcing function represented by the right-hand-side of equation (2.12). This acceleration can be expressed in terms of sinusoids in the form of a Fourier series. Considering the form of $\chi = \chi_o e^{i\omega t}$ yields $\ddot{\chi} = -\omega^2\chi_o e^{i\omega t}$; thus, the solution to the differential equation (2.14) is given by

$$\delta(t) = De^{-\zeta\omega_n t}\sin\left(\sqrt{1-\zeta^2}\,\omega_n t + \theta\right) + \frac{\left(\frac{\omega}{\omega_n}\right)^2 \chi_o e^{i\omega t}}{1 - \left(\frac{\omega}{\omega_n}\right)^2 + 2i\zeta\frac{\omega}{\omega_n}} \tag{2.15}$$

where D is the amplitude of the motion, ω is the circular frequency of the forcing function, ω_n is the circular undamped natural frequency, θ is the phase angle of the steady state response relative to the excitation, ω/ω_n is the ratio of the frequency of forcing function and undamped natural frequency and ζ is the damping factor of the system. In addition, the form of the derived solution also helps in deducing the force transmissibility to the thrust measurement rig due to the applied force. Transmissibility of the dynamic force is presented in the form of the transmissibility factor given by

$$TR = \frac{\sqrt{1 + \left(2\zeta \frac{\omega}{\omega_n}\right)^2}}{\sqrt{\left[1 - \left(\frac{\omega}{\omega_n}\right)^2\right]^2 - \left(2\zeta \frac{\omega}{\omega_n}\right)^2}} \tag{2.16}$$

which is defined as the ratio of the magnitude of the dynamic force transmitted to the force that would be transmitted to the thrust measurement rig if the same force was applied statically. Similarly, the phase of the quotient of equation (2.16) is given by

$$\tan\theta = \frac{2\zeta \frac{\omega}{\omega_n}}{1 - \left(\frac{\omega}{\omega_n}\right)^2} \tag{2.17}$$

Figure 2.4 depicts the transmissibility factor and the phase represented by equations (2.16) and (2.17) for different values of system's damping factors. Figure 2.4 (a) shows that for an underdamped system, the transmissibility of the force increases and leads the system to resonance when the frequency of the forcing function is close to the natural vibration frequency. The value of force transmissibility is more than unity for a relatively low value of frequency ratio. A closer observation suggests that the transmissibility factor is greater than unity when the frequency ratio is as low as 0.05. Hence, since the system is not critically damped, the amount of the dynamic force transmitted by the PDE (which is analogous to the mass in Fig. 2.3) to the thrust measurement rig (which is analogous to the base) is higher than unity for excitation frequencies which are lower than the undamped natural frequency. However, the trend is reversed when the frequency ratio is higher. Figure 2.4 (b) illustrates that the motion of the base and forcing function are in phase for lower values of frequency ratios and becomes out of phase for higher values of frequency ratios.

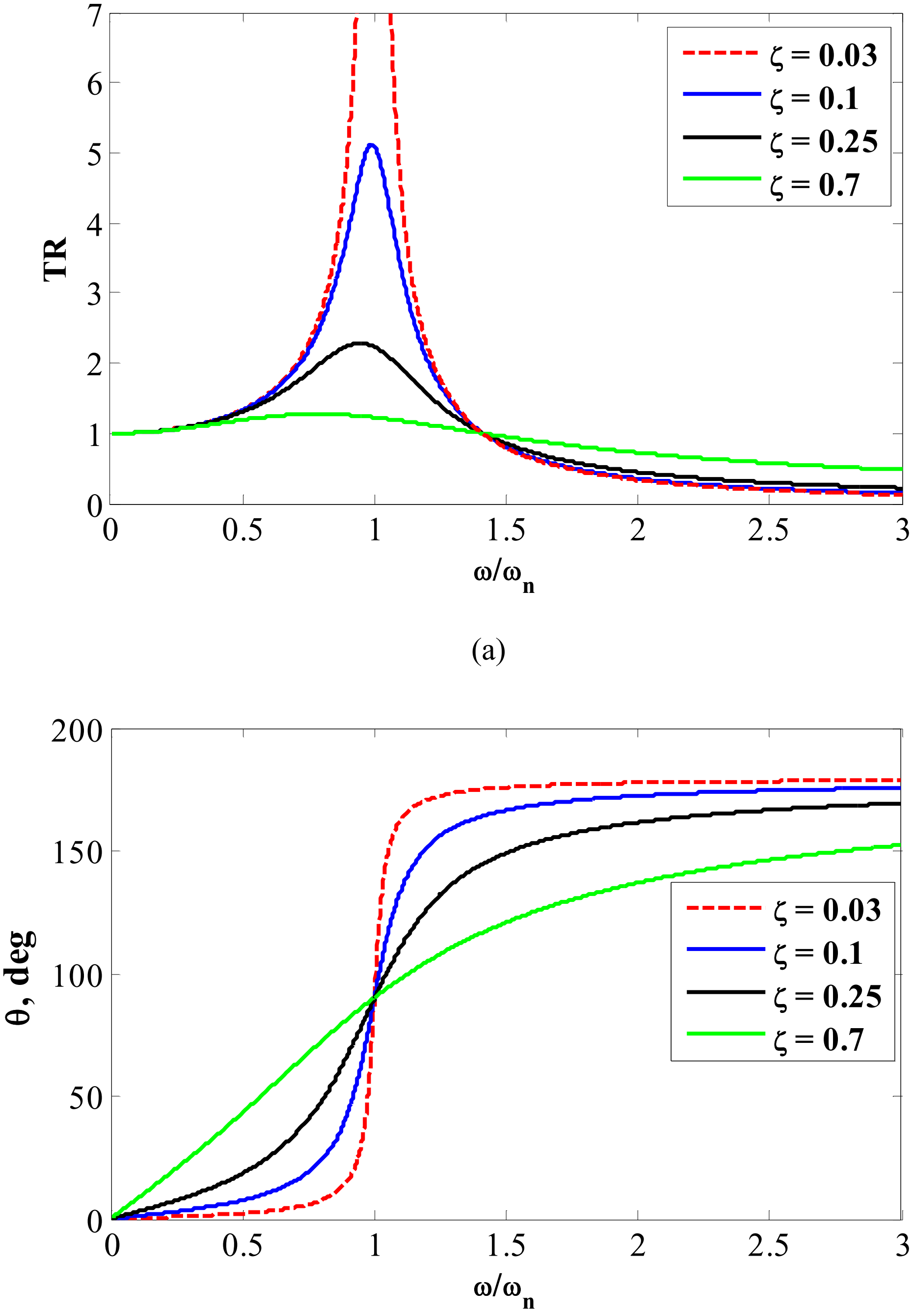

(a)

(b)

Figure 2.4: (a) Transmissibility factor and (b) phase angle of response due to applied force and base excitation.

As discussed above, the dynamic characteristics of the system illustrates that the motion of the base or the thrust measurement rig induces inertial forces which are added to the applied force. These inertial forces are due to the vibrations of a large and massive test model. This added inertial force has to be accounted for in order to obtain the true force applied to the system, that is, the thrust generated by the PDE.

Assuming a linear relation between acceleration of the thrust measurement rig and the corresponding inertial force, the measured thrust can be expressed as [27, 28]

$$\tilde{F}(t) = F_{act}(t) + m_{eff}a_{meas}(t) \tag{2.18}$$

where $\tilde{F}(t)$ is the force measured by the load cell, m_{eff} is the effective mass of the structure that is actively oscillating and contributing to the inertial force, a_{meas} is measured acceleration of the base and $F_{act}\,(t)$ is the actual thrust generated by the PDE. In order to facilitate the acceleration compensation procedure, equation (2.18) can also be written as

$$F_{comp}\,(t) = \hat{F}(t) - m_{eff}a_{filt}(t) \tag{2.19}$$

where $\hat{F}(t)$ is the deconvolved thrust signal obtained using the system transfer function and $\tilde{F}(t)$, m_{eff} is the effective mass of the structure that is actively oscillating and contributing to the cyclic load, a_{filt} is the filtered acceleration signal which is obtained after truncating the measured acceleration signal of the base to retain the acceleration information and F_{comp} is the actual thrust generated by the PDE, where the subscript comp indicates acceleration compensated. This method of applying acceleration compensation is termed as *rig-based acceleration compensation* as the acceleration of the thrust measurement rig is monitored and used to account for inertial forces arising due to base motion.

The use of the deconvolved thrust $\hat{F}(t)$ in equation (2.19) is another feature of this experimental approach as it confirms that the compensated thrust is free from any artifacts brought about by convolution of the thrust with high frequency content. The parameter m_{eff} is also determined for the implementation of acceleration compensation technique and described in detail in section 3.2.2. Hence, with all the parameters known, the total impulse per pulse for the PDE can be expressed as,

$$I_p = \int_0^{t_{exh}} \hat{F}(t)dt - \int_0^{t_{exh}} m_{eff}a_{filt}(t)dt \tag{2.20}$$

where I_p represents the total impulse per pulse in a cycle obtained after accounting for any pulse-to-pulse interaction, influences of system dynamics and added inertial forces. This is the actual impulse generated by the PDE per pulse.

2.2 Determination of Thrust using Semi-empirical Methods

Thrust is generated by a PDE utilizing intermittent pulses of detonation. The occurrence of propagating detonation waves in the PDE tube brings about the rate of change of momentum in the volume enclosed and the pressure differences on the end sections and on the walls. The combined effects of the rate of change of momentum and pressure differences support thrust generation. The rate of change of momentum incorporates contribution from unsteady changes inside the enclosed volume and the contribution from the transport or flux of momentum into and out of the PDE. The pressure rise is brought about by the detonation process itself. Both momentum change and pressure rise brought about by the detonation process change with time.

One way of analytically estimating the thrust generated by the PDE is by determining the pressure history at the closed end, known as the thrust wall. The areas bounded by the pressure history curves and time are a measure of the thrust [1]. Hence, the thrust from a PDE can be obtained by integrating the pressure history at the closed end of the tube. The use of this method to calculate thrust through pressure histories at the thrust wall provides a means of comparing experimental values of thrust with analytical ones. However, Cooper et al. [3] showed that when DDT enhancement devices such as obstacles were used, the head pressure was no longer a reliable measure of the performance. In addition to this, a pressure transducer installed near the head end of the tube will not be able to provide a crisp pressure profile as it measures all the pressure changes occurring inside the tube starting from the initiation of the combustion process to the DDT process leading to a fully-formed detonation wave. Also, this pressure transducer is subjected to intense heating which can deteriorate the quality of the measured pressure signals due to thermal drift. These phenomena complicate the thrust estimation process via pressure measurement at the thrust wall. Although there are complications associated with measurement of pressure history at the thrust wall, an analytical approach can still be very helpful to make optimistic estimates of thrust generated by the PDE.

In this research, a series of PCB pressure transducers was installed along the length of the PDE to measure the pressure history along the tube. Figure 2.5 shows the evolution of the detonation wave from such a measurement. The thrust wall is represented by location 0 in the figure. Unfortunately, no pressure transducer was installed at the thrust wall. The first pressure transducer i.e., location 1, was 20 cm away from the thrust wall. The remaining pressure transducers were equidistant and were 10 cm apart denoted by location 2–5. It is important to note that the integration of pressure history at location 1 i.e., close to the thrust wall will underestimate the thrust. Due to the experimental configuration, direct measurement of the pressure gain at the thrust wall was not pragmatic and the pressure gain was deduced analytically, which is discussed later in this chapter.

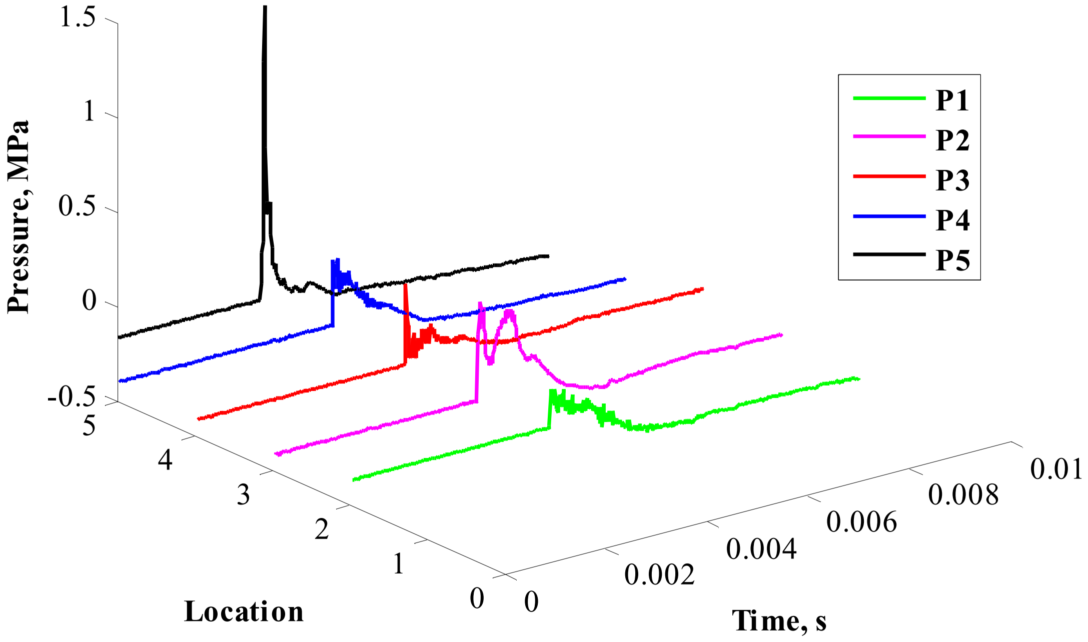

Figure 2.5: Evolution of detonation wave along the length of the tube.

In this section, control volume analysis for thrust is discussed. In addition to that, a description of gas dynamics within the PDE is also presented which provides useful insight in determining the contribution of nonstationary changes in the rate of change of momentum within the PDE. Moreover, the study of gas dynamics inside the PDE will assist in analytically determining the pressure history at the thrust wall of the PDE.

2.2.1 Control Volume Analysis of the PDE

The thrust generated by a PDE can be estimated using a control volume analysis with a control surface drawn just outside the wall which encloses the detonation tube where detonation occurs as shown in Fig. 2.6.

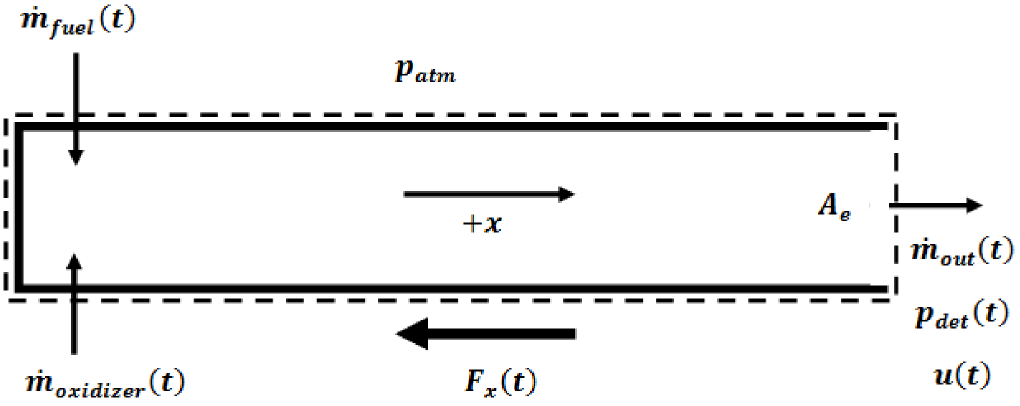

Figure 2.6: Control surface enclosing the PDE.

The PDE used for this research project was operated in the rocket mode and the amount of fuel and oxidizer added while filling the tube is the source of mass entering the control volume. The added mass is accumulated in the PDE which is ignited near the end of the filling phase. Ideally, all the injected mass is expected to remain inside the control volume until the end of the filling phase. However, small fraction of mass is likely to exit the control volume when the chamber is overfilled or for high supply pressure. Hence, the continuity equation for this unsteady flow enclosed by the control volume under consideration is given by

$$\dot{m}_{fuel}(t) + \dot{m}_{oxidizer}(t) - \dot{m}_{out}(t) = \frac{\partial}{\partial t}\int_0^l [\rho(t)A_e]\,dx \qquad (2.21)$$

where the term on the right hand side of equation (2.21) represents the rate of mass accumulation in the control volume during the filling phase of the PDE cycle. For a regular PDE operation, an over-filled chamber is not advantageous and the supply pressure has to be maintained such that the detonable mixture does not exit the chamber too rapidly while filling. Hence, in practice, it is desired that the term $\dot{m}_{out}(t) = 0$ in equation (2.21) such that all of the mass is accumulated in the tube at the end of the filling phase. Considering the control volume is fully filled with no mass exiting the PDE, the total mass accumulated in the control volume is equal to the total mass injected into it. This value of total mass injected into the control volume can be calculated by taking the integral of the left hand side of equation (2.21) for the time period of the filling phase.

The PDE cycle also includes a purge phase. During this phase, purge gas which is usually dry air or some inert gas, is injected into the engine. The momentum and pressure changes during this phase is neglected in control volume analysis as they are insignificant when compared to the momentum and pressure changes brought about by detonation wave.

The mass flow rates are time dependent as they change during a cycle. As described earlier, the fuel and oxidizer are pumped into the detonation chamber only during the filling phase of the cycle for a designated time so as to achieve a desired filling fraction. The gaseous fuel and oxidizer are injected perpendicularly into the control volume and have negligible contribution to the momentum change in the axial direction where the thrust prevails, i.e.,

$$u_{fuel}(t) = u_{oxidizer}(t) = 0 \tag{2.22}$$

Finally, it is assumed that the fuel and oxidizer expands in the detonation tube upon injection and mixing to reach 1 atm.

For momentum conservation in the x-direction, the forces to be considered are the rate of change of momentum in the control volume which includes the contribution from an unsteady term due to the propagating waves in the detonation chamber, the contribution due to the momentum flux of the burnt products that exit the PDE, and the forces arising due to the pressure gain. The net force on the control volume due to the momentum and pressure terms is R_x. The combination of appropriate terms yield the momentum equation for any point inside the control volume given by

$$\frac{\partial}{\partial t}\left[\int_{CV} \rho(t)u(t)dV\right] + \dot{m}_{exh}(t)u(t) + [p_{det}(t) - p_{atm}]A_e = R_x(t) \qquad (2.23)$$

The first term on the left-hand side of equation (2.23) represents the rate of change of momentum due to unsteady changes inside the control volume. This quantity is determined by the study of gas dynamics inside the detonation chamber which is detailed in section 2.2.2. The momentum flux into the PDE is taken as zero since the injection is perpendicular to the x-direction. The momentum flux coming out of the PDE is also relatively small as the mass of detonable mixture injected into the PDE is very small and in O(mg). Also, the force due to pressure at the left end section is zero as it bounds the thrust wall on the inside and exposed to the ambient atmosphere on the outside.

In the first term on the left-hand side of equation (2.23), V is the volume which encloses the detonation chamber where the nonstationary momentum change occurs. Let the length of the control volume shown in Fig. 2.6 be l. The integration of equation (2.23) in the x-direction along length l gives the total force exerted on the control volume at any point in time. The unsteady term in equation (2.23) can then be rewritten to yield

$$\frac{\partial}{\partial t}\int_0^l [\rho(t)u(t)A_e]\,dx + \dot{m}_{exh}(t)u(t) + [p_{det}(t) - p_{atm}]A_e = R_x(t) \tag{2.24}$$

The integral form of the momentum equation is valid when there are frictional forces and regions of dissipation within the control surface, provided that these are absent at the inlet and outlet [48]. Liepmann and Roshko [48] illustrate that the discussion is valid because integration of the momentum equation corresponds to the summation of forces on adjacent fluid elements and of the flows into them, since these forces on the adjacent internal faces are equal and opposite, and are cancelled in summation. Hence, by Newton's third law, the thrust is given by

$$F_x(t) = -R_x(t) \tag{2.25}$$

For equation (2.25), the negative sign is usually neglected to represent the direction of thrust. Using continuity and momentum conservation and considering one pulse during the operation, the impulse generated by the PDE is given by

$$I_p = \int_0^{t_{exh}} \left[\frac{\partial}{\partial t}\int_0^l [\rho(t)u(t)A_e]\,dx + \dot{m}_{exh}(t)u(t) + [p_{det}(t) - p_{atm}]A_e\right] dt \tag{2.26}$$

where $p_{det}(t)$ is the pressure history of the detonation wave measured at the exit of the PDE, p_{atm} is ambient pressure surrounding the PDE, t_{exh} is the time duration of one pulse or equivalent thrust generation period in a cycle and $u(t)$ is the exit velocity of the burnt products.

For the calculation of impulse per pulse in a cycle via equation (2.26), first, the unsteady changes in the momentum contributing to the thrust is calculated using the procedure described in section 2.2.2. The pressure gain due to the detonation wave is measured at the exit of PDE. The velocity of the detonation wave and burnt products is calculated using the relations presented in section 2.2.2. Finally, mass flow rates of fuel and oxidizer is estimated using the known mass of fuel and oxidizer injected into the control volume. The process of calculating mass per injection of fuel and oxidizer is described in Chapter 3. The mass per injection is very low and in O(mg) as the detonation chamber is small and hydrogen, a low molecular weight gas, is used as fuel. With all the parameters known, the impulse generated per pulse in a cycle can be estimated via equation (2.26).

2.2.2 Overview of Gas Dynamics in the PDE

This section describes the analysis of the gas dynamics in the PDE. The equations described in this section are used to calculate the contribution of unsteady changes inside the control volume to the rate of change of momentum. In addition, this study helps to analytically estimate the pressure history at the thrust wall which upon integration over the cycle time gives the impulse for a cycle per unit cross-sectional area. Hence, the results of this formulation help to predict the impulse per cycle of the PDE which can later be compared with experimental results.

For this analysis, it is assumed that the tube is completely filled with a uniform detonable, stoichiometric oxyhydrogen mixture at the end of the filling phase. Initially, the local gas properties of the unburned detonable mixture have the values of p_1, ρ_1 and γ_1. The initial pressure is $p_1 = 1\,\text{atm}$, initial density of the detonable mixture is $\rho_1 = 0.4879\,\text{kg/m}^3$ and $\gamma_1 = 1.4$. The velocity u_1 of the detonable mixture is zero initially as the gas is at rest. In order to provide a better overview of the gas dynamics in the PDE, a schematic of a simplified displacement (*x*–*t*) diagram of the unsteady, ideal wave processes in the tube is shown in Fig. 2.7 up to a time when the PDE comes to a completely relaxed state and the pressure drops to ambient pressure of 1 atm. At $t = 0$, an igniter located near the closed end of the tube initiates a detonation wave which travels towards the open end compressing and burning the detonable mixture. In this analysis, it is assumed that the detonation wave is formed instantly. The burned gas at the rear surface of the detonation wave has the values of u_2, p_2, ρ_2 and γ_2. The detonation wave is a compression wave followed by a Taylor rarefaction wave. This model used to represent a detonation wave is also referred to as a Chapman–Jouguet (CJ) model of the detonation wave. The gases at the rear surface of the detonation wave has a finite velocity and propagates in the same direction as the detonation wave [49]. The rarefaction wave following the detonation wave decelerates the burned gas to rest at the closed end. In this flow process, the front boundary of the rarefaction wave coincides with the rear surface of the detonation wave and the gas at the rear surface of the rarefaction wave is characterized by u_3, p_3, ρ_3 and γ_3. The criteria are that the velocity $u_3 = 0$ and $\gamma_3 = \gamma_2$. Also, the rear boundary of the rarefaction travels towards the open end and the entire unsteady Taylor rarefaction facilitates the exhausting of the burned gases out of the tube.

In Fig. 2.7, the first shock wave which starts at time $t = 0$ and reaches the non-dimensional length $x/L = 1$ at time t_{CJ} is the detonation wave. The time t_{CJ} is the characteristic time in this analysis and represents the duration for which the detonation wave resides in the tube. The velocity of the detonation wave is also a characteristics property of the flow and represented by D_{CJ}. The value of D_{CJ} for stoichiometric oxyhydrogen detonation at 1 atm and 300 K is calculated to be 2835.7 m/s using NASA

CEA code [39]. Some of the other detonation parameters for CJ detonation of stoichiometric oxyhydrogen mixture at 1 atm and 300 K are calculated using NASA CEA code and shown in Table 2.1. The detonation wave is followed by the unsteady Taylor rarefaction wave which also reaches the open the end after the detonation wave exits the tube.

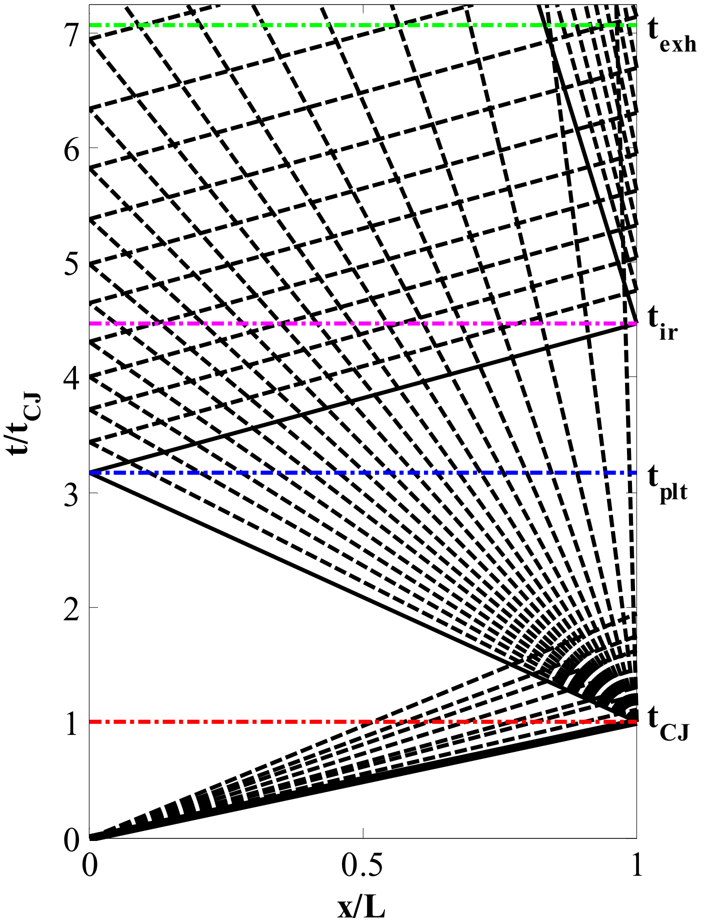

Figure 2.7: Simplified *x–t* diagram of characteristics in the PDE.

Table 2.1: Detonation parameters of stoichiometric oxyhydrogen detonation at 1 atm and 300 K.

Detonation Parameters	
p_2/p_1	18.657
T_2/T_1	12.253
ρ_2/ρ_1	1.8384
Mach number (M_{CJ})	5.256
Detonation velocity (D_{CJ}), m/s	2835.7
γ_2	1.1288

The analysis is started by dividing the total time period under consideration into four intervals. The time period under consideration starts at $t = 0$ when the detonation wave is initiated and extends up to $t = t_{exh}$ when the PDE returns to the relaxed state of 1 atm when all of the burned gases are exhausted. The first time interval is characterized as $0 \leq t \leq t_{CJ}$ when the detonation wave initiated at the closed end reaches the open end of the PDE. The second time interval is characterized as $t_{CJ} \leq t \leq t_{plt}$ when the leading expansion wave originated at the open end travels into the tube and reaches the close end. The third time interval is characterized as $t_{plt} \leq t \leq t_{ir}$ when the leading expansion waves reflected from the closed end reach the open end. The final time interval $t_{ir} \leq t \leq t_{plt}$ incorporates time when any remaining burned gases are exhausted and the pressure inside the PDE drops to the ambient value of 1 atm. To determine the first term on the right-hand side of equation (2.26), each individual time interval is divided into 100 subintervals. For each subinterval, the density ρ and velocity u is calculated. The calculated values are substituted in equation (2.26) to get the value of unsteady momentum changes due to the propagation of shock and expansion waves in the tube.

As mentioned above, the first time interval in this analysis, $0 \leq t \leq t_{CJ}$ in Fig. 2.7, involves the propagation of the detonation wave from the closed end to the open end until it exits the tube. The location of the leading edge of the unsteady Taylor rarefaction or rear edge of the detonation wave at any point of time within this time period is given by

$$x_2 = D_{CJ}t \tag{2.27}$$

For simplicity, the thickness of the detonation wave is insignificant and neglected for this analysis. Conversely, for a known tube length, L, the time for which the detonation wave resides in the tube is given by

$$t_{CJ} = L/D_{CJ} \tag{2.28}$$

Although the detonation parameters can easily be calculated using the NASA CEA code, the state of the burned gas at the rear surface of the detonation wave can also be calculated using the relations presented in [42] and [50], which is given by,

$$p_2 = \frac{\gamma_1 M_{CJ}^2 + 1}{\gamma_2 + 1} p_1 \tag{2.29}$$

$$\rho_2 = 2\left(\frac{\gamma_2 + 1}{2\gamma_2}\right)\rho_1 \tag{2.30}$$

$$a_2 = \frac{\gamma_1 M_{CJ} + 1}{\gamma_1 M_{CJ}^2} \frac{\gamma_2}{\gamma_2 + 1} D_{CJ} \tag{2.31}$$

$$u_2 = \frac{\gamma_1 M_{CJ}^2 - \gamma_2}{\gamma_1 M_{CJ}^2} \frac{1}{\gamma_2 + 1} D_{CJ} \tag{2.32}$$

The trailing edge of the Taylor rarefaction also travels towards the open end during $0 \leq t \leq t_{CJ}$. Let the location of the trailing edge of the unsteady Taylor rarefaction at a point in time when the detonation wave is at x_2 be x_3. Then, the state of the gas inside the unsteady Taylor rarefaction in the region $x_3 \le x \le x_2$ is given by [42, 50]

$$p(x) = \left(\frac{1}{\gamma_2} + \frac{\gamma_2 - 1}{\gamma_2}\frac{x}{x_2}\right)^{2\gamma_2/(\gamma_2 - 1)} p_2 \tag{2.33}$$

$$\rho(x) = \left(\frac{1}{\gamma_2} + \frac{\gamma_2 - 1}{\gamma_2}\frac{x}{x_2}\right)^{2/(\gamma_2 - 1)} \rho_2 \tag{2.34}$$

$$a(x) = \frac{\gamma_1 M_{CJ}^2 + \gamma_2}{\gamma_1 M_{CJ}^2}\frac{1}{\gamma_2 + 1} D_{CJ} + \frac{\gamma_2 - 1}{\gamma_2 + 1}\frac{x}{t} \tag{2.35}$$

$$u(x) = -\frac{\gamma_1 M_{CJ}^2 + \gamma_2}{\gamma_1 M_{CJ}^2}\frac{1}{\gamma_2 + 1} D_{CJ} + \frac{2}{\gamma_2 + 1}\frac{x}{t} \tag{2.36}$$

The boundary conditions for equations (2.33)–(2.36) are such that the leading edge of the unsteady Taylor rarefaction wave coincides with the CJ detonation wave. The state of gas at the trailing boundary of the unsteady Taylor rarefaction wave, which also characterizes the state of the gas in the tube from $0 \le x \le x_3$, i.e., from the closed end to the trailing boundary of the unsteady Taylor rarefaction wave, is given by [42, 50]

$$p_3 = \left[\frac{\gamma_1 M_{CJ}^2 + \gamma_2}{2\gamma_2}\left(\frac{\gamma_1 M_{CJ}^2 + \gamma_2}{\gamma_1 M_{CJ}^2 + 1}\frac{1 + \gamma_2}{2\gamma_2}\right)^{(\gamma_2 + 1)/(\gamma_2 - 1)}\right] p_1 \tag{2.37}$$

$$\rho_3 = \left[2\left(\frac{1 + \gamma_2}{2\gamma_2}\right)^{(\gamma_2 + 1)/(\gamma_2 - 1)}\right] \rho_1 \tag{2.38}$$

$$a_3 = D_{CJ} \Big/ \left[2\frac{\gamma_1 M_{CJ}^2}{\gamma_1 M_{CJ}^2 + \gamma_2}\right] \tag{2.39}$$

$$u_3 = 0 \tag{2.40}$$

Finally, the location of the trailing boundary of the unsteady Taylor rarefaction wave at any time t within $0 \le t \le t_{CJ}$ is given by

$$x_3 = a_3 t \tag{2.41}$$

Hence, using equations (2.27)–(2.41), the state of the gas within the tube for time $0 \leq t \leq t_{CJ}$ is calculated. Figure 2.8 shows sample unsteady profiles of velocity, pressure and density of the gases in the tube at different instances of time in this interval.

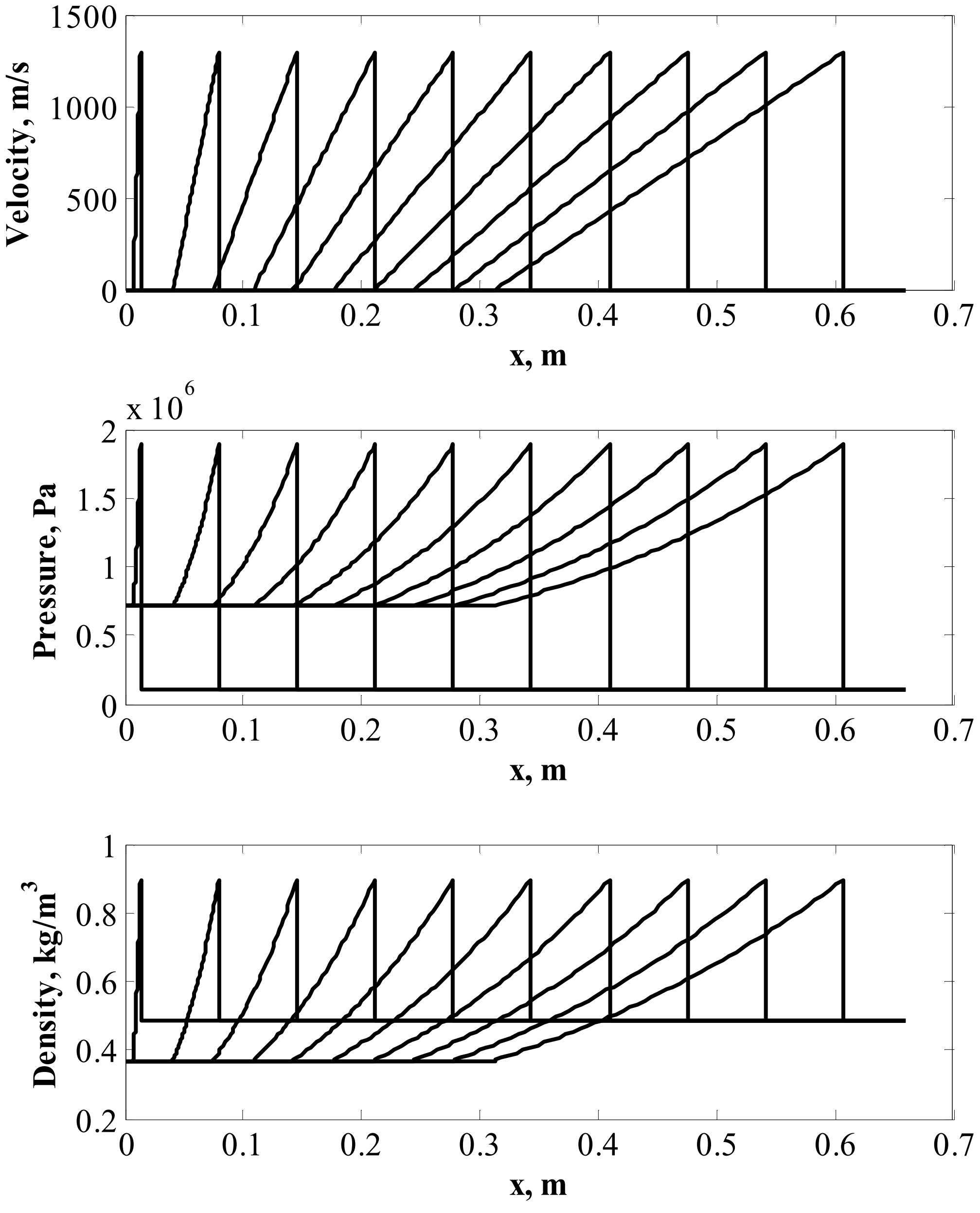

Figure 2.8: Unsteady profiles for velocity, pressure and density of gases for $0 \leq t \leq t_{CJ}$.

Among the calculated variables, the values of density ρ and velocity u at each point of time are integrated over the length of the tube. Finally, the discretized time and the integrated values of ρu with the cross section area of the tube yield the rate of change of momentum enclosed by the tube for this time period.

It can be noted that the time period for the above procedure is restricted to $0 \leq t \leq t_{CJ}$. A similar evaluation has to be carried out for the rest of the time intervals, i.e., $t_{CJ} \leq t \leq t_{exh}$, until all the burned gases exit the tube so as to calculate the total contribution of unsteady changes in the rate of change of momentum. The detonation wave rapidly decays after leaving the tube [51]. A rarefaction wave starts to propagate upstream from the open to the closed end to empty the remaining burned gas from the tube. The calculation of the properties for the remaining time intervals is further described.

The second period is $t_{CJ} \leq t \leq t_{plt}$, where t_{CJ} is the time when the detonation wave exits the tube and t_{plt} is the time when the leading boundary of the unsteady rarefaction generated due to the exit of detonation wave reaches the closed end of the tube. The rarefaction wave generated due to the exit of the detonation wave is responsible for exhausting the remaining burned gas from the open end of the tube. The leading boundary of this rarefaction wave propagates into and intersects with the rear boundary of the unsteady Taylor rarefaction wave, and finally impinges at the closed end where the uniform gas is at rest characterized by $u_3 = 0$, p_3, ρ_3 and $\gamma_3 = \gamma_2$. Endo et al. [42] presented a detailed analysis of the interaction of this rarefaction wave with an unsteady

Taylor rarefaction. However, for this analysis, this interaction phase is neglected as it lasts for a very short period of time.

Endo et al. [42] discuss that the pressure at the closed end is kept constant at p_3 until the leading boundary of the rarefaction reaches the closed end at time t_{plt}. Hence, in the interval $0 \leq t \leq t_{plt}$, the pressure at the closed end shows a plateau. Although the pressure at the closed end shows a plateau, the state of gas along the length of the tube is changing because the rarefaction wave travels towards the closed end. This rarefaction wave propagates from the open to the closed end starting at time t_{CJ}. The location of the leading characteristics is given by the following relation [42]

$$x_r = \frac{D_{CJ} t}{\gamma_2 - 1}\left[\gamma_2 \frac{\gamma_1 M_{CJ}^2 + 1}{\gamma_1 M_{CJ}^2}\left(\frac{t_{CJ}}{t}\right)^{2(\gamma_2-1)/(\gamma_2+1)} - \frac{\gamma_1 M_{CJ}^2 + \gamma_2}{2\gamma_2}\right] \tag{2.42}$$

However, the validity of equation (2.42) is ensured only when $x_3 \leq x_r$ [42]. The location $x_r = x_3$ indicates the intersection of leading boundary of the rarefaction with the trailing boundary of the Taylor rarefaction wave. The time at which the intersection of the two characteristics occurs is denoted by t_{int} and the location of intersection is denoted by x_{int}. The values for these parameters are calculated using the following relations [42]

$$t_{int} = \left(\frac{\gamma_1 M_{CJ}^2 + \gamma_2}{\gamma_1 M_{CJ}^2 + 1}\frac{1 + \gamma_2}{2\gamma_2}\right)^{-(\gamma_2+1)/2(\gamma_2-1)} t_{CJ} \tag{2.43}$$

$$x_{int} = \frac{1}{\delta_{A2}}\left(\frac{\gamma_1 M_{CJ}^2 + \gamma_2}{\gamma_1 M_{CJ}^2 + 1}\frac{1 + \gamma_2}{2\gamma_2}\right)^{-(\gamma_2+1)/2(\gamma_2-1)} L \tag{2.44}$$

where

$$\delta_{A2} = 2\left(\frac{\gamma_1 M_{CJ}^2}{\gamma_1 M_{CJ}^2 + \gamma_2}\right) \tag{2.45}$$

This intersection point helps to determine the value of t_{plt} given by [42]

$$t_{plt} = t_{int} + x_{int}/a_3 \tag{2.46}$$

$$t_{plt} = 2\left(\frac{\gamma_1 M_{CJ}^2 + \gamma_2}{\gamma_1 M_{CJ}^2 + 1}\frac{1 + \gamma_2}{2\gamma_2}\right)^{-(\gamma_2+1)/2(\gamma_2-1)} t_{CJ} \tag{2.47}$$

After time t_{int}, the leading boundary of the unsteady rarefaction wave propagates towards the closed end with the speed of sound a_3. The location of this characteristic is given by $x_r = a_3 t$ where $t_{int} \leq t \leq t_{plt}$. During this time interval, $t_{int} \leq t \leq t_{plt}$, unsteady changes will provide the maximum contribution to the rate change of momentum enclosed by the PDE. The gas dynamics in the tube at each discrete time due to the propagating rarefaction wave is calculated using the following relations [50]

$$p(x) = \left[\frac{1}{\gamma_2 + 1}\left(2 + (\gamma_2 - 1)\frac{L - x}{L - x_r}\right)\right]^{2\gamma_2/(\gamma_2-1)} \rho_3 \tag{2.48}$$

$$\rho(x) = \left[\frac{1}{\gamma_2 + 1}\left(2 + (\gamma_2 - 1)\frac{L - x}{L - x_r}\right)\right]^{2/(\gamma_2-1)} \rho_3 \tag{2.49}$$

$$u(x) = \frac{1}{\gamma_2 + 1}\left(1 - \frac{L - x}{L - x_r}\right) D_{CJ} \tag{2.50}$$

Figure 2.9 shows the properties of the state variables inside the tube due to the propagating rarefaction wave generated after the exit of the detonation wave. From these calculated values, the contribution of unsteady changes to the rate of change of momentum is estimated for the time interval $t_{int} \leq t \leq t_{plt}$. As mentioned earlier, the contribution of unsteady flow to the momentum changes between $t_{CJ} \leq t \leq t_{int}$ is neglected because the time interval is small and the rate of change of momentum in this interval is insignificant compared to that generated in the time interval $t_{int} \leq t \leq t_{plt}$.

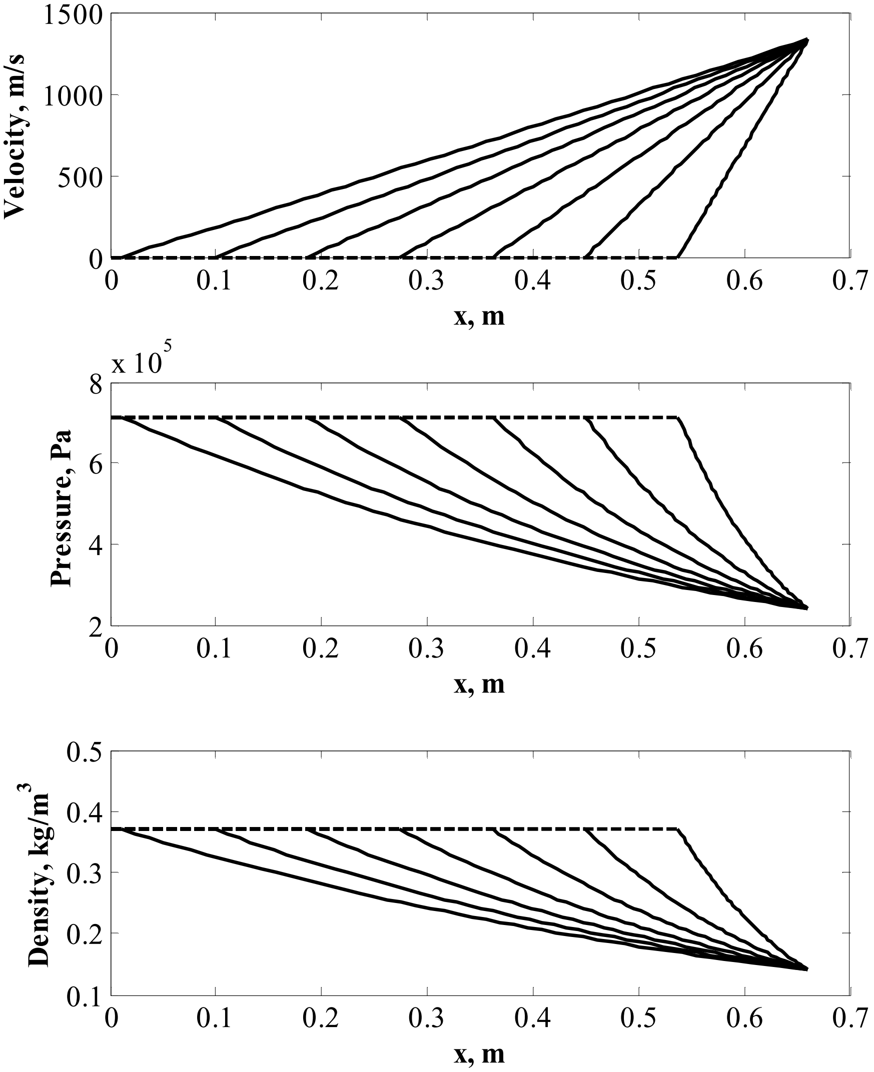

Figure 2.9: Properties of gases in the tube due to the propagation of rarefaction wave after the exit of the detonation wave at various times.

Thereafter, this leading boundary of the rarefaction wave is reflected from the closed end as the leading edge of a reflected rarefaction wave. This reflected rarefaction wave travels towards the open end of the tube and the time at which its leading boundary reaches the open end is denoted by t_{ir} as shown in Fig. 2.7. The pressure at the closed end decays as the tube is further emptied by the rarefaction waves travelling from the open end toward the closed end and their subsequent reflections. The oncoming rarefaction waves and their reflections from the wall further aid in exhausting any remaining gas out from the open end. The time when the pressure at the thrust wall decreases to initial pressure of 1 atm is t_{exh}.

Using a similar analysis as above, the contribution of unsteady changes to the rate of change momentum in the time interval $t_{plt} \leq t \leq t_{ir}$ is estimated. This interval represents the period when the reflected rarefaction waves travel from the closed end to the open end. Figure 2.7 shows an obvious interference between the rarefaction wave generated due to the exit of detonation wave and its reflection from the closed end of the tube. The leading boundary of this reflected rarefaction wave starts to propagate towards the open end at $t = t_{plt}$. The reflected waves are weak in nature and they are almost parallel to each other as shown in Fig. 2.7. In other words, it can be assumed that the rarefaction wave generated due to the exit of the detonation wave expands and exhausts most of the burned gas. This time interval has very little contribution to the momentum. However, to ensure completeness in the results, the unsteady momentum change for this time interval is also calculated. The analysis is simplified by an approximation which considers that the gas is in a state which is reached after it is expanded by the unsteady rarefaction wave generated by the exit of detonation wave. This state of the gas is calculated using the following relations [42]

$$p_{ex} = [2/(\gamma_2 + 1)]^{2\gamma_2/(\gamma_2 - 1)} p_3 \tag{2.51}$$

$$\rho_{ex} = [2/(\gamma_2 + 1)]^{2/(\gamma_2 - 1)} \rho_3 \tag{2.52}$$

$$a_{ex} = [2/(\gamma_2 + 1)]a_3 \tag{2.53}$$

$$u_{ex} = a_{ex} \tag{2.54}$$

The above approximation allows equations (2.48)–(2.50) to be used to estimate the state of the gas in the tube in the interval $t_{plt} \leq t \leq t_{ir}$. The only change that has to be introduced in using equations (2.48)–(2.50) is that the parameters with subscript “3” have to be replaced by the parameters described in equations (2.51)–(2.54) with subscript “ex” as the gas has this new state. Also, x_r is described by a new position function which determines the location of the leading boundary of the reflected expansion wave given by

$$\begin{aligned} x_{ir} = L - \frac{\gamma_2 + \gamma_1}{\gamma_2 - \gamma_1} a_3 \left(t - t_{plt} + \frac{L}{a_3}\right) & \\ \times \left\{\left[\left(t - t_{plt} + \frac{L}{a_3}\right)\right]^{-2(\gamma_2-1)/(\gamma_2+1)} - \frac{2}{\gamma_2 + 1}\right\} & \end{aligned} \tag{2.55}$$

The time at which this leading boundary of the reflected expansion wave reaches the open end is given by [42]

$$t_{ir} = \left(\delta_B + \delta_{A2}\left\{\left[\frac{2}{\gamma_2 + 1}\right]^{-(\gamma_2+1)/2(\gamma_2-1)} - 1\right\}\right) t_{CJ} \tag{2.56}$$

where

$$\delta_B = 2\left(\frac{\gamma_1 M_{CJ}^2 + \gamma_2}{\gamma_1 M_{CJ}^2 + 1} \frac{1 + \gamma_2}{2\gamma_2}\right)^{-(\gamma_2+1)/2(\gamma_2-1)} \tag{2.57}$$

The effect of any unsteady momentum changes after $t = t_{ir}$ is neglected in this analysis since the reflected waves are much weaker and their contribution to the rate of change of momentum is insignificant.

The final parameter that needs to be defined is the time t_{exh} when the pressure at the closed end decreases to the initial pressure of 1 atm. The time interval represented by $t_{plt} \leq t \leq t_{exh}$ renders a decaying pressure profile at the closed end of the tube. The detailed description of the formulation of the decay is presented in [42]. Based on the description and relations presented in [42], the equation used to calculate t_{exh} is given by

$$t_{exh} = \{\delta_{A2}[f_n(\delta_{A1}) - 1] + \delta_B\}t_{CJ} \tag{2.58}$$

where

$$\delta_{A1} = \frac{\gamma_1 M_{CJ}^2 + \gamma_2}{2\gamma_2}\left(\frac{\gamma_1 M_{CJ}^2 + \gamma_2}{\gamma_1 M_{CJ}^2 + 1}\frac{1 + \gamma_2}{2\gamma_2}\right)^{(\gamma_2+1)/(\gamma_2-1)} \tag{2.59}$$

and f_n is a function which estimates the decay portion of the pressure history at the closed end. The approximate function representing the pressure decay history for an arbitrary value of γ_2 is obtained by interpolating the two f_ns for appropriate value of n shown in Table 2.2 [42] and f_n is interpolated using the following relations [42]

$$n = (3 - \gamma_2)/2(\gamma_2 - 1) \tag{2.60}$$

$$f_n(\delta_{A1}) = (1 - X)f_{n_a}(\delta_{A1}) + (X)f_{n_b}(\delta_{A1}) \tag{2.61}$$

$$X = (\gamma_2 - \gamma_a)/(\gamma_b - \gamma_a) \tag{2.62}$$

$$\gamma_a = (2n_a + 3)/(2n_a + 1) \tag{2.63}$$

$$\gamma_b = (2n_b + 3)/(2n_b + 1) \tag{2.64}$$

Here, an oxyhydrogen mixture is used with $\gamma_2 = 1.1288$. Hence, to ensure truthful pressure decay, interpolation is carried out to obtain an appropriate f_n with $n_a = 6$ and $n_b = 10$ utilizing relations in Table 2.2.

Table 2.2 Function describing the decay portion of the pressure history at the closed end of the PDE [42].

n	γ_2	f_n
1	$\frac{5}{3} = 1.667$	$f_1(\theta) = \frac{1}{2}(\theta)^{\frac{1}{5}} + \frac{1}{2}(\theta)^{\frac{3}{5}}$
2	$\frac{7}{5} = 1.4$	$f_2(\theta) = \frac{3}{2^3}(\theta)^{\frac{1}{7}} + \frac{1}{2^2}(\theta)^{\frac{3}{7}} + \frac{3}{2^3}(\theta)^{\frac{5}{7}}$
3	$\frac{9}{7} = 1.286$	$f_3(\theta) = \frac{5}{2^4}(\theta)^{\frac{1}{9}} + \frac{3}{2^4}(\theta)^{\frac{3}{9}} + \frac{3}{2^4}(\theta)^{\frac{5}{9}} + \frac{5}{2^4}(\theta)^{\frac{7}{9}}$
4	$\frac{11}{9} = 1.222$	$f_4(\theta) = \frac{35}{2^7}(\theta)^{\frac{1}{11}} + \frac{5}{2^5}(\theta)^{\frac{3}{11}} + \frac{9}{2^6}(\theta)^{\frac{5}{11}} + \frac{5}{2^5}(\theta)^{\frac{7}{11}} + \frac{35}{2^7}(\theta)^{\frac{9}{11}}$
6	$\frac{15}{13} = 1.154$	$f_6(\theta) = \frac{231}{2^{10}}(\theta)^{\frac{1}{15}} + \frac{63}{2^9}(\theta)^{\frac{3}{15}} + \frac{105}{2^{10}}(\theta)^{\frac{5}{15}} + \frac{25}{2^8}(\theta)^{\frac{7}{15}} + \frac{105}{2^{10}}(\theta)^{\frac{9}{15}} + \frac{63}{2^9}(\theta)^{\frac{11}{15}} + \frac{231}{2^{10}}(\theta)^{\frac{13}{15}}$
10	$\frac{23}{21} = 1.095$	$f_{10}(\theta) = \frac{46189}{2^{18}}(\theta)^{\frac{1}{23}} + \frac{12155}{2^{17}}(\theta)^{\frac{3}{23}} + \frac{19305}{2^{18}}(\theta)^{\frac{5}{23}} + \frac{2145}{2^{15}}(\theta)^{\frac{7}{23}} + \frac{8085}{2^{17}}(\theta)^{\frac{9}{23}} + \frac{3969}{2^{16}}(\theta)^{\frac{11}{23}} + \frac{8085}{2^{17}}(\theta)^{\frac{13}{23}} + \frac{2145}{2^{15}}(\theta)^{\frac{15}{23}} + \frac{19305}{2^{18}}(\theta)^{\frac{17}{23}} + \frac{12155}{2^{17}}(\theta)^{\frac{19}{23}} + \frac{46189}{2^{18}}(\theta)^{\frac{21}{23}}$

Using the relations shown above, the value of t_{exh} and the corresponding pressure decay at the wall are calculated for the time interval $t_{plt} \leq t \leq t_{exh}$. Figure 2.10 shows the analytically calculated pressure history at the closed end of the PDE utilizing the description presented in [42], [50]. Figure 2.10 also shows the values of important instances with $t_{CJ} = 0.2327$ ms, $t_{plt} = 0.7364$ ms, $t_{ir} = 1.042$ ms and $t_{exh} = 1.642$ ms. The plateau pressure remains constant until time t_{plt} with a value of 7.14 atm with decays to 1 atm at time $t = t_{exh}$.

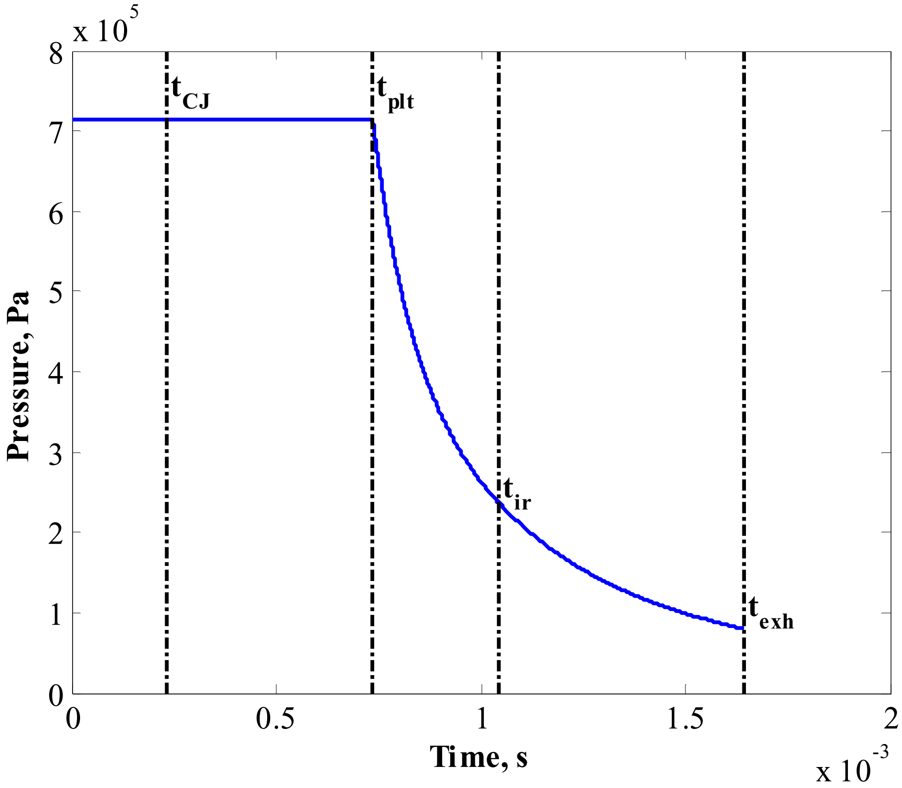

Figure 2.10: Analytically-derived pressure history at the closed end of the PDE.

The pressure gain at the closed end is the main contributor to thrust generation. Hence, the pressure gain at the closed end is used to calculate the impulse per unit cross section per cycle and it is given by [42]

$$I_{cyc} = (p_3 - p_1)t_{plt} + \int_{t_{plt}}^{t_{exh}} (p_w - p_1)\,dt \tag{2.65}$$

where p_w denotes the pressure history at the closed end during the decay portion. The calculated value of impulse generated per cycle using equation (2.65) will be compared against the impulse per pulse obtained from the control volume analysis and the experimental results. The detailed comparison is shown in Chapter 4.

The representation of the pressure history at the thrust wall can also be used to find the mass flow rate of burned products out of the control volume. First considering isentropic conditions, the temperature history at the thrust wall has to be calculated using the pressure and density history. Since the velocity of the particle at the wall is zero, the pressure and temperature at the wall can be referred to as total pressure and temperature of the flow. The analytically estimated total pressure and temperature can be used to find the mass flow rate of burned products out of the tube via mass flow parameter relation. Note that the exhaust of burned products start only after time t_{CJ} once the detonation wave exits. Hence, calculation of velocity at the exit for time interval $t_{CJ} \leq t \leq t_{exh}$ and estimated mass flow rate using pressure and temperature history at the thrust wall can better predict $\dot{m}_{exh}$ for the PDE. This is possible concept that could be adopted in future for a more detailed control volume analysis.

2.3 Finite Element Analysis

Detonations are a sudden and rapid phenomenon. Thrust is generated in a PDE by utilizing intermittent detonations. In this process, the force is applied at the thrust wall suddenly. Due to this sudden and rapid loading, a dynamic analysis is required to determine the transient response of the system. As in most instances for dynamic analysis, the time history of a quantity in the form of displacement, velocity or acceleration that depicts the motion is solved. ANSYS 13.0 is used to facilitate the dynamic simulation of the PDE under a detonation loading. The ANSYS Transient solver is used to solve for resultant loads and acceleration of the model under this transient loading.

A three-dimensional model of the PDE and its supporting structure was first developed using Creo Parametric 2.0 design software as shown in Fig. 2.11. This solid model was imported into the ANSYS Transient solver; proper boundary conditions were imposed and the entire solid model was meshed. The finite element analysis of the meshed model provided resulting loads and acceleration induced in the model due to dynamic loading. This section briefly describes the objectives of the finite element analysis, basics of structural dynamics followed by dynamic response analysis methodology, modeling specifications and mesh sensitivity analysis.

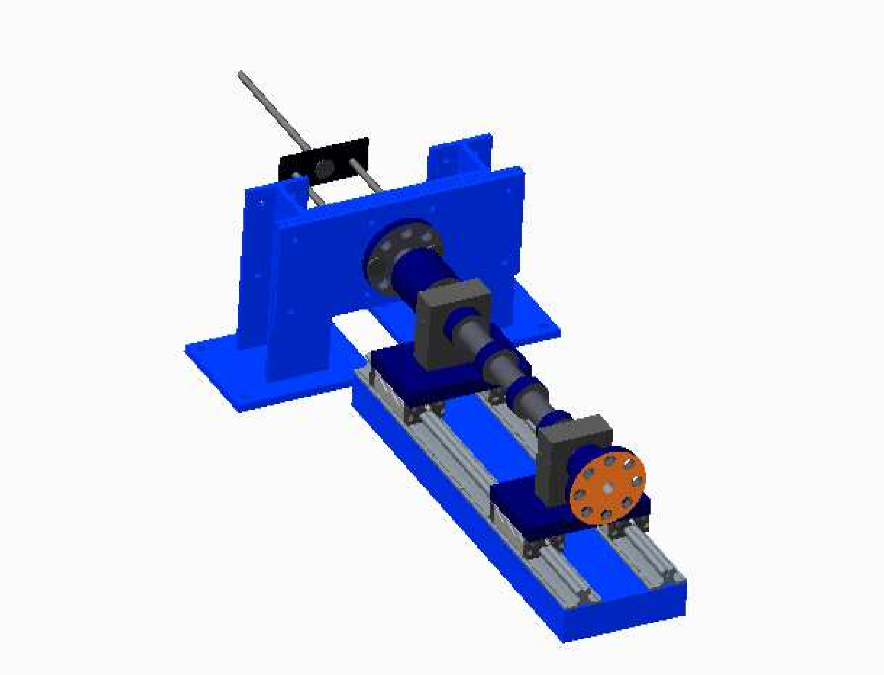

Figure 2.11: Three dimensional model of the PDE created using Creo 2.0.

2.3.1 Objectives of Finite Element Analysis

Finite element analysis of the PDE is expected to provide validation for the experimental approach. The maximum operating frequency achieved in test runs without any misfires was 20 Hz. Hence, the experimental approach was used to extract actual thrust from measured signals only up to 20 Hz. It has been suggested that PDEs should be operated at frequencies between 20 to 100 Hz if they are to be integrated in an aircraft. Hence, this calls for the need of validation of the experimental approach for aircraft integration when the operating frequency is in the higher end. In addition to this, at higher operating frequencies, a prominent interference between the thrust and structural response is also expected. Hence, input loads with frequencies of 50 and 100 Hz will be applied to the finite element model and the calculated output will be processed using the developed experimental approach. Therefore, the effectiveness of the approach to account for any interference will be ensured.

2.3.2 Basics of Structural Dynamics

A system with single degree of freedom with a block of mass m, a single linear spring with stiffness of k and a viscous damper with a damping coefficient c is shown in Fig. 2.12. This system is excited by a time varying force $f(t)$. The application of Newton's law of motion on this system yields the following governing equation:

$$m\ddot{u} + c\dot{u} + ku = f(t) \tag{2.66}$$

The damping incorporates both structural and material damping. The solution of the above equation of motion yields the required acceleration and resultant loads for a loading under consideration.

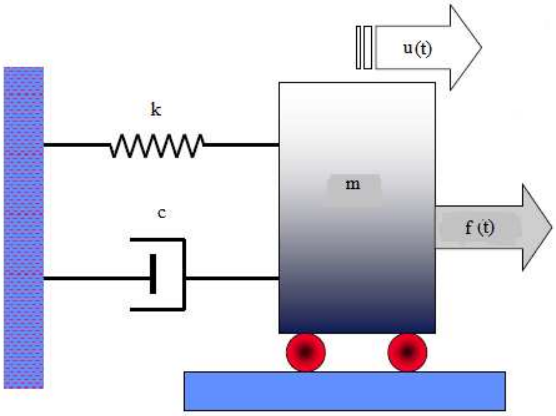

Figure 2.12: A single degree-of-freedom model acted upon by a time varying force.

Similarly, for a finite element model with more than one degree-of-freedom, the displacement u is replaced by a vector $\mathbf{U}$ of nodal degree of freedom and the force $f(t)$ is replaced by a load vector $\mathbf{F}(t)$. Also, a stiffness matrix $\mathbf{K}$, a damping matrix $\mathbf{C}$ and a mass matrix $\mathbf{M}$ replace k, c and m respectively. The equivalent differential equation of motion for a multi degree-of-freedom system is given by

$$\mathbf{M\ddot{U}} + \mathbf{C\dot{U}} + \mathbf{KU} = \mathbf{F}(t) \tag{2.67}$$

For a structural dynamic problem, all forces in equation (2.67) are time dependent. In general, the objective is to compute displacements $\mathbf{U}$, velocities $\mathbf{\dot{U}}$ and accelerations $\mathbf{\ddot{U}}$ as a function of time using known $\mathbf{K}$, $\mathbf{C}$ and $\mathbf{M}$. The analytical solution of the governing differential equation are presented in detail in [52]. ANSYS Transient solver is used to solve the governing equations to get required accelerations and resultant forces.

2.3.3 Dynamic Response Analysis

As discussed earlier, dynamic response analysis incorporates the calculation of the response of a structure under arbitrary time-dependent loading. In this type of analysis, vectors of displacements, velocities and accelerations are calculated at each point of time to determine the resultant forces in the body. The instances of time for calculating the response is separated by a time increment or step Δt. This time step should be small enough to resolve the motion of the structure and this will be discussed in section 2.3.3.1

ANSYS not only supports "modal analysis" for evaluating dynamic response by solving the eigenvalue problem but also is able to perform "direct integration" for calculating dynamic response which does not require transformation to a special form [53]. Modal analysis of the PDE is used to investigate the dynamic characteristics of its free vibrations. This study of free vibrations yields the natural frequencies and their corresponding mode shapes. Modal analysis is also utilized to compare the sensitivities of various mesh sizes and will be further discussed in the section 2.3.5. Direct integration could be performed either via a central difference method or the Newmark method [53]. The Newmark method is a built-in algorithm in ANSYS to perform direct integration.

Direct integration via the Newmark method is based on the following equations which are further described in [53]:

$$U_{n+1} \approx U_n + \Delta t \dot{U}_n + \frac{(\Delta t)^2}{2}\left\{(1-2\psi)\ddot{U}_n + 2\psi \ddot{U}_{n+1}\right\} \tag{2.68}$$

$$\dot{U}_{n+1} \approx \dot{U}_n + \Delta t\left\{(1-\kappa)\ddot{U}_n + \kappa \ddot{U}_{n+1}\right\} \tag{2.69}$$

where ψ and κ are chosen by the user. The displacements, velocities and accelerations are used to calculate the resultant stresses and loads. Certain choices of ψ and κ make the Newmark method unconditionally stable; a slightly more stringent criterion for unconditional stability includes $0 \leq \zeta \leq 1, \kappa \geq \frac{1}{2}$ and $\psi \geq \frac{1}{4}\left(\kappa + \frac{1}{2}\right)^2$ [53].

2.3.3.1 Integration Time Step

It is suggested that the integration time step be about 1⁄20 of the response period to capture the detailed behavior of the structural response [53, 54]. However, for a PDE, determination of an exact response period is difficult as it depends on the dimensions of the engine and the amount of damping in the system. Cook [53] mentions that for a direct integration of dynamic response by the Newmark method, the time step should at least be equal to or smaller than the load representation interval. In the present study, the time varying load applied to the system is introduced with a discretization interval of 20 μs. In order to properly resolve the motion of the structure and capture the propagation of high-frequency stress waves, a minimum time step of 2 μs is used. The maximum time step chosen for analysis is 20 μs. The in-built algorithm in ANSYS is capable of changing the integration time step between the minimum and maximum value depending on the value of the input load so as to speed up the calculation process.

2.3.3.2 Damping

Damping is the collection of all energy dissipating mechanism and causes the amplitude of free vibration to decay with time [53]. Three categories of damping can be identified in the system. The first type is viscous damping which is introduced due to the interaction of the structure with the surrounding fluid. The second type is material damping brought about by the internal friction in the material. Finally the third type is called dry or Coulomb friction arising due to the friction in the connection between structural members [54]. The damping observed in the experimental setup is the combined effects of all the sources contributing to make the system damped. However, in the current experimental setup, material damping is a significant source of damping.

Material damping, in other words, can be described as the complex physical effects that convert kinetic and strain energy in a vibrating mechanical system consisting of a volume of solid matter into heat [55]. It can be noted that all forms of damping for a structural problem are relatively small and idealized as viscous regardless of the actual damping mechanism [53]. The aggregate damping is represented by c or matrix $\mathbf{C}$ as shown in equations (2.66) and (2.67) respectively. Note that a material cannot be characterized using a damping coefficient or a damping matrix as these are not the intrinsic properties of a material. In finite element analysis, certain parameters are used to propose a mathematical form which characterizes the material. Hence, for a system with multiple degrees of freedom, the damping matrix is defined using an arbitrary and nonphysical relation given by [53]

$$\mathbf{C} = \alpha\mathbf{M} + \beta\mathbf{K} \tag{2.70}$$

The parameters α and β are used to characterize the damping property of the material. Equation (2.70) depicts that damping is roughly proportional to the mass and the stiffness of the structure. The same equation (2.71) can be written in terms of frequency and damping ratio as

$$\zeta = \frac{\alpha}{2\omega} + \frac{\beta\omega}{2} \tag{2.71}$$

Hence, the parameters α and β can be obtained by simultaneously solving equation (2.71) for a system with a set of two measured damping ratios ζ for corresponding two natural vibration frequencies ω_n.

For the current experimental setup, first, the damping ratio of the entire system was calculated using the logarithmic decrement method. To facilitate this method, the system was excited by an impact hammer and the response of the load cell was measured. The amplitude of the load u_P at the beginning of a cycle and the amplitude u_Q at the end of the cycle were determined. Using the known values of amplitudes of loads for a damped natural period T_d, the damping factor of the system was obtained using,

$$\zeta = \frac{1}{2\pi}\ln\frac{u_P}{u_Q} \tag{2.72}$$

The application of equation (2.72) is illustrated in Fig. 2.13 which depicts the decaying response of an arbitrary underdamped system. The figure shows the amplitudes at the beginning and at the end of a damped natural period.

Similarly, the response of the PDE system measured by the load cell was analyzed and one of the appropriate damping factors portraying the system was found to be 0.165 for a damped circular natural frequency of 3142 rad/s.

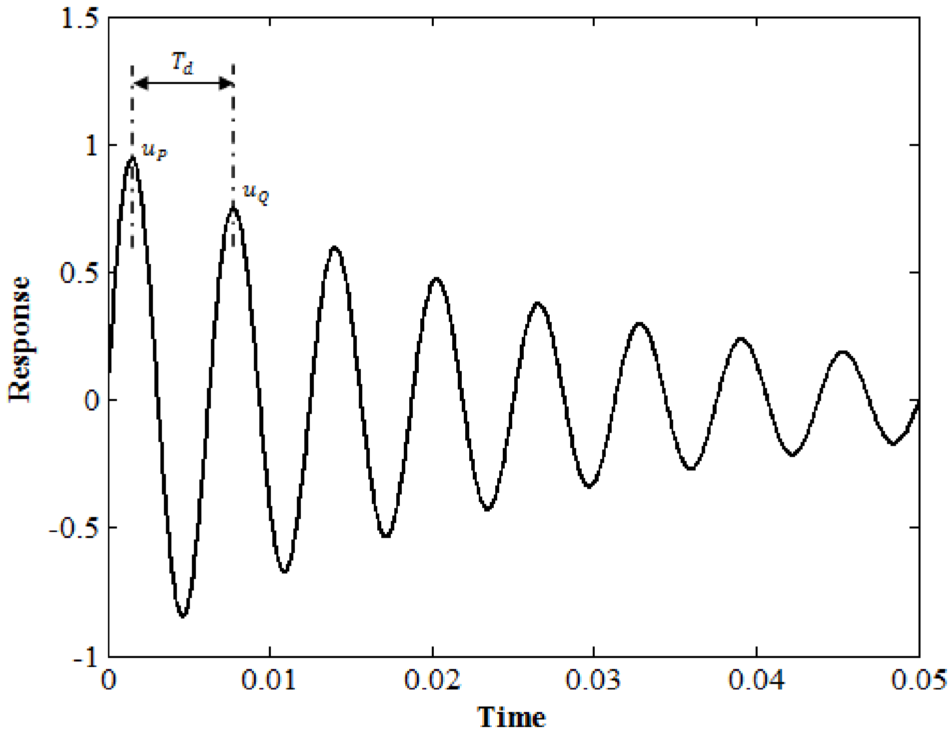

Figure 2.13: Decay record of an arbitrary damped system.

Hence, for a circular damped natural frequency of 3142 rad/s and a damping ratio of 0.165, the values of α and β were found to be 1036.73 and 1.05×10^{-4} respectively. Figure 2.14 shows the variation of α and β for different values of natural frequencies and the corresponding damping factors. It is interesting to note that the figure shows infinite damping at $\omega_n = 0$, which is not physically correct and nevertheless physically unrealizable, but the curves can be used for the representation of damping over the frequency range of interest. Another important information the plot depicts is that the form $\mathbf{C} = \alpha\mathbf{M}$ damps the lower modes heavily while the form $\mathbf{C} = \beta\mathbf{K}$ damps the higher modes heavily [53]. In the current version of ANSYS Workbench used in this work, the global α value is assumed to be zero while it does allow the user to input the global β value. This assumption of $\alpha = 0$ is acceptable as the lower modes which have prominent impact on the inertial forces occurring in the finite element model are rather underdamped compared to the higher modes. It is also physically realizable as the higher frequency modes are rapidly damped by the material itself.

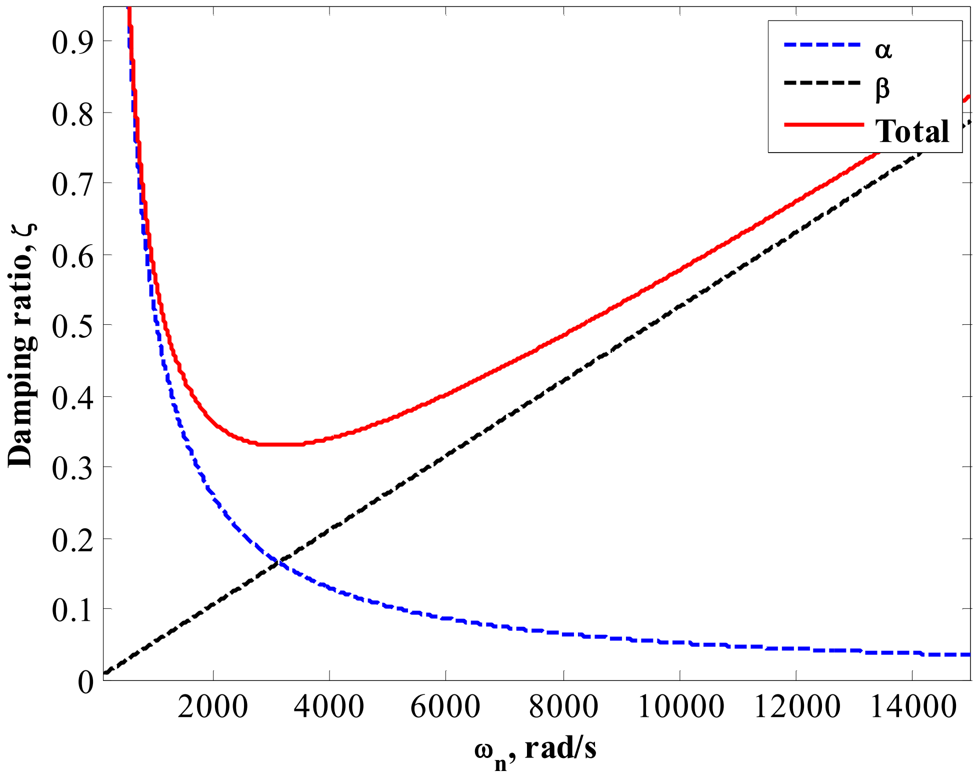

Figure 2.14: Variation of α and β damping parameters for different natural frequencies and corresponding damping factors.

2.4 Modeling Specifications

A finite element model was developed so as to replicate the actual experimental hardware used in this research work. The details of the experimental setup are further described in Chapter 3. In this study, all finite element simulations were carried out at room temperature i.e., 22 ºC. The material used for modeling the experimental setup was T300 series stainless steel, with Young's modulus of elasticity of 210 GPa and a Poisson ratio of 0.3.

The effects of generated thrust are predominant in the axial direction. Hence to decrease the computational time and the complexity of the model, a line body model was first created in ANSYS 13.0 Design Modeler by connecting coordinate points in the (x, y) plane. The cross-sections and lengths of the line bodies were determined based on the actual engine geometry. Each line body represented a segment of the engine and these segments were connected together. Figure 2.15 shows the meshed, three-dimensional line-body model of the PDE.

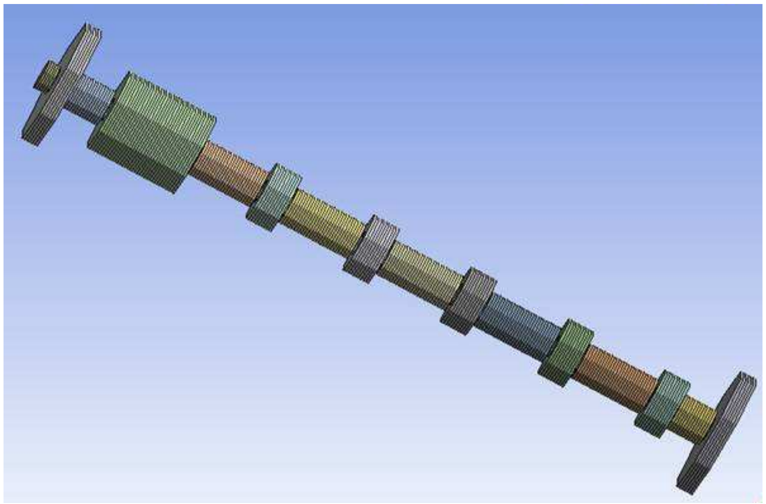

Figure 2.15: Line body model of the PDE.

ANSYS used beam 188 elements to create a fine mesh of the model with 5286 nodes and 2635 elements. No pre-stress was applied and the left-most end was fixed. The surfaces of the models were constrained such that they allowed displacement only in the axial direction. Modal analysis of this line body model showed predominantly axial modes. The analysis yielded a frequency of 1412 Hz for the first axial model. However, modal analyses of the solid model shown in Fig. 2.11 revealed a range of bending modes ahead of the axial mode, the details of which will be further discussed in the next subsection. A careful examination of the setup which is analogous to the solid model shown in Figure 2.11 explained the likelihood of occurrence of bending modes due to the installation of the PDE on the mount with vertical support. The vertical supports were securely fastened to the engine and the linear bearings. The application of any load to the closed end will therefore excite bending modes in the system. Hence to include all possible excited modes of vibration, the solid model finally was chosen for analysis instead of the line body model.

Figure 2.16 shows the solid model of the PDE with the settings used in the Transient solver for finite element analysis. The base of the thrust stand was assigned to be the fixed support as in the experimental setup. The base of the engine mounts were assigned as frictionless supports since they rested on the linear bearings which were free to roll on the slide. The linear bearings in fact allowed for axial motion of the PDE as they were coupled with the rails of the slide. Additionally, in the solid model, the side walls of the mounting base were given displacement boundary conditions such that they were free to move only in the axial direction. The contact region of the load cell and the thrust stand was assigned as an elastic support to enable the calculation of the force reaction due to loading. The stiffness of the load cell as per manufacturer's specification was $2.1 \times 10^{11}\ \mathrm{N/m}$. This value of stiffness and the effective cross-sectional area of the load cell were used to calculate the foundation stiffness. The value of the foundation stiffness for elastic support at the contact region of the thrust stand and the load cell surface was calculated to be $1.156 \times 10^{13}\ \mathrm{N/m^3}$. The end of the pre-load mechanism was also assigned as the elastic support. The pre-load tension rods were made out of steel with a diameter of 11.43 mm (0.45 in.) and were comparable to stiff springs. The equivalent stiffness of the pre-load mechanism was calculated to be $3.42 \times 10^{7}\ \mathrm{N/m}$ and using this value of equivalent stiffness, a foundation stiffness of $5.5 \times 10^{11}\ \mathrm{N/m^3}$ was assigned to this elastic support.

Loads were applied at the thrust wall. The force reaction at the contact region of the thrust stand and the load cell was calculated. The accelerations of the PDE, thrust stand and load cell were also calculated.

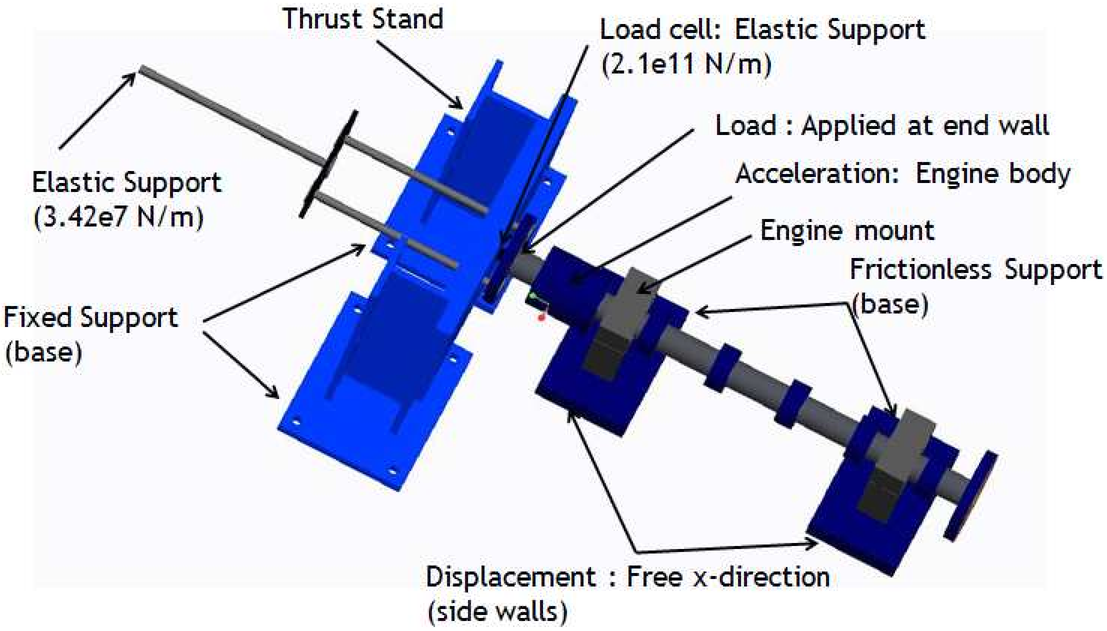

Figure 2.16: Transient solver settings for the finite element analysis of PDE.

2.4.1.1 Modal Analysis and Mesh Sensitivity

Modal analyses of the solid model of the PDE helped to investigate the dynamic characteristics of its free vibrations. The settings described in the previous sections were applied to the finite element model. The modal solver in ANSYS Workbench was used to perform the modal analyses. This study of free vibrations facilitated the understanding of natural frequencies and their corresponding mode shapes. The purpose was to determine the number of modes to be retained since the model will have thousands of modes. Opinions on how many modes to retain for analysis differ and reliable a priori rules are unavailable. In order to answer this question, the magnitude spectrum of the response was examined [53].

A sample magnitude spectrum for the model when excited by a force in the form of a delta function with a magnitude of 693 N is shown in Fig. 2.17. The figure shows that modes with frequencies higher than 1275 Hz were not significantly excited. Hence, structure modes with natural vibration frequencies less than 1275 Hz were retained. A trial simulation with a fine mesh indicated that the 22nd mode had a natural frequency of 1330.3 Hz which exceeds the upper bound of 1275 Hz. Thus, only the first twenty-two modes needed to be considered.

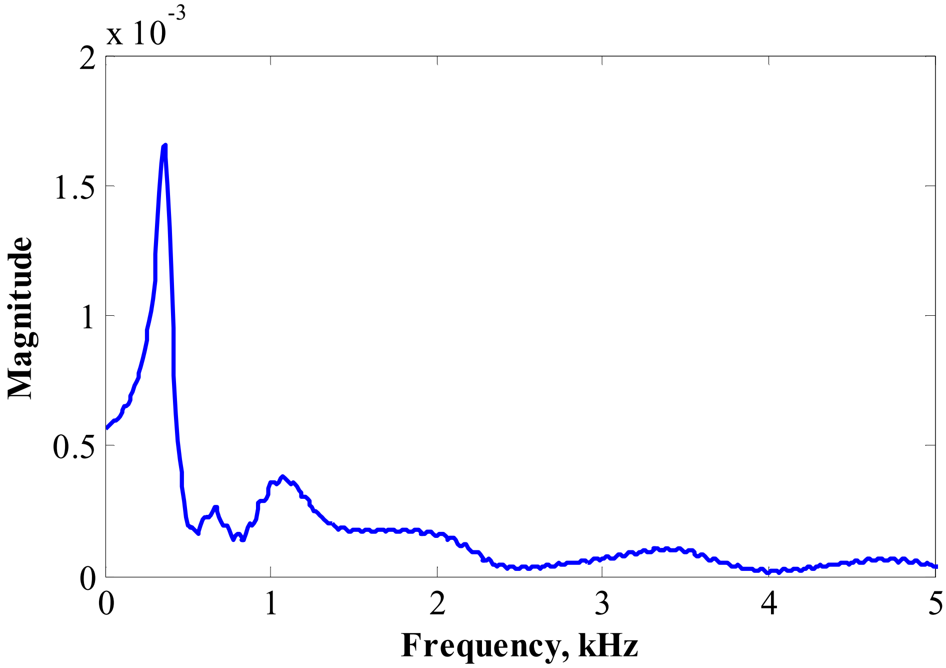

Figure 2.17: Sample magnitude spectrum of the response to estimate highest mode of vibration.

Modal analysis was performed using the mode superposition method. Although this method is the cheapest way of solving a structural dynamics problem, direct integration was chosen due to the impulsive nature of loading. However, modal analysis will be employed to check the sensitivity of the mesh. In fact, the sensitivity of the different meshed model will be evaluated by two methods. First the dynamic response of the meshed models under same input load will be compared followed by the mode shape comparison.

ANSYS Workbench was used to generate meshes of different sizes for the solid model of the PDE. ANSYS uses tetrahedral elements to mesh the model. The quality of the mesh considered was fine, medium, coarse and coarser. Table 2.3 shows the statistics of the different meshes for the finite element model.

Table 2.3: Mesh statistics for the finite element model of PDE

Type	Number of Elements	Number of Nodes
I (Fine)	58,166	121,626
II (Medium)	18,946	58,228
III (Coarse)	12,542	44,582
IV (Coarser)	7,426	20,757

These four different types of meshes were compared to choose the most suitable to carry out the finite element analysis. A force input in the form of a delta function with a magnitude of 300 N was applied at the thrust wall. The dynamic response of all four meshed models was calculated. The reaction for all four meshed models under the same applied impulse is shown in Fig. 2.18 and it was observed that there was no change in the reaction obtained for all the four meshed models. This shows that a coarser mesh could be used for transient analysis that saves computational cost. However, a similar agreement in findings has to be reached after the comparison of results obtained from modal analysis.

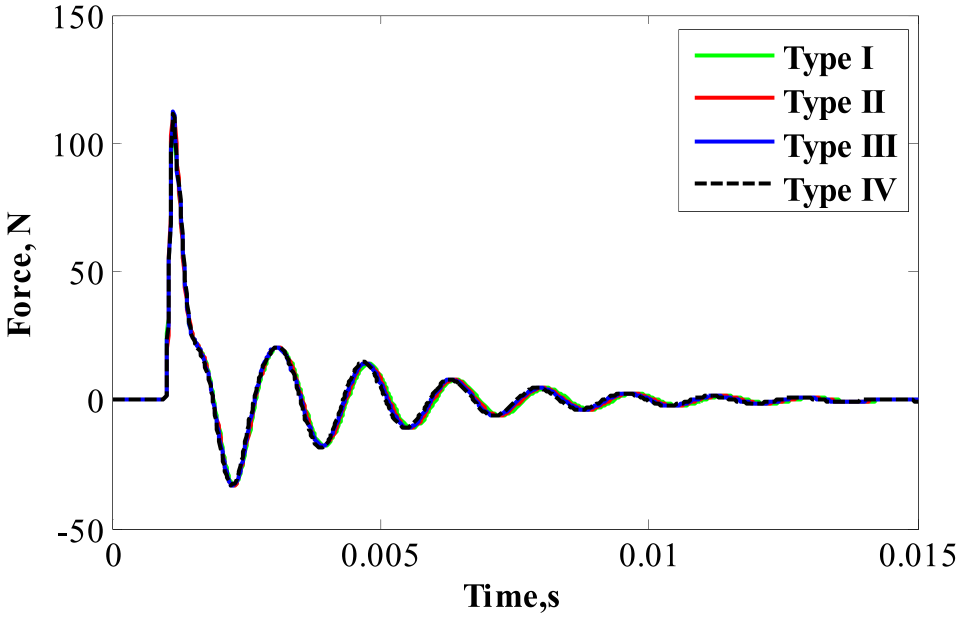

Figure 2.18: Comparison of force reaction for different mesh sizes under 300 N force input.

Modal analysis was performed on all four meshed models and the first twenty-two modes were compared. The average of frequencies obtained for each mode from all four cases are presented in Table 2.4. The table also shows the standard deviation calculated for frequencies obtained for each mode from all four cases expressed as percentage of the calculated average. The mode shapes were numbered according to frequency, starting with the lowest. Mode 1, with an average frequency of 60.1 Hz, was bending of the preload tension rods. Modes 2 to 6, with higher frequencies were due to other bending modes of the preload tension rods. Mode 7 with an average frequency of 611.1 Hz was the first bending mode of the PDE tube and mode 14 was the second PDE bending mode (Figure 2.19). Other modes identified included higher modes of bending of preload tension rods, torsion of the thrust stand beams and higher modes of bending of the PDE tube.

It was observed that the natural vibration frequency for all four cases were close to each other. The highest standard deviation of 10% was found for the fifth mode. However, the standard deviation in frequencies for the other modes was significantly low. The comparison shows that the dynamic response calculated for the Type IV mesh will be very close to that of the fine mesh. Although the results show that the Type IV mesh was sensitive enough, in order to ensure the reliability of the solution, the Type III mesh was chosen for finite element analysis.

Hereafter, Type III mesh was used for analysis. Figure 2.20 shows the meshed model used for analysis. In order to increase the accuracy of the result, a level 1 mesh refinement was applied at the thrust wall where the force input was applied. Figure 2.21 shows the mesh refinement applied at the thrust wall. The mesh refinement increased the number of elements to 13,673 and the number of nodes to 46,349. Force inputs at 10, 20, 50 and 100 Hz were applied to the thrust wall and the response was computed. Detailed results of the finite element analysis are presented in Chapter 4.

Table 2.4: Modes of vibration and average of corresponding natural frequencies for different types of mesh.

Mode	Average Frequency (Hz)	Standard Deviation
1	60.1	7.5%
2	69.9	2.6%
3	139.0	2.7%
4	141.4	2.0%
5	493.6	10.2%
6	574.6	6.2%
7	611.1	0.9%
8	648.5	3.6%
9	692.7	3.7%
10	735.5	4.8%
11	756.3	4.2%
12	762.7	3.9%
13	820.7	1.0%
14	866.9	2.7%
15	916.9	1.8%
16	925.0	1.1%
17	941.1	2.4%
18	964.0	2.6%
19	986.8	1.4%
20	1101.0	3.6%
21	1114.0	3.8%
22	1364.5	1.9%

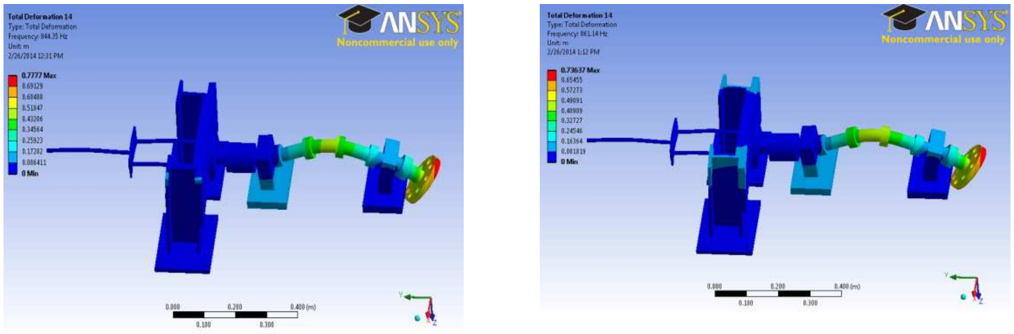

Type I

Type II

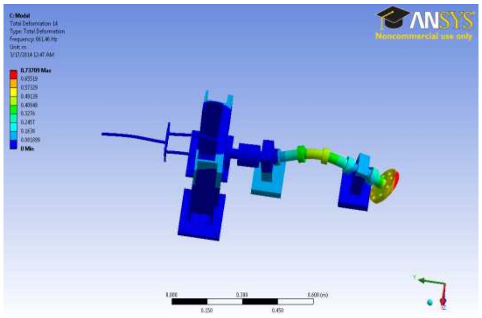

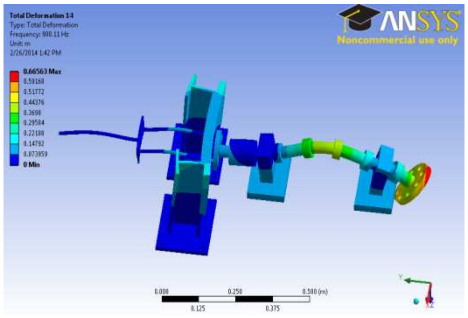

Type III

Type IV

Figure 2.19: Comparison of fourteenth mode shape for different mesh sizes.

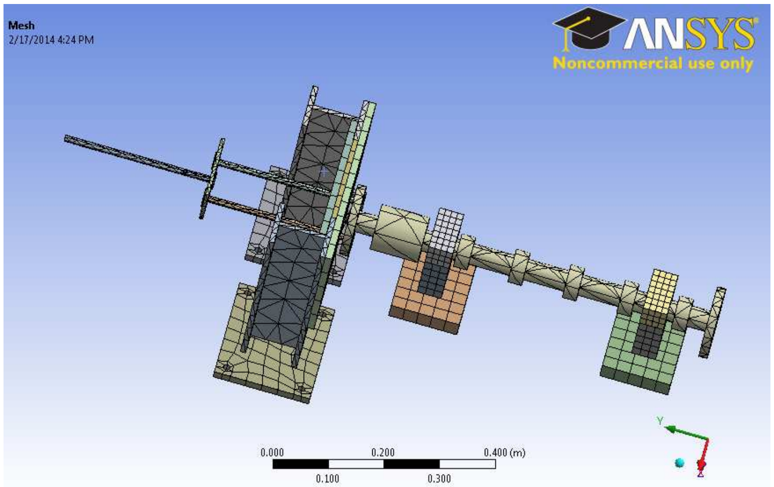

Figure 2.20: Meshed model used for finite element analysis.

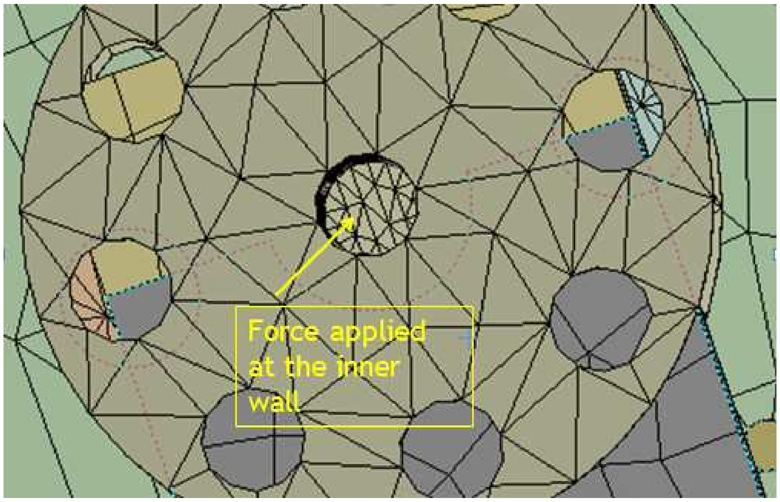

Figure 2.21: Mesh refinement at the thrust wall.

Chapter 3

Experimental Setup

3.1 Description of Experimental Setup

A PDE was developed that consisted of a straight wall detonation tube with one end closed and the other end open to the ambient atmosphere. Gaseous hydrogen and oxygen were injected intermittently near the closed end. Gaseous hydrogen and oxygen were selected as fuel and oxidizer respectively because of reliable detonation initiation of the mixture in a short length. This fuel/oxidizer mixture when ignited from an automotive spark plug detonated and provided thrust when the burned gases exit the tube.

A schematic of the PDE is shown in Fig. 3.1. Figure 3.2 shows photographs of the experimental setup with (a) Dayton and (b) AFS solenoid valves respectively. The valve configurations are further described in section 3.1.1.

The PDE consisted of a stainless steel pipe that was 660 mm (26 in.) long with an inner diameter of 25.4 mm (1 in.). The pipe had a thickness of 6.35 mm (0.25 in). The mounts for the engine were machined in-house which allowed the PDE to rest on a linear motion bearing. The linear bearings allowed the PDE to roll on the guide rails. The linear motion bearing was manufactured by Techno-Isle Inc, New Hyde Park, New York. Although the manufacturer specified that the bearing offers almost zero frictional resistance, the practicality of the bearings was tested through a cut-weight test and is further described in Section 3.2.

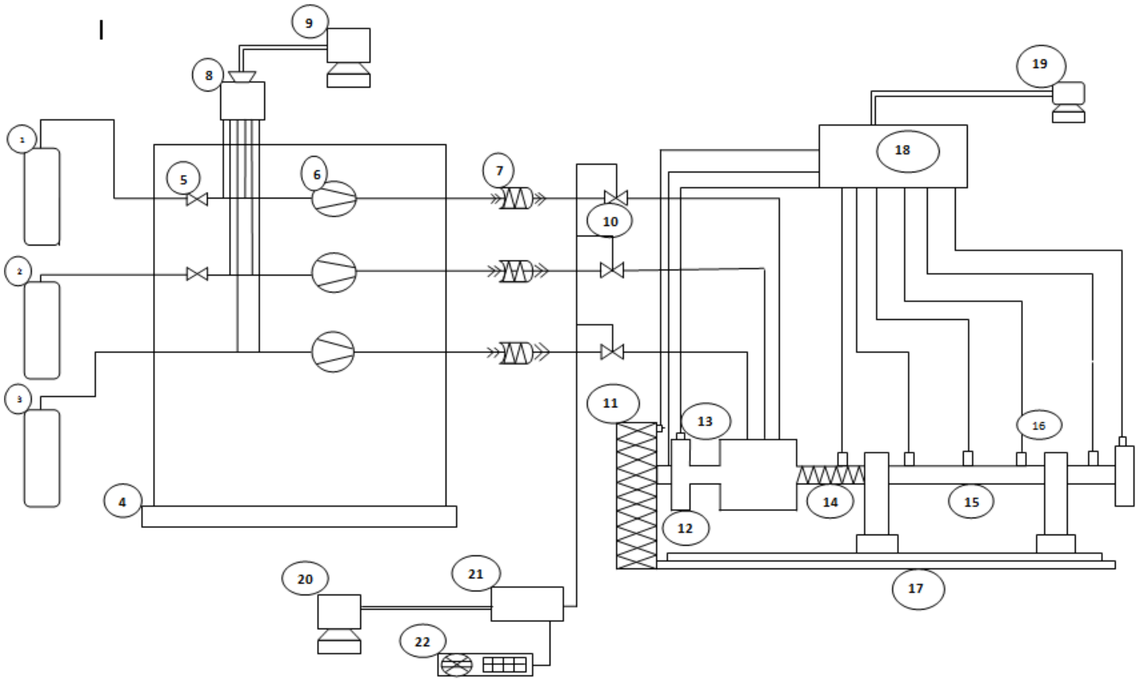

1. Hydrogen cylinder
2. Oxygen cylinder
3. Compressed air
4. Gas-supply cart
5. Pneumatic valves
6. Critical flow nozzles
7. Flashback arrestors
8. SCB68 connector box
9. Gas cart monitoring computer
10. AFS fuel supply Solenoid valves
11. Thrust Stand
12. Load Cell
13. Accelerometer
14. Schelkin spiral
15. PDE tube
16. Pressure transducers
17. Slide
18. Signal Conditioner
19. High Speed DAQ
20. TTL Control DAQ
21. Current buffer amplifier
22. DC power supply

Figure 3.1: Schematic of the PDE setup

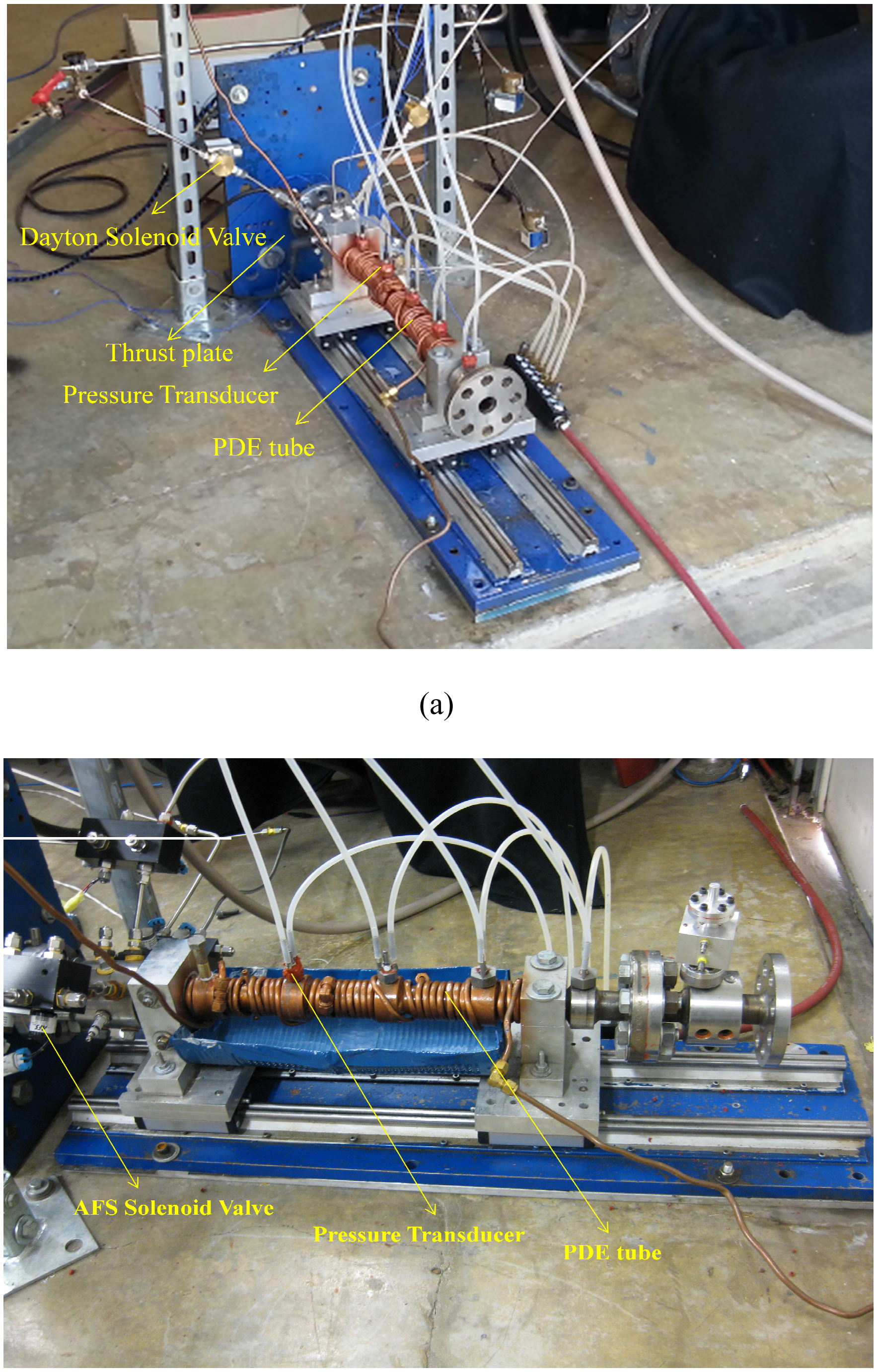

(a)

(b)

Figure 3.2: Photographs of the PDE with (a) Dayton valves and (b) AFS valves

As shown in Fig. 3.2, the PDE had a closed flange on the left and an open flange at the right. On the left, the PDE was butted against a load cell (PCB Model 201B03) supported by a thrust stand and preloaded with a constant force of 1350 N. The pressure of the detonation wave was measured along the tube through a series of dynamic pressure transducers (PCB Model 111A24). The arrangement of pressure transducers had been described in Chapter 2. Copper tubes were wound around the detonation tube through which cold, tap water flowed to cool the engine. A coat of conductive paint was applied to reduce the contact resistance between the detonation tube and the copper tubes. All pressure transducers were placed inside water cooled adapters from PCB. Two accelerometers (PCB 353B03), one on the engine and another on the thrust stand, were mounted to measure the acceleration of the entire structure during engine operation.

Near the closed end, the detonation tube had an interface to connect fuel, oxidizer and purge lines into the engine. This section also held the igniter used to detonate the mixture. The igniter used was an automotive spark plug which produced sparks based on a TTL signal transmitted by the control DAQ. A Shchelkin spiral, shown in Fig. 3.3 was installed in the tube after the injection section to enhance the deflagration-to-detonation transition (DDT) process. The spiral aided in mixing of the fuel and oxidizer and made the flow field turbulent and hence supported DDT. The spiral used was 3 in long with an outer diameter of 1 in. and inner diameter 0.625 in. An important parameter characterizing the Shchelkin spiral is its blockage ratio, which is defined as the ratio of area covered by the device to total internal area of tube [31]. The Shchelkin spiral used in the setup offered a blockage ratio of 34 % which was in the 40% range that is desired for reliable DDT [31].

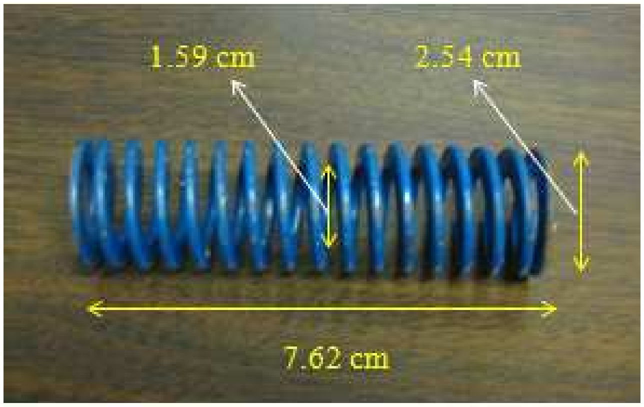

Figure 3.3: Schelkin spiral used inside the PDE to enhance DDT.

The hydrogen and oxygen from the gas cylinders were regulated for use. Starting from the fuel tank, the fuel and oxidizer lines made up separate assembly lines consisting of pneumatic check valves, critical flow nozzles, flash arrestors and finally the solenoid valves which were used to pulse the flow into the engine. Figure 3.4 illustrates the gas supply cart assembly used in this project. The pneumatic check valves were installed as a safety feature. Critical flow nozzles can be used for determining mass flow rates of the gases. However, a more elaborate methodology to estimate the intermittent mass flow rates of gases has been developed as a part of this work which accounts for the change in injection area and flow losses. The methodology is described in detail in section 3.2. The assembly also had flash arrestors installed (SIMAX EN-730) to prevent any potential backward traveling combustion waves from entering the fuel or oxidizer tanks. In addition to this, the supply lines had fittings which held static pressure transducers (Omega PX-313-200G5V) and Omega Type T thermocouples to measure the supply pressure and temperature.

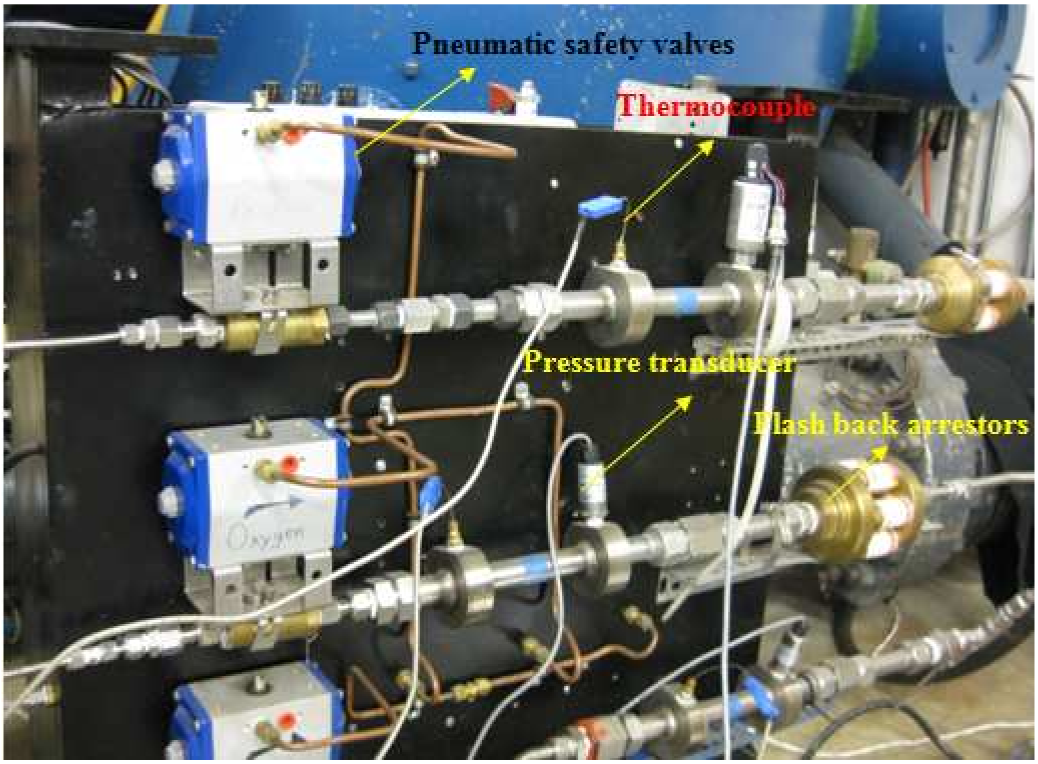

Figure 3.4: Gas supply cart assembly used for the PDE operation.

3.1.1 Operation and Data Acquisition

The name “pulse detonation engine” is indicative of this type of engine because of its pulsed mode of operation. The operation of the engine is essentially dependent upon the frequency of fuel/oxidizer injection and its mode of combustion. In other words, the operation of a PDE depends on the exact timing of its valves and the firing of the igniter. As described in Section 1.2.3, a typical PDE cycle has four phases. The first phase is the purging phase. The purge phase is followed by filling phase which incorporates gas recharge or filling of the PDE with a detonable mixture. The third phase is the combustion of the mixture by utilizing an igniter. The combustion facilitates to form a detonation wave which travels through the detonable mixture. The combustion phase is followed by a blow down phase resulting in the exhaust of the burned gases. After blow down, the purge phase restarts which involves injection of an inert buffer gas preventing the pre-ignition of the detonable mixture by separating the blow down and filling phase. Figure 3.5 below shows the phases of a PDE cycle.

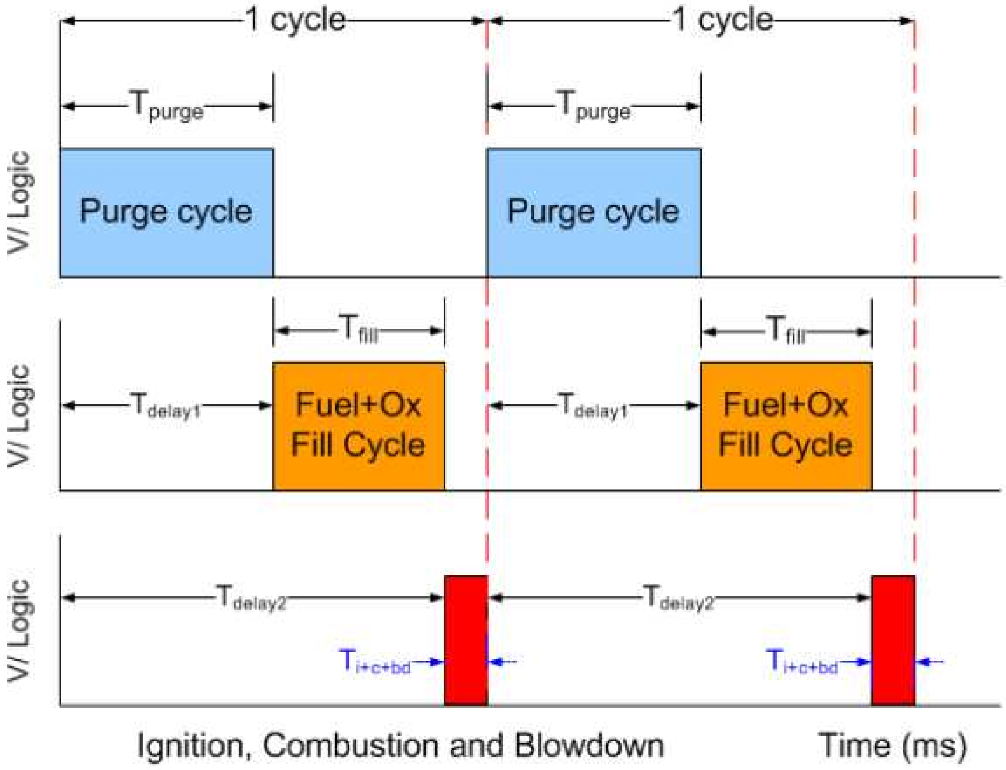

Figure 3.5: Various phases of a PDE operation cycle.

The different phases of the PDE cycle were achieved by the timed opening of the solenoid valves and the firing of the igniter. The timing of the phases was controlled using TTL signals from a LabVIEW™-based control program. A separate DAQ and a different control program were employed to control the operation of the PDE. For safety reasons, the TTL signal for the purge phase was made the master and TTL signals for the filling and ignition phases were made slaves with proper time delays, these delays being based on the frequency of operation. The front panel of the LabVIEW™ virtual instrument allowed the user to input the desired frequency and time delays to generate TTL signals and is shown in Fig. 3.6.

The control program commanded the DAQ to generate 5VDC TTL signals which were first digitally emitted through the NI-PXI 6722 I/O module and later converted to an analog signal by the BNC-2110 module so that they were recognized by the intended device. These TTL signals drove the solenoid valves used for the purge, fuel and oxidizer lines. In addition, a TTL signal from the control program drove the ignition spark plug. Table 3.1 below shows the timings chosen for the operation of the PDE with different operating frequencies.

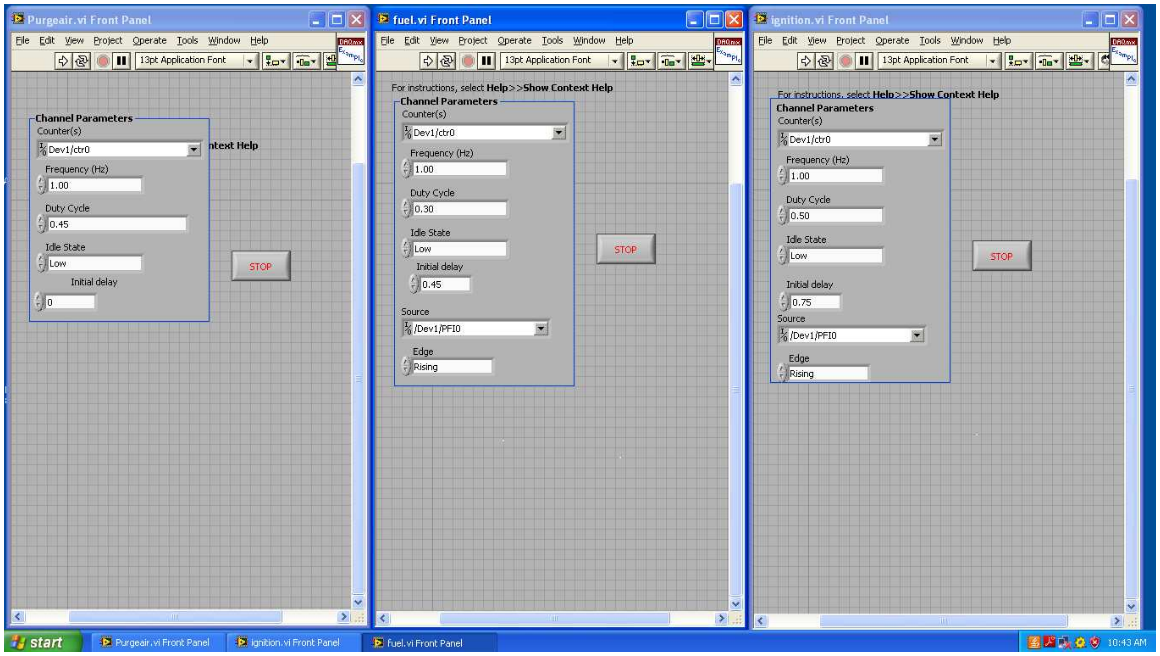

Purgeair.vi Front Panel

ntext Help

Channel Parameters
Counter(s): Dev1/ctr0
Frequency (Hz): 1.00
Duty Cycle: 0.45
Idle State: Low
Initial delay: 0

fuel.vi Front Panel

For instructions, select **Help>>Show Context Help**

Channel Parameters
Counter(s): Dev1/ctr0
Frequency (Hz): 1.00
Duty Cycle: 0.30
Idle State: Low
Initial delay: 0.45
Source: /Dev1/PFI0
Edge: Rising

ignition.vi Front Panel

For instructions, select **Help>>Show Context Help**

Channel Parameters
Counter(s): Dev1/ctr0
Frequency (Hz): 1.00
Duty Cycle: 0.50
Idle State: Low
Initial delay: 0.75
Source: /Dev1/PFI0
Edge: Rising

Figure 3.6: Front panel of the VI used to control the operation of the PDE.

Table 3.1: Sample timing selections for the operation of the PDE.

Frequency (Hz)	Duty Cycle	Initial Delay (s)	Duty Cycle	Initial Delay (s)	Duty Cycle	Initial Delay (s)
	(Purge)		(Fuel)		(Ignition)	
1	45%	0	30%	0.45	5%	0.75
5	45%	0	30%	0.09	5%	0.15
10	45%	0	30%	0.045	5%	0.075
20	45%	0	30%	0.0225	5%	0.0375
50	45%	0	30%	0.009	5%	0.015

Table 3.1 also presents a “duty cycle” parameter which refers to the percentage of time in period or cycle when the valves are active, i.e., open. Initially, solenoid valves manufactured by Dayton Corporation were used but were later replaced by AFS (Calgary, Canada) Gs Series injectors because of the latter’s superior performance. The AFS injectors offered a higher mass flow rate for the same supply pressure. A model of the AFS solenoid valve assembly is shown in Fig. 3.7. AFS injectors are compatible with gaseous hydrocarbon fuels, dry air and gaseous hydrogen.

The driver module for the AFS injectors required a nominal 8 A peak and a 2 A hold current control signal. Figure 3.8 shows typical injector current, voltage, valve position and logical signal traces as provided by AFS. Trace 4 presented in Fig. 3.8 shows an active high input control signal which is the TTL signal transmitted by the control program. Based on this input control signal, the current needed to be varied such that it ramped to peak close to 8 A for approximately 1.5 ms before switching to the hold current mode with a value of 2 A. This facilitated the rapid and precise opening of the injector valve while minimizing excess heat production in the hold phase. Trace 2 shows the injector valve position, illustrating the profile of how the valve opens and closes.

Based on this profile, the change of the injecting surface area was determined which enabled the calculation of time varying mass flow rate through the injector for different gases. The process is further described in Section 3.2. Trace 3 illustrates how the injector voltage is pulsed to keep an average current at both the peak and hold levels.

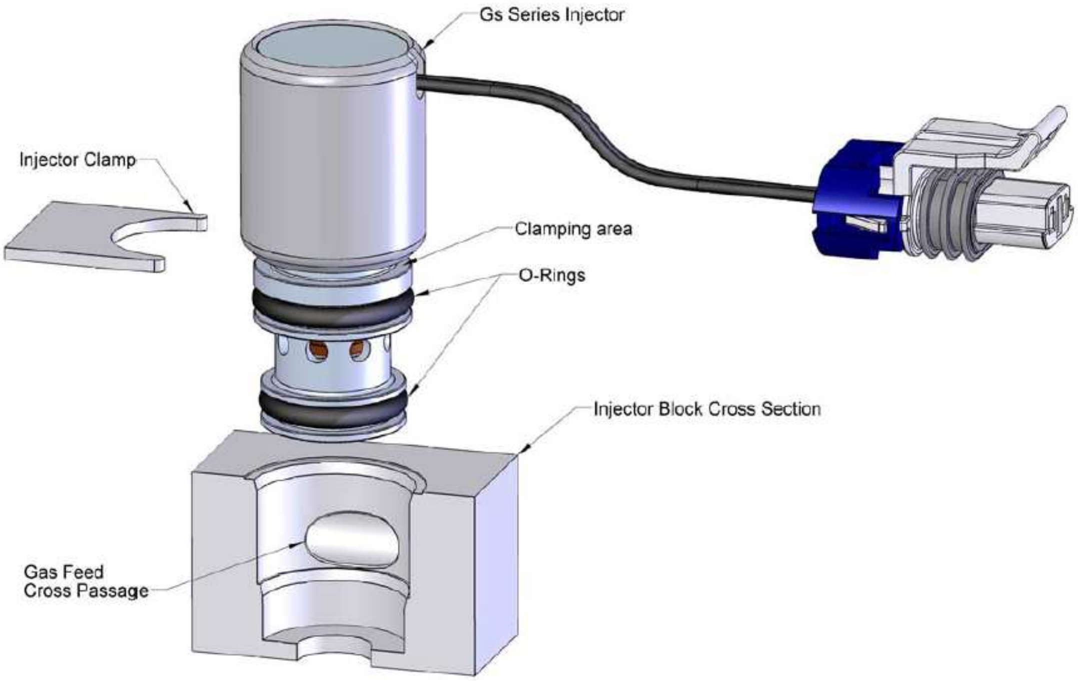

Figure 3.7: Assembly of the AFS solenoid valve [56].

In order to meet the manufacturer's specifications for optimum performance of the AFS valves and achieve the shortest opening time, a current buffer amplifier circuit was constructed to control the operation of the AFS valves. Figure 3.9 shows the circuit diagram of the current buffer amplifier used. The construction of this amplifier was important as the TTL signals from the LabVIEW code cannot be directly used to operate the AFS valves. The built circuit took in the TTL signal, and based on its logic and utilizing a separate current source, the input current was magnified using a Linear Technology (LT 1010) power buffer. The LT 1010 power buffer is a fast, unity-gain buffer that could increase the output capability by more than an order of magnitude [57].

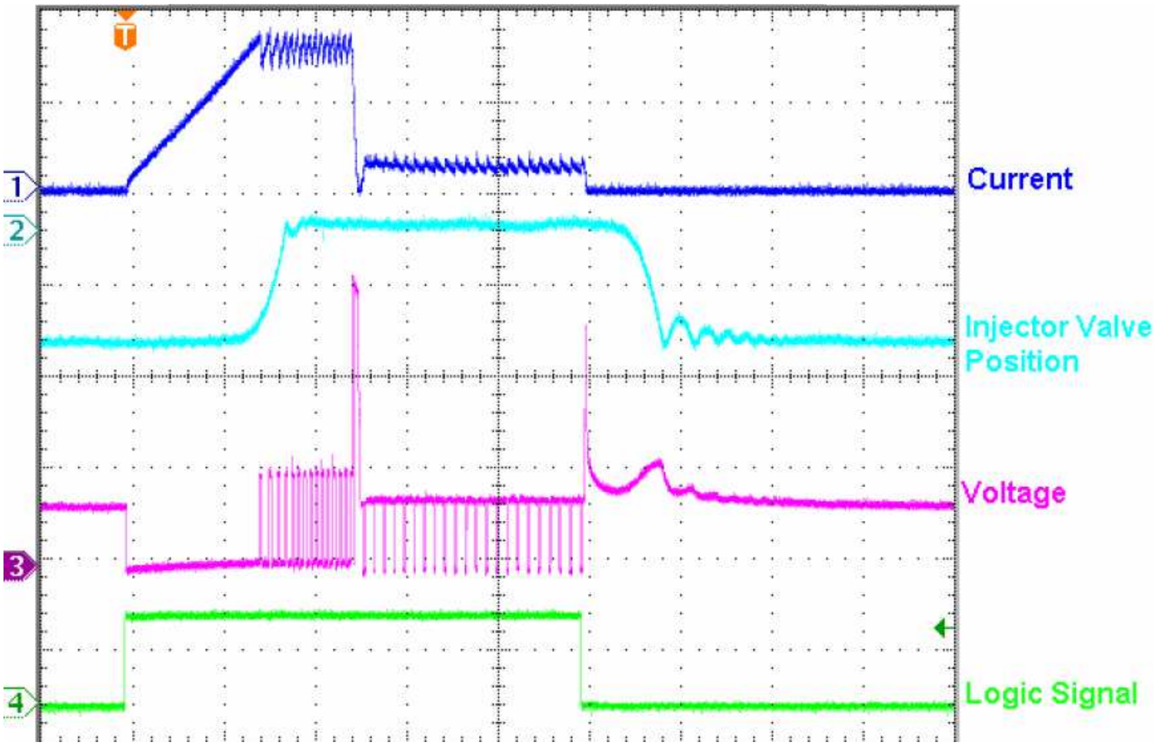

Figure 3.8: : Injector current, valve position, voltage and logic signal for AFS injectors [56].

This magnified current was fed into the control module manufactured by AFS. The control module thereafter controlled the current supply to the injector such that trace 1 shown in Fig. 3.8 was achieved for the optimum operation of the AFS valves. Hence, a TTL signal from the control program, a buffer current amplifier circuit and AFS control modules were used in coordination to properly time the cycle and operate the PDE.

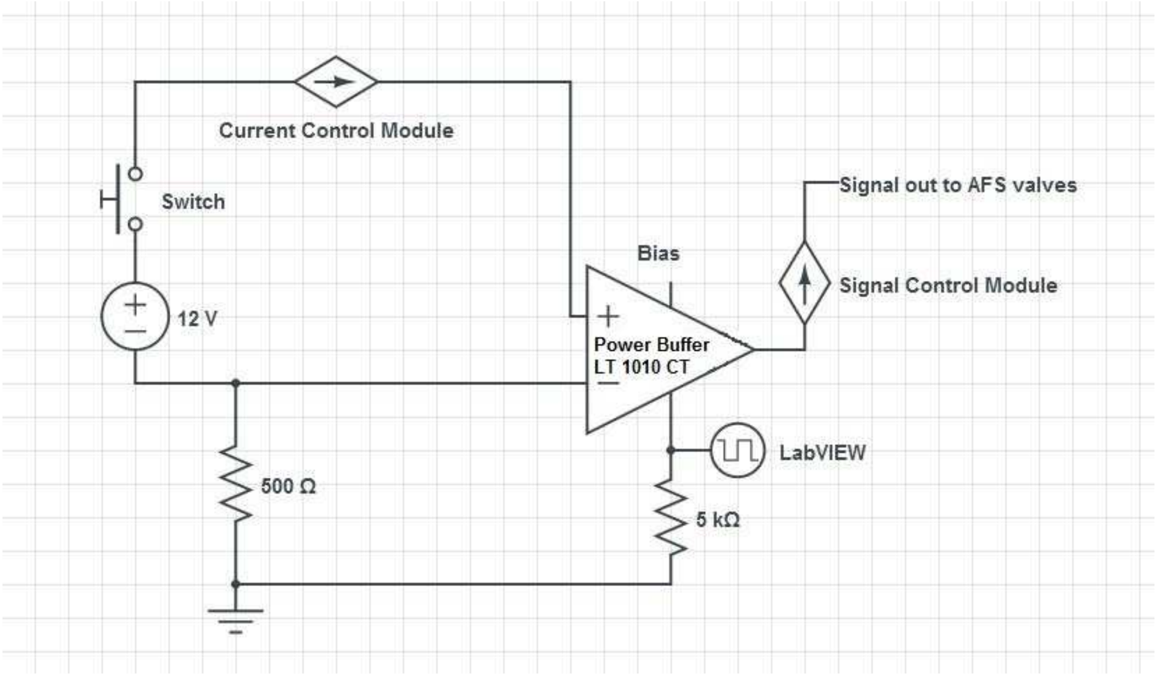

Figure 3.9: Circuit diagram of the current buffer amplifier.

In addition to this, a TTL signal emitted by the control program was sent to the ignition driver system which further magnified the voltage and drove the Bosch Platinum 4 automotive spark plug. The ignition system incorporated a Mallory Hyfire 1A ignition driver and a Mallory ProMaster 29440 Coil, with rated spark energy of 135 mJ [31]. The ignition driver was powered by a 12 V automotive lead acid battery which was recharged before use to ensure proper functioning. The ignition was triggered by means of a transistor control circuit that accepted the TTL signal from the DAQ. The precisely controlled operation and timing of this control circuit was the key for the proper functioning of the PDE. The Bosch Platinum 4 automotive spark plugs had a closed circuit resistance of 3.2 kΩ, ensuring that the spark current was reduced and the resulting electromagnetic interference (EMI) does not distort the measurement of the weak signals of the transducers [31]. The spark plug ignited the detonable mixture causing it to deflagrate. The combustion front transitions into a detonation wave as it travels along the tube, aided in this process by the Shchelkin spiral. This detonation wave upon exiting the tube generated the thrust.

Data were gathered by a simultaneous sample-and-hold system at 700 kHz/channel for 1 s using an NI model PXIe 8130 controller and an NI PXI 6133 DAQ card. A LabVIEW-based program was used for controlling the data acquisition system. The front-end interface allowed the user to change the sampling rate and the number of samples.

3.2 Determination of Important Parameters

Some important parameters were required beforehand for estimating thrust and specific impulse generated by the PDE. In this section, first the response of the system due to a step input force was studied, followed by a description of the methodology to calculate the effective mass and unsteady mass flow rates of gases.

3.2.1 Cut Weight Test

The PDE movement in the *x*-direction makes it possible for the load cell to measure the generated thrust. A cut weight test was performed to examine if there was any substantial effect of friction on the motion of the PDE. A set of calibrated weights were suspended at the open end of the detonation tube and were cut off which provided a step load to the engine that was measured by the load cell. A schematic of the setup for the cut weight test and a sample load cell response when the suspended load was 71 N is shown in Fig. 3.10.

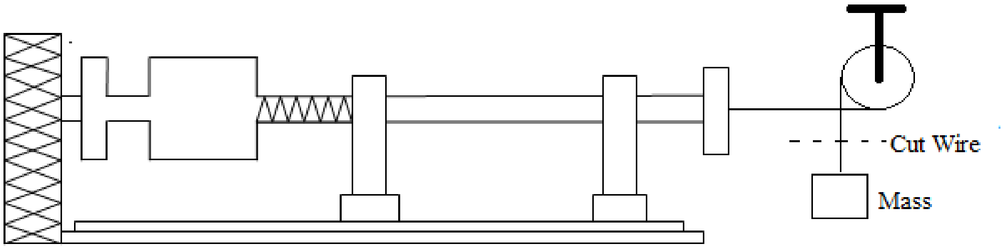

(a)

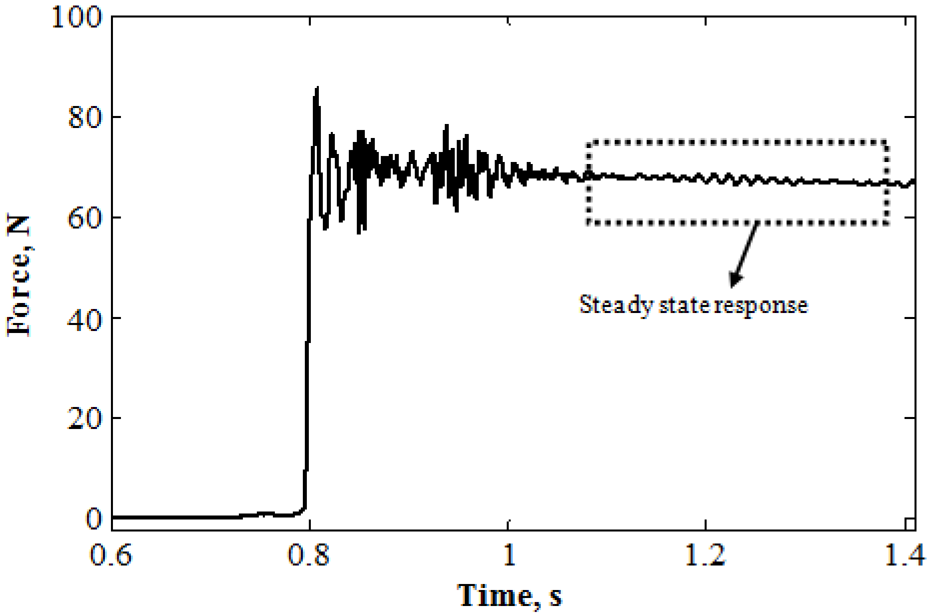

(b)

Figure 3.10: (a) Schematic of setup and (b) sample load cell response for Cut Weight test.

For each case, the average of measured force was taken after the transient response period ended. This allowed for the determination of steady-state force measured due to applied step load which was not convolved by the transient response of the system. As illustrated in Fig 3.11, the slope of the straight line obtained from the linear fit was 0.93 and the measured force was found to be 4.5% less than the applied force. However, during the operation of the PDE, dynamic friction is present between the rails and the linear bearings which is much lower than the static friction. Hence, for PDE operation, the effect of dynamic friction on the measured thrust can be neglected. Figure 3.11 also shows the excellent linearity of the load cell where the linear least-squares fit yielded a correlation coefficient of 0.996.

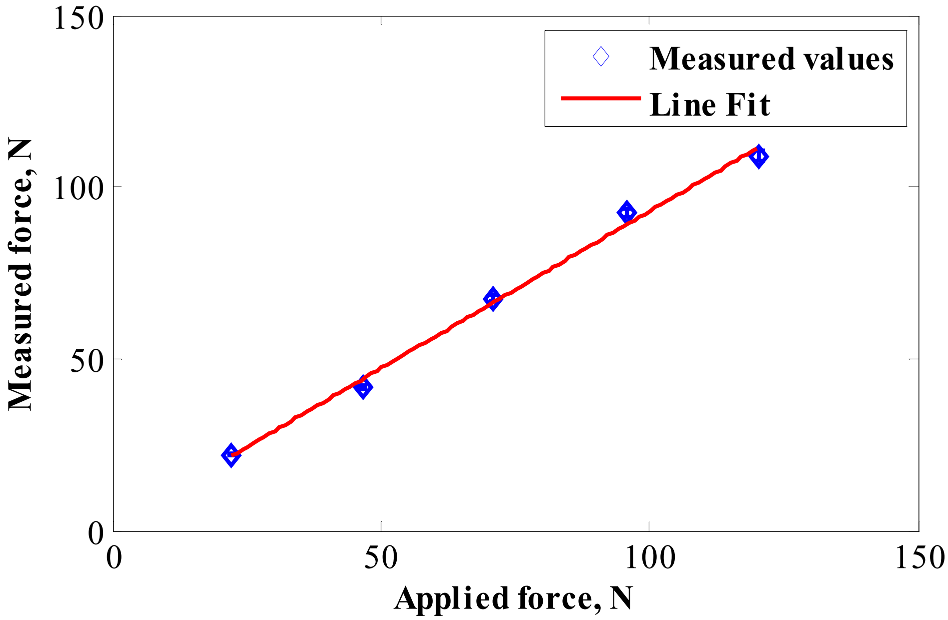

Figure 3.11: Force measured by the load cell for different values of applied step load.

3.2.2 Determination of Effective Mass

The whole PDE structure undergoes cyclic acceleration while in operation. Even though the system displacements were extremely small due to preloading, large oscillatory inertial forces may be experienced due to the prevalent acceleration. Equation (2.18) introduces a term m_{eff} which is the "effective" oscillating mass [28, 58]. This effective oscillating mass represents the mass that is actively oscillating while in operation and contributes to the inertial force which is measured by the load cell in addition to the actual generated thrust.

The acceleration compensation procedure described in Chapter 2 is known as the *rig-based acceleration compensation*. In this procedure, the acceleration of the thrust measurement rig is monitored which is used to estimate the inertial forces added into the measured thrust predominantly due to base motion. In the experimental setup, the thrust measurement rig is fixed to the ground. The entire mass of this structure is not actively involved in generating inertial forces. However, the structure can oscillate and transmit force. Hence, the term “effective mass” represents the actively oscillating mass which introduces inertial forces in the measured signals.

Many attempts have been made in different applications to apply acceleration compensation to account for inertial force superimposed to the measured force by determining the effective mass. However, no such studies have been reported in the literature for PDEs. A method which uses measured acceleration of the base support and empirically determined effective mass has been extensively described by Fujii [59–63]. Runyan et al. [64] discussed a need to account for the dynamic excitation of the supporting base to estimate the actual thrust generated by small rockets. Ren et al. [65] used an analytical model which utilized weight coefficient analogous to the effective mass to implement acceleration compensation. The concept of effective mass was comprehensively presented and utilized for implementing acceleration compensation in aerodynamic force measurements in hypervelocity facilities by Storkmann et al. [27, 28]. Based on the published information, a method was developed in this research project to determine the effective mass of the system.

The method used for determining the effective mass requires the study of the free vibration of the system. A possible way to allow the system to vibrate freely is by applying an impulsive force using an instrumented impact hammer. The response due to the impulsive force and the resulting structural oscillations were measured by the load cell and the accelerometer mounted in the thrust stand respectively. The data were sampled at 200,000 samples per second. The impulsive force, as typified by Fig. 3.12, was applied such that it was within the measurable range of the load cell.

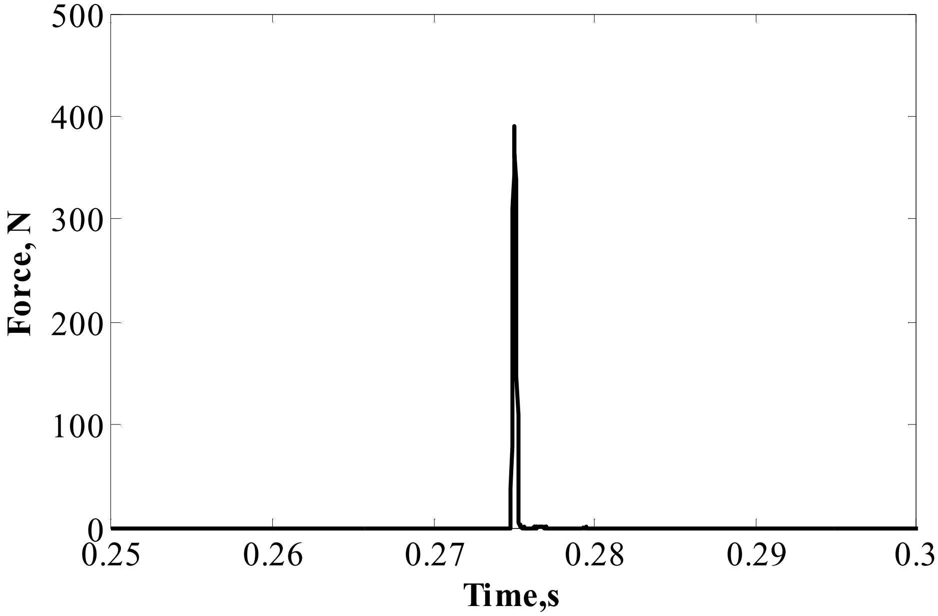

Figure 3.12: Sample input impulse.

When the PDE setup is allowed to vibrate freely without any thrust being generated, equation (2.18) becomes

$$\tilde{F}(t) = m_{eff} a_{meas}(t) \tag{3.1}$$

The measured force and acceleration are then used to determine the effective mass using

$$m_{eff} = \frac{\tilde{F}(t)}{a_{meas}(t)} \tag{3.2}$$

Figure 3.13 shows typical force and acceleration traces as measured by the load cell and the accelerometer respectively due to an impulsive force. Figure 3.13 also portrayed the lightly damped nature of the system through the decaying force and acceleration signals along the null line. Although both force and acceleration are time varying, it is more suitable to represent the effective mass of the system as a single value. Hence, the rms of the signals were taken to estimate the force and acceleration values in order to get a value of the effective mass. The duration of the impulsive force was very small, of $O(0.3 \pm 0.01)$ ms. However, the period of structural oscillations was much longer as seen in Fig. 3.13. Thus, a time interval window had to be determined for which the rms value was calculated. The window should not be too large as the possible time dependence of the effective mass will be lost, nor can it be too short such that the response of the system is not captured due to averaging over a longer period. Thus, a proper time interval is needed to avoid calculating improved estimates of the force and acceleration values.

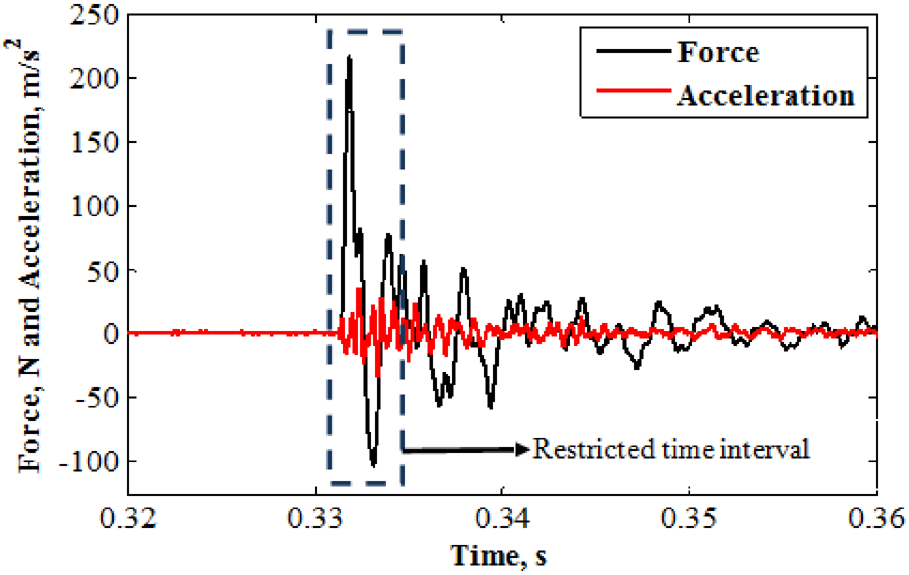

Figure 3.13: Sample restricted time interval to find the rms of force and acceleration.

As discussed above, an optimum time window needs to be selected to capture the sections of the signals which display prominent oscillation magnitudes due to impulsive loading. For the selection of a proper time interval, the damped nature of the system was utilized. For every signal, a characteristic time constant was calculated. This characteristic time constant was chosen to represent the restricted time interval window. The characteristic time constant is defined as the time required for the amplitude of the signal to be reduced by a factor of $1/e$ or 63%. This value was determined based on the procedure discussed in Section 2.3.3.2. Hence, for every case, a restricted time interval was determined and the rms of the force and acceleration within the time interval was calculated, and which were then used to calculate the effective mass from

$$m_{eff} = \frac{F_{rms}}{a_{rms}} \tag{3.3}$$

In this project, analyses were carried out both computationally and experimentally. The effective mass for both experimental and finite element models was calculated separately. For the experimental setup, several data sets with different impulses were analyzed and the restricted time interval window was found to be 2.00 ± 0.25 ms. Hence, a restricted time interval with its starting point at the start of excitation of the system was used to calculate the rms values. Moreover, the same time window was applied to find the rms of the acceleration signals. With the calculated rms values of the measured force and resulting oscillations, the effective mass was then obtained via equation (3.3).

Figure 3.14 shows the values of effective mass for different values of measured peak force. The calculation yielded the effective mass of the thrust measurement rig and any other associated features upon excitation by an impact hammer remained somewhat constant and a representative value of $16.8 \pm$ 1.4 kg is taken. This value of m_{eff} is used in equation (2.20) to apply the acceleration compensation procedure to obtain the actual thrust. The uncertainty bar is the 95 % confidence level of the standard deviation of the measured effective mass values.

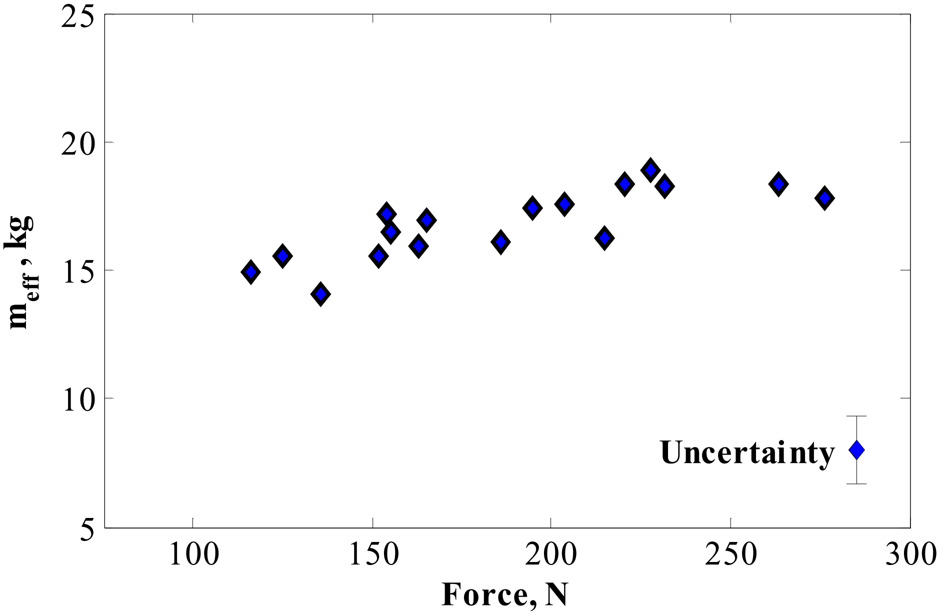

Figure 3.14: Effective mass for different peak force measured by load cell.

Similarly, for the finite element analysis, impulsive forces of different magnitudes in the form of delta functions were applied to the model. The magnitudes of the force inputs were varied but the width of delta function was kept constant at 0.2 ms. Calculations were performed for two values of damping ratios of the system. The first was 0.165 with a corresponding circular frequency of 3142 rad/s and the second damping ratio used was 0.0003 for the same corresponding frequency as before.

For the first case with a damping ratio of 0.165, the value of the effective mass for all values of peak forces remained constant at 12.5 kg showed no deviation and the time interval window also remained constant at 0.77 ms. Figure 3.15 shows the values of effective mass for different peak forces calculated. This case is analogous to the actual experimental setup as damping factor obtained for experimental setup was applied.

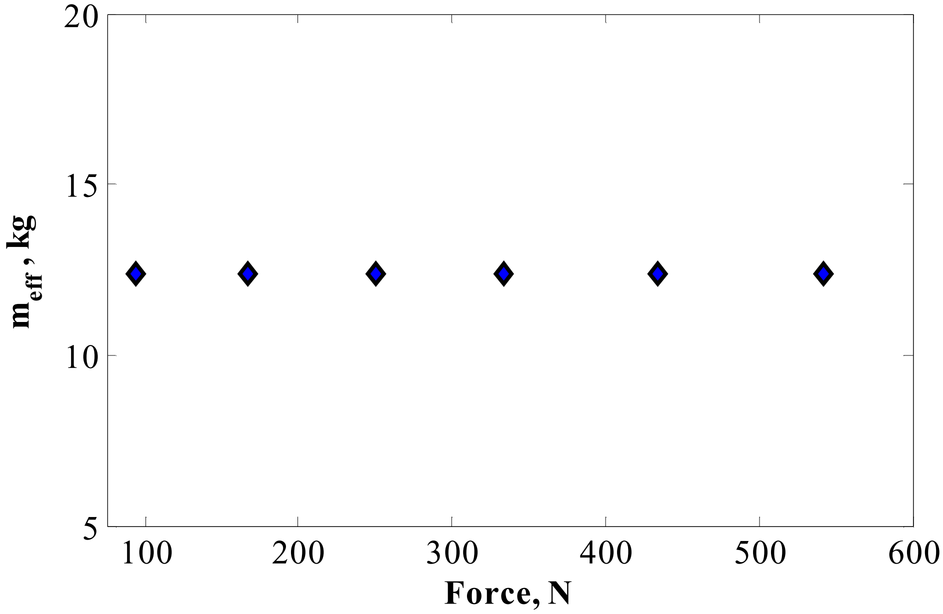

Figure 3.15: Effective mass calculated for finite element model with ζ =0.165.

Figure 3.16 shows the values of effective mass for finite element model when the damping ratio for the system was assigned to be 0.0003. For this case as well, the effective mass remained somewhat constant and the value of 5.26 ± 0.42 kg was taken as a representative. The restricted time interval remained constant at 3.3 ms. It is observed that the effective mass of the system decreased when the system is less damped. As the system undergoes a higher magnitude of oscillations, the rms of the calculated acceleration upon substitution in equation (3.3) decreases the value of effective mass.

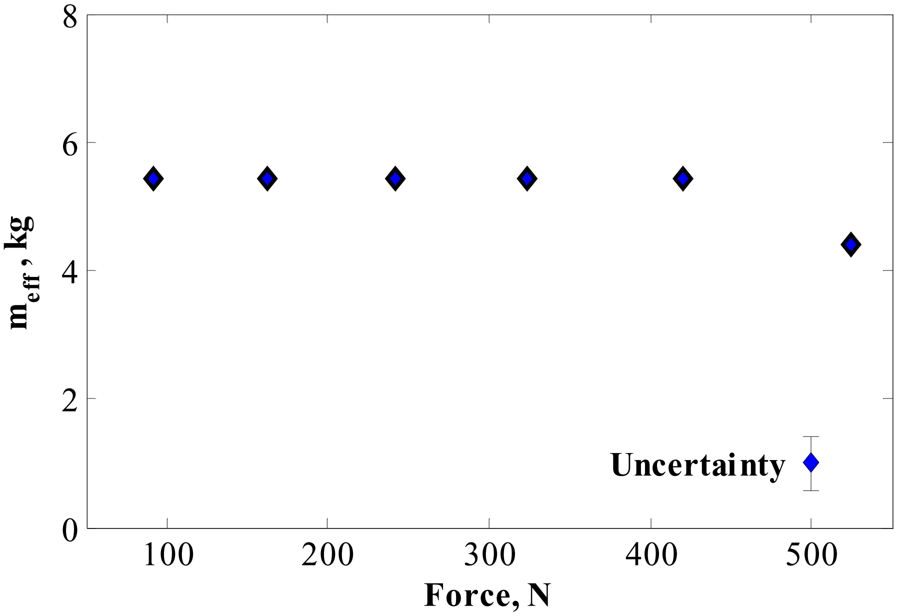

Figure 3.16: Effective mass calculated for finite element model with ζ =0.0003.

3.2.2.1 Remarks on Effective Mass and Acceleration Compensation

The acceleration compensation technique helped to account for the added inertial forces due to the vibration of the thrust measurement rig. In this section, a transfer function between the measured force and acceleration of the thrust measurement rig is studied in the frequency domain. Figure 3.17 shows the frequency response function between the measured force and the acceleration of the thrust measurement rig or the base. In this case, the base acceleration was taken to be input and force as output. The vibrating systems included the thrust measurement rig and the PDE as well. For free vibrations, a distinction was made that the PDE vibration was induced due to the vibration of the thrust measurement rig, i.e., the vibration of thrust measurement rig applies inertial force on the PDE and therefore to the load cell. Figure 3.17 shows a prominent mode at 843 Hz and numerous lower modes of vibrations between 0 to 200 Hz and few more modes between 200 to 800 Hz but with much lower magnitudes. The frequency of 843 Hz was one of the natural frequencies of the system. For lower modes with frequency of 200 Hz, $\omega/\omega_n = 0.24$. Hence, from Fig. 2.4 it can be concluded that for this value of frequency ratio, the dynamically transmitted force was higher than unity and it was in phase with the forcing function.

This comparison shows that the lower modes of vibrations which add inertial forces in the measured force was successfully accounted for by using the acceleration compensation technique. For oscillation frequencies below 843 Hz, the dynamically transmitted force which was in phase with the forcing function can be characterized by the measured acceleration of the base and the effective oscillating mass. Hence, the acceleration compensation technique implemented using equation (2.20) successfully accounted for the inertial forces for lower values of frequency ratios The acceleration compensation technique might not be effective for higher values of frequency ratios. However, any convolution effects due to higher frequency oscillations are accounted for when the system transfer function is used to reconstruct the deconvolved thrust given by $\hat{F}(t)$ in equation (2.20). Therefore, by using the developed experimental approach, the actual thrust was expected to be recovered accounting for pulse-to-pulse interaction, interference due to stress waves and any added inertial forces.

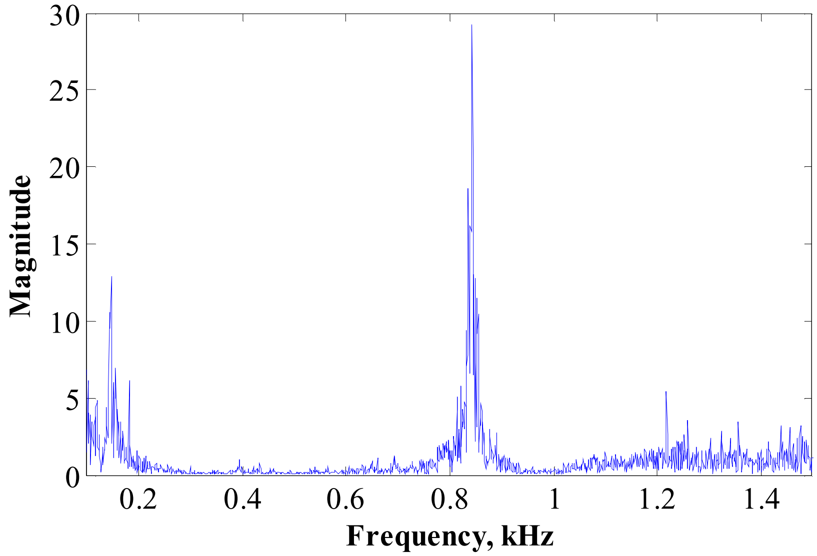

(a)

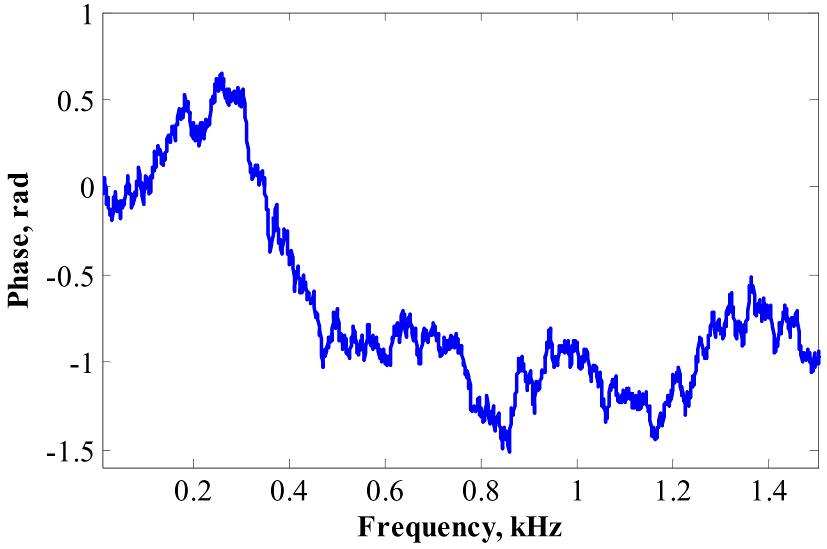

(b)

Figure 3.17: (a) Magnitude and (b) phase spectra of frequency response function between the measured force and acceleration of the thrust measurement rig.

In addition to this experimental discussion, supporting results were obtained from finite element analysis as well. The modal analysis of the thrust stand showed that the first mode of vibration was at 775 Hz which is close to the experimentally obtained first mode of vibration. Figure 3.18 illustrates the mode shape associated with first mode of vibration for the thrust stand.

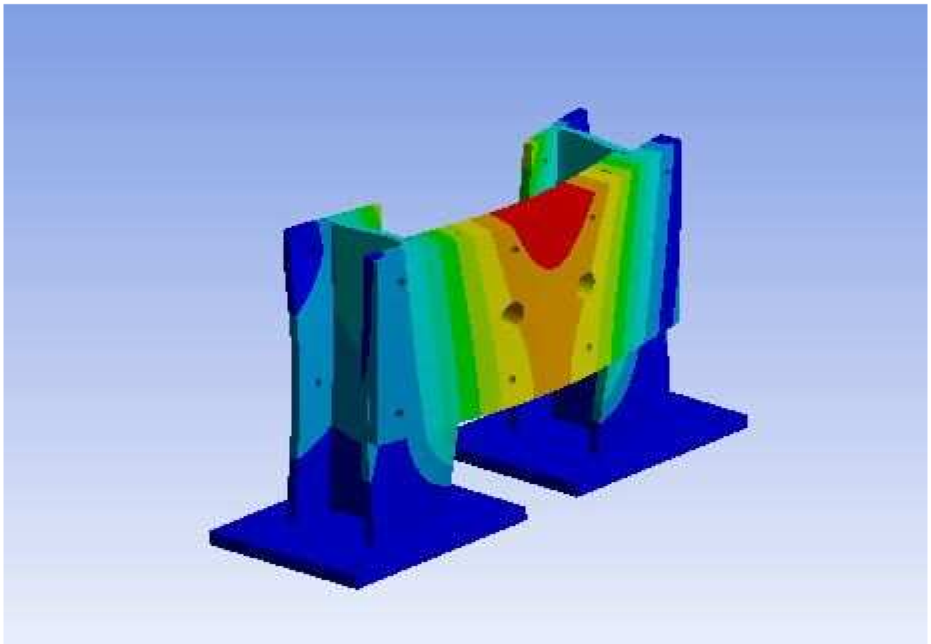

Figure 3.18: Mode shape for the first mode of vibration at 775 Hz for the thrust stand.

3.2.2.2 Remarks on the Use of Impact Hammer

The impact hammer was used in this project to excite the system impulsively and predict the effective mass of the system. The input from the impact hammer was also used to establish the system transfer function for application of developed approach to recover actual aerodynamic drag experienced by a blunt nose cone model in a nominal Mach 8–9 flow. Hence, proper use of the impact hammer is necessary to get meaningful results. Impact hammers are equipped with different types of interchangeable tips. The most common ones are made out of steel, plastic and rubber. Figure 3.19 shows the instrumented hammer and replaceable tips used in this project.

Figure 3.19: Impact hammer with different tips.

The impulses from each type of tips were studied and it was found that the steel tip exhibited significant ringing. And the time window of force application was much longer for rubber tip. Among the three, plastic tip was found to be most suitable as the time window of force application was still small and no significant ringing was observed. Figure 3.20 shows the measured impulses for the impact hammer with different tips. Hence, it is concluded that an impact hammer with plastic tip is the most suitable combination to be used for impact testing. Figure 3.21 shows the magnitude spectrum of transfer function between hammer input and resultant acceleration of the thrust measurement rig. It is observed that modes excited by all three tips were in good agreement. However, a plastic tip was chosen to be the suitable candidate because of its ability to generate a crisp input.

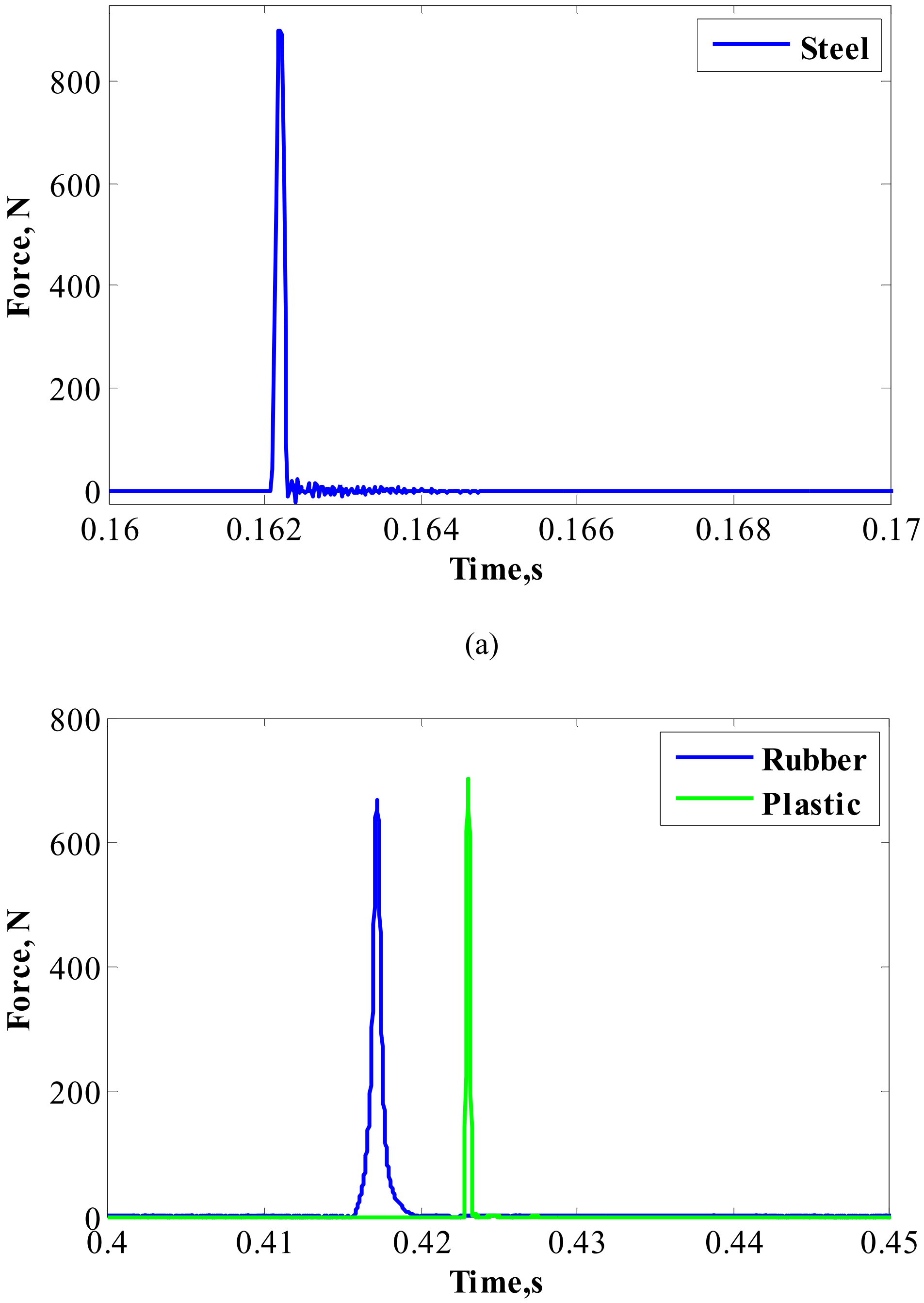

(a)

(b)

Figure 3.20: Measured input of the impact hammer for (a) steel tip (b) plastic and rubber tips.

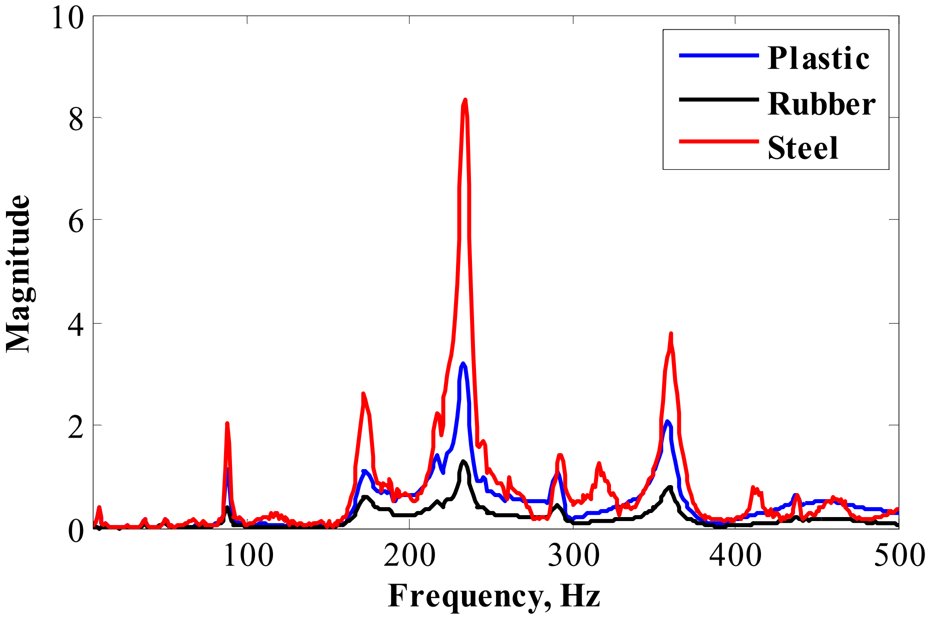

Figure 3.21: Magnitude spectrum for transfer between hammer input and thrust stand acceleration.

3.2.3 Mass Flow Rate Measurement

The measurement of mass flow rates of fuel and oxidizer is important for determining the performance parameters of a pulse detonation engine such as its specific impulse. In addition, flow rates were used for the calculation of filling fraction of the detonation tube. Both of these parameters have a large impact on determining the effectiveness and practicability of a PDE. The propellant mass flowing into the PDE is intermittent which complicates the entire measurement process. The propellant injected can either be liquid or gaseous. It is considered that the pulsed mass flow rate measurement of a gas is more difficult compared to that of a liquid [66]. This section of the research work describes a general methodology developed to correctly estimate the mass of gaseous propellants injected during the filling phase for any frequency. In addition, the method accounted for the losses due to viscous effects which could be significant in case of heavy gases.

Recent work on thrust measurements of PDEs include numerous methods to measure the mass flow rates of fuel and oxidizer injected into a PDE. Kasahara et al. [7] described a total mass-weighted method to estimate propellant mass flow measurement for one cycle obtained from the total mass decrease in the propellant cylinders divided by the total number of cycles. In the same paper, the authors described another method to estimate the propellant flow rate which required the measurement of cylinder pressure differences before and after an experiment. Henceforth, mass differences were estimated from the pressure differences and the equation of state. These two methods were applied simultaneously to ensure the credibility of propellant mass flow rate measurements. The presented methods might impose some error as they do not take into account the unused gases which could still remain in the tubes connecting the PDE and the gas tanks. An error which may be significant may be incurred if the drop in mass is small, as will likely be the situation due to the heavy cylinder. Moreover, it is also not certain that utilizing these methods will account for losses throughout the supply path.

Li et al. [66] described the operation of a PDE with liquid kerosene as fuel and gaseous oxygen as oxidizer. These authors discussed the use of an orifice meter to measure the mass flow rate of liquid kerosene. A method of gas collection in a cold-state experiment, during which oxygen was intermittently supplied into the detonation tube without ignition, was used to obtain a time-averaged flow rate of the oxidizer. The time-averaged flow rate was based on the amount of gas collected at the exit of the detonation tube in a certain period of time. This method can be accurate when the calibration duration is performed for a very long time such that the total mass of gas collected at the exit is much greater than any gas left inside the tube.

A new method was developed as a part of this research work to correctly measure the mass flow rate of gaseous fuel and oxidizer injected into a PDE. This method first determined the ideal mass flow rate of gases injected into a PDE. The ideal mass flow rates were calculated using the mass flow parameter of the gas used in the operation. The mass flow parameter of a gas is dependent on the total pressure and temperature at the supply. In addition, the mass flow parameter is also dependent on the area of the injecting surface and, for a calorically perfect gas, on the specific heat ratio and Mach number. For a PDE, the area of injecting surface varies with time during a cycle. For a typical test run in the present work, the supply pressures and temperatures were measured using static pressure transducers and thermocouples installed on the gas supply cart respectively. The area of the injecting surface changes as the solenoid valves were pulsed. A simple “ramp” model of a typical time varying injecting surface area was used for the calculation since a more complex opening and closing profile such as a cosine window would not yield much improved accuracy. The prepared model was proposed for the area variation of Gs series AFS solenoid valves.

With the measured values of total pressure and temperature at the supply and a known profile of the surface area of injection, the mass flow rate of gaseous fuel or oxidizer injected into the PDE can be calculated using

$$\dot{m}(t) = \frac{A(t)P_t}{\sqrt{T_t}}\sqrt{\frac{\gamma_i}{R_i}}M\left(1+\frac{\gamma_i-1}{2}M^2\right)^{\frac{-(\gamma_i+1)}{2(\gamma_i-1)}} \tag{3.4}$$

where P_t is the supply total pressure, T_t is the total temperature of the supply, γ_i is the specific heat ratio , R_i is the gas constant, M is the exit Mach number and $A(t)$ is the time varying area of injecting surface.

The fuel and the oxidizer were injected intermittently into the PDE by moving the injector inside of the AFS solenoid valve. When the injector inside the valve was moved up rapidly, an exposed surface in the form a cylinder was created which allowed the gas to flow into the PDE. This area of the injecting surface changed with time throughout a cycle. When completely opened, the injector was lifted up 0.254 mm (0.01 in.) from its closed position. The radius of the outlet for the solenoid valve is 6.86 mm (0.27 in.). At the fully open position, the surface area available for injection is 5.47 mm^2, which is the surface area of the virtual cylinder formed when the injector is completely lifted up. According to the manufacturer's specifications, it takes the injector less than 2 ms to reach the fully open position. Based on the available information and measured area, a model of the change in injection area during a 10 Hz operation is shown in Fig. 3.22. Moreover, by maintaining a minimum critical pressure ratio between the supply and the exhaust of the valve during the entire injection cycle, the flow was always choked during PDE operation.

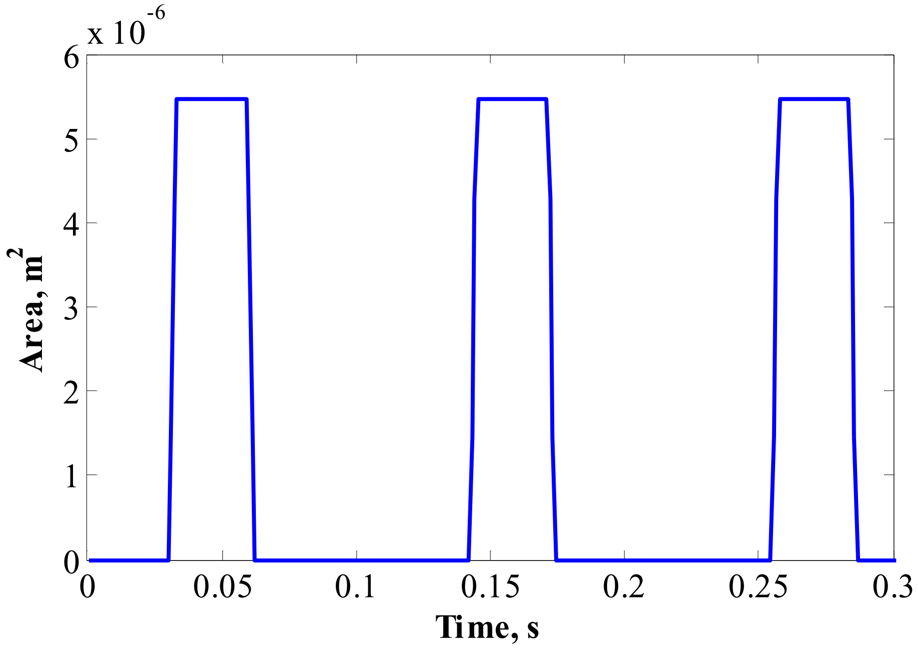

Figure 3.22: Time varying area of injecting surface for a 10 Hz operation of the PDE.

The conditions for the choked flow is given by

$$\frac{p_u}{p_d} \geq \left(\frac{\gamma_i + 1}{2}\right)^{\frac{\gamma_i}{\gamma_i - 1}} \tag{3.5}$$

where p_u is the upstream supply pressure and p_d downstream pressure which is the ambient atmospheric and taken to be 0.101 MPa (14.7 psia). The upstream pressure is the supply pressure. Hence for discharge into the ambient, a minimum pressure of 0.193 MPa was maintained at the supply when the gas used was hydrogen and a supply pressure of 0.192 MPa was maintained when the gas used is air or oxygen to achieve choked flow at the exit of the solenoid valve. The supply pressures are maintained such that the flow is always choked while injecting, hence, equation (3.4) can written in a simplified form as

$$\dot{m}(t) = \frac{A(t)P_t}{\sqrt{T_t}} \sqrt{\frac{\gamma_i}{R_i}\left(\frac{2}{1 + \gamma_i}\right)^{\frac{(\gamma_i + 1)}{2(\gamma_i - 1)}}} \tag{3.6}$$

The value of $\dot{m}$ calculated via equation (3.6) gives an ideal value of mass flow rate. Non-ideal effects bring about head loss that cannot be calculated theoretically. Thus, a discharge coefficient C_d is used to take these effects into account. Typically, the value of the discharge coefficient is a function of the inlet and outlet diameters and the Reynolds number of the flow [67]. Further losses are also incurred by the complex assembly of the AFS solenoid valves as shown in Fig. 3.7. Moreover, this complex geometry of the valve and mounting chamber prevents any pressure measurement through pressure taps. Therefore, the discharge coefficient for the valve assembly had to be determined experimentally.

The experimental determination of the discharge coefficient required steady flow to be maintained. The valves were kept fully open for 4 s. An Omega 2621 mass flow meter was connected to the exit of the solenoid valve assembly. The mass flow meter measured the mass flow rates through the valves for different values of supply pressures. The ratio of measured value of mass flow rate and the corresponding ideal value of mass flow rate for the same supply pressure calculated via equation (3.6) yielded the discharge coefficient for the valves given by

$$C_d = \frac{\dot{m}_{measured}}{\dot{m}_{ideal}} \tag{3.7}$$

Figures 3.23–3.25 show the variation of discharge coefficient with supply pressure for oxygen, dry air and hydrogen respectively. Figures 3.23 and 3.24 show that the value of the discharge coefficient remained fairly constant when the supply pressure was greater than 0.40 MPa (58 psia) for oxygen and dry air. For PDE operations considered in this work, the supply pressure of air and oxygen was greater than 0.40 MPa. Hence, for dry air and oxygen, discharge coefficient values of 0.74 and 0.57 respectively were taken as representative. The supply pressure of hydrogen was varied for different test cases to control the filling fraction of the tube and to maintain stoichiometry. The trend shown in Fig. 3.25 for the discharge coefficient was expected to reach a steady value when the supply pressure was greater than 0.80 MPa. However, for all the PDE tests, hydrogen pressures varied between 0.20–0.80 MPa so that a constant C_d value could not be assumed. Instead, a third-order, least-squares fit was chosen to portray the variation of discharge coefficient with the supply pressure. The equation is given by

$$C_{d,hyd} = 2.96p^3 - 5.02p^2 + 2.94p + 0.192 \tag{3.8}$$

where p is the supply pressure in MPa and $C_{d,hyd}$ is the discharge coefficient for hydrogen gas. The value of the correlation coefficient for this fit is 0.99. Hence, for hydrogen at a measured supply pressure, a value of discharge coefficient was calculated via equation (3.8).

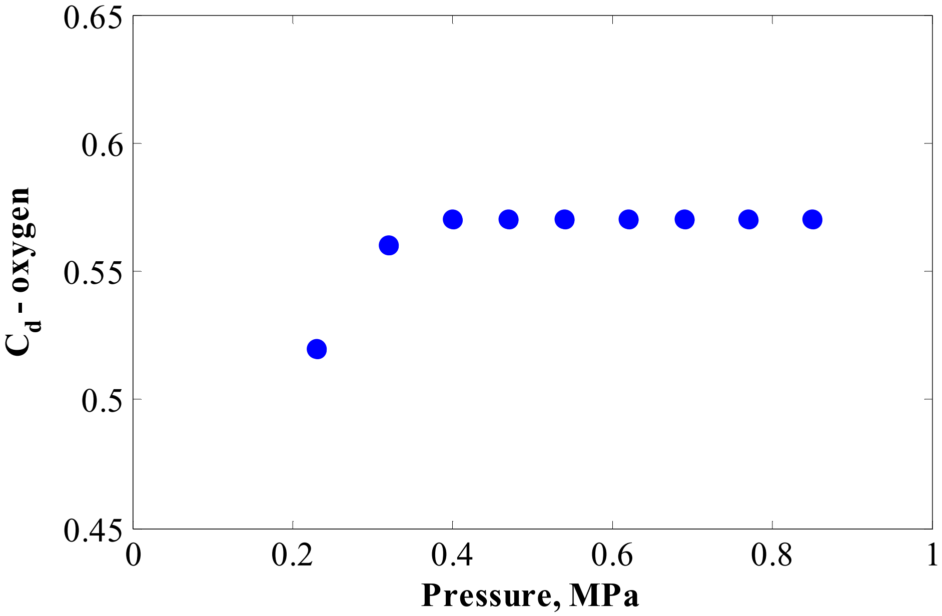

Figure 3.23: Variation of C_d with supply pressure for gaseous oxygen.

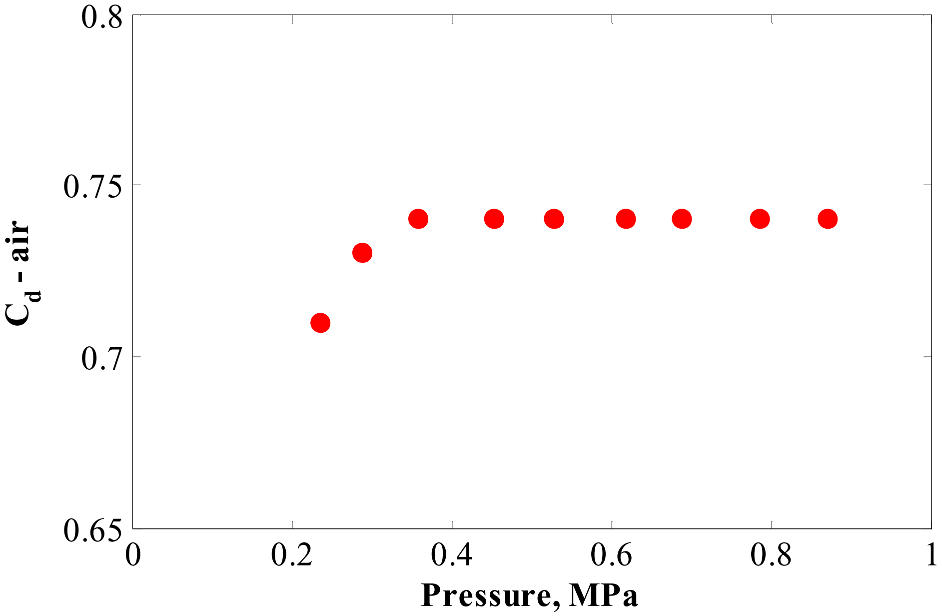

Figure 3.24: Variation of C_d with supply pressure for dry air

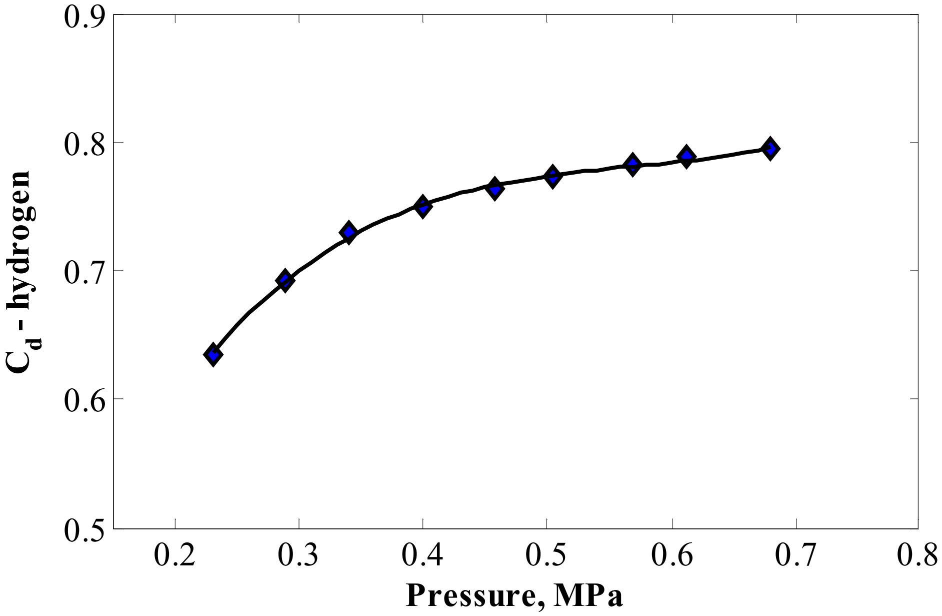

Figure 3.25: Variation of Cd with supply pressure for gaseous hydrogen

For a typical PDE operation, first, an ideal mass flow rate of a respective gas was calculated via equation (3.6), which was further multiplied by the C_d value to get actual mass flow rate. Figures 3.26–3.28 show the time varying mass flow rates of dry air, oxygen and hydrogen for the operation of PDE at 10 Hz. The chosen duty cycle for the hydrogen and oxygen solenoid valves was 30% and the duty cycle for the purge air solenoid valve was 45%. The mass flow rates depended on the supply pressure and temperature. The supply pressure for dry air, oxygen and hydrogen were 0.81, 0.40 and 0.49 MPa respectively. All the gases were at 300 K. The value of discharge coefficient calculated for hydrogen gas via equation (3.8) was 0.78. The calculated profiles of mass flow rates for gases upon integration with respect to time yielded the total mass of fuel injected into the detonation chamber per injection.

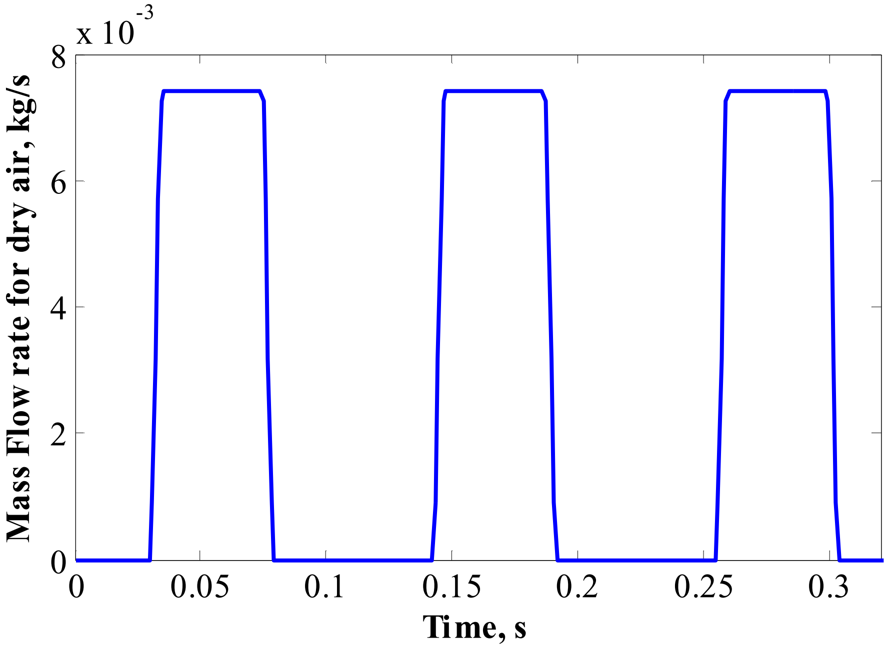

Figure 3.26: Time varying mass flow rate of dry air for a 10 Hz operation with a supply head pressure of 0.49 MPa.

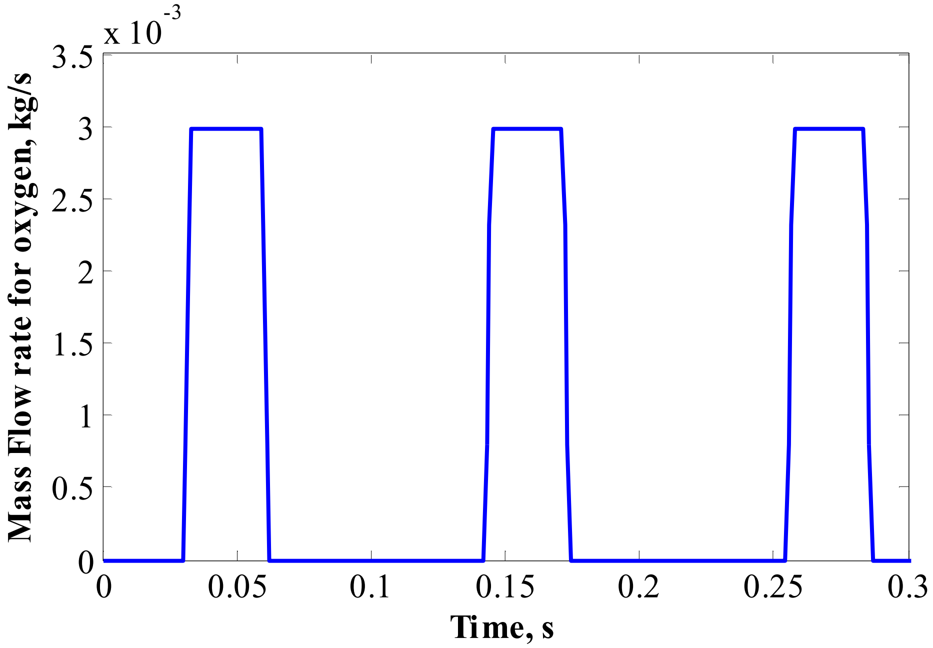

Figure 3.27: Time varying mass flow rate of oxygen for a 10 Hz operation with a supply head pressure of 0.49 MPa.

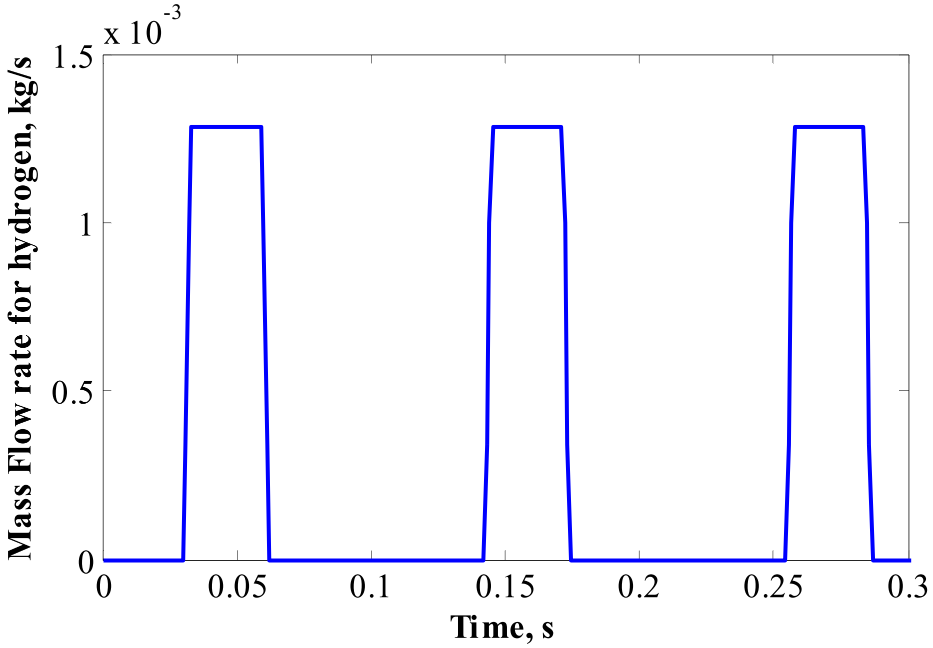

Figure 3.28: Time varying mass flow rate of hydrogen for a 10 Hz operation with a supply head pressure of 0.49 MPa.

Chapter 4

Results and Discussion

The unsteady thrust generated by a PDE is analyzed using the general approach described in Chapter 2. The thrust values obtained are used to find the impulse and specific impulse of the PDE. This chapter first highlights the experimental results followed by the results of semi-empirical calculations and finite element analysis. The experimental results section also presents mass flow rates which are needed to calculate the specific impulse. The experimental results are compared against the semi-empirical results obtained using the control volume analysis and finally against the finite element results. Specific impulse is used as the parameter to compare the results obtained from all methods. The experimental results are presented for 1, 10 and 20 Hz operation. The finite element approach is extended to calculate specific impulse for 50 and 100 Hz operation in addition to 1, 10 and 20 Hz operation cases.

4.1 Experimental Results

The operation of the PDE at 1, 10 and 20 Hz allowed the measurement of the generated force and the induced acceleration of the system due to repetitive detonations. These measured signals were processed to obtain the true value of thrust. The measured thrust was first deconvolved using the system transfer function. The deconvolved thrust and measured acceleration of the thrust measurement rig were used to calculate the acceleration compensated impulse generated by the PDE.

Thrust is generated by the PDE by means of combustion of a fresh detonable mixture and exhaust of the burned products. While in operation, the filling of the combustion chamber of the PDE can be controlled by precise timing of the valves. The tube can be fully, partially or over filled. In the over filled case, the excess reactants form a cloud just outside the exit the PDE. The combustion of this excess fuel outside the PDE does not contribute in the generation of the thrust. However, partial filling is expected to increase the specific impulse of the PDE [68]. In addition, the PDE can also be operated with the detonable mixture at different equivalence ratios, i.e., the concentration of the fuel and oxidizer injected in the PDE can be varied. In this research project, the developed approach was applied to get the impulse of the PDE for a fully and a partially filled case and for different equivalence ratios. The results are further discussed. In this section, the results of the deconvolution procedure are first illustrated followed by the results of the acceleration compensation procedure.

4.1.1 Thrust Reconstruction

The system transfer function using a single pulse of detonation wave as input and measured force as output was obtained in the frequency domain via equation (2.7). The pressure transducer and load cell signals representing the input and output respectively were each acquired at 700,000 samples per second to increase the temporal and frequency resolution. An example of a single-shot detonation pressure profile is shown in Fig. 4.1 and the associated load cell output is shown in Fig. 4.2. The magnitude and phase spectra of the transfer function are shown in Figs. 4.3 and 4.4 respectively. These figures show the frequency in kHz, revealing substantial high-frequency content which did not directly affect the low-frequency measurement. Because the entire system was considered to be linear, even though the transfer function was obtained from a single shot of detonation, it was expected to apply to any arbitrary excitation. Before the deconvolution process was carried out, the validity of the established transfer function was verified. The transfer function was used to reconstruct both input from the measured output and vice versa for the same and different experiments. Proper reconstruction of all the signals was successful and illustrated in figures 4.5–4.8. It can be seen that the reconstructed signals appeared to be extremely similar to the measured ones. The successful reconstruction of respective output and input for same and different experiments also indicated the linearity of the system.

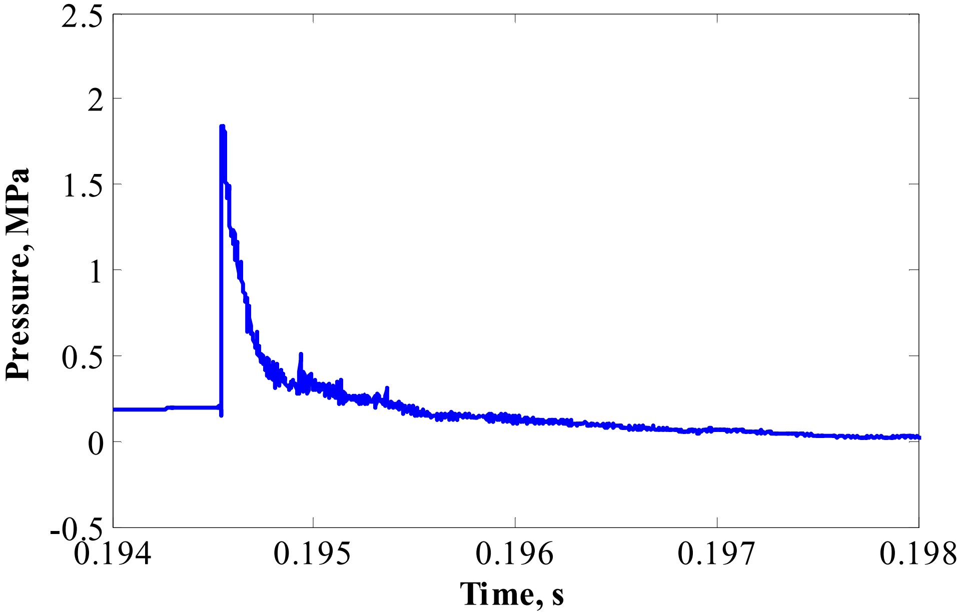

Figure 4.1: Pressure profile for a single shot of detonation.

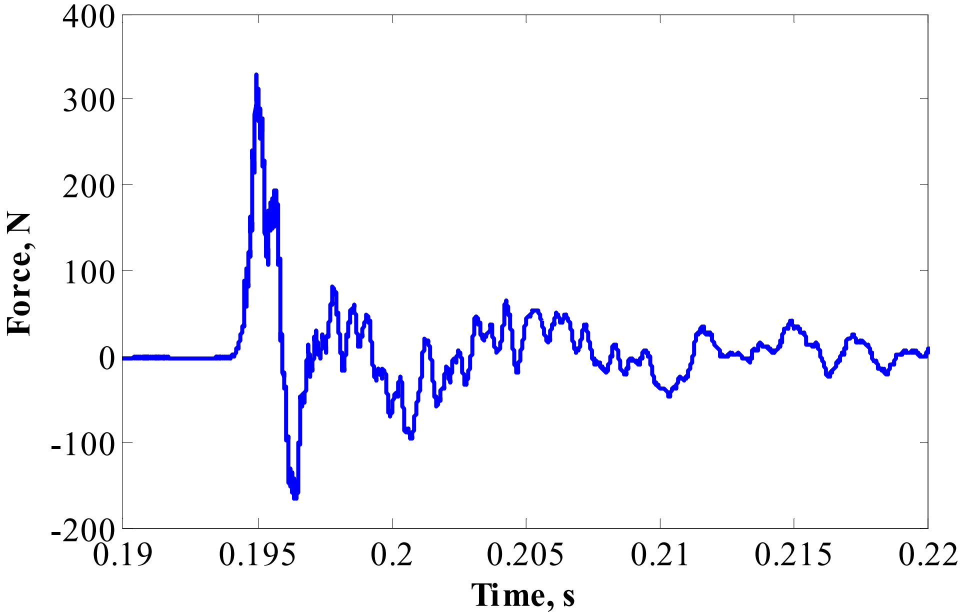

Figure 4.2: Load cell response due to single shot of detonation.

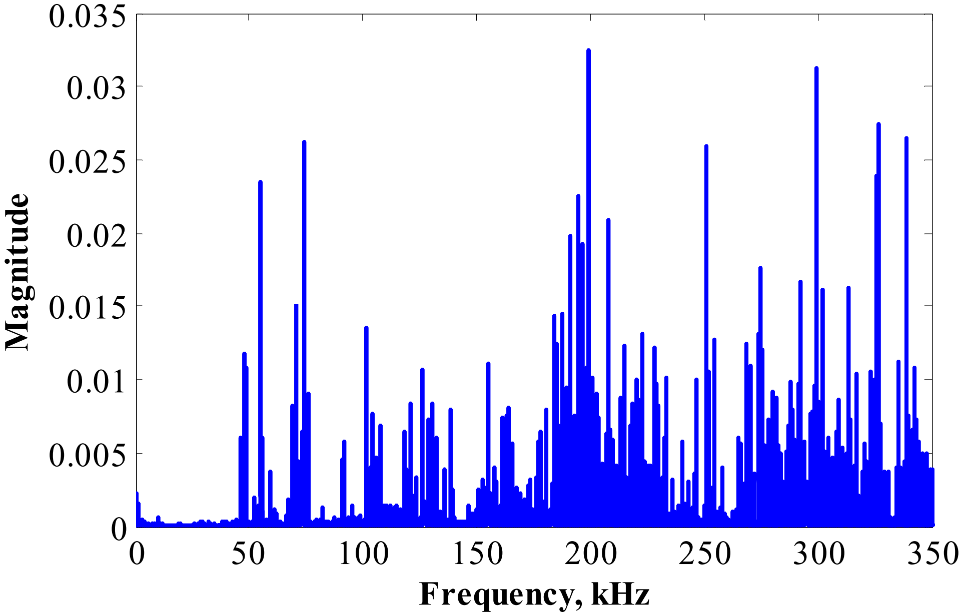

Figure 4.3: Magnitude spectrum of the established experimental transfer function.

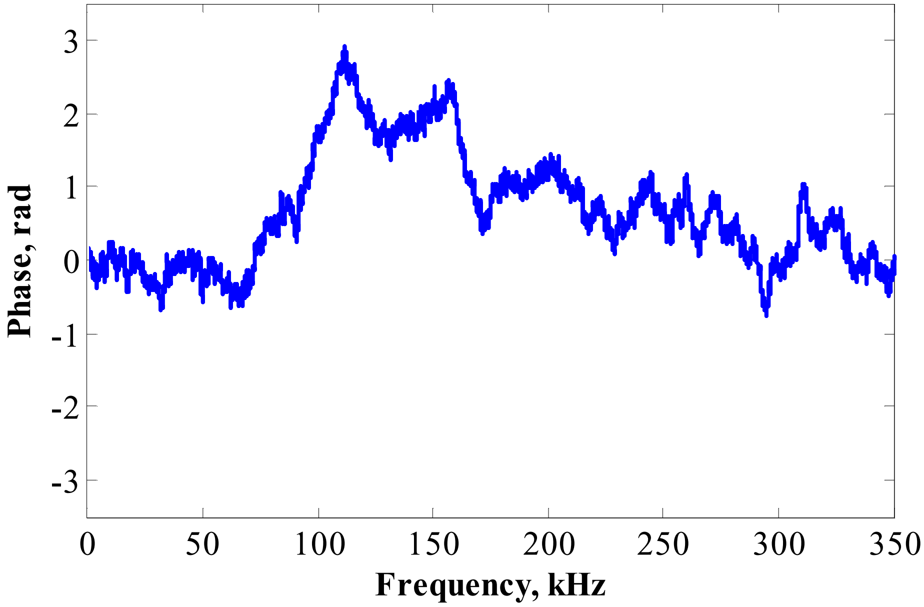

Figure 4.4: Phase spectrum of the established experimental transfer function.

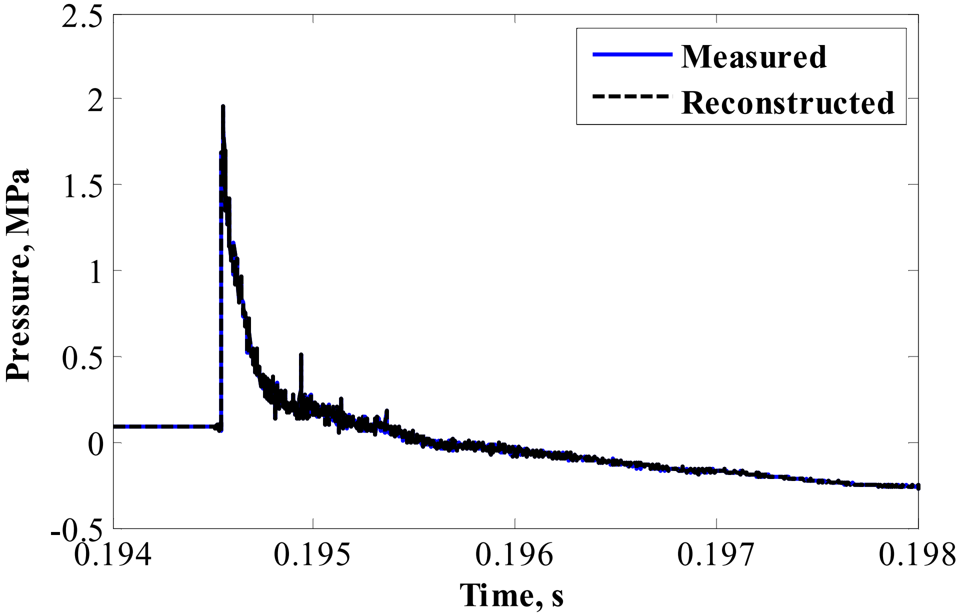

Figure 4.5: Input reconstruction for same experiment.

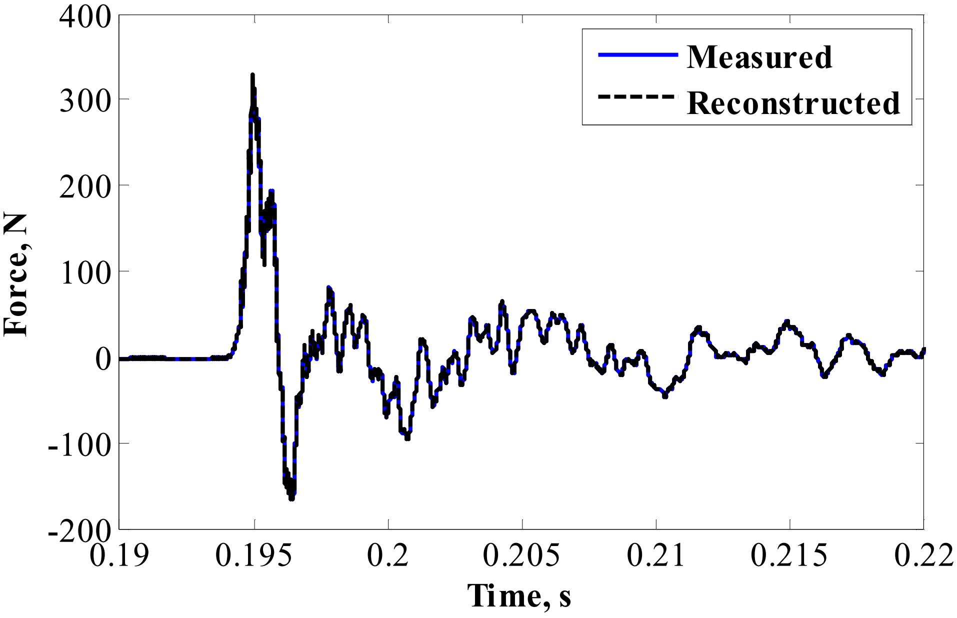

Figure 4.6: Output reconstruction for the same experiment.

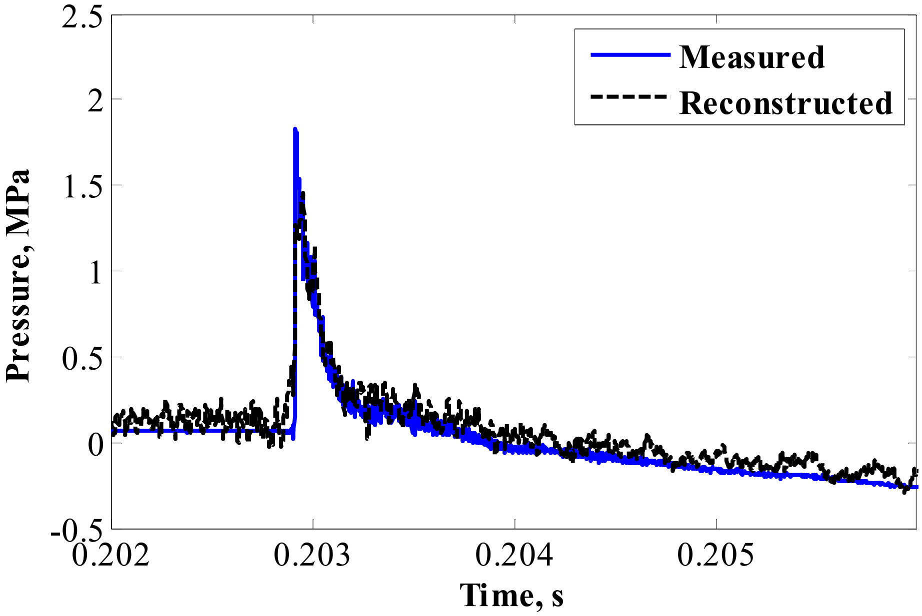

Figure 4.7: Reconstruction of input for different experiment using established experimental transfer function.

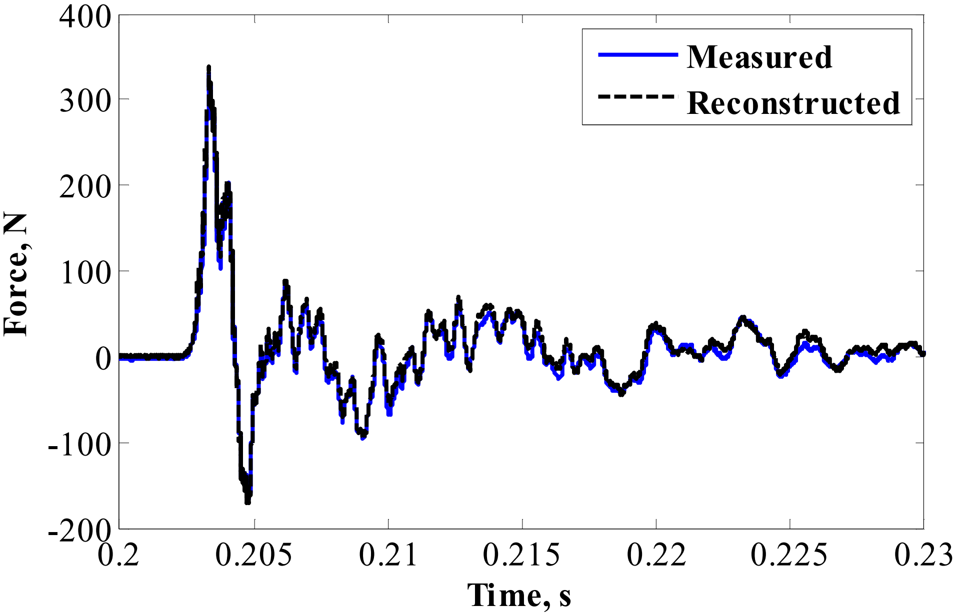

Figure 4.8: Reconstruction of output for different experiment using established experimental transfer function.

As depicted in Figs. 4.5–4.8, the reconstruction of both input and output was feasible using the experimental transfer function. Of particular interest are Figs. 4.7 and 4.8 as the transfer function, and the input and output signals were from two different experiments. Some discrepancy was observed when the input pressure was reconstructed as the signal obtained after deconvolution contained high-frequency noise and slightly lower in magnitude. This was expected since, for the reconstruction of input, equation (2.7) had to be arranged such that the measured output was divided by the established transfer function. This division process magnified the high-frequency content in the transfer function and caused a decrease in the gain of the entire system. However, a proper reconstruction of the output was achieved for this case as shown in Fig. 4.8. In this case, a multiplication was carried out in the frequency domain between the established transfer function and measured input signal. Although the transfer function already involved division, a severe effect of magnification of high frequency content as presented in Fig. 4.7 was not observed. With this knowledge, the measured pressure histories were chosen as the candidate that would be used as input for the established transfer function to reconstruct the output. It can be noted that no digital filters were applied to any of the raw signals used to establish and validate the transfer function.

The excitations that were used currently were the pressure histories measured at the exit of the PDE operating at 10 and 20 Hz. Figures 4.9 and 4.10 illustrate the experimental input pressures used to facilitate the deconvolution procedure. The raw input signals were first filtered using a bandpass Butterworth filter at 0.04–125 kHz to remove any high-frequency content which could adversely affect the deconvolution procedure. Figures 4.11 and 4.12 illustrate the reconstructed thrust using the input shown in Figs. 4.9 and 4.10 respectively.

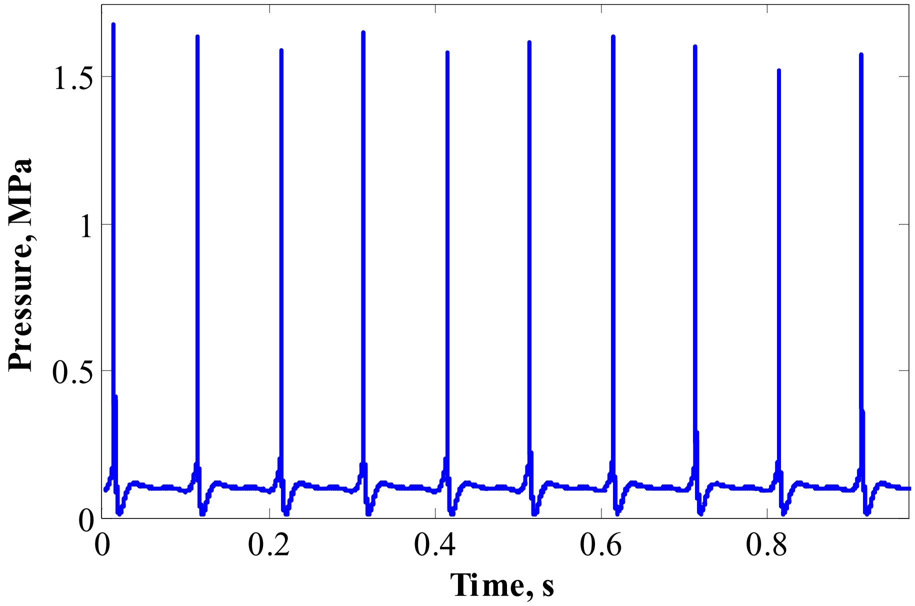

Figure 4.9: Input excitation of 10 Hz used to get deconvolved thrust value.

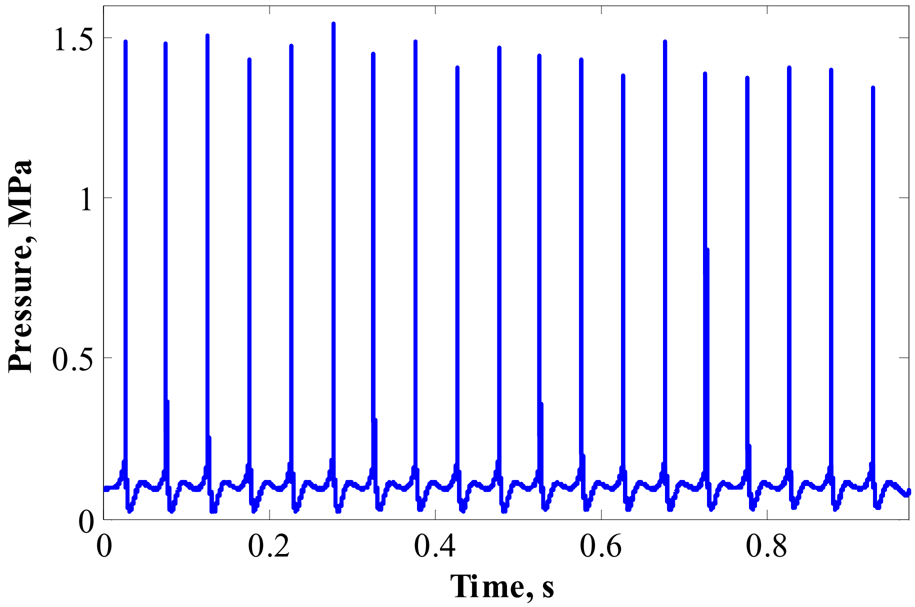

Figure 4.10: Input excitation of 20 Hz used to get deconvolved thrust value.

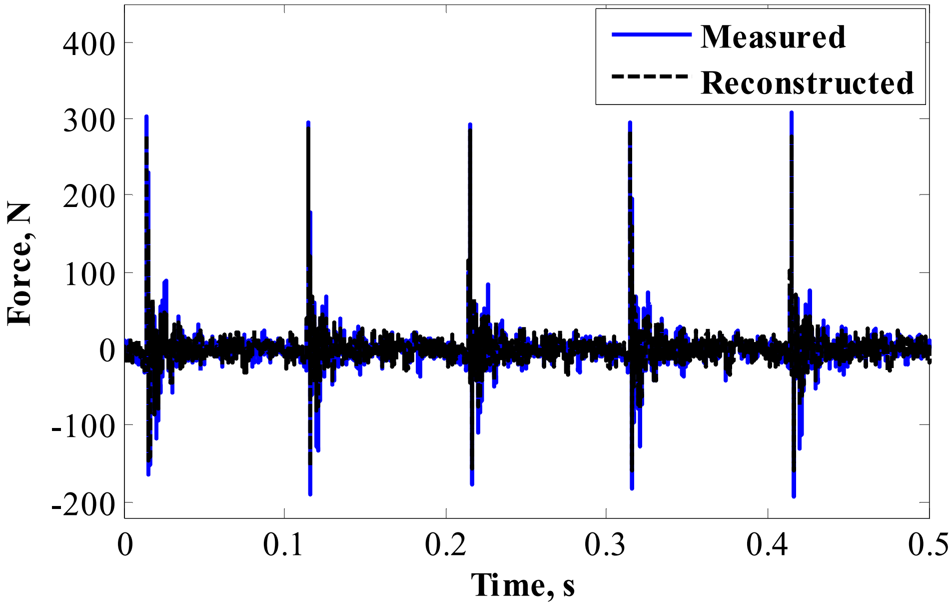

Figure 4.11: Measured and reconstructed thrust for 10 Hz operation.

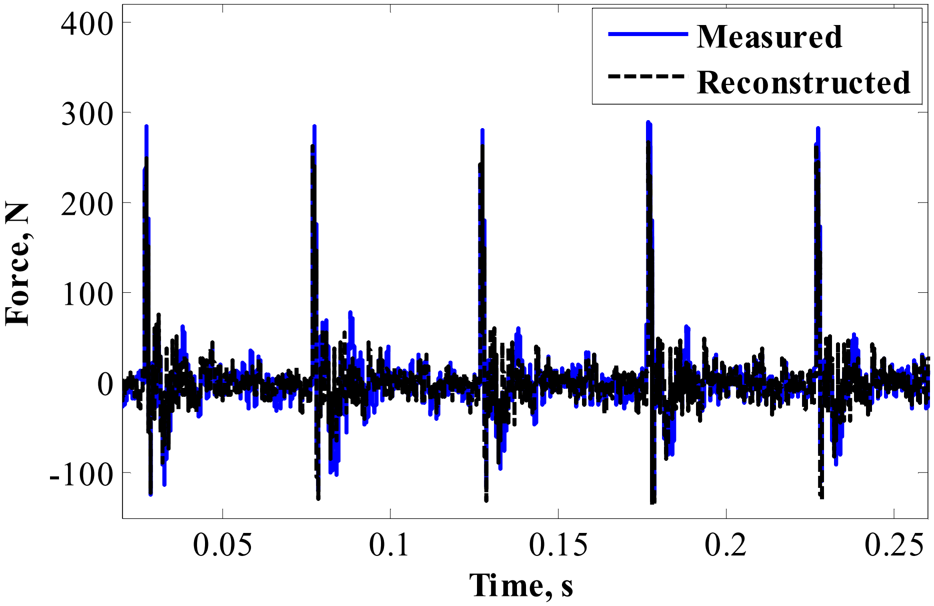

Figure 4.12: Measured and reconstructed thrust for 20 Hz operation.

In order to evaluate the effectiveness of the transfer in accounting for any pulse-to-pulse interaction, a separate experiment was conducted. In this case, a different load cell (PCB 301B01) was used which required only 440 N of preload which was lower as compared to the regular experiments. This lower preload allowed the engine to oscillate more such that the oscillations would remain in the system for a longer duration. For this test case, using the pressure history as an input and the established transfer function, the output was reconstructed and the result is shown in Fig. 4.13. The figure shows that the reconstructed signal exhibited lower oscillations as compared to the measured one indicating that the established transfer function eliminated oscillations due to structural response. This is a favorable result signifying that the developed approach is able to account for any potential pulse-to-pulse interaction in a higher-frequency operation.

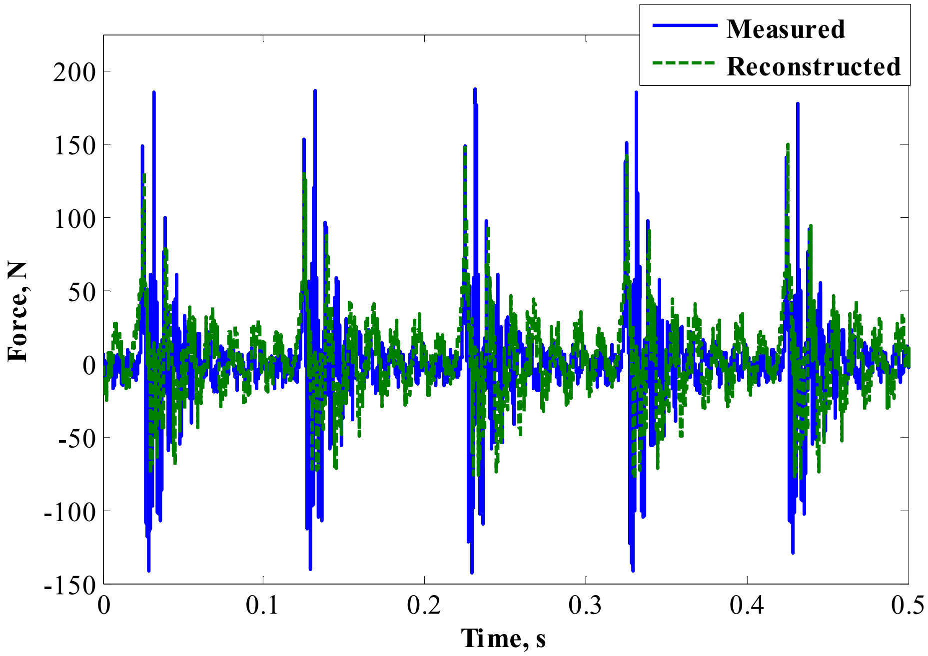

Figure 4.13: Measured and reconstructed thrust for lower preload.

It is important to note that the thrust was reconstructed using the pressure histories. As long as two consecutive detonation waves do not overlap with each other forming a continuous detonation wave, the result of the deconvolution via equation (2.7) was able to account for any pulse-to-pulse interaction caused by structural vibration. In this work, the detonation tube length is 0.66 m and the velocity of the detonation wave calculated via the time-of-flight method was $2.72 \pm 0.16\,\mathrm{km/s}$. Hence it took a detonation wave approximately 0.24 ms to exit the detonation tube and approximately another 1.4 ms for relaxation to ambient atmospheric pressure. For a 50 Hz operation, the cycle duration was 20 ms. This meant that detonation waves occurred every 20 ms which was a longer duration compared to the time needed for the detonation wave to travel through the entire tube. One can conclude that it would be unlikely for two consecutive detonation waves to overlap. Therefore, the thrust reconstructed using this procedure was able to account for the interference of thrust with structural response.

Various parameters can be used to characterize a PDE and its performance. Two of these important parameters are the filling fraction (ff) and equivalence ratio (ϕ). The filling fraction refers to the volume of the tube that is filled by the detonable mixture during the filling phase in a PDE cycle. As mentioned earlier, over filling the PDE does not help in generating more thrust as this excess fuel is burned outside the engine. On the other hand, investigations have shown that partial filling is beneficial and promotes superior performance of the PDE. Sato et al. [68], Schauer et al. [69], Cooper et al. [70], Li et al. [71], etc. have provided extensive results on the effect of partial filling on the performance of the PDE. In the present research work, the effect of filling fraction on PDE performance was not examined in detailed. However, an attempt was made to implement the developed experimental approach to recover actual thrust generated by the PDE operating with different filling fractions. Three different filling fractions of 0.58 ± 0.03, 0.88 ± 0.05 and 1.15 ± 0.06 were achieved for 1, 10 and 20 Hz operation. The specific impulse of the PDE at different values of filling fractions were compared and further discussed. Similarly, the equivalence ratio was changed to run the PDE in fuel lean and rich states. Equivalence ratios of 0.79 ± 0.06, 1.00 ± 0.05 and 1.45 ± 0.07 were achieved by varying the injection pressure and valve duty cycle. For each case, the actual thrust was recovered and later used to calculate the specific impulse. For operation of the PDE with different filling fractions and equivalence ratios, following the general approach, first a system transfer function was established and this established transfer function was used to reconstruct the thrust. Figures 4.14–4.17 show the results of thrust reconstruction for different filling fractions and equivalence ratios. For all cases, a proper reconstruction of the thrust was observed.

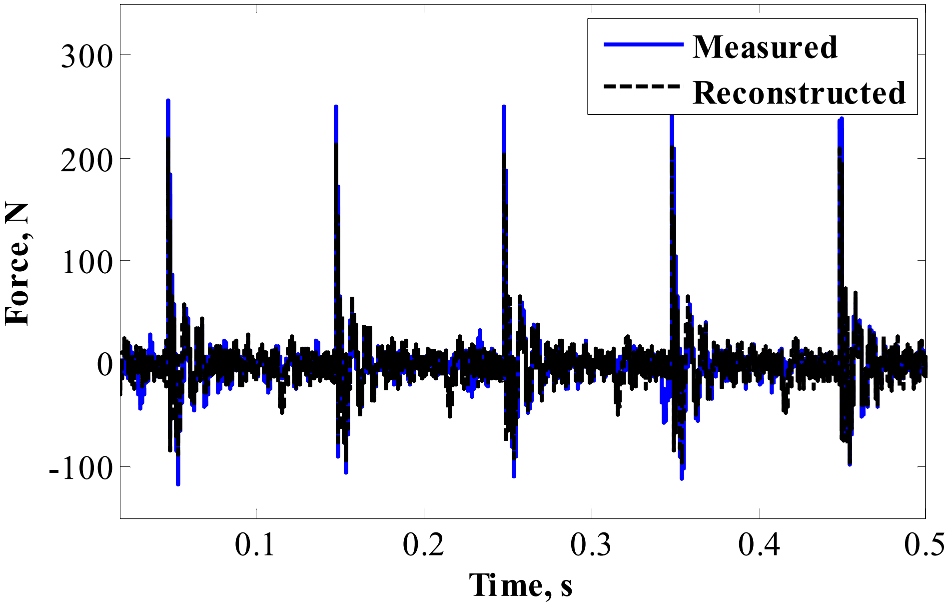

Figure 4.14: Thrust reconstruction for operation of PDE at 10 Hz with ff = 0.58.

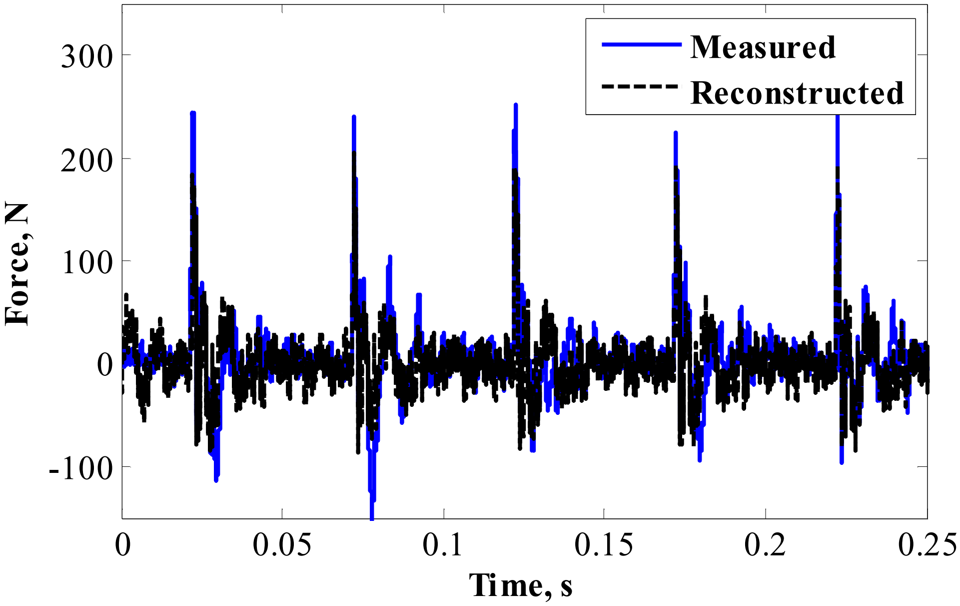

Figure 4.15: Thrust reconstruction for operation of PDE at 20 Hz with ff = 0.88.

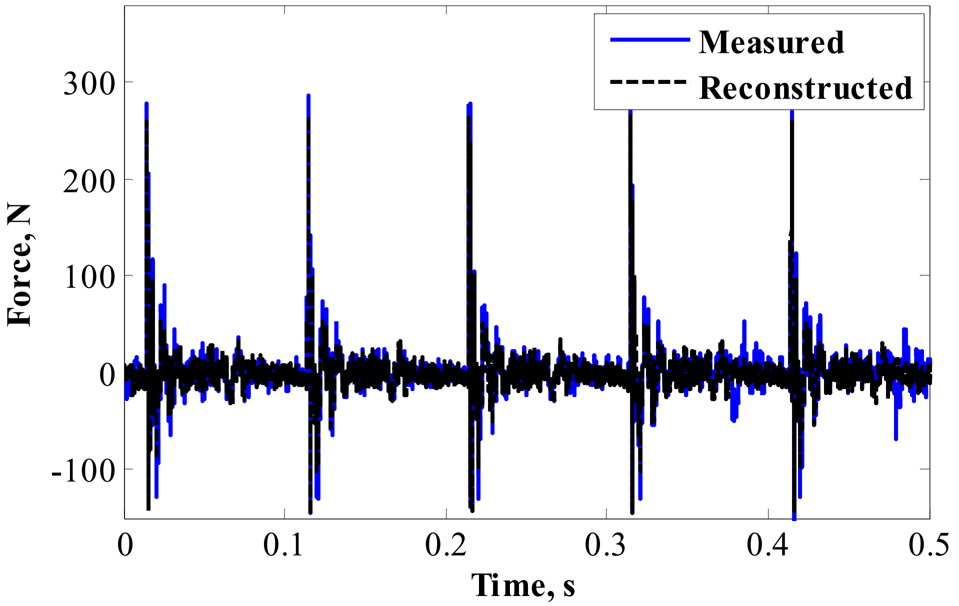

Figure 4.16: Thrust reconstruction for operation of PDE at 10 Hz with $\phi = 1$.

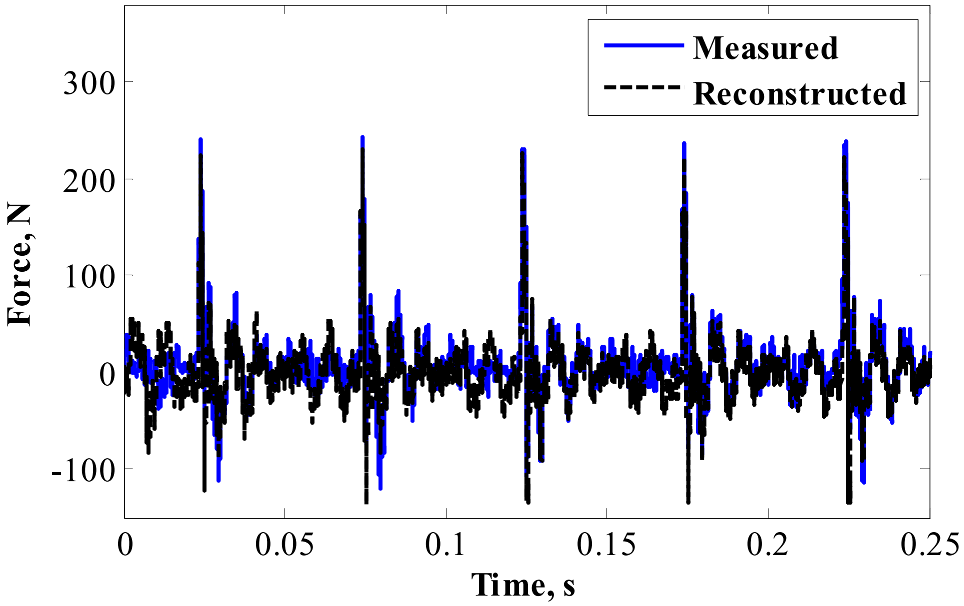

Figure 4.17: Thrust reconstruction for operation of PDE at 20 Hz with $\phi = 0.79$.

4.1.2 Mass Flow Rate Calculations

The calculation of specific impulse required the determination of the mass of gases injected into the PDE as shown in equations (2.21) and (2.23). The calculations were carried out using the procedure described in Section 3.2.3. Two different parameters were varied: first, the filling fraction and secondly the equivalence ratio. In the first case, the equivalence ratio was kept constant at unity while the duty cycles and supply pressures were changed to vary the filling fraction of the detonation tube. Table 4.1 details the duty cycle of the valves and the supply pressure used to vary filling fraction while keeping the equivalence ratio constant at unity. The three filling fractions achieved were 0.58 ± 0.03, 0.88 ± 0.05 and 1.15 ± 0.06.

Table 4.1: Duty cycle and supply pressures used to vary the filling fraction.

Frequency (Hz)	Duty Cycle (ms)	Hydrogen (MPa)	Oxygen (MPa)	Filling fraction	Equivalence Ratio
1	20	0.26	0.62	0.58	1
10	20	0.26	0.62	0.58	1
20	20	0.26	0.26	0.58	1
1	30	0.26	0.62	0.88	1
10	30	0.26	0.62	0.88	1
20	30	0.26	0.26	0.88	1
1	40	0.26	0.62	1.15	1
10	40	0.26	0.62	1.15	1
20	30	0.35	0.82	1.15	1

Similarly, Table 4.2 shows details of the duty cycle and supply pressure used to vary the equivalence ratio. In this case, the filling fraction of the tube was kept constant at unity. Three different equivalence ratios were achieved with values of 0.79 ± 0.06, 1.00 ± 0.05 and 1.45 ± 0.07.

Table 4.2: Duty cycle and supply pressures used to vary equivalence ratio.

Frequency (Hz)	Duty Cycle (ms)	Hydrogen (MPa)	Oxygen (MPa)	Filling fraction	Equivalence Ratio
1	40	0.21	0.62	1	0.79
10	40	0.21	0.62	1	0.79
20	34	0.25	0.744	1	0.79
1	35	0.26	0.62	1	1
10	35	0.26	0.62	1	1
20	35	0.26	0.62	1	1
1	26	0.38	0.62	1	1.45
10	26	0.38	0.62	1	1.45
20	26	0.38	0.62	1	1.45

Figures 4.18 and 4.19 show values of mass of hydrogen and oxygen injected into the PDE respectively to achieve the corresponding filling fraction of the tube as shown in Table 4.1. Figures 4.18 and 4.19 also present the mass of hydrogen and oxygen required to fully fill the tube. The mass of hydrogen and oxygen needed to fully fill the tube was used to find specific impulse in ideal operating cases. Similarly, figures 4.20 and 4.21 show the mass of hydrogen and oxygen injected into the tube respectively to achieve the variation in equivalence ratio as shown in Table 4.2. The amount of mass injected per pulse was kept constant to maintain filling fraction of 1 for different operating frequencies by varying the duty cycle of the valves and supply pressures. It can be noted that the amount of mass injected into the PDE depended on the temperature of the gases. For the present experiments, the gases used were at 300 K.

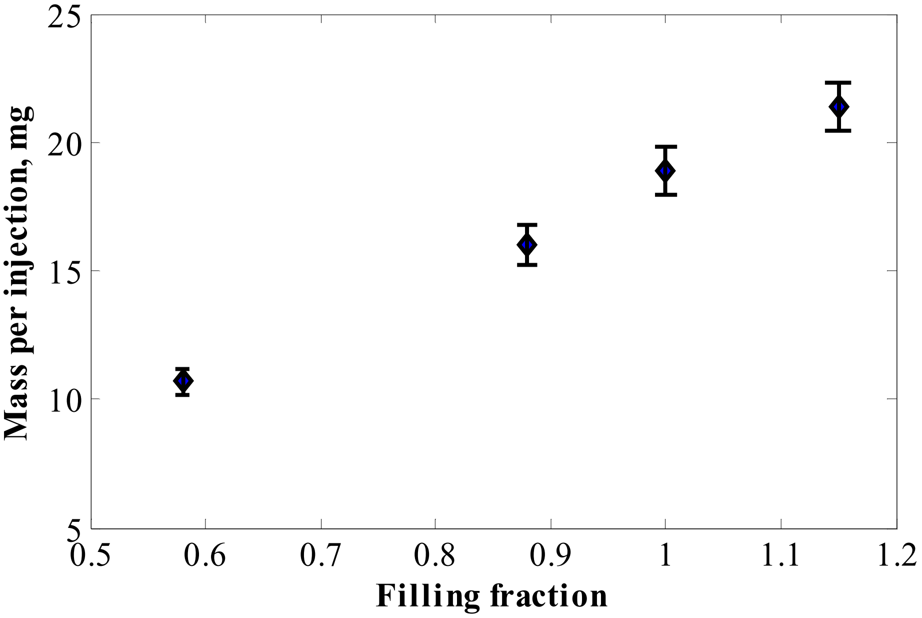

Figure 4.18: Mass of hydrogen gas injected per pulse for different filling fraction.

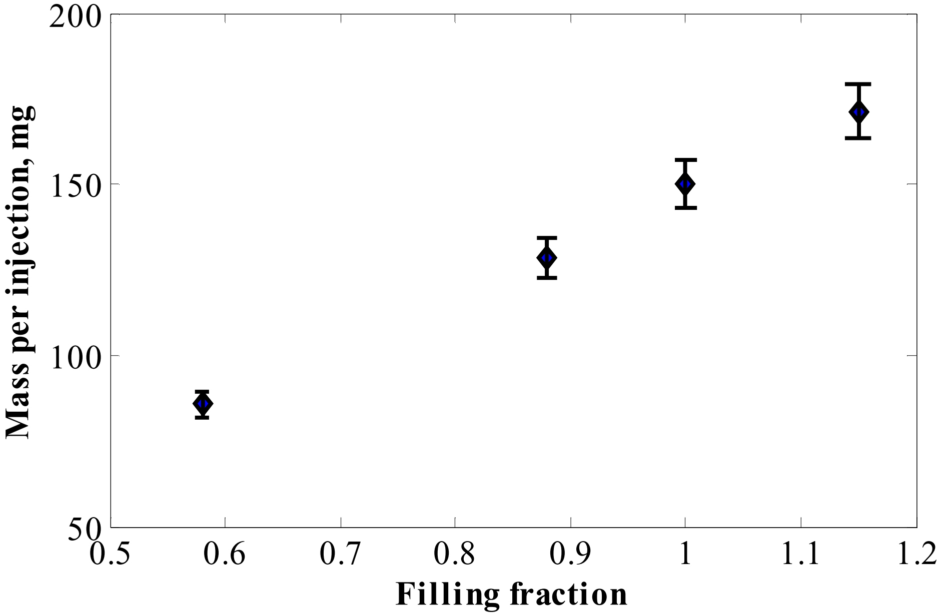

Figure 4.19: Mass of oxygen gas injected per pulse for different filling fraction.

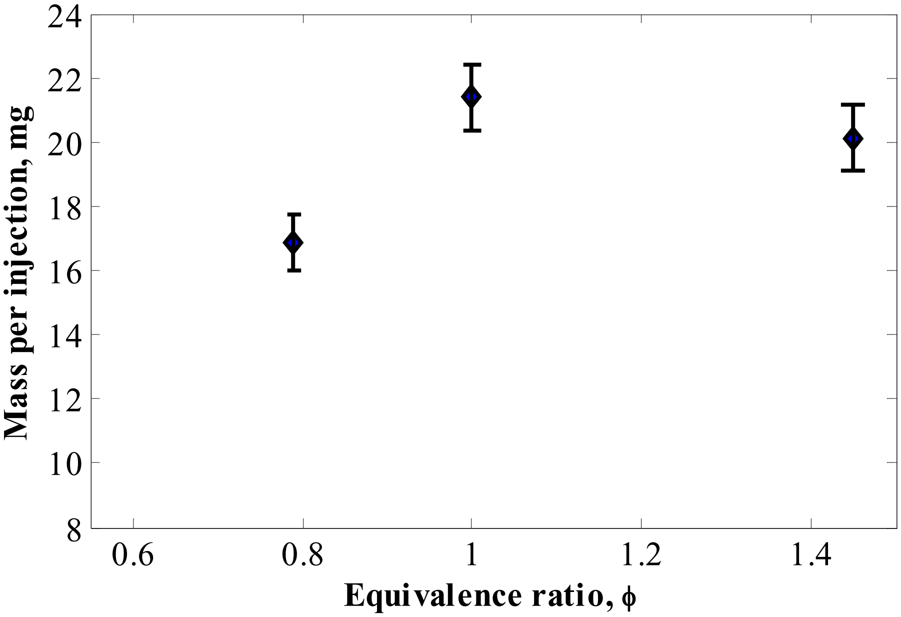

Figure 4.20: Mass of hydrogen injected per pulse for different equivalence ratio.

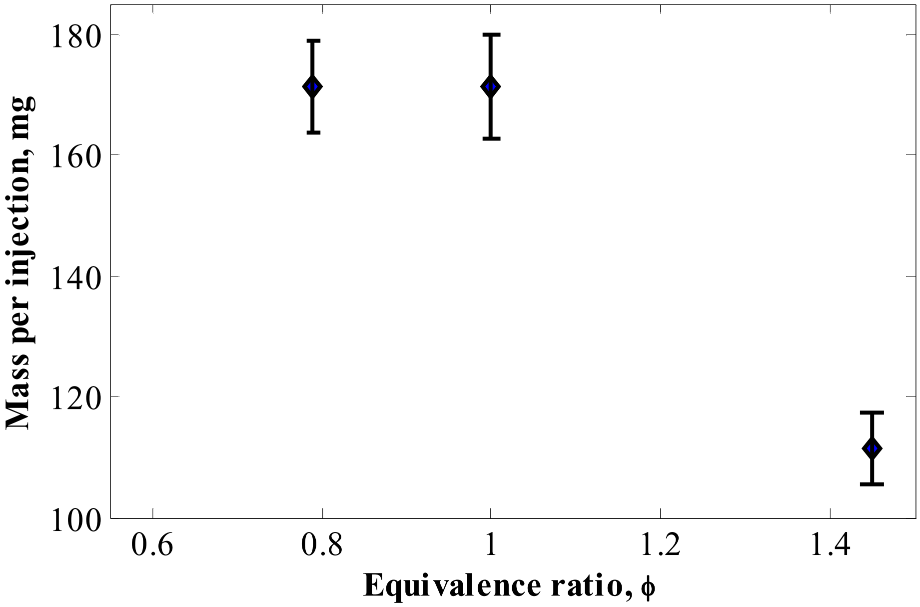

Figure 4.21: Mass of oxygen injected per pulse for different equivalence ratio.

4.1.3 Acceleration Compensation

The acceleration compensation procedure described in Chapter 2 is known as the *rig-based acceleration compensation*. The acceleration compensation procedure was applied using equation (2.20). This equation utilizes the deconvolved thrust to get the actual thrust generated by the PDE. The procedure to obtain deconvolved thrust has been described in detail in the earlier part of this chapter. From this deconvolved thrust, inertial forces were subtracted to get the actual thrust. Recall that the inertial force is the product of effective mass and the acceleration of the thrust measurement rig. The effective mass of the thrust measurement rig was first determined and the representative value of 16.8 ± 1.4 kg was taken for experimental calculations. The details of the calculations for effective mass have been presented in Chapter 3. The actual mass of thrust stand when weighed was 35.8 kg. The effective mass was almost equal to half of the actual mass. The results illustrated by Fujii [63] also indicated the value of effective mass was equal to the half of the actual mass for an underdamped system. This agreement in results somewhat acknowledges the feasibility of the method used to determine the effective mass. This agreement is also crucial as the concept of acceleration of compensation in unsteady thrust measurements for PDEs has not been reported in literature in the past. Additionally, equation (2.20) also introduces an acceleration term which is the acceleration of the thrust measurement rig measured while the PDE is in operation. The measured acceleration contains all the excited modes of vibration of the thrust measurement rig. However, the acceleration compensation procedure was centered towards accounting for the inertial loads due to vibration of the thrust measurement rig with lower modes. Hence, using the raw acceleration signal in equation (2.20) could cause the inertial force to be overestimated. Thus, the measured acceleration was filtered before it was used to predict the inertial forces. One possible way to truncate the acceleration signal is to pass it through a Butterworth filter. Such a filter, although effective, can significantly truncate the signals along with the actual information contained in them if the bandpass frequency is too narrow. Instead, a 0.7 ms moving average filter was used to truncate the acceleration signal. Figure 4.22 and 4.23 show sample plots for filtered acceleration measured during a typical PDE operation.

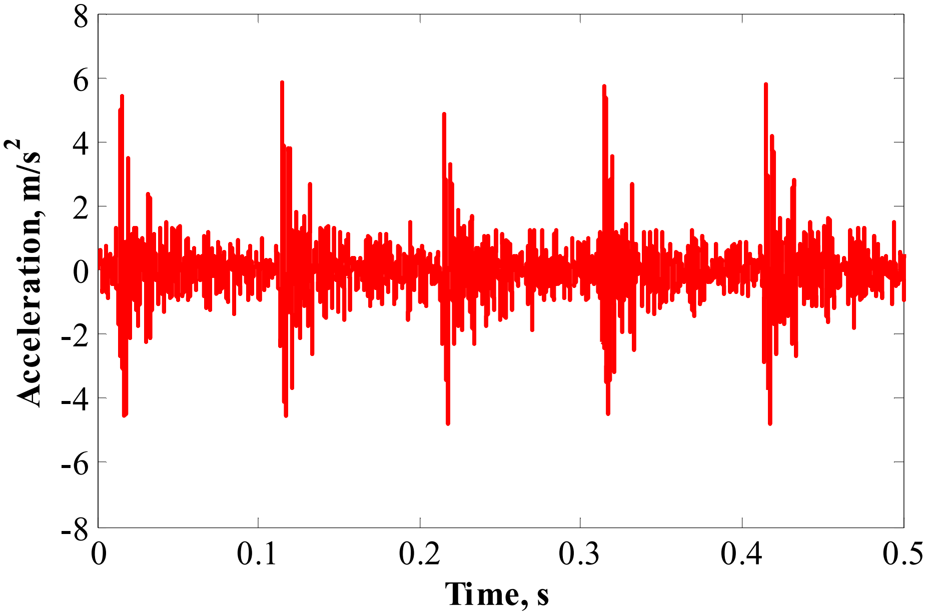

Figure 4.22: Filtered acceleration of the thrust measurement rig for PDE operating at 10 Hz.

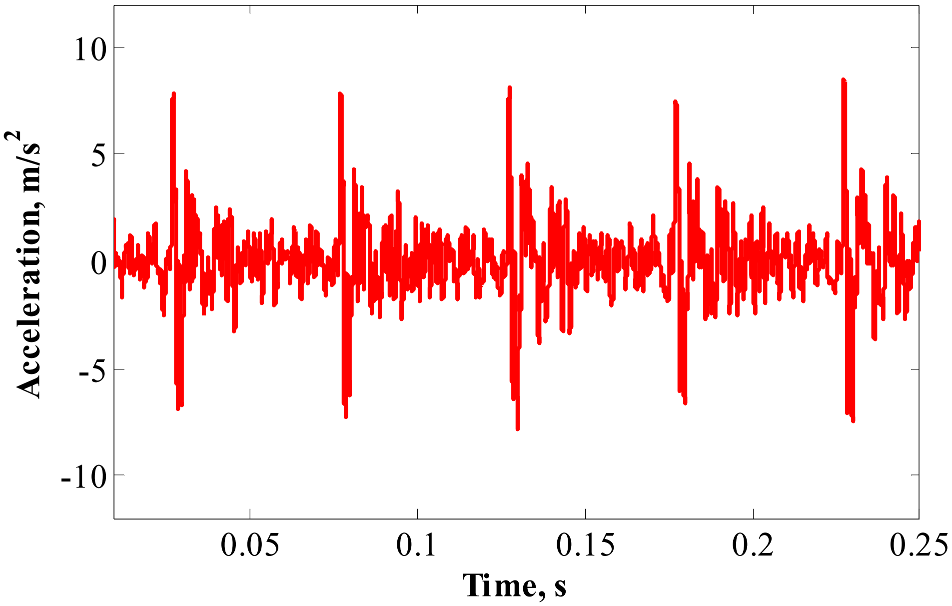

Figure 4.23: Filtered acceleration of the thrust measurement rig for PDE operating at 20 Hz.

A characteristic time defined in Chapter 2 is t_{exh} which signifies the time taken for the detonation tube to return to the initial ambient state after the occurrence of a detonation wave. This period is $0 \leq t \leq t_{exh}$, where the starting and ending times of “0” and t_{exh} are arbitrary and in general can be replaced by t_0 (itself an arbitrary initial time) and $(t_{exh} + t_0)$ respectively. This period includes the propagation of detonation wave in the tube, blow down of burned products and further relaxation by expansion waves that decreases the pressure to ambient conditions. In practice, thrust is generated by the PDE only during this period. This period is dependent on the geometry of the engine, the detonation properties of the mixture used and the initial conditions of the tube at which the fuel/oxidizer is injected. For the PDE used in this research operating with stoichiometric oxyhydrogen mixture at 1 atm, the period was found to be equal to 1.64 ms. Figure 2.10 depicts the pressure history at the thrust wall during this period. This led to the conclusion that when the number of pulses occurring per second was small, the effective thrust generating phase in a PDE was short. Therefore the total impulse was low for PDEs operating at low frequencies. On the other hand, a higher operating frequency corresponded to a higher value of impulse per second which led to high overall total impulse.

One possible way of expressing equation (2.20) is to take the average of the entire deconvolved thrust history and the average of the entire acceleration history measured during a test run and use the mean values to calculate the total impulse. However, as discussed earlier, taking the average of an entire record for a PDE operating with low frequency yields a very low value for thrust. In addition, it will be difficult to comprehend the time dependence of the thrust and acceleration signals when a long record is considered for a PDE with a relatively low frequency. Therefore, the analysis is carried out per pulse with an integration window equal to the time period during which thrust is generated by a PDE. As described above, this period is represented by $0 \leq t \leq t_{exh}$. Moreover, the impulse calculated via equation (2.20) portrays the acceleration compensated impulse generated by the PDE per pulse. This is also an indication that the experimental approach developed in this project is based on in-depth analysis of the time dependent thrust signals. It is important to note that the pulses occur in a repeated manner at a constant time interval based on the operating frequency of the PDE. Hence, the thrust generation period can be easily monitored and the impulse can be calculated for each pulse. This led to the calculation of total impulse for a cycle which was the summation of impulses for all the pulses in that cycle. It is concluded that for a successful use of PDE as a propulsion device, the frequency of operation should be in the range of the inverse of the period of the thrust generation phase. For the PDE used in this research project, the frequency analogous to this period was 608 Hz. In practice due to other considerations, such high frequency most likely could not be achieved.

Integration of the deconvolved thrust and inertial force with respect to the time interval of the thrust generation phase allowed the calculation of the impulse per pulse via equation (2.20). Figure 4.24 shows the impulse per pulse for different filling fractions of the PDE operating at different frequencies. The impulse per pulse presented in Figs 4.24–4.27 represented the impulse per pulse per unit area of cross section of the closed end or thrust wall. Figures 4.25–4.27 show the impulse per pulse per unit area at frequencies of 1, 10 and 20 Hz. It was observed that the impulse per pulse per unit area had the highest value for the filling fraction of 1.15. Although, the impulse per pulse was higher the overall performance of PDE was compromised as a higher volume of fuel was spent which decreased the specific impulse of the PDE. Figures 4.24–4.27 present both measured and compensated impulse per pulse per unit area. And, it can be observed that the compensated values were 8.54 ± 2.1 % lower that the measured values.

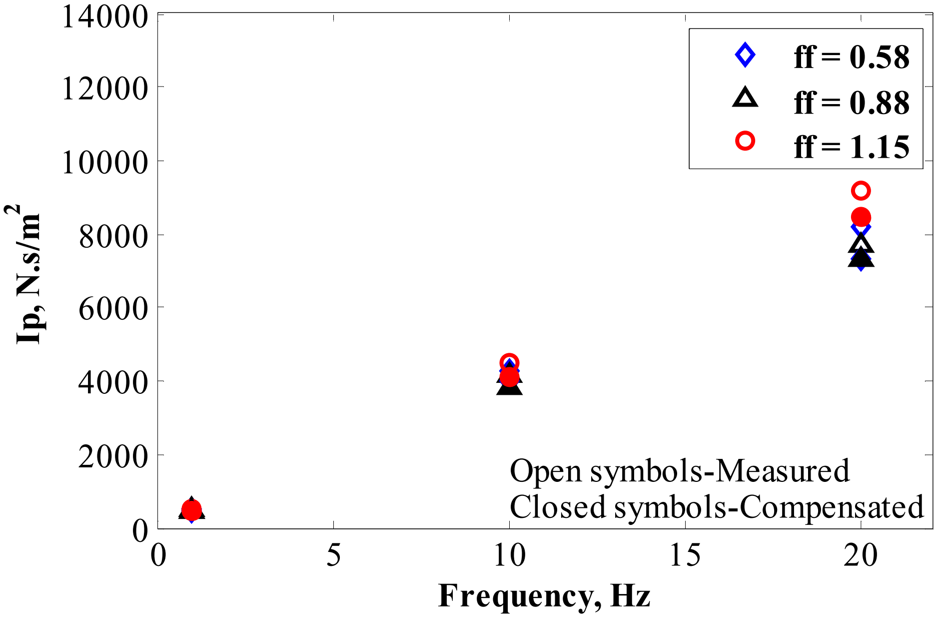

Figure 4.24: Impulse per pulse for different filling fractions and operating frequencies.

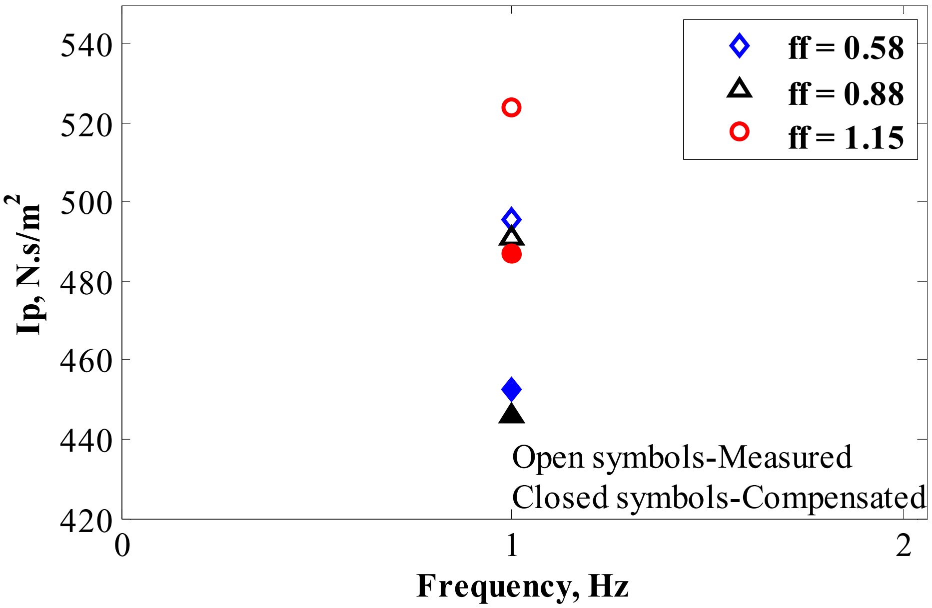

Figure 4.25: Impulse per pulse at 1 Hz for different filling fractions of the PDE.

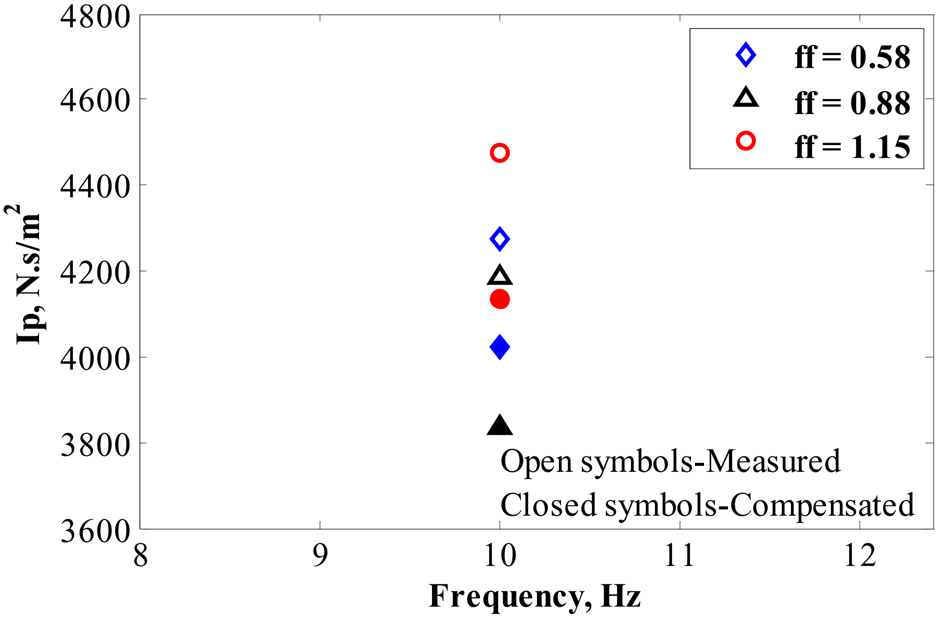

Figure 4.26: Impulse per pulse at 10 Hz for different filling fractions of the PDE.

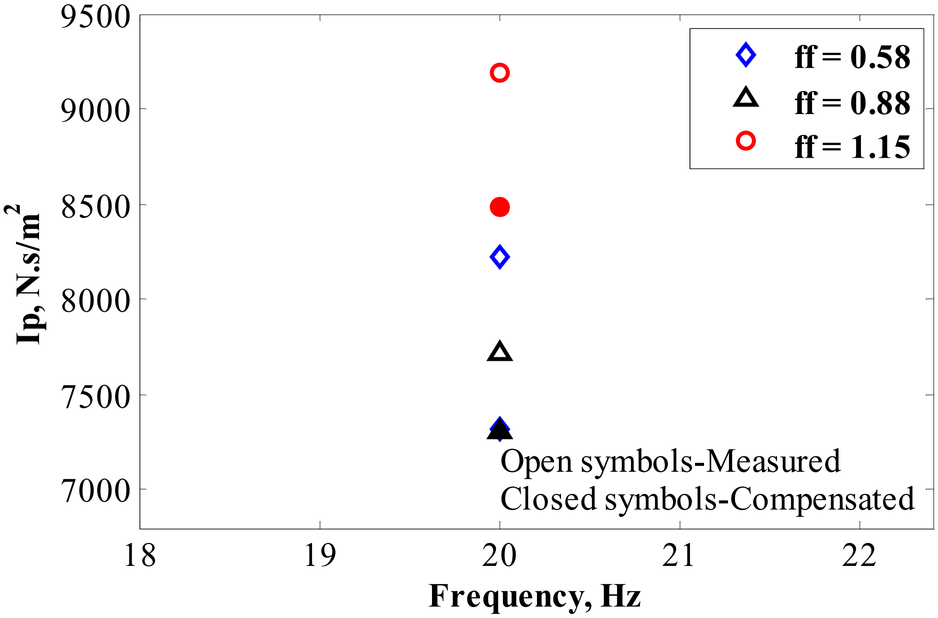

Figure 4.27: Impulse per pulse at 20 Hz for different filling fractions of the PDE.

The calculation of impulse per pulse per unit area facilitated the evaluation of the specific impulse and the fuel-based specific impulse of the PDE for different values of filling fractions. Figure 4.28 shows the specific impulse of the PDE for different values of filling fraction and it was found that the specific impulse decreased with increase in filling fraction. In other words, the PDE was able to generate more specific impulse when the tube was partially filled. A possible reason for this situation is the pumping of the purge air or previous cycle products by the detonation wave. This in turn increased the velocity of mass exhausted at the exit and hence increased the specific impulse. Another possible reason is addition of the reaction force offered by the cold buffer gas when pushed by the detonation wave which contributes to higher thrust and thus higher specific impulse in partially filled case.

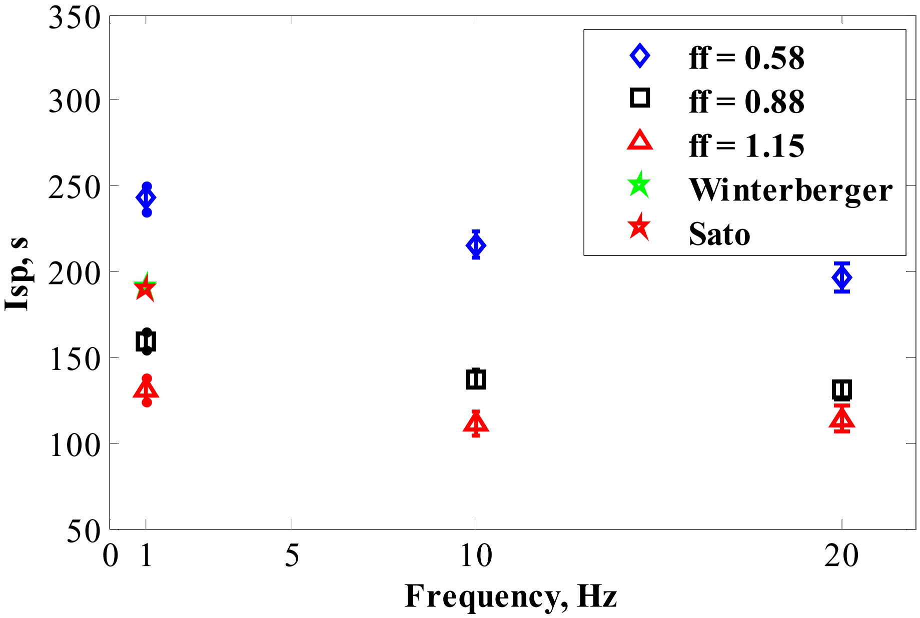

Figure 4.28: Variation of specific impulse with filling fraction.

Figure 4.28 also shows the specific impulse measured for a fully-filled, single-shot detonation tube utilizing stoichiometric oxyhydrogen mixture by Winterbeger et al. [43] and the numerical value by Sato et al. [68]. The specific impulses reported in both cases were higher than the current results for the fully-filled case. Improper mixing of the fuel and oxidizer due to cyclic operation of the PDE and the use of a Shchelkin spiral might have imposed some practical problems resulting in lower specific impulse. Figure 4.29 shows the fuel-based specific impulse for different filling fraction of the PDE. Figure 4.29 indicates that the fuel-based specific impulse of a partially filled PDE is superior compared to the fully filled one.

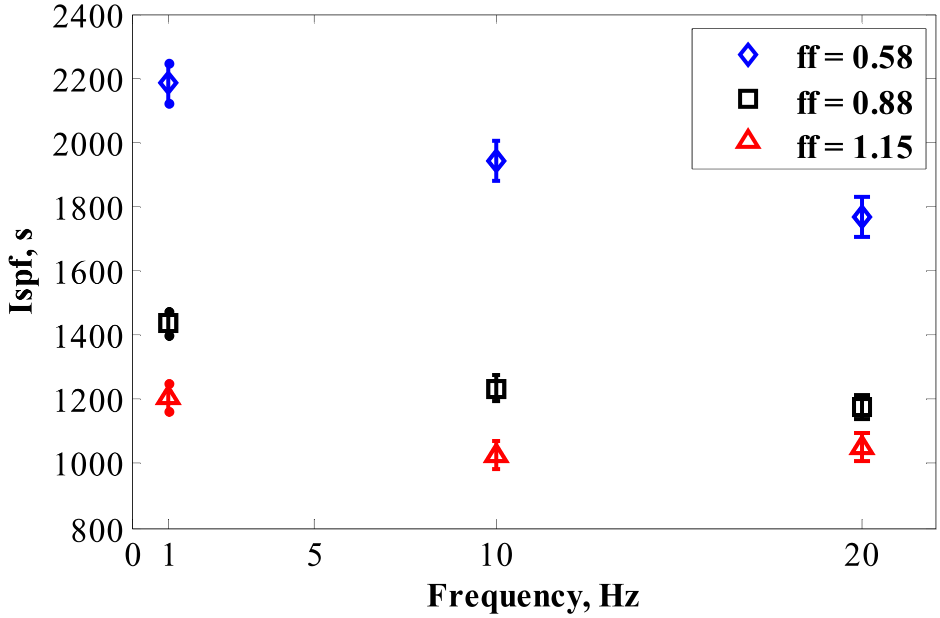

Figure 4.29: Fuel based specific impulse for different filling fractions.

In addition to the filling fraction, the equivalence ratio of the fuel/oxidizer ratio injected into the PDE was also varied and the impulse of the PDE was calculated. The equivalence ratios of 0.79 ± 0.06, 1.00 ± 0.05 and 1.45 ± 0.07 were achieved for operating frequencies of 1, 10, and 20 Hz. Figure 4.30 shows the values of measured and compensated impulse per pulse per unit area for different operating frequencies and equivalence ratios. Figures 4.31–4.33 show the impulse per pulse per unit area at 1, 10 and 20 Hz operation. However, no detonations were observed for the operation of PDE at 20 Hz with an equivalence ratio of 1.45. The value of impulse per pulse per unit area was found to be highest for equivalence ratio of 1. Also, after implementation of the acceleration compensation procedure, the compensated impulse values were found to be $7.37 \pm 1.1\ \%$ lower than the uncompensated values.

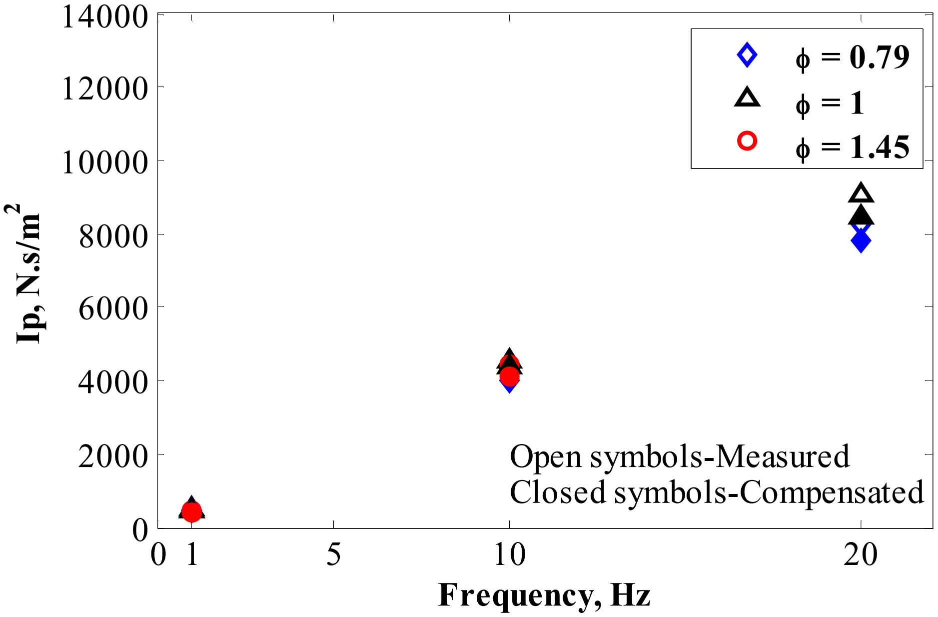

Figure 4.30: Impulse per pulse for different equivalence ratios and operating frequencies.

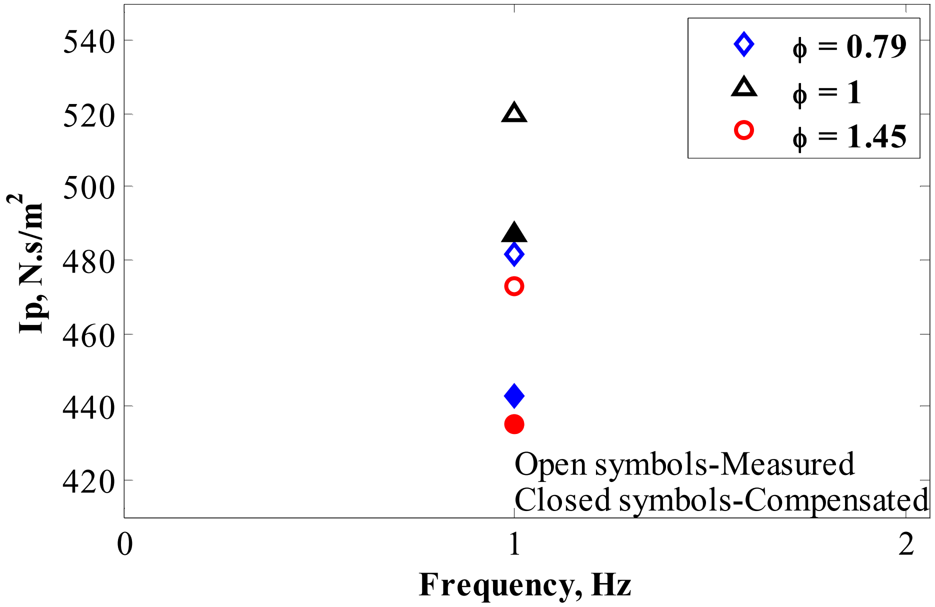

Figure 4.31: Impulse per pulse at 1 Hz for different equivalence ratios.

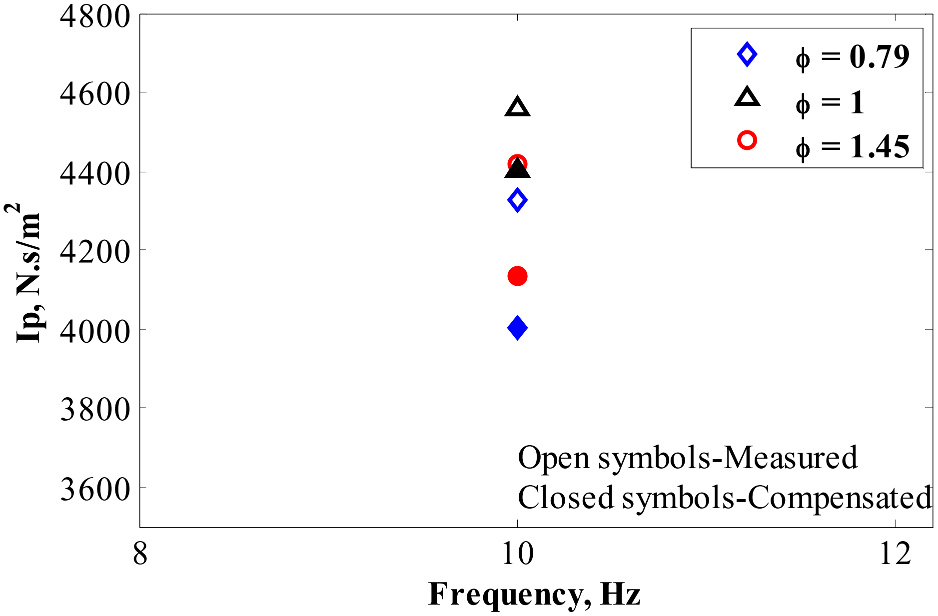

Figure 4.32: Impulse per pulse at 10 Hz for different equivalence ratios.

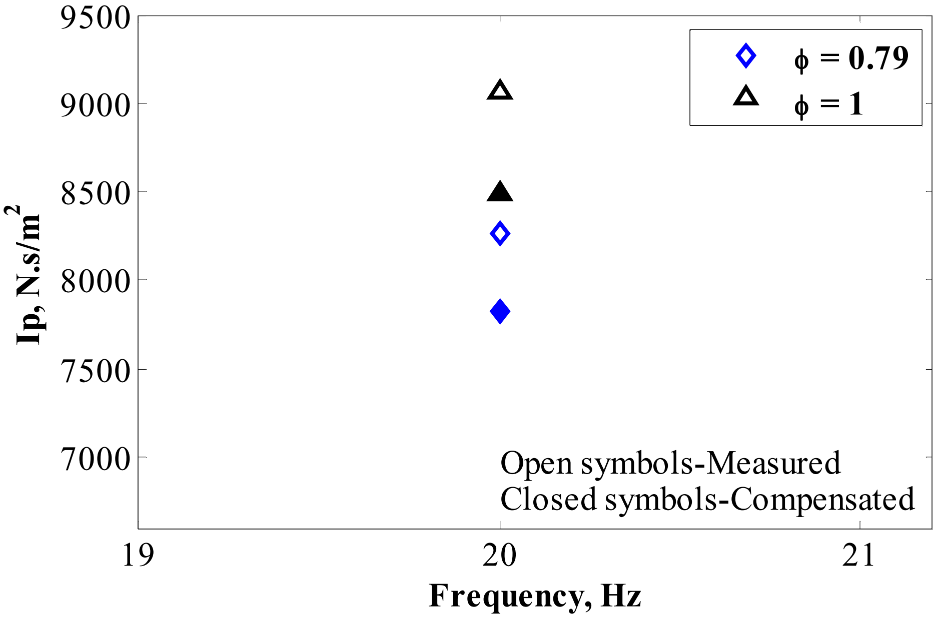

Figure 4.33: Impulse per pulse at 20 Hz for different equivalence ratios.

Figures 4.34 and 4.35 present the specific impulse and fuel-based specific impulse of the PDE when operated with different equivalence ratios. For all cases, the specific impulse was observed to be higher for the equivalence ratio of unity. As shown in Fig. 4.34, the calculated values of specific impulse re lower than the published information in the literature. The losses in mixing of fuel and oxidizer brought about by the operation of the engine in the pulsed mode unlike a single shot experiment and the added drag due to the Shchelkin spiral might have affected the obtained results. Figure 4.35 shows that the operation of PDE with a high equivalence ratio significantly decreases the fuel-based specific impulse. However, the fuel-based specific impulse for equivalence ratios of 0.79 and 1.0 were close to each other. The specific impulse for the 20 Hz operation with equivalence ratio of 1.45 was not calculated as no detonations were observed.

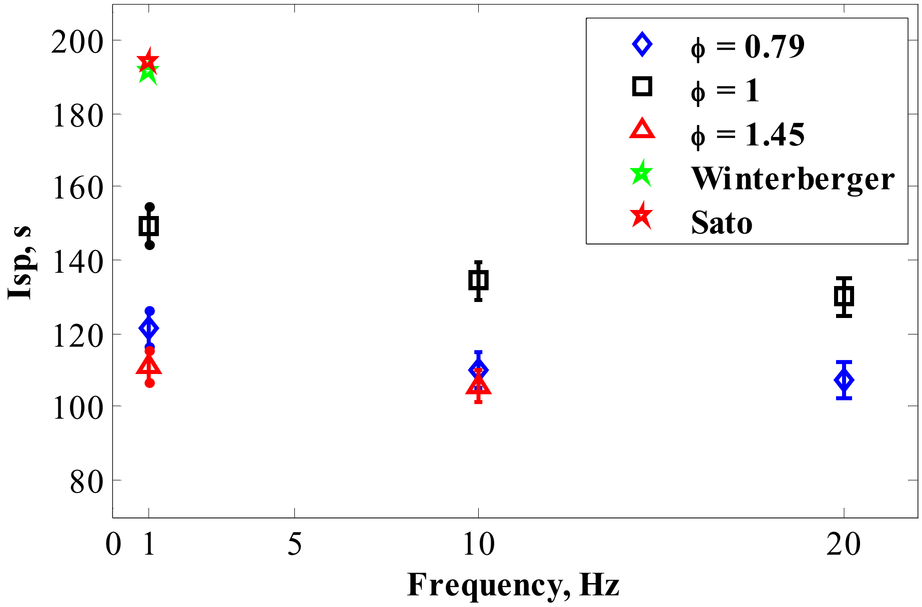

Figure 4.34: Variation of specific impulse with equivalence ratio.

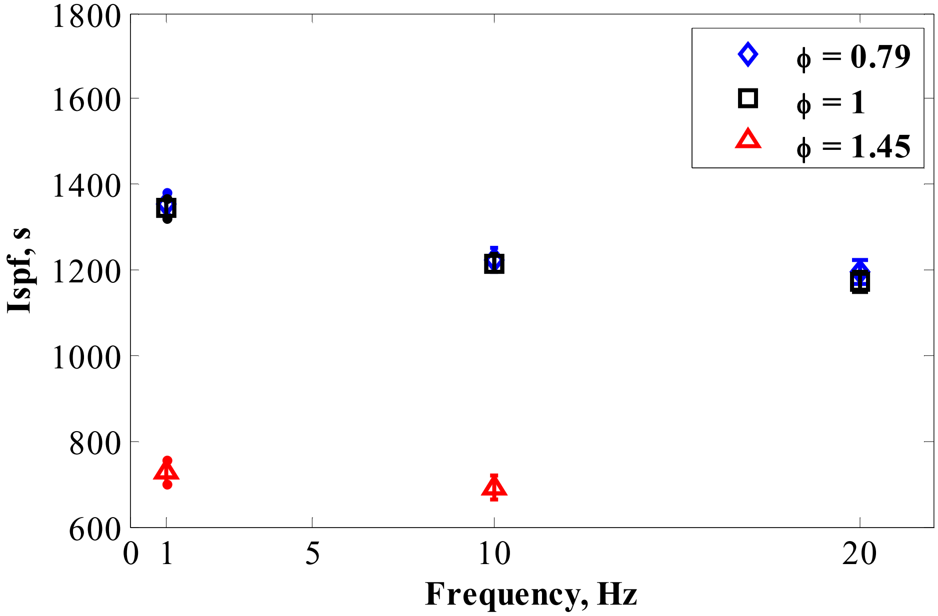

Figure 4.35: Fuel based specific impulse for different equivalence ratios.

4.2 Semi-empirical Analysis Results

The effects of the rate of change of momentum in the control volume which included the contribution from unsteady changes in the momentum, and the contribution from the momentum flux of the burnt products that exited the PDE, and the forces arising due to the pressure gain were considered in the semi-empirical analysis to estimate the thrust generated by the PDE. The contribution of unsteady momentum changes was calculated using the methodology described in Chapter 2, the momentum flux of the burnt products was known since the mass flow rates and exhaust velocity were known and finally the pressure history measured at the exit end of the PDE was integrated with respect to time and used in equation (2.26) to calculate the impulse per pulse per unit area of the PDE. Figure 4.36 shows the sample duration of pressure gain at the exit of the PDE due to the exit of the detonation wave.

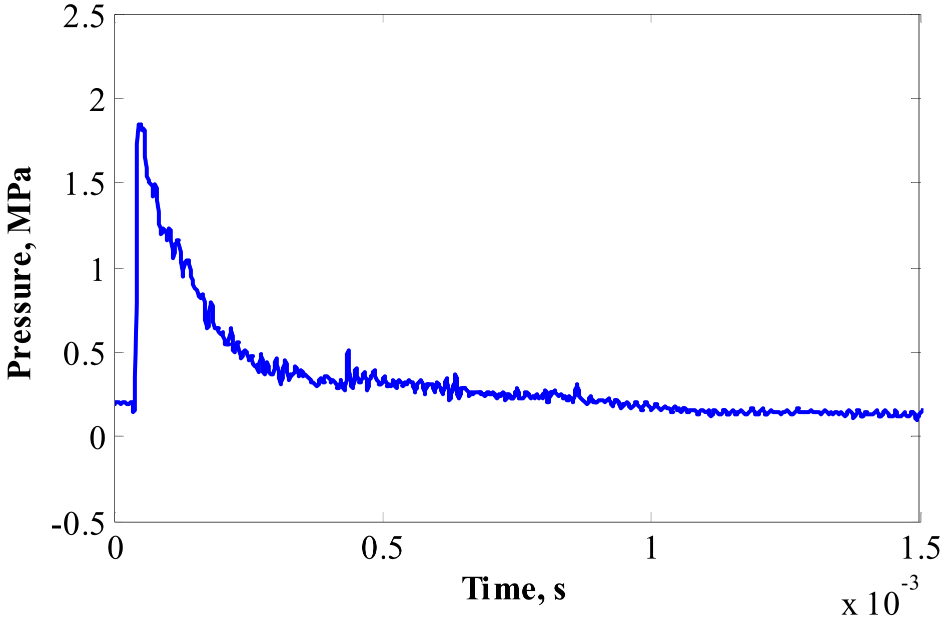

Figure 4.36: Sample pressure history at the exit of the PDE.

Following the procedure described in Chapter 2, first, the impulse per pulse per unit area of cross section was determined and the results are presented in Fig. 4.37 for different values of filling fraction. Figures 4.38–4.40 illustrate the specific impulse calculated via the semi-empirical method for filling fractions of 0.58, 0.88 and 1.15 respectively. These figures also present the comparison of the calculated specific impulse obtained from analytical models developed by previous researchers. The first comparison is made against the analytical model developed by Endo et al. [42]. A detailed discussion of this analytical model was presented in Chapter 2. The second analytical model used for comparison was developed by Kailasanath [1], in which the impulse per pulse per unit area is given by

$$I_p = 4.85(p_3 - p_{amb})t_{CJ} \tag{4.1}$$

where I_p is the impulse per pulse per unit area, p_3 is the plateau pressure, p_{amb} is the ambient atmospheric pressure and t_{CJ} is the time for which detonation wave resides inside the tube. The third analytical model used for comparison was developed by Winterbeger et al. [43] wherein the impulse per pulse per unit area is given by

$$I_p = 4.3(p_3 - p_{amb})\frac{AL}{D_{CJ}} \tag{4.2}$$

where I_p is the impulse per pulse, p_3 is the plateau pressure, p_{amb} is the ambient atmospheric pressure and D_{CJ} is the detonation wave velocity, A is the area of cross section of the thrust wall and L is the length of the detonation tube. Using these analytical models, the impulse was calculated and using the known mass of gases needed to be injected into the tube for corresponding filling fraction, the specific impulse was calculated. The analytically predicted values were then compared against the values obtained by using the semi-empirical method developed in this project and presented in Figs. 4.38–4.40. Finally, Fig. 4.41 shows the fuel-based specific impulse calculated using the same semi-empirical method.

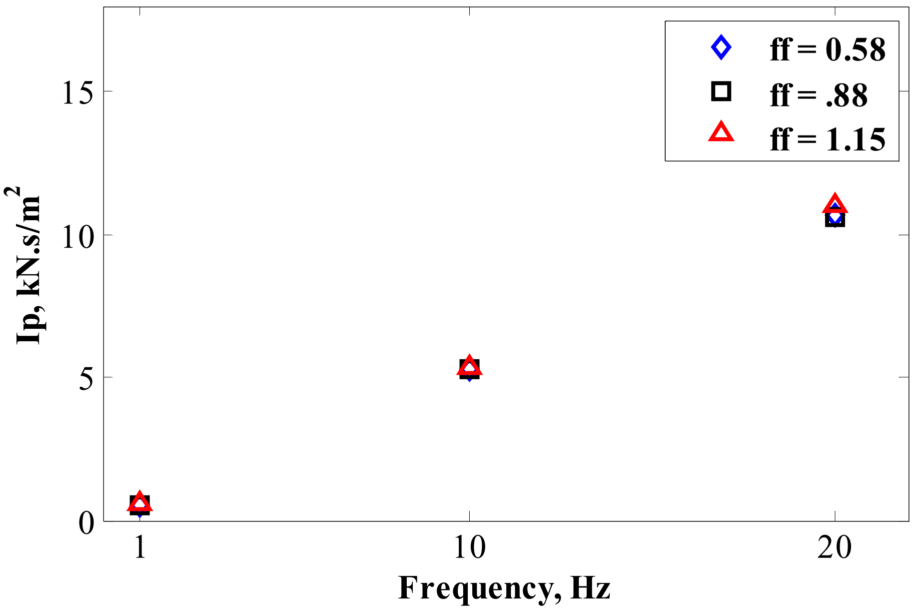

Figure 4.37: Semi-empirically calculated impulse per pulse for different filling fractions of the tube.

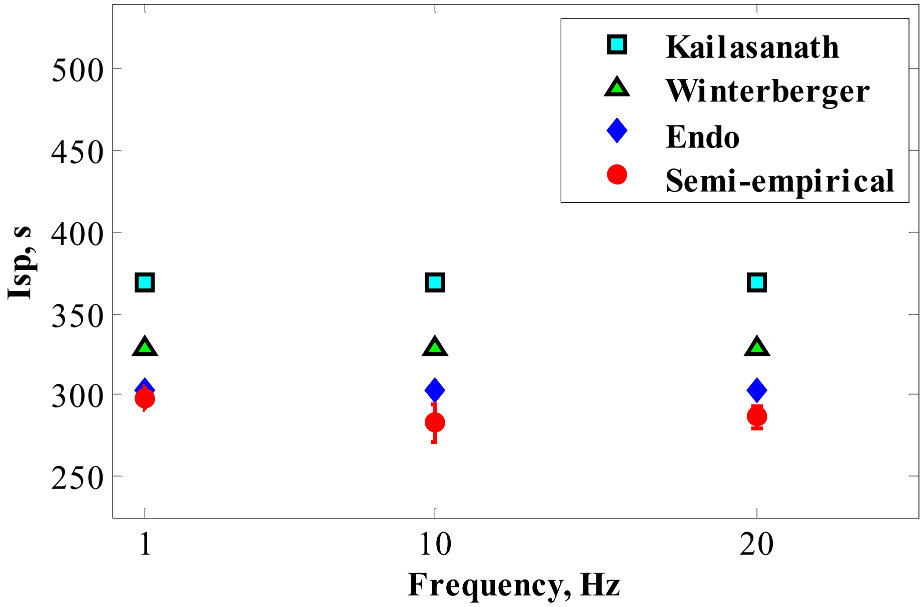

Figure 4.38: Semi-empirically calculated specific impulse of the PDE for $ff = 0.58$.

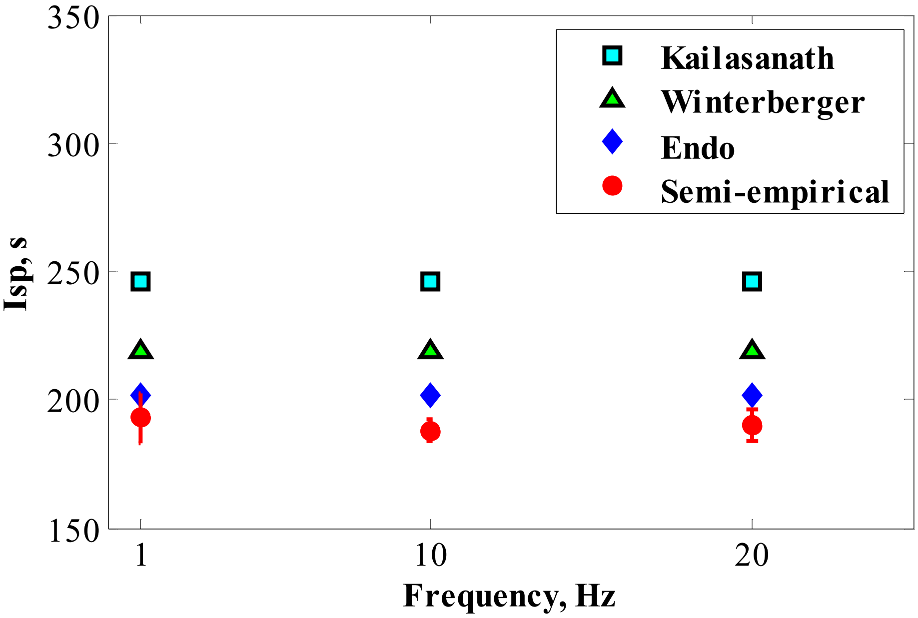

Figure 4.39: Semi-empirically calculated specific impulse of the PDE for ff = 0.88.

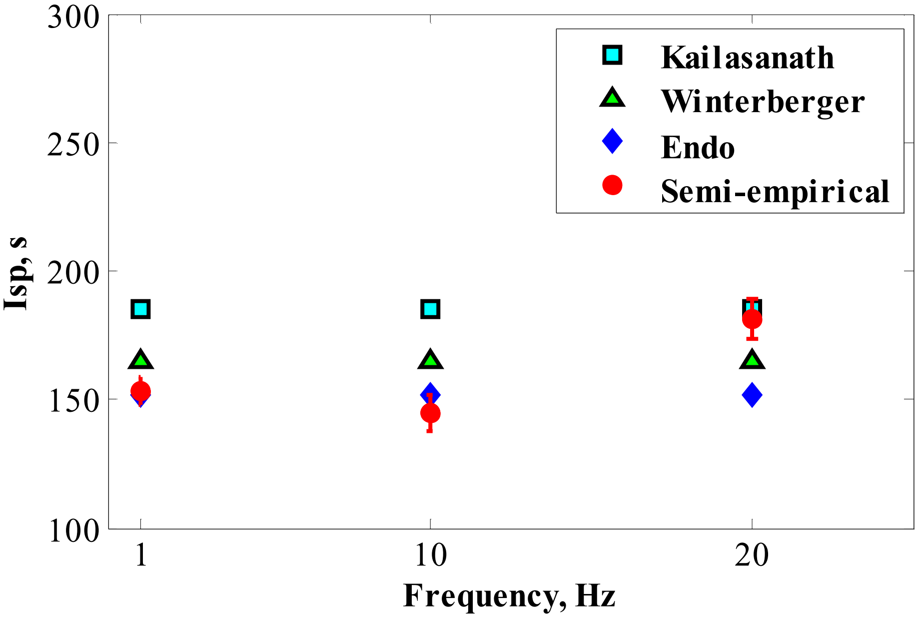

Figure 4.40: Semi-empirically calculated specific impulse of the PDE for ff = 1.15.

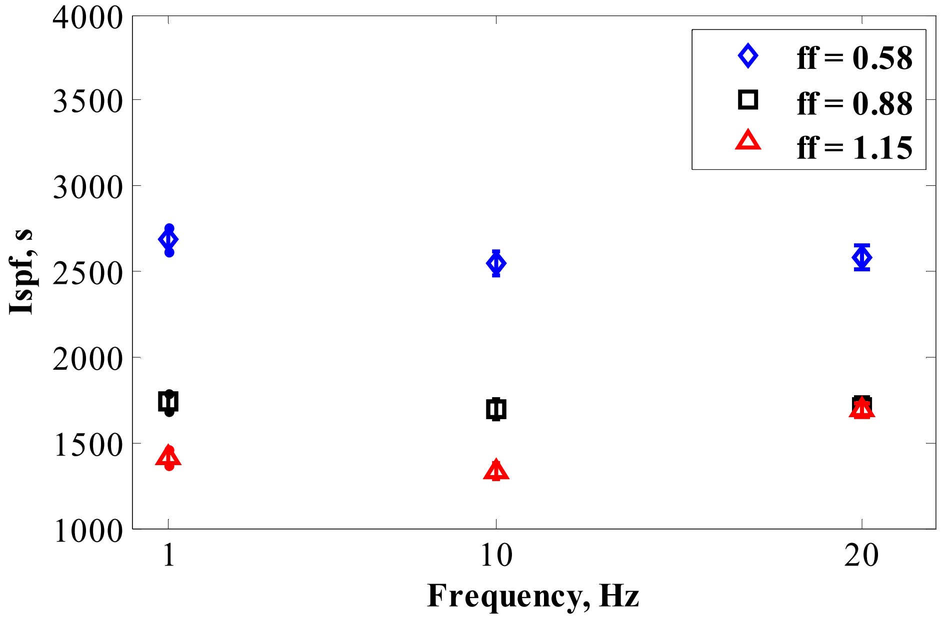

Figure 4.41: Semi-empirically calculated fuel based specific impulse for different filling fractions.

Figures 4.38–4.40 indicate that the specific impulse calculated for partially-filled cases are higher than fully or over-filled engines. Similarly, the fuel-based specific impulse for partially-filled cases is higher. Figures 4.38–4.40 also illustrate that the analytically estimated specific impulse using Endo's model were close to the semi-empirically calculated specific impulse. However, the specific impulses obtained using the analytical model by Kailasanath and Winterberger models were relatively higher. The semi-empirical method in this study utilized the actual velocity of the detonation wave and the experimentally determined values of mass flow rates. Hence, the losses incurred in practical operation scenarios were the major reason for the lower values of the semi-empirically calculated specific impulse.

The semi-empirical method was also used to calculate the specific impulse of the PDE for different values of equivalence ratios. Figure 4.42 shows the impulse per pulse per unit area for different equivalence ratios. Figures 4.43–4.45 shows the variation of specific impulse for different values of equivalence ratios. Finally, Fig. 4.46 illustrates the fuel based specific impulse for different equivalence ratios.

Figure 4.42 shows that the total impulse increases as the number of impulses per second increases. It is observed that the impulse per pulse per unit area for the operation of the PDE with equivalence ratio of unity is the highest. Similarly, Figs. 4.43–4.45 show that the specific impulse is highest for operation with equivalence ratio of unity. In each case, the semi-empirically determined specific impulse was compared against specific impulse calculated using various other analytical models. The specific impulse determined semi-empirically was slightly lower as compared to others.

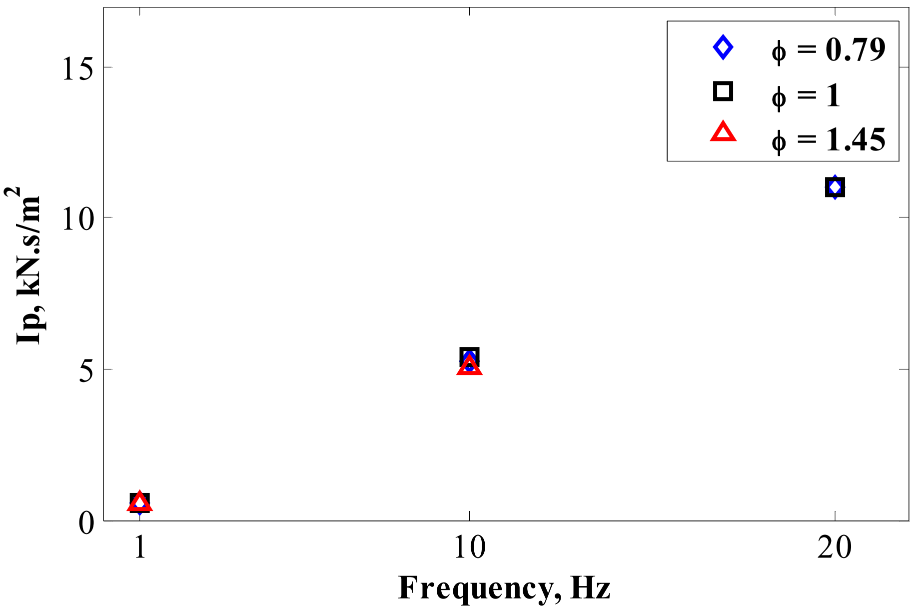

Figure 4.42: Semi-empirically calculated impulse per pulse per unit area for different equivalence ratios.

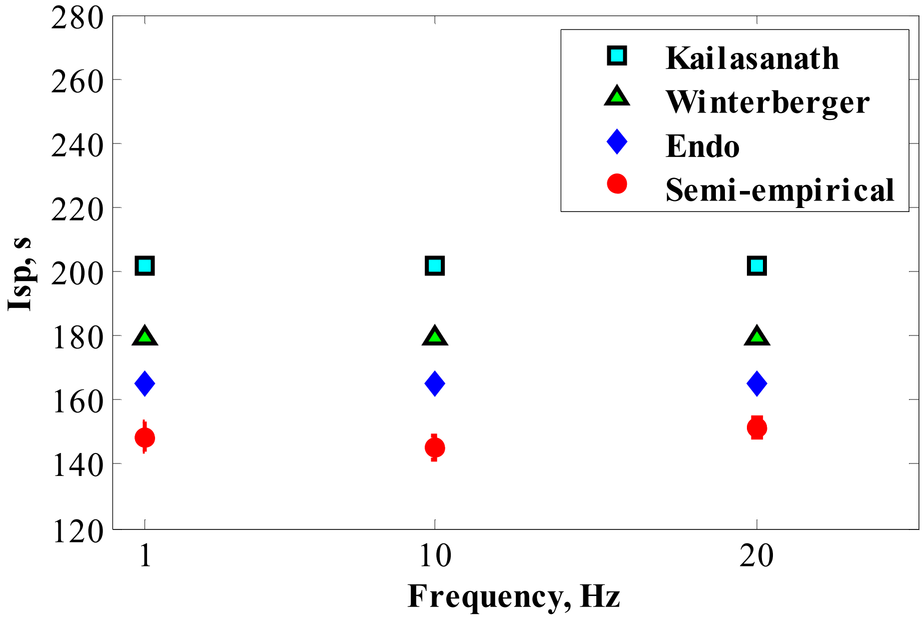

Figure 4.43: Semi-empirically calculated specific impulse of the PDE for $\phi = 0.79$.

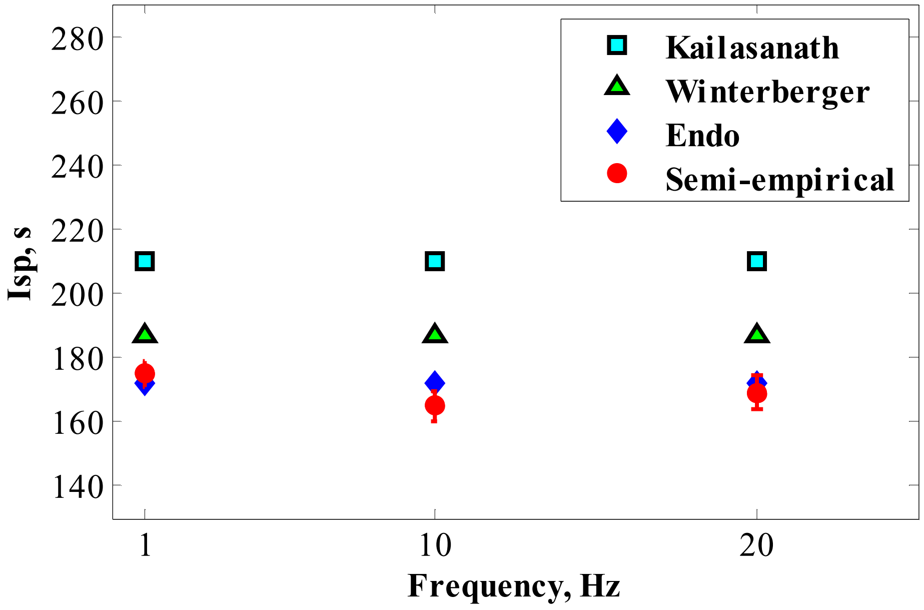

Figure 4.44: Semi-empirically calculated specific impulse of the PDE for $\phi = 1.0$.

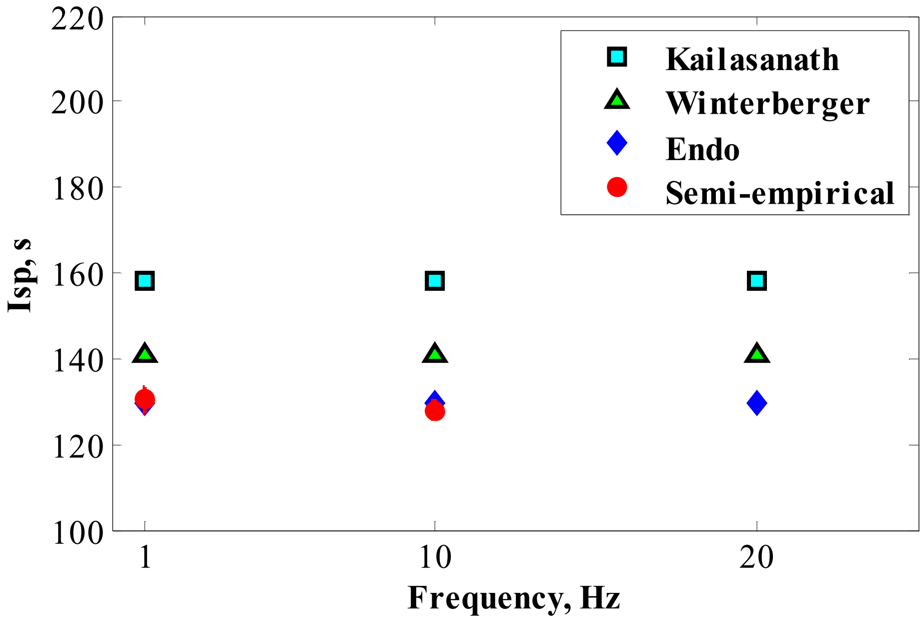

Figure 4.45: Semi-empirically calculated specific impulse of the PDE for ϕ = 1.45.

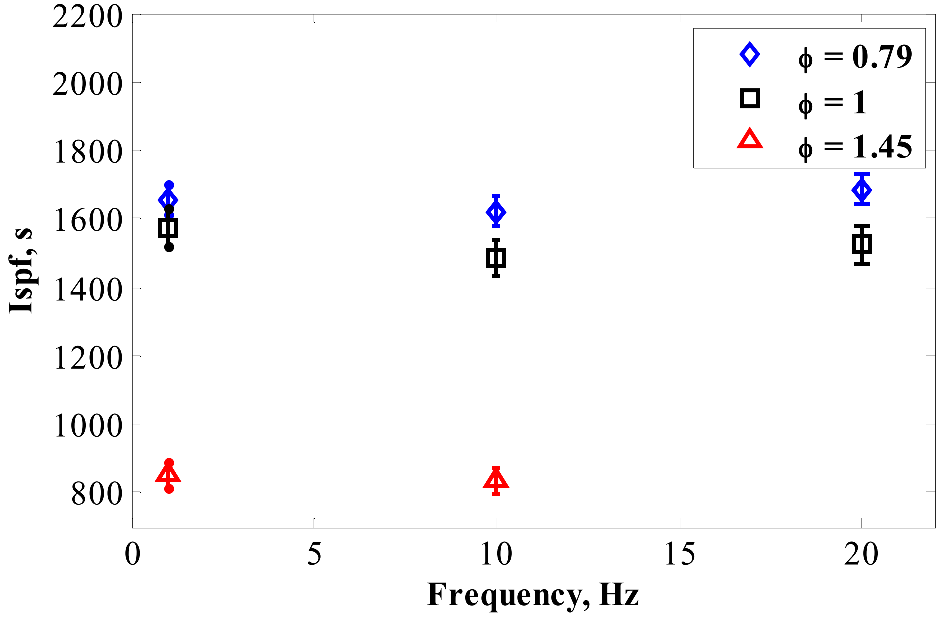

Figure 4.46: Semi-empirically calculated fuel based specific impulse for different equivalence ratios.

Figure 4.46 shows that the fuel-based specific impulse was much lower for high values of equivalence ratios as compared to lower values. It is also important to note that no detonations were observed for operation of the PDE with a frequency of 20 Hz and equivalence ratio of 1.45. The short mixing time and low concentration of oxygen were the possible causes of misfire.

4.3 FEA Results

The feasibility of the general approach was further confirmed by the results obtained from finite element analysis. The thrust calculated using finite element method was processed using the general approach. First, the system transfer function was established which was used to deconvolve the calculated thrust value and acceleration compensation was applied to account for the inertial forces. The finite element model as illustrated in Chapter 2 was used for analysis. In case of a PDE, the thrust is generated due to the pressure applied at the closed end by the burned gases. Following this notion, time varying pressure loads in the form of pressure history at the closed end as shown in Fig. 2.10 was applied as input for finite element analysis. The force reaction and acceleration of the entire system was calculated for the applied load. The pressure loads were applied with a frequency of 10, 20, 50 and 100 Hz to replicate PDE operation. The analysis was carried out for the dynamical model with a damping factor of 0.165 with the corresponding circular frequency of 3142 rad/s. In this section, first, the thrust reconstruction results are illustrated followed by the total impulse results after applying acceleration compensation technique. A comprehensive comparison of results obtained from experimental, semi-empirical and finite element analysis is also presented.

4.3.1 Thrust Reconstruction

Thrust was reconstructed using an established system transfer function. For finite element analysis, a pulse of pressure resembling the pressure history at the thrust wall was used as input and the force reaction calculated at the contact region between the load cell and the thrust stand, assigned as an elastic support, was used as output. An example of input and calculated output used to construct the system transfer function are shown in Figs. 4.47 and 4.48 respectively. Figures 4.49 and 4.50 show the magnitude and phase spectrum of the system function used in the finite element analysis. The established system transfer was first validated and later used to reconstruct thrust for 10, 20, 50 and 100 Hz operation. The validation procedure was similar to the one adopted in the experimental approach. The established system transfer was used to reconstruct thrust for same and different cases and illustrated in figs. 4.51 and 4.52.

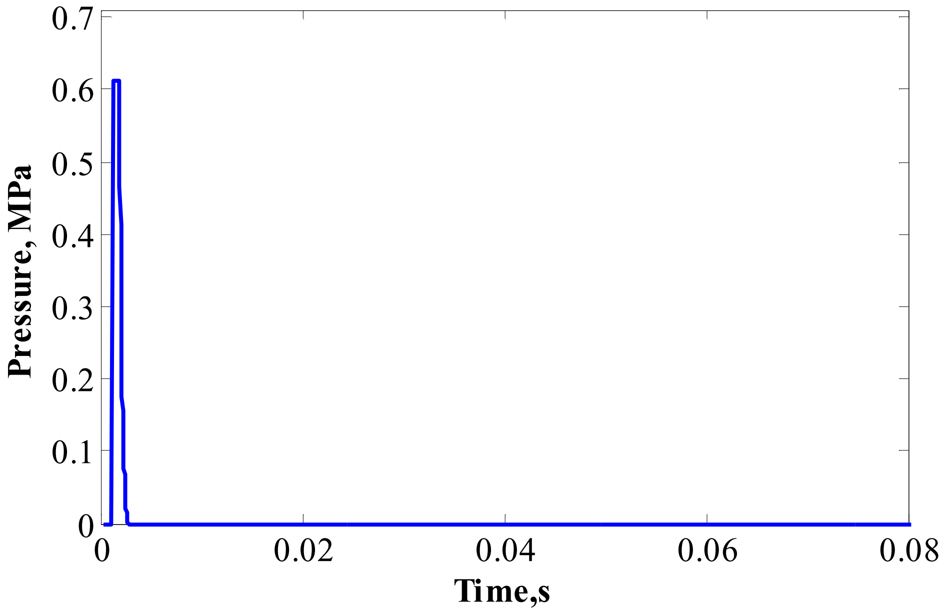

Figure 4.47: Pressure profile of the input used in finite element analysis.

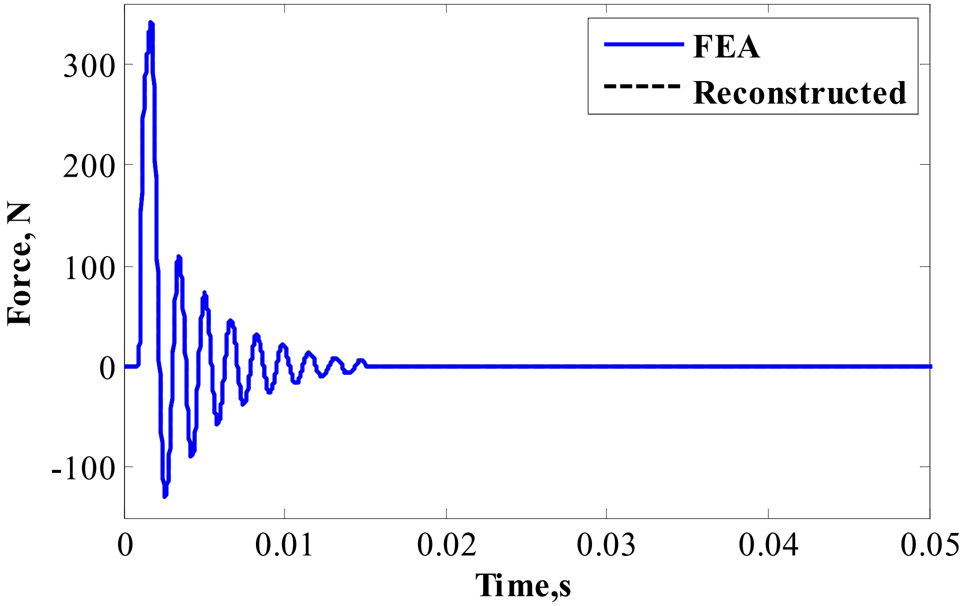

Figure 4.48: : Output calculated using finite element analysis for single pressure input.

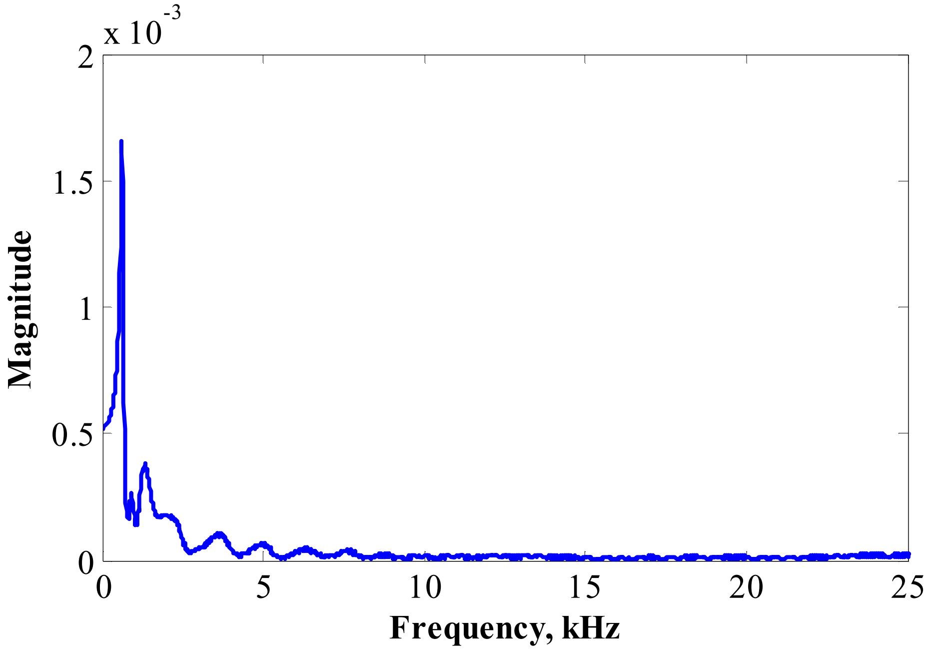

Figure 4.49: Magnitude spectrum of the system transfer function for finite element analysis.

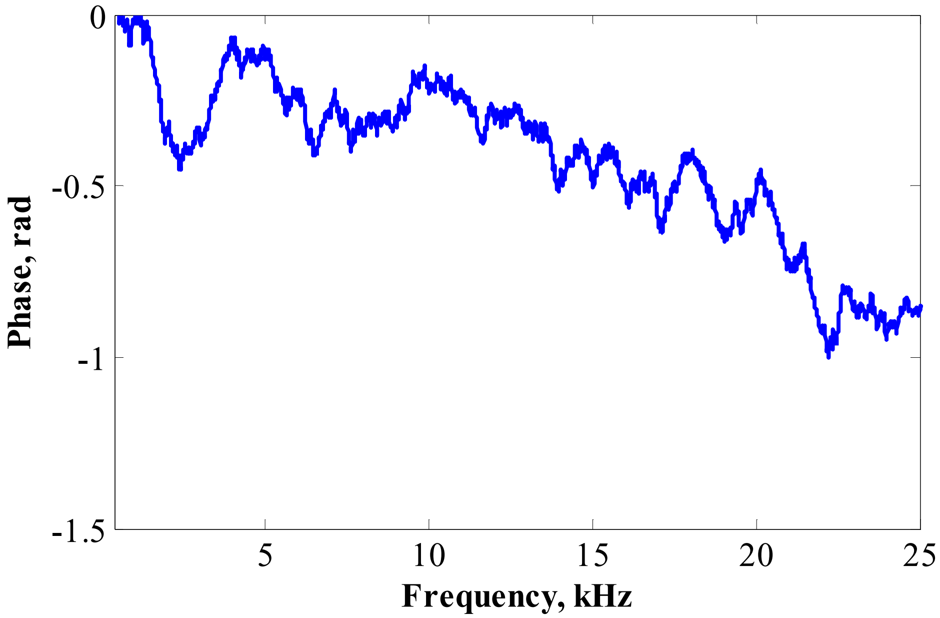

Figure 4.50: Phase spectrum of the system transfer function for finite element analysis.

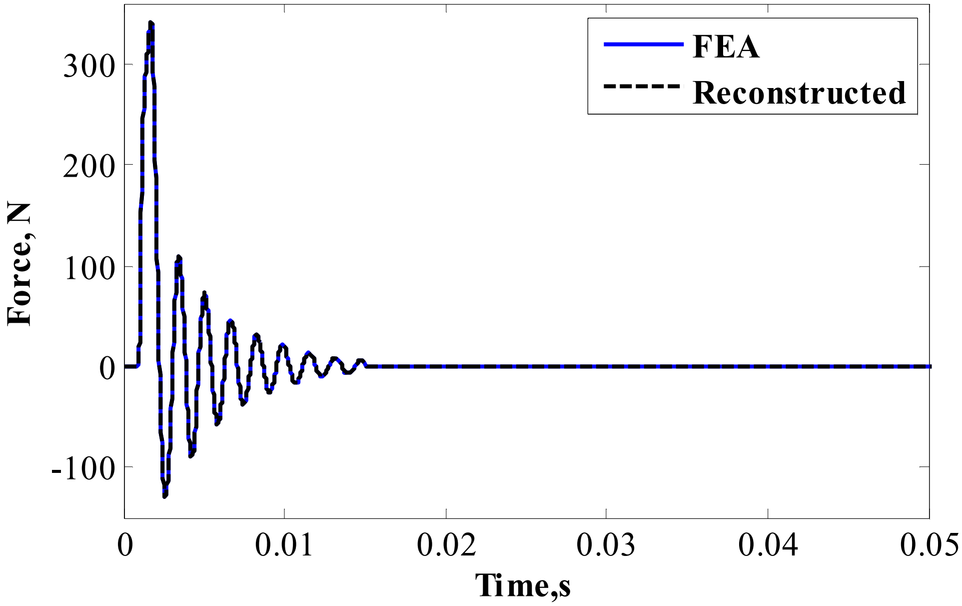

Figure 4.51: Reconstruction of output for same case with the established system transfer function.

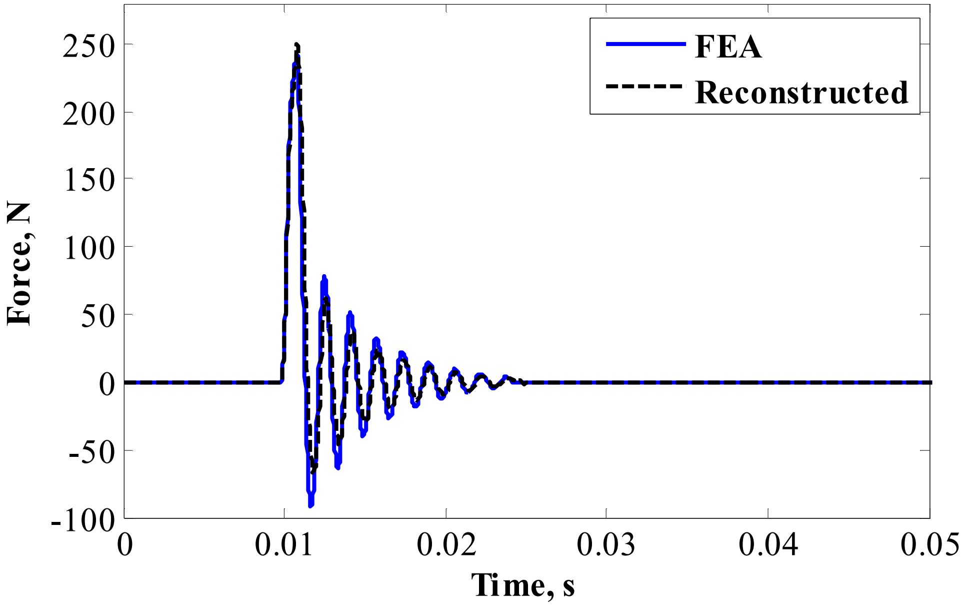

Figure 4.52: Reconstruction of output for different case with the established system transfer function.

The validity of the established transfer function was confirmed since the reconstructed thrust for the same and for different inputs matched well with the calculated ones. The outputs of different magnitudes were obtained by varying the magnitude of input pressure pulse which was further used to reconstruct the thrust for validity.

For analysis, the pulses were repeated in fixed intervals with frequencies of 10, 20, 50 and 100 Hz in order to resemble PDE operation. Figures 4.53–4.56 show the input excitations of different frequencies used to calculate the thrust via finite element analysis. These inputs were later used to get deconvolved thrust using established transfer function. Figures 4.57–4.60 show the measured and reconstructed thrust values.

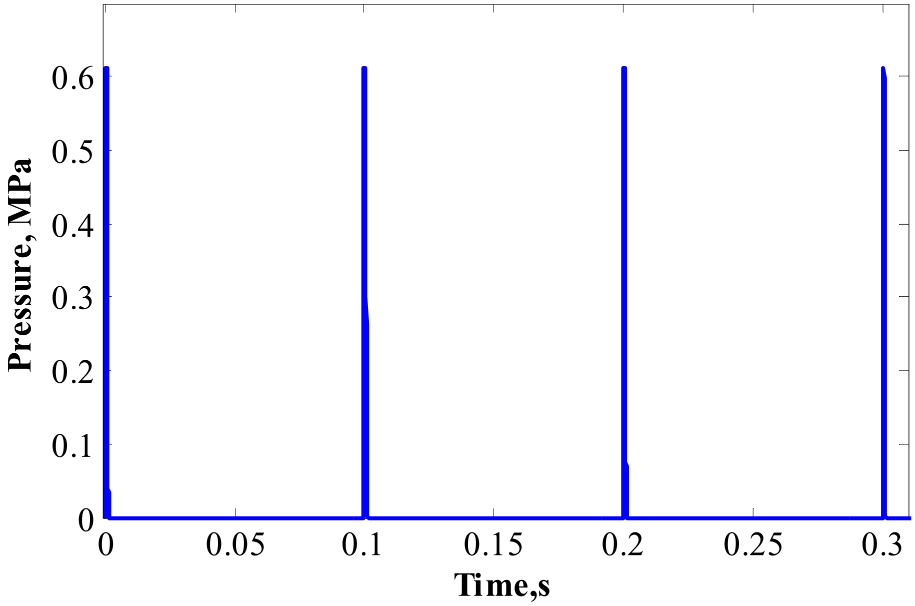

Figure 4.53: Input excitation at 10 Hz used in finite element analysis to calculate thrust.

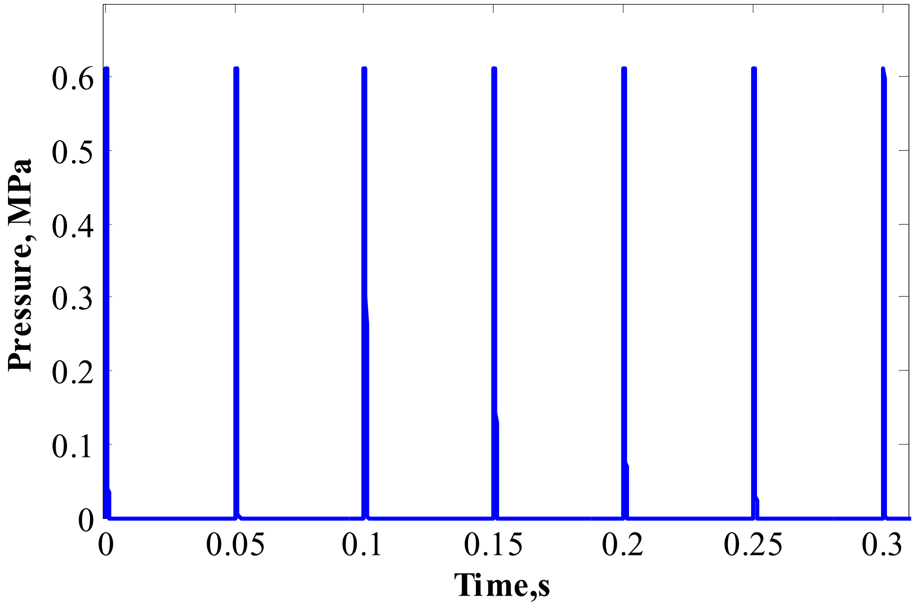

Figure 4.54: Input excitation at 20 Hz used in finite element analysis to calculate thrust.

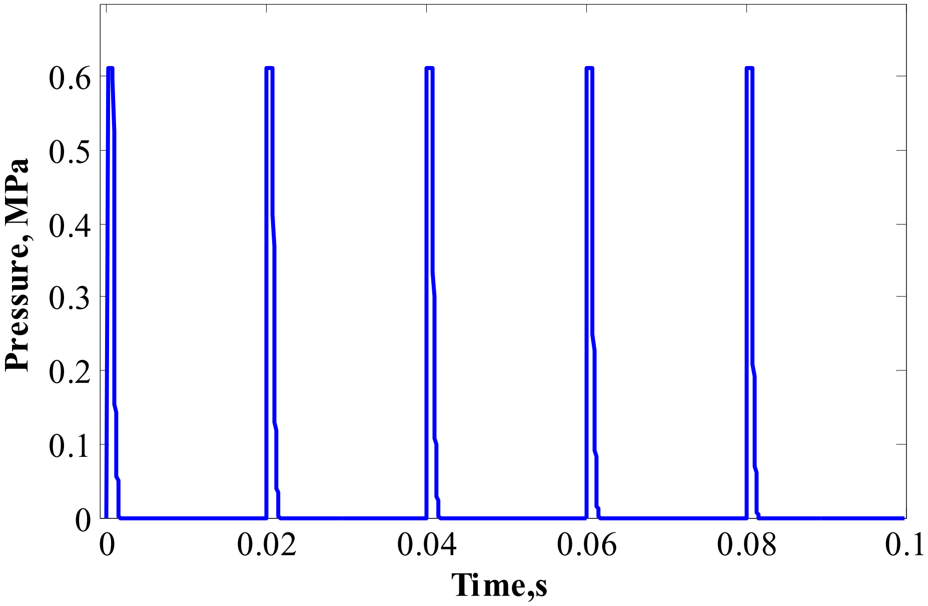

Figure 4.55: Input excitation at 50 Hz used in finite element analysis to calculate thrust.

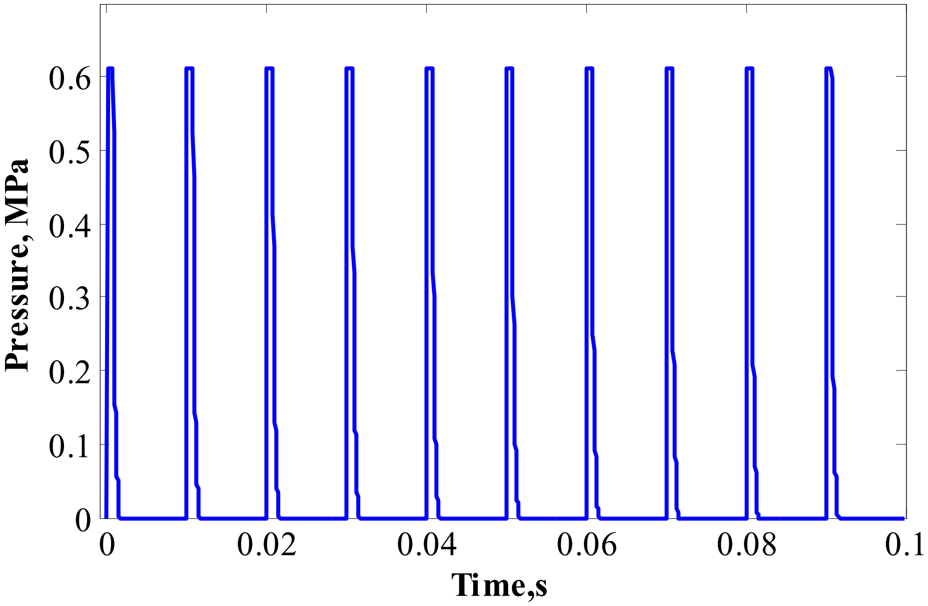

Figure 4.56: Input excitation at 100 Hz used in finite element analysis to calculate thrust.

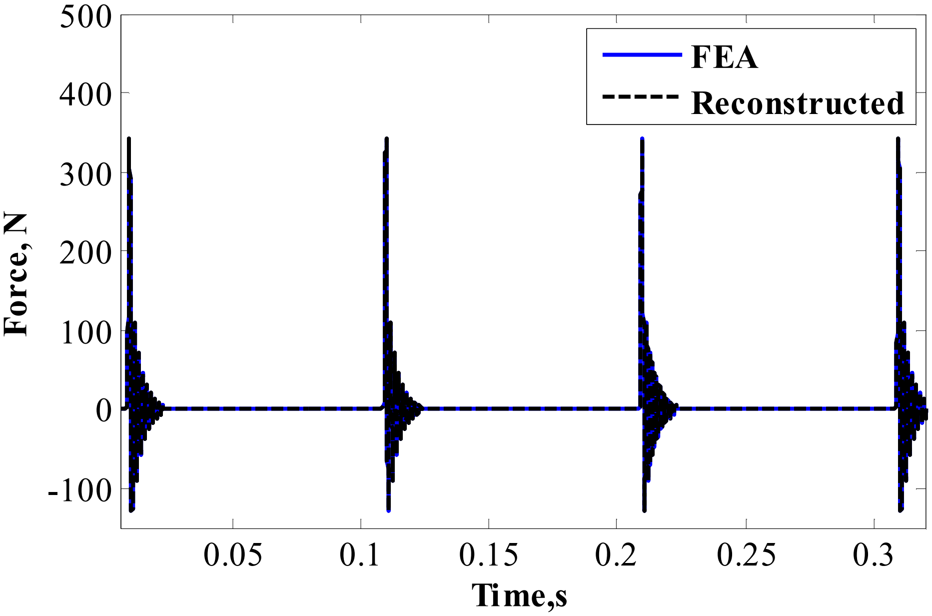

Figure 4.57: Calculated and reconstructed thrust at 10 Hz.

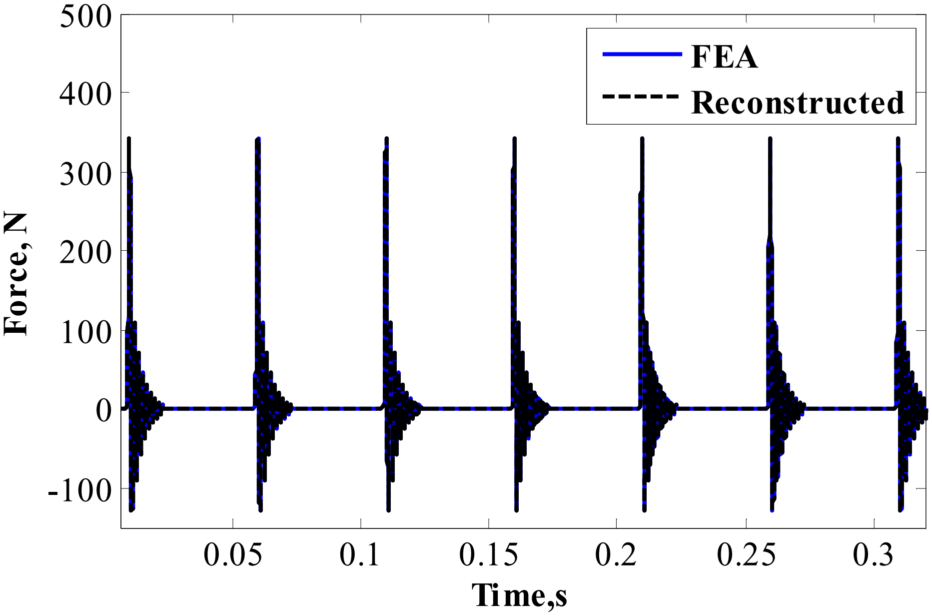

Figure 4.58: Calculated and reconstructed thrust at 20 Hz.

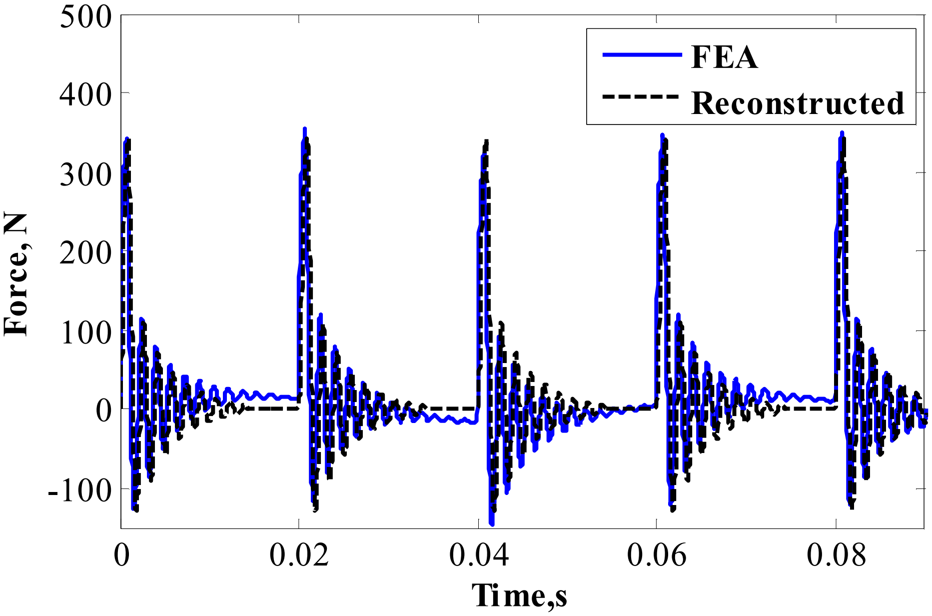

Figure 4.59: Calculated and reconstructed thrust at 50 Hz.

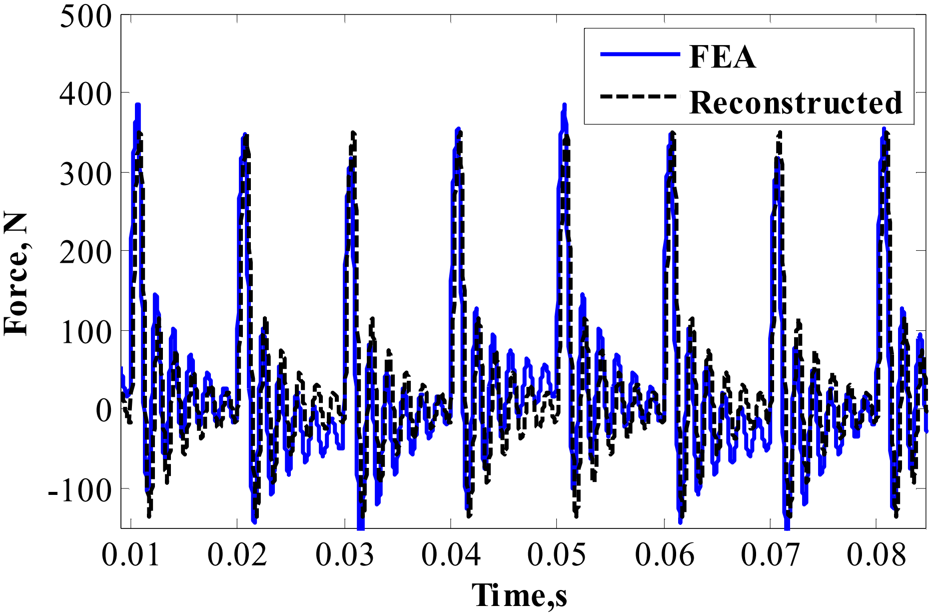

Figure 4.60: Calculated and reconstructed thrust at 100 Hz.

Figures 4.57–4.60 show that the calculated and reconstructed signals were very close to each other when the excitation frequency was low. However, at higher frequencies, the calculated values were observed to be superimposed to one of the lower modes of excited frequency of the dynamical model. The reconstructed values appeared to be free of this superposition. For all the cases of excitation frequencies, a proper reconstruction of thrust was achieved.

4.3.2 Acceleration Compensation

The acceleration compensation procedure used for the experimental approach was implemented in this analysis as well. Acceleration of the thrust measurement rig due to the loading was calculated. The calculated acceleration along with the determined effective mass of 12.5 kg was used to apply the acceleration compensation technique via equation (2.20). For simplicity the compensated thrust was represented as impulse per pulse per unit area. This value of impulse was later used to calculate the specific impulse.

Figure 4.61 shows the typical acceleration of the thrust measurement rig calculated due to the applied excitation. The plot presents the directional acceleration of the thrust measurement rig solved by ANSYS. The maximum acceleration refers to the acceleration in the direction of thrust and minimum refers to the acceleration in the opposite direction to the thrust. The summation of two gave the effective acceleration of the thrust measurement rig. However, instead of taking the mean, the acceleration values were first integrated within the time interval of the pulse width and the obtained values were added. A pulse width of 1.64 ms was used for finite element analysis which is equal to the pulse width used for experimental analysis.

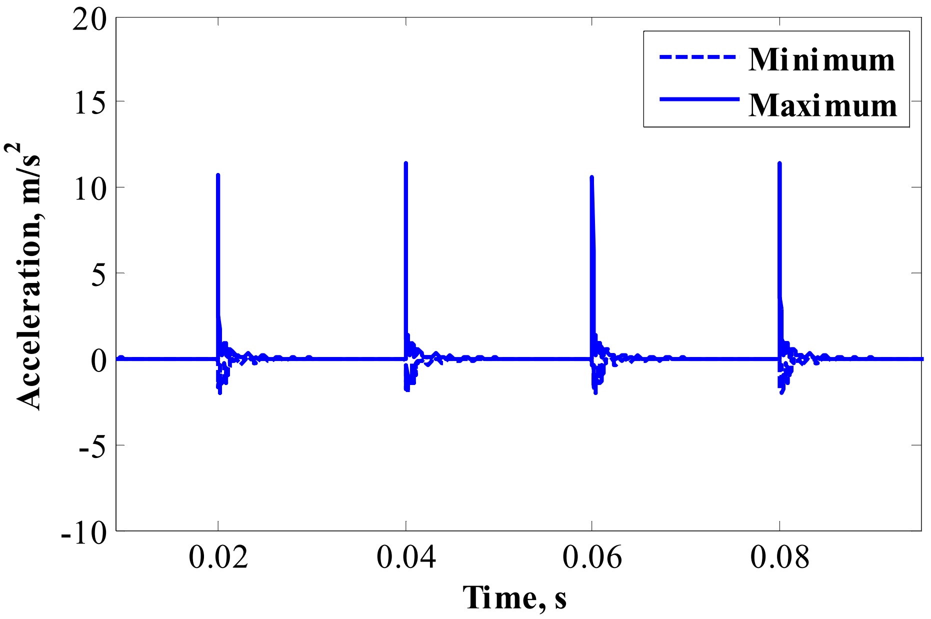

(a)

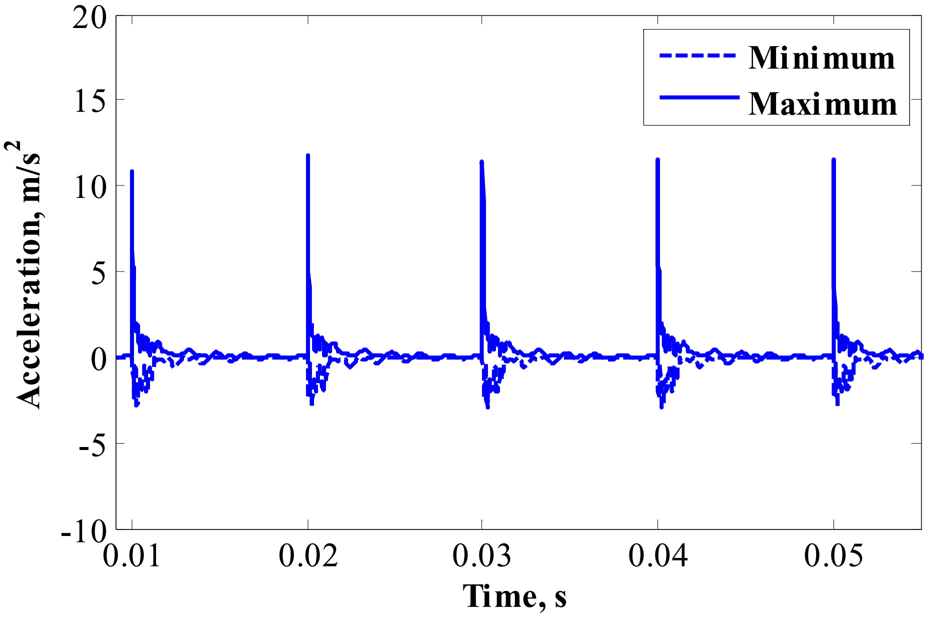

(b)

Figure 4.61: Sample acceleration of the thrust measurement rig calculated using finite element analysis at (a) 50 Hz and (b) 100 Hz.

Using the known values of acceleration per pulse and the effective mass, the inertial force was estimated and subtracted from the calculated impulse. Figure 4.62 illustrates the calculated and compensated impulse per pulse per unit area of the PDE for applied excitations. The plot shows that the compensated values are lower than the calculated values by 5.5%.

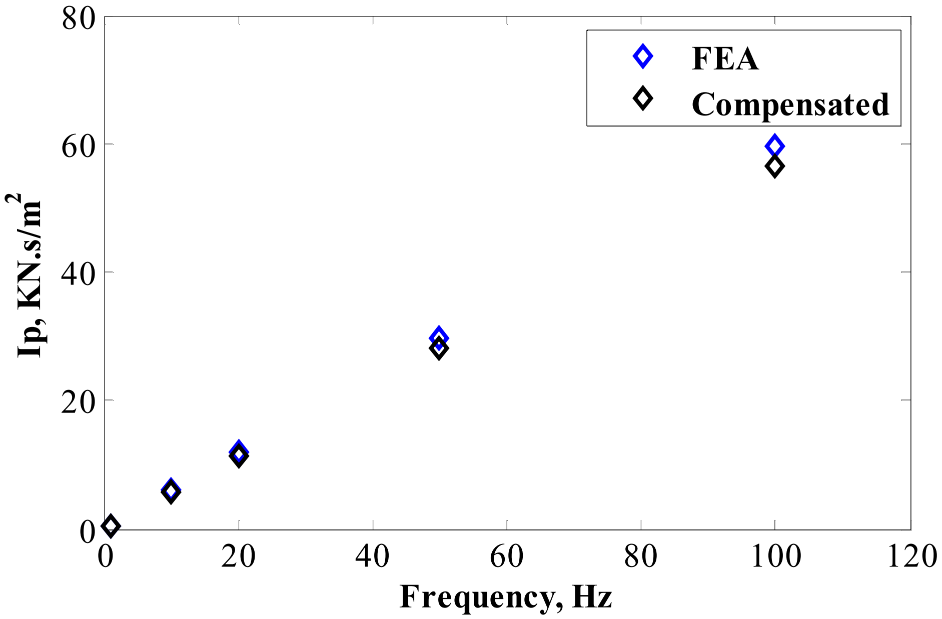

Figure 4.62: Calculated and compensated impulse per pulse per unit area of the PDE from finite element analysis.

Finally, using the compensated impulse, the specific impulse of the PDE was calculated. In this case, the assumption was made that the PDE was fully filled and the equivalence ratio was unity. The specific impulse obtained using finite element analysis was compared against the specific impulse obtained using the semi-empirical method and experiments. Figure 4.63 illustrates the comparison of the specific impulse obtained via three methods described in this project. The specific impulse calculated using the semi-empirical method and the finite element analysis were very close to each other. However, the experimental values were much lower. The comparatively low values of the experimental specific impulse can be explained. The use of the Shchelkin spiral was expected to decrease the generated thrust due to additional drag on the inner surface of the tube. Also, the friction offered by linear motion bearings affected the measured thrust values. Hence, the experimental impulse was lower as compared to the values obtained semi-empirically and numerically. In addition, Figs. 4.9 and 4.10 shows that the pressure measured at the exit for experimental cases were lower than 1.86 MPa. This value of 1.86 MPa is critical as it is the CJ detonation pressure parameter of the stoichiometric oxyhydrogen mixture. Hence, detonations observed in PDE operation were sub-stoichiometric-CJ detonations. This diminished the generated thrust as the pressure at the thrust wall was lower than predicted. Furthermore, the DDT process required some time for a detonation wave to be fully formed. This also affected the pressure gain at the thrust wall and hence the generated thrust.

For better validation of the developed technique, improvised pressure input of lower magnitudes with frequencies of 10 and 20 Hz were applied to the finite element model. The new pressure inputs were constructed based on the detonation pressure measured at the exit of the PDE as shown in Figs. 4.9 and 4.10. Using the new pressure input, the thrust was calculated via finite element analysis and further processed utilizing the general approach. The results of this analysis are also presented in Fig. 4.63. The open dark blue diamond symbols represent the specific impulse calculated for improvised pressure inputs. It can be observed that the new values of specific impulse lie close to the experimentally measured values for 10 and 20 Hz operation. Therefore, it can be concluded that the developed general approach can effectively recover actual thrust generated by the PDE accounting for any pulse-to-pulse interaction, stress wave interference and added inertial forces.

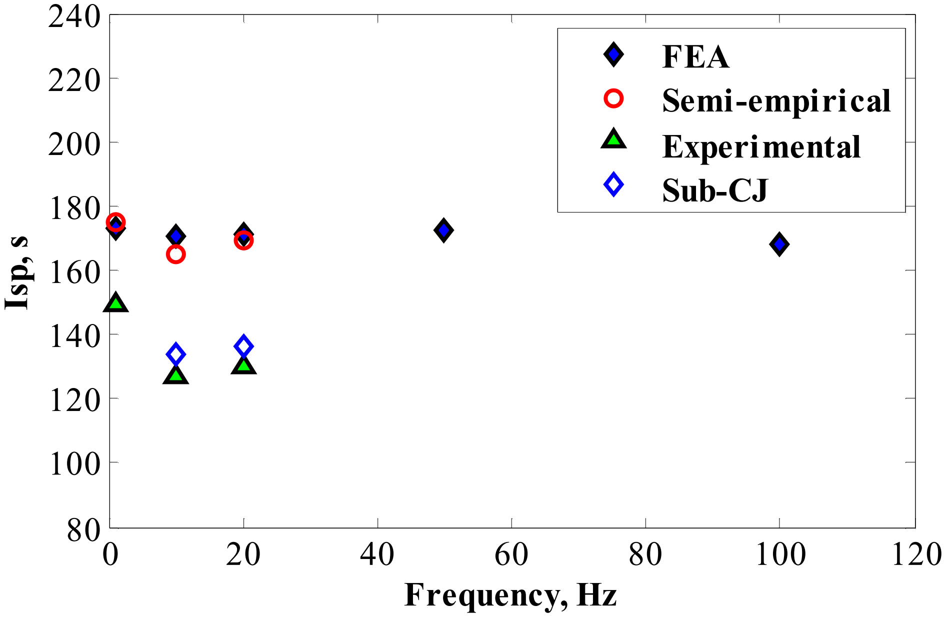

Figure 4.63: Comparison of specific impulse calculated using different methods.

Chapter 5

Application of Developed Technique

5.1 Introduction to the Problem

Short-duration facilities such as shock tunnels and their variants are well-known for their hypersonic testing capabilities. Unfortunately, such facilities have test times in the micro to millisecond range which complicates force measurement [11]. Of particular concern is the dynamics of the force balance when subjected to the sudden aerodynamic loading. The short test time also likely prevents the force balance from attaining a steady state. The development of force and moment measurement techniques in shock tunnels is almost as old as the development of such facilities and a comprehensive summary of early developments are presented in [11]. As was recognized from the outset, of particular concern for shock tunnels is their short, quasi-steady test duration, a concern which is still being addressed such as through improved design and data processing techniques [17, 18, 21, 22, 24–26, 72–74].

A relatively recent breakthrough that uses finite element analysis in its design and advanced data processing is known as the stress wave force measurement technique (SWFM) [17]. This method analyzes the stress waves that propagate through the model−balance structure, realizing that the force balance and model do not reach steady state during the short test duration. The technique requires that the structure, assumed to be linear, be dynamically calibrated. The calibration procedure is to obtain the impulse response function $g(t)$ from applying an impulsive force $x(t)$ and a measurement of output strain at some location on the structure $y(t)$. The relationship between these three parameters is given by the convolution integral [17] similar to equation (2.1),

$$y(t) = \int_0^t g(t-\tau)x(t)d\tau \tag{5.1}$$

A Fourier transform can be applied to deconvolve equation (5.1) to yield the system transfer function,

$$G(f) = \frac{Y(f)}{X(f)} \tag{5.2}$$

where $X(f)$ and $Y(f)$ are the Fourier transforms of the input and output, respectively. Once the transfer function is known, then an arbitrary input force can be backed out from the output in a straightforward manner through rearranging equation (5.2) and performing a deconvolution procedure. Usually, the input is an impulse load and the output is a strain [15].

A distinction is now made on the stress waves that are transmitted and reflected in the model–balance structure and the structural acceleration. If the entire structure and the shock tunnel are rigid, then acceleration is not a factor in reducing the stress wave data to obtain forces. However, the lightly damped structure means that it will vibrate to-and-fro. Given that the steady test time is short, it is likely that the vibrations are not damped out for the model-balance structure to attain a steady state during the test time. Hence, force measurements would need to correct for the inertial forces due to vibration of the model-balance structure. In other words, the SWFM technique highlighted above has to be supplemented by acceleration compensation. Previous work on implementing the SWFM method, including by the author [45] did not address acceleration compensation.

On the other hand, Storkmann et al. [28] considered solely acceleration compensation but their technique was not based on stress waves. This section of the dissertation describes the combined stress wave and acceleration compensation approach which was applied to determine the drag at Mach 8–9 on a spherically-blunt cone mounted in a shock tunnel.

5.2 Implementation

5.2.1 Method

For the force-balance system, assuming a linear relation between inertial forces and estimated input force using the measured force and system transfer function, the added inertial force can be compensated using [27, 28,58],

$$F_{comp} = \hat{F} - m_{eff} a_{filt} \tag{5.3}$$

In equation (5.3), $\hat{F}$ is the estimated input force (namely, the uncompensated drag) using the impulse transfer function and is F_{comp} the actual aerodynamic drag. The acceleration compensation term which is subtracted from the deconvolved force consists of the effective mass of the system m_{eff} and a filtered acceleration term a_{filt}. The entire procedure requires the determination of the three terms on the RHS of equation (5.3) with separate dynamic calibration of the force balance, which was also used to obtain the system transfer function. The entire dynamic calibration process was performed *in situ* with the usual assumptions of a linear system and that the transfer function remains constant between the calibration and the subsequent testing. To facilitate the discussion, the experimental facility, instrumentation and test conditions are briefly described next, with further details available in [45].

5.2.2 Experimental Facility and Test Conditions

The major components of the UTA Hypersonic Shock Tunnel include the driver section, driven tubes, conical nozzle, test section, diffuser and dump tank, which are shown schematically in Fig. 5.1.

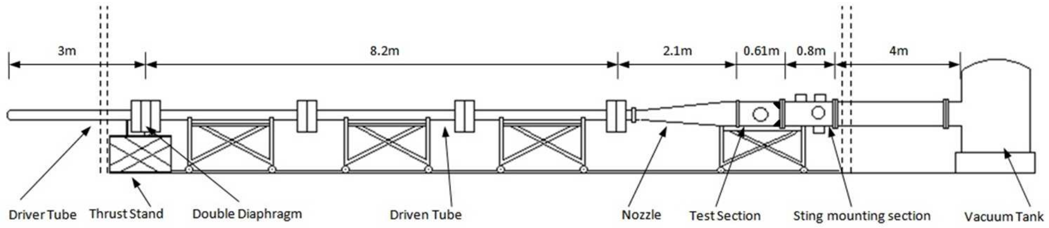

Figure 5.1: Schematic of hypersonic shock tunnel [45].

The driver tube is a single section which is 3 m long with an internal diameter of 152.4 mm and a wall thickness of 25.4 mm. One end is closed off with a hemispherical end cap. The double diaphragm section separates the driver from the driven tube and it holds two steel diaphragms. The driven tube is constructed in three segments, each 2.74 m long. The nozzle has interchangeable throat inserts to provide a discrete test Mach number from 5 through 16. The test section is 0.61 m long and 0.4 min diameter. The hypersonic shock tunnel was run at two enthalpy levels. For the low-enthalpy condition, dried air at 27.6 MPa was used as the driver gas. The driven tube was filled with dried air at 0.1 MPa. The high-enthalpy condition was achieved with a detonation driver [75,76]. The detonation driver filled an upstream section of the driven tube, next to diaphragm section, with a stoichiometric oxyhydrogen mixture. This mixture supported the formation of a shock-induced detonation wave when the double diaphragms were ruptured by the pressurized, cold air, driver gas. The detonation wave then drove the test gas, which was dried air at 0.1 MPa in the driven tube in a downstream propagating mode of operation.

Table 5.1 below shows the measured freestream and stagnation conditions for the two different enthalpy levels named Case A and B respectively.

Table 5.1: Experimental test conditions

Properties	Case A	Case B
Stagnation enthalpy h_0, MJ/kg	$0.65 \pm 3.1\%$	$0.90 \pm 2.2\%$
Freestream Mach number M_∞	$8.05 \pm 3.7\%$	$9.0 \pm 3.3\%$
Stagnation pressure p_0, MPa	$2.6 \pm 1.2\%$	$4.22 \pm 0.71\%$
Stagnation temperature T_0, K	$922 \pm .54\%$	$1139 \pm 0.44\%$
Free stream static pressure p_∞, Pa	$70.6 \pm 0.4\%$	$142 \pm 0.31\%$
Free stream static temperature T_∞, K	$52 \pm 9.6\%$	$72.6 \pm 6.9\%$
Free stream velocity u_∞, km/s	$1.154 \pm 3.5\%$	$1.518 \pm 2.6\%$
Specific heat ratio of test gas, γ	1.377	1.365

5.2.3 Instrumentation

Figure 5.2 shows the external drag balance with a sphere-cone model to demonstrate the technique. The drag balance was made of 6061 aluminum alloy from a single block to prevent stress concentrations that would otherwise be present at joints created by fastening of separate members. The drag balance was 20.9 cm long, 10.8 cm high and 2.4 cm wide. Further details on the design of the drag balance can be found in [45]. As shown in Fig. 5.2, a model in the form of a sphere-cone, whose drag was to be measured, was attached to the balance's front. The blunt cone was made of steel with a base radius of 40 mm, a nose radius of 3.55 mm, a length of 88.9 mm, a nose semi-angle of 18.5° and a mass of 0.907 kg. A PCB Model 111A24 dynamic pressure transducer was mounted at the nose of the blunt cone to measure the stagnation pressure. The drag balance was instrumented with a strain gage made of piezoelectric film (Measurement Specialties Model DT1-052k) and an accelerometer (PCB model 350B04) as shown in the figure. The strain gage detected stress waves propagating in the drag balance structure and was fixed on the horizontal stress bar as shown in Fig. 5.2. The accelerometer was mounted at the center of the back of the balance, aligned to the axis of the axial bar to measure the axial acceleration of the model-balance structure. Instrumentation wiring from the transducer was channeled through a narrow interior cavity to the rear to be taken out of the tunnel, together with other wiring. Data were gathered by a simultaneous sample-and-hold system at 2.5 MHz/channel using a NI model PXIe 8130 controller and NI PXI 6133 card.

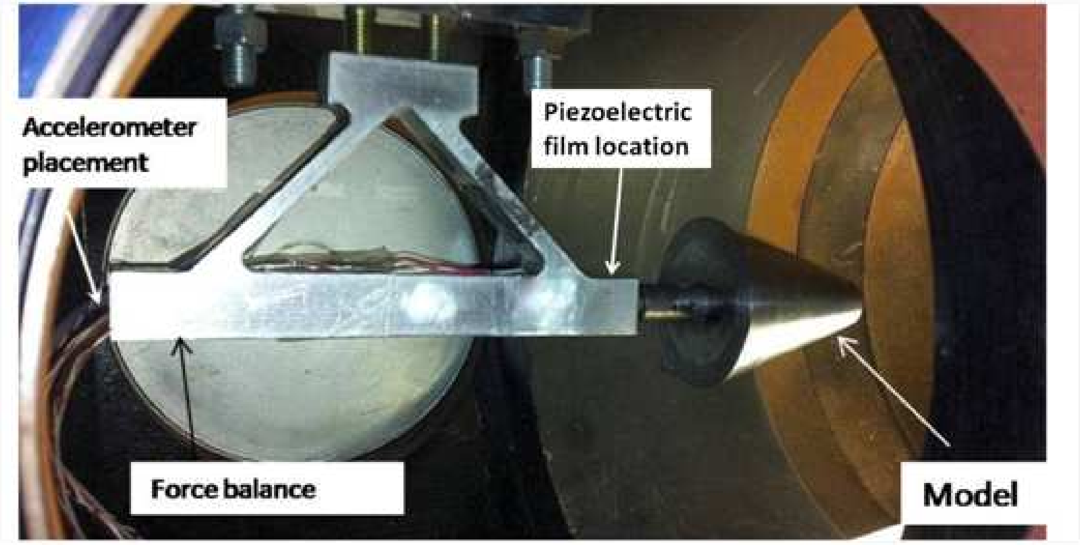

Figure 5.2: Drag balance with sphere-cone model mounted in shock tunnel. Flow from right to left.

5.3 Results and Discussion

5.3.1 Signal Reconstruction

The system transfer function for the model–balance structure was determined by striking the nose of the cone impulsively using a PCB model 086C01 impact hammer. The same test also allowed the effective mass to be determined. A sample result of such an impact test is shown in Fig. 5.3 which displays the input measured by the load cell mounted on the impact hammer and the output measured by the piezoelectric film gage mounted on the balance. Knowing both the input and the output allowed the transfer function to be estimated by equation (5.2). For completeness, Figs. 5.4 and 5.5 show the magnitude and phase spectra of the established transfer function.

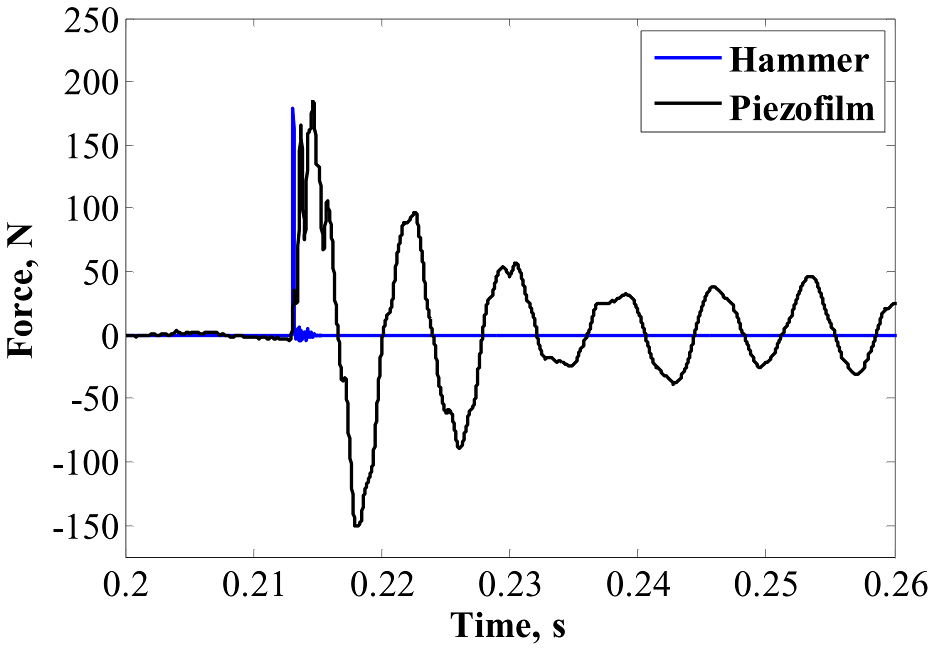

Figure 5.3: Impulsive input and corresponding piezofilm response.

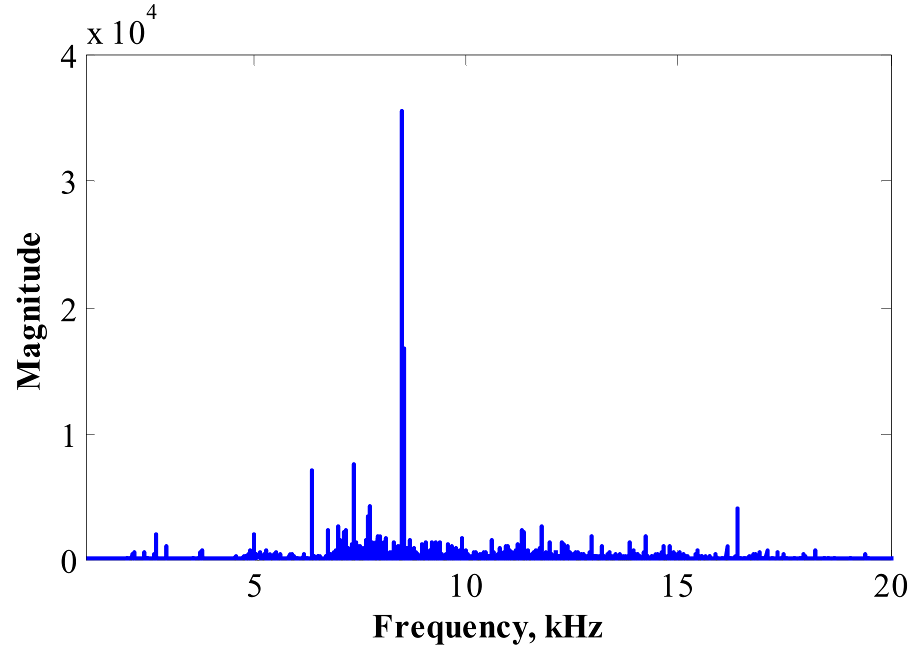

Figure 5.4: Magnitude spectrum of experimental transfer function.

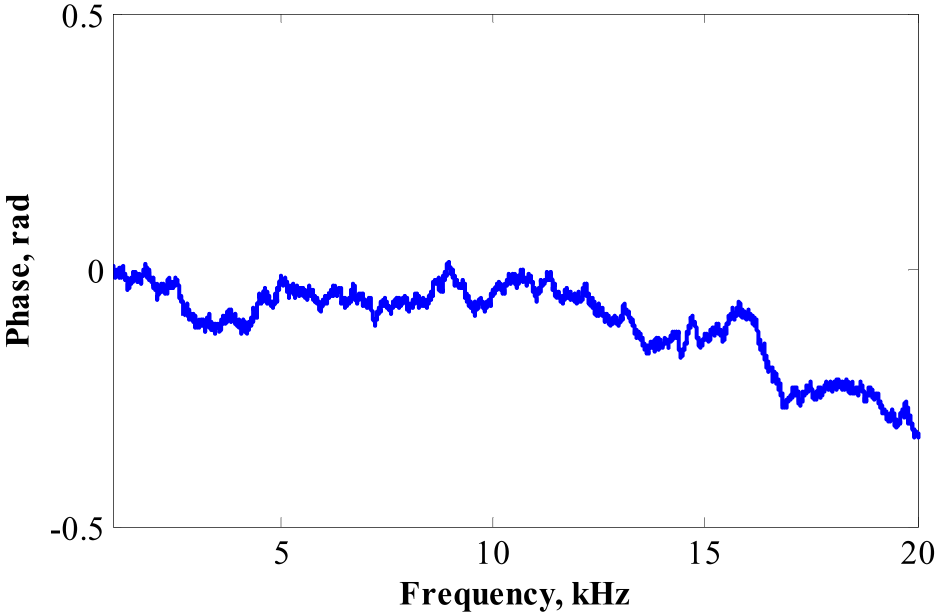

Figure 5.5: Phase spectra of experimental transfer function.

The transfer function was validated by its ability to reconstruct the input from strain gage data. All the signals were sampled at 2.5 MHz for 80 ms and the results are shown in Fig. 5.6. Figure 5.6 shows that the reconstructed signal followed the input signal measured by the load cell mounted on the impact hammer perfectly. Further, Fig. 5.7 shows the reconstruction of the input signal from the response registered by the piezoelectric film gauge measured by a different impact test with the same transfer function obtained previously. Again, the reconstruction is good with slight departures following the peak. This second result is crucial in that it demonstrates the ability of the transfer function obtained from a calibration to replicate an input from a measurement of the response registered by the piezoelectric film gage on the model–balance structure. The validated system transfer function was then used to reconstruct the drag force experienced by the model-balance structure for the flow conditions shown in Table 5.1.

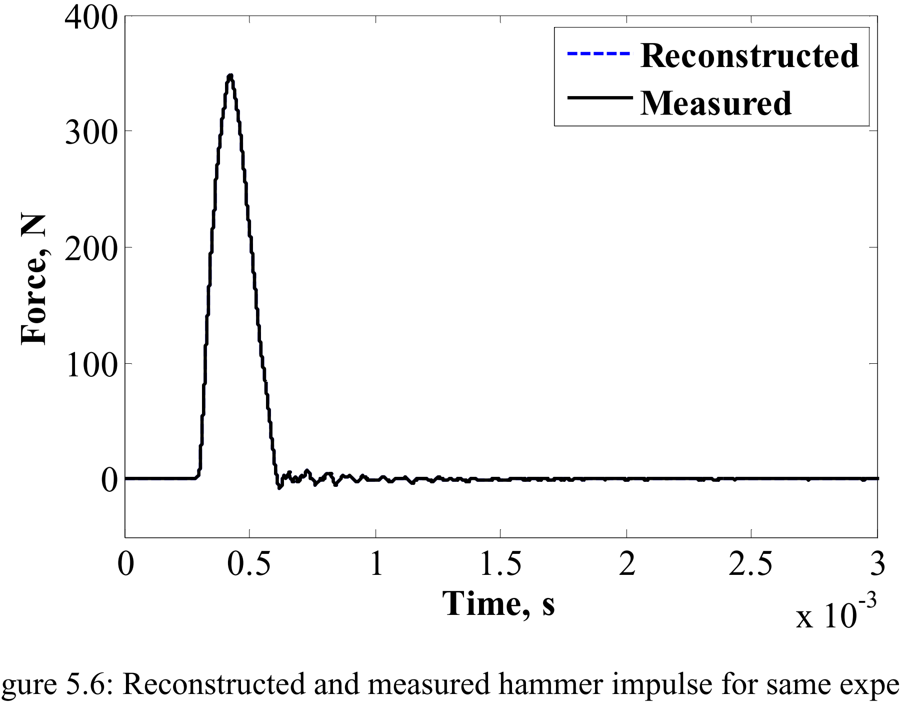

Figure 5.6: Reconstructed and measured hammer impulse for same experiment.

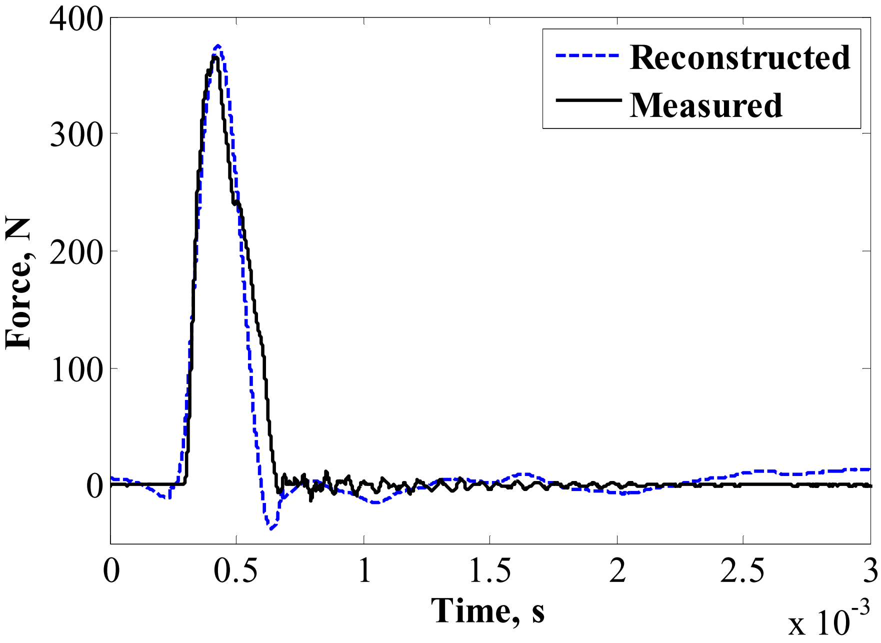

Figure 5.7: Reconstructed and measured hammer impulse for different experiments.

Figure 5.8 is an example of the pressure signal from the transducer located at the nose of the sphere–cone test model after low-pass filtering at 40 kHz. The figure shows a quasi-steady test time of about 110 μs. A slight recess of the transducer could be the cause of the oscillation shown by the measured pressure signal.

The response measured by the piezofilm gauge for this quasi-steady test time is the output of the model–balance system. This measured output along with the system transfer function was used to reconstruct the input, which is the uncompensated aerodynamic drag force experienced by the model–balance structure for the given test condition. Figures 5.11 and 5.12 show these results together with the compensated drag results in the form of dimensionless coefficient of drag that will be discussed later.

Figure 5.11 shows the measured drag force with a Butterworth bandpass of 1.2–120 kHz for Case A and the reconstructed drag force, which is the input for the system or the uncompensated aerodynamic drag experienced by the model in the flow. Since the reconstructed drag force exhibited the inclusion of high-frequency content, a 25-point moving average of the signal was taken to smoothen the curve. Similar results for Case B are shown in Fig. 5.12.

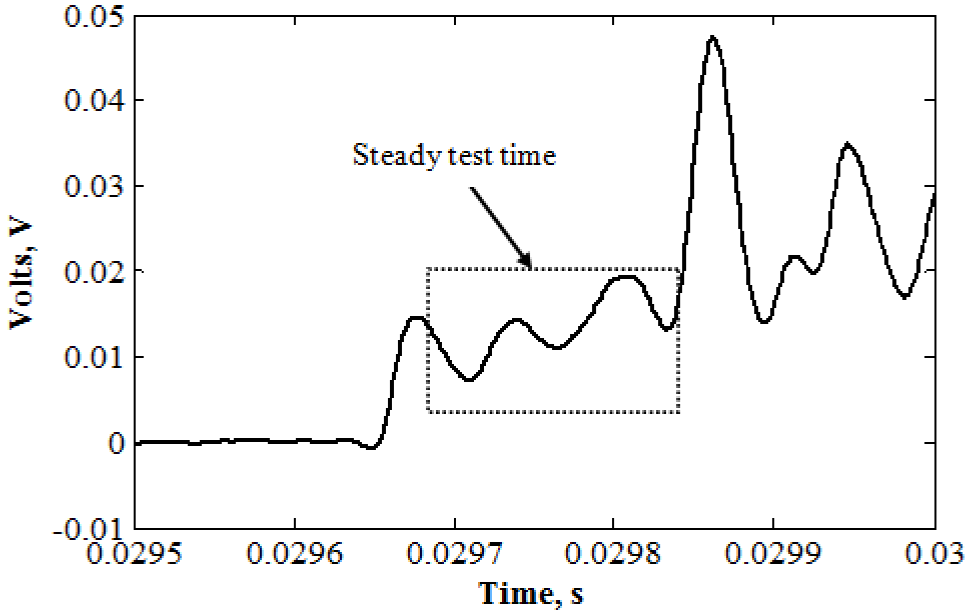

Figure 5.8: Filtered pitot signal and steady test time.

5.3.2 Acceleration Compensation

The effective mass m_e in equation (5.3) represents the active oscillating mass of the model-balance system under aerodynamic loading. This oscillating mass along with acceleration induced by vibration of the entire system produces an inertial force that is also recorded by the balance. Thus, acceleration compensation requires the effective mass to be determined. The effective mass was determined by applying impulses of different magnitudes to the tip of the cone using an instrumented hammer. The response of the system and the acceleration due to the applied impulses were measured for each impulse. Hence, the effective mass of the system can be determined using

$$m_{eff} = \frac{J}{a_{meas}} \tag{5.4}$$

where m_{eff} is the effective mass of the system, J is the rms of the response registered by the piezoelectric film gauge and a_{meas} is the rms of the measured acceleration induced by the impulsive force.

The system was underdamped. Hence, the settling time for the response registered by the piezoelectric film gauge and the acceleration as shown in Fig. 5.9 was far longer than the duration of the impulse shown in Fig. 5.3. The effect of the inertial force was prominent only in the front part of the response period; hence, considering the entire acceleration record would yield erroneous values of m_{eff} and a_{filt} in this nonstationary process. It is therefore necessary to restrict the time interval window. Before determining the time interval window, the damping factor of the system must first be determined. The damping factor was found using the logarithmic decrement technique described in Chapter 2 to be 0.06 ± 0.002. The time window was also set by the logarithmic decrement technique which is when the amplitude decreased to 63 percent of the initial amplitude [52]. This restricted time interval window was found to be 1.18 ± 0.4 ms. Next, the rms of the acceleration obtained within this window was used for calculating the effective mass. For the same time interval, the rms of the measured force was also calculated. The restricted time interval window focused on the part of the signal where its amplitude was prominent and was considered to involve the effects of oscillations of the system. This time interval window was a part of the calibration process and bore no relation to the steady test time of the test cases.

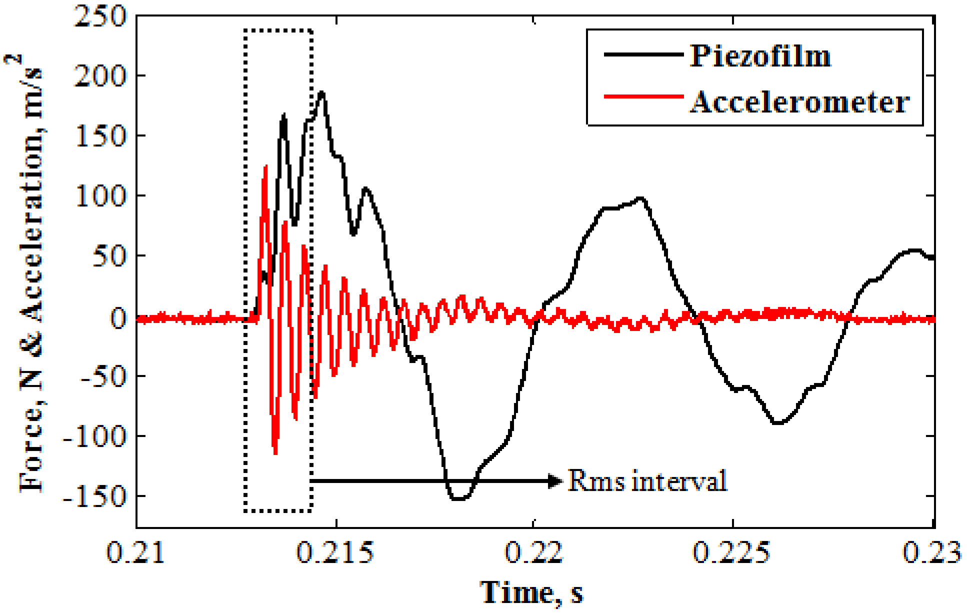

Figure 5.9: Typical rms interval for calculation of effective mass.

The rms values of the acceleration and force allowed the effective mass m_e to be obtained from equation (5.4). Figure 5.10 shows the calculated values of effective mass for the range of applied impulses. The figure shows that the effective mass did not change much for the range of applied impulsive force. Hence, an average effective mass of 1.78 ± 0.14 kg was taken to be representative.

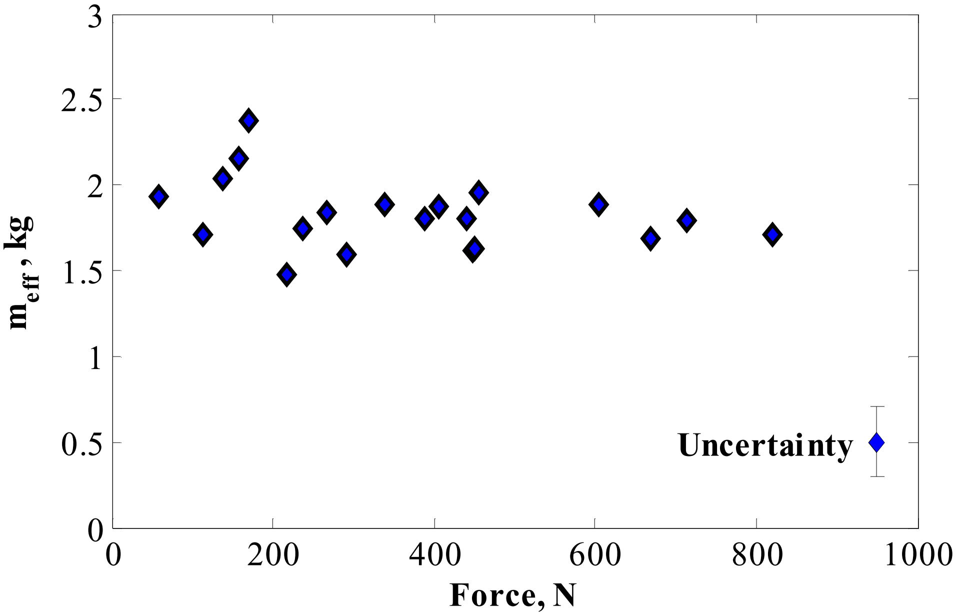

Figure 5.10: Effective mass calculated for a range of impulses applied.

Acceleration compensation was applied to the reconstructed signal to obtain the actual drag force by subtracting the inertial force per equation (5.3). The product of the effective mass and the measured acceleration during the steady test time gave the inertial force for a test run. As mentioned above, the effective mass was almost constant for a range of impulsive forces at 1.78 kg. However, the measured acceleration signal was different based on the test conditions and was evaluated separately for each test. The data were sampled at a very high frequency of 2.5 MHz and weak stress waves propagating in the system due to the impact interfered with the acceleration signal. Hence, the signal had to be filtered before it could be used to calculate the inertial force. For this purpose, the data were band passed by a Butterworth filter at 15–25 kHz.. The filtered acceleration signal oscillated around the zero line; hence, the rms of this signal was taken. This filtered, rms value of acceleration a_{filt} was multiplied with the effective mass of the model-balance structure to obtain the inertial forces. Figures 5.11 and 5.12 show the moving average of the reconstructed signal, and the acceleration compensated signal for the two test cases under consideration in the form of drag coefficient. The uncertainty bar is the 95% confidence level of the standard deviation of the acceleration compensated signal that is used to represent the uncertainty of the signals. The figures also show the predicted drag coefficient using modified Newtonian theory. It can be clearly seen that acceleration compensated drag coefficient values obtained experimentally lie close to the theoretical value showing the effectiveness of the developed approach. The technique was observed to be effective for the low-enthalpy case, with the drag coefficient agreeing well with theory. The discrepancy shown for the high-enthalpy case may be due to the higher inertial force that was experienced.

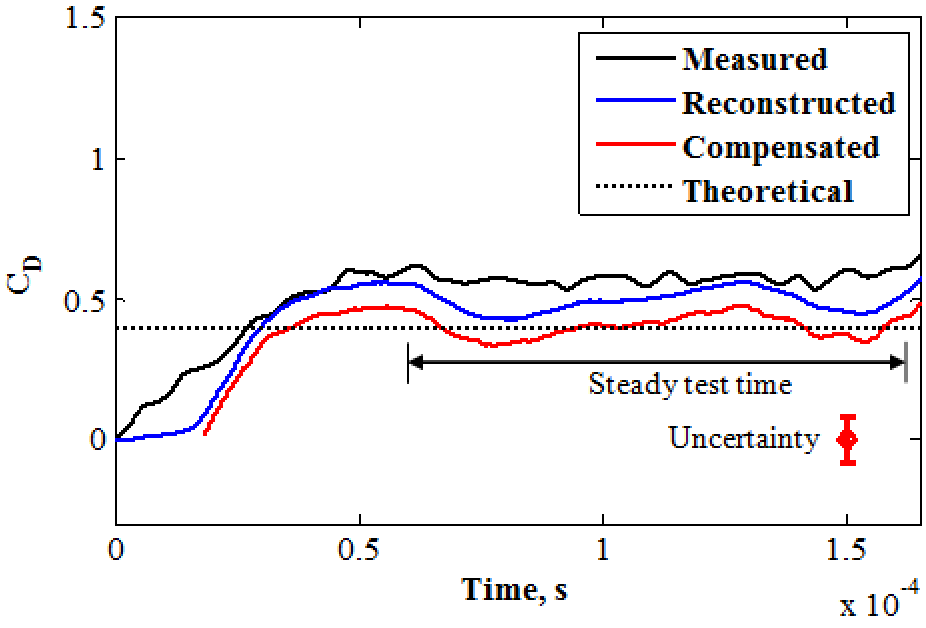

Figure 5.11: Measured, reconstructed, acceleration and theoretical drag for Case A.

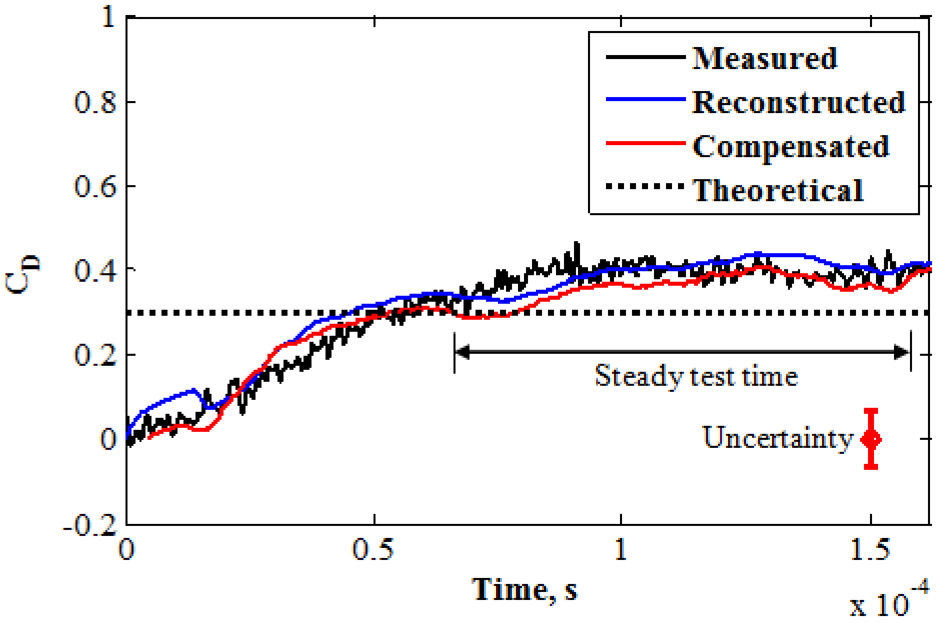

Figure 5.12: Measured, reconstructed, acceleration and theoretical drag for Case B.

Chapter 6

Conclusion and Remarks

A PDE was developed to study unsteady thrust characteristics. The effects of pulse-to-pulse interaction in the generated thrust for a fast operating PDE, interference due to propagating and reflecting stress waves initiated by the detonation waves and inertial forces due to oscillation of the thrust measurement rig were accounted to recover the actual thrust generated by the PDE.

In order to recover actual thrust generated by the PDE considering all the practical issues discussed above, a general approach was developed. The general approach consisted of two steps. The first step accounted for pulse-to-pulse interaction and stress wave interference by utilizing a deconvolution procedure. The deconvolution procedure incorporated reconstruction of deconvolved thrust through an experimentally established transfer function and measured input in the form of pressure history at the exit of the PDE. The second step was acceleration compensation to account for inertial forces still prevailing in the deconvolved thrust.

The PDE was operated at different levels of filling fractions and equivalence ratios of the mixture at 10 and 20 Hz. The thrust measured from experimental tests were analyzed and processed using the developed approach to recover actual thrust. The established transfer function was able to reconstruct the deconvolved thrust well from the measured input. A detailed description of acceleration compensation procedure was provided and implemented to account for inertial forces brought about by the acceleration of the thrust measurement rig. Finally, the compensated thrust values were used to determine of impulse of PDE which was later expressed as specific impulse for comparison.

In addition, control volume analysis was used to predict the thrust generated by the engine. An analytical study of the gas dynamics of the PDE while in operation was performed to predict the effects of unsteady momentum changes on thrust generation. Furthermore, the pressure history of the detonation wave measured at the exit of the PDE while in operation and the predicted contribution of unsteady momentum changes were used to determine the impulse generated by the PDE in a cycle. The calculated impulse was expressed in the form of specific impulse for comparison against experimentally measured specific impulse.

A dynamical model of the PDE was also developed to evaluate the developed technique through finite element analysis. Input excitations at 10, 20, 50 and 100 Hz were applied to the dynamical model. The response was calculated using ANSYS Transient solver. The calculated response was analyzed using the developed general approach and the results were expressed in the form of specific impulse.

Upon comparison, the specific impulse values obtained from semi-empirical analysis and finite element analysis match significantly. The experimentally measured specific impulse values were slightly lower than the other two. This was expected as there are practical complexities which affect the thrust generation process. The use of Shchelkin spiral, improper mixing due to high operating frequencies and prevailing frictional forces of the linear motion bearings all affect the experimentally measured thrust values.

Finally, the developed technique was applied to recover actual drag force experienced by a blunt nose cone model in a nominal Mach 8–9 flow. The results showed the effectiveness of the developed approach as the final drag force obtained after applying the developed approach matched the values predicted using modified Newtonian theory.

6.1 Major Contributions

- Development of a general approach to recover actual thrust generated by a pulse detonation engine
    - Proper reconstruction of thrust for all operating frequencies and effective subtraction of inertia forces
- Introduction of *rig-based acceleration compensation procedure* to account for inertial forces added into the measured thrust signals
    - 8% reduction in experimentally calculated impulse and 6% reduction in impulse calculated using FEA
    - Effective reduction of added inertial forces
- A methodology to estimate effective oscillating mass of the system based on the system dynamics
    - Proper quantification of effective oscillating mass
- A method to accurately estimate the intermittent mass flow rates of the gases injected into a pulse detonation engine
    - A semi-empirical model of a time-varying area profile of the injecting surface
    - Proper calibration to account for loses due to viscous effects

- An analytical approach to predict the effect of nonstationary changes in the rate of change of momentum arising due to the unsteady flow in the detonation chamber
- A refined control volume analysis to determine the thrust generated by a pulse detonation engine
- An insight in the use of finite element analysis for studying the unsteady thrust characteristics of a pulse detonation engine
    - Development of high fidelity model and analysis procedure
- A new method to accurately determine the aerodynamic drag in hypervelocity facilities

6.2 Possible Future Directions

This research project on “Unsteady Thrust Measurement Techniques for Pulse Detonation Engines” has opened doors for further research in this subject matter. The first possible step that could be taken is the application of wavelets and wavelet transform for the reconstruction of thrust. Currently, a FFT technique is used for thrust reconstruction and replacing this technique by wavelet transform is expected to be beneficial as wavelets provide both time and frequency localization. Wavelets are better for functions with sharp peaks like detonation waves and can accurately reconstruct finite, non-periodic or non-stationary signals.

The results of this research work show the feasibility of the developed general approach to accurately estimate the actual thrust generated by the PDE. Therefore, the general approach can be used to accurately predict the thrust generated by a PDE with and without a Shchelkin spiral. Hence, the effect of Shchelkin spiral on thrust generation process can be characterized.

The method described to accurately estimate the unsteady mass flow rate of the fuel and oxidizer in this project can be utilized to estimate the fuel flow rates for PDEs operating on rotary valves.

Various dynamical models of the PDE can be created and finite element analysis can be performed to calculate the unsteady thrust generated based on the input loading. The calculated thrust could be further processed using the developed general approach to accurately estimate the actual unsteady thrust generated. This methodology can be utilized to select the most suitable design configuration and assist in the integration of the engine to the aircraft.

Finally, the acceleration compensation technique can be further extended. The procedure described in this project is known as *rig-based acceleration compensation.* An *engine-based acceleration compensation* can also be implemented. However, this technique will require a free floating engine structure which can be achieved by using aero-bearings. This technique will utilize the mass levitation method (MLM). Therefore, the measurement of the actual mass of the engine structure and induced acceleration while in operation will yield thrust generated by the PDE. The thrust measured using this procedure can be compared against the thrust measured by the load cell to quantify the inertial forces.

Appendix A

Modified Newtonian Theory

Newtonian theory assumes that the oncoming flow can be considered as a stream of particles. When the particles come in contact with a surface at very high speed, they lose all their momentum component perpendicular to the surface. The pressure coefficient predicted by Newtonian theory is given by

$$C_p = 2\sin^2\theta \tag{A.1}$$

where θ is the inclination angle of the surface. This equation illustrates that for high speed flow the pressure distribution is related to the square of the inclination angle. The modified Newtonian theory was proposed by Lees in 1955 which related the pressure coefficient with the flow Mach number and given by

$$C_{p,max} = \left[\frac{p_{t2}}{p_\infty} - 1\right]\frac{2}{\gamma M_\infty^2} \tag{A.2}$$

where $C_{p,max}$ is the maximum pressure coefficient behind a normal shock wave at the stagnation point and p_{t2}/p_∞ is calculated using the Rayleigh-Pitot formula [77] given by

$$\frac{p_{t2}}{p_\infty} = \left[\frac{(\gamma+1)M_\infty^2}{2}\right]^{\frac{\gamma}{(\gamma-1)}}\left[\frac{(\gamma+1)}{2\gamma M_\infty^2 - (\gamma-1)}\right]^{\frac{1}{(\gamma-1)}} \tag{A.3}$$

The axial force coefficient is calculated by the following relation [78]

$$\begin{aligned} C_A = 2C_{p,t_2}\left(\frac{R_N^2}{R_B^2}\right)\Bigg[\Bigg(&\frac{(0.5\cos^2\alpha(1-\sin^4\theta_c)}{2} \\ &+0.125\sin^2\alpha\cos^4\theta_c) \\ &+\tan\theta_c(\cos^2\alpha\sin^2\theta_c + 0.50\sin^2\alpha\cos^2\theta_c) \\ &\times\left(\frac{(R_B/R_N)-\cos\theta_c}{\tan\theta_c}\cos\theta_c + \frac{\left((R_B/R_N)-\cos\theta_c\right)^2}{2\tan\theta_c}\right)\Bigg] \end{aligned} \tag{A.4}$$

where,

R_N is the nose radius of the blunt cone

R_B is the base radius of the blunt cone

θ_c is the half cone angle

α is the angle of attack

Thereafter, the normal force coefficient is calculated using the following [78]

$$C_N = 2C_{p,t_2}\left(\frac{R_N^2}{R_B^2}\right)\Bigg[\Bigg(\frac{0.5\sin\alpha\cos\alpha\cos^4\theta_c}{2} \\ +\sin\alpha\cos\alpha\sin\theta_c\cos\theta_c\Bigg) \\ \times\left(\frac{(R_B/R_N)-\cos\theta_c}{\tan\theta_c}\cos\theta_c+\frac{\left((R_B/R_N)-\cos\theta_c\right)^2}{2\tan\theta_c}\right)\Bigg] \tag{A.5}$$

The following relation is used to calculate the lift-to-drag ratio

$$\frac{L}{D} = \frac{C_N\cos\alpha - C_A\sin\alpha}{C_N\cos\alpha + C_A\sin\alpha} \tag{A.6}$$

Drag is estimated using,

$$D = \frac{1}{2}\rho v^2 S C_D \tag{A.7}$$

$$v^2 = M^2\gamma RT \tag{A.8}$$

$$\rho = \frac{p}{RT} \tag{A.9}$$

Substituting equations (A.8) and (A.9) into (A.7) yields

$$D = \frac{1}{2}\gamma p M^2 S C_D \tag{A.10}$$

However, as shown in Chapter 5, drag is usually expressed in the form of drag coefficient for completeness and it is expressed as

$$C_D = \frac{D}{\frac{1}{2}\rho_\infty v_\infty^2 S} \tag{A.11}$$

In addition, the Rayleigh-Pitot formula given in equation (A.3) can also be written as [79]

$$p_{pit} = p_\infty \left[\frac{(\gamma+1)M_\infty^2}{2}\right]^{\frac{\gamma}{(\gamma-1)}} \left[\frac{(\gamma+1)}{2\gamma M_\infty^2 - (\gamma-1)}\right]^{\frac{1}{(\gamma-1)}} \tag{A.12}$$

For high values of M_∞, $2\gamma {M_\infty}^2 \gg (\gamma-1)$, equation (A.12) can be written as

$$p_{pit} \approx p_\infty \left[\frac{(\gamma+1)}{2}\right]^{\frac{(\gamma+1)}{(\gamma-1)}} \gamma^{\frac{1}{(\gamma-1)}} M_\infty^2 \tag{A.13}$$

Also,

$$p_\infty = \rho_\infty R T_\infty \tag{A.14}$$

$${M_\infty}^2 = \frac{{v_\infty}^2}{\gamma R T_\infty} \tag{A.15}$$

Upon substituting equations (A.14) and (A.15) into (A.13),

$$p_{pit} \approx \left[\frac{(\gamma+1)}{2}\right]^{\frac{(\gamma+1)}{(\gamma-1)}} \gamma^{\frac{\gamma}{(\gamma-1)}} \rho_\infty {v_\infty}^2 \tag{A.16}$$

Substituting equation (A.16) into equation (A.11),

$$C_D = \left[\frac{2\left(\frac{(\gamma+1)}{2}\right)^{\frac{(\gamma+1)}{(\gamma-1)}} \gamma^{\frac{\gamma}{(\gamma-1)}}}{S}\right] \frac{D}{p_{pit}} \tag{A.17}$$

Hence, for a given flow condition γ and S remain constant and a simultaneous measurement of p_{pit} and D can be used to estimate the coefficient of drag, which can be expressed as a time-dependent quantity.

References

[1] K. Kailasanath, “Recent Developments in the Research on Pulse Detonation Engines,” *AIAA J.*, vol. 41, no. 2, pp. 145–159, 2003.

[2] G. D. Roy, S. M. Frolov, A. A. Borisov, and D. W. Netzer, “Pulse Detonation Propulsion: Challenges, Current Status, and Future Perspective,” *Prog. Energy Combust. Sci.*, vol. 30, no. 6, pp. 545–672, 2004.

[3] M. Cooper, S. Jackson, J. Austin, E. Wintenberger, and J. E. Shepherd, “Direct Experimental Impulse Measurements for Detonations and Deflagrations,” *J. Propuls. Power*, vol. 18, no. 5, pp. 1033–1041, 2002.

[4] M. Cooper and J. E. Shepherd, “Effect of Porous Thrust Surfaces on Detonation Transition and Detonation Tube Impulse,” *J. Propuls. Power*, vol. 20, no. 5, pp. 811–819, 2004.

[5] D. Allgood, E. Gutmark, J. Hoke, R. Bradley, and F. Schauer, “Performance Measurements of Multicycle Pulse-Detonation-Engine Exhaust Nozzles,” *J. Propuls. Power*, vol. 22, no. 1, pp. 70–77, 2006.

[6] A. Glaser, J. Brumberg, A. Rasheed, R. A. Dunton, and V. E. Tangirala, “Investigations of Thrust Generated by a Valved, Multitube PDE with Exit Nozzles,” *AIAA Paper 2008–4692,* 2008.

[7] J. Kasahara, M. Hirano, A. Matsuo, Y. Daimon, and T. Endo, “Thrust Measurement of a Multicycle Partially Filled Pulse Detonation Rocket Engine,” *J. Propuls. Power*, vol. 25, no. 6, pp. 1281–1290, 2009.

[8] K. Matsuoka, M. Esumi, K. B. Ikeguchi, J. Kasahara, A. Matsuo, and I. Funaki, “Propulsive Performance of a Liquid Kerosene/Oxygen Pulse Detonation Rocket Engine,” *Exp. Therm. Fluid Sci.*, vol. 35, no. 1, pp. 265–271, 2011.

[9] K. Matsuoka, M. Esumi, K. B. Ikeguchi, J. Kasahara, A. Matsuo, and I. Funaki, “Optical and Thrust Measurement of a Pulse Detonation Combustor with a Coaxial Rotary Valve,” *Combust. Flame*, vol. 159, no. 3, pp. 1321–1338, 2012.

[10] H. Kolsky, *Stress Waves in Solids*. Mineola, NY: Dover, 2003.

[11] L. Bernstein, “Force Measurement in Short-Duration Hypersonic Facilities,” *AGARDograph AGARD-AG-214*, 1975.

[12] K. W. Naumann, H. Ende, and G. Mathieu, “Techniques for Aerodynamic Force Measurement within Milliseconds in Shock Tunnel,” *Shock Waves*, vol. 1, no. 3, pp. 223–232, 1991.

[13] H. Tanno, M. Kodera, T. Komuro, K. Sato, M. Takahasi, and K. Itoh, “Aerodynamic Force Measurement on a Large-Scale Model in a Short Duration Test Facility,” *Rev. Sci. Instrum.*, vol. 76, no. 3, art. 035107, 2005.

[14] H. Tanno, T. Komuro, M. Takahashi, K. Takayama, H. Ojima, and S. Onaya, “Unsteady Force Measurement Technique in Shock Tubes,” *Rev. Sci. Instrum.*, vol. 75, no. 2, p. 532, 2004.

[15] D. J. Mee, “Dynamic Calibration of Force Balances for Impulse Hypersonic Facilities,” *Shock Waves*, vol. 12, no. 6, pp. 443–455, 2003.

[16] R. Joarder and G. Jagadeesh, “A New Free Floating Accelerometer Balance System for Force Measurements in Shock Tunnels,” *Shock Waves*, vol. 13, no. 5, pp. 409–412, 2004.

[17] S. R. Sanderson and J. M. Simmons, “Drag Balance for Hypervelocity Impulse Facilities,” *AIAA J.*, vol. 29, no. 12, pp. 2185–2191, 1991.

[18] M. V. Joshi and K. P. J. Reddy, “Aerodynamic Force Measurements over Missile Configurations in IISc Shock Tunnel at M_∞=5.5,” *Exp. Fluids*, vol. 4, no. 6, pp. 338–340, 1986.

[19] N. Sahoo, D. R. Mahapatra, G. Jagadeesh, S. Gopalakrishnan, and K. P. J. Reddy, “Design and Analysis of a Flat Accelerometer-Based Force Balance System for Shock Tunnel Testing,” *Measurement*, vol. 40, no. 1, pp. 93–106, 2007.

[20] N. Sahoo, D. R. Mahapatra, G. Jagadesh, S. Gopalakrishan, and K. P. J. Reddy, “An Accelerometer Balance System for Measurement of Aerodynamic Force Coefficients Over Blunt Bodies in a Hypersonic Shock Tunnel,” *Meas. Sci. Technol.*, vol. 14, no. 3, pp. 260–272, 2003.

[21] K. Satheesh and G. Jagadeesh, “Analysis of an Internally Mountable Accelerometer Balance System for use with Non-Isotropic Models in Shock Tunnels,” *Measurements*, vol. 42, no. 6, pp. 856–862, 2009.

[22] M. Robinson, J. M. Schramm, and K. Schramm, “An Investigation into Internal and External Force Balance Configurations for Short Duration Wind Tunnels,” *Notes Numer. Fluid Mech. Multidiscip. Des.*, vol. 96, pp. 129–136, 2008.

[23] M. J. Robinson, D. J. Mee, and A. Paull, “Scramjet Lift, Thrust and Pitching-Moment Characteristics Measured in a Shock Tunnel,” *J. Propuls. Power*, vol. 22, no. 1, pp. 85–95, 2006.

[24] W. J. T. Daniel and D. J. Mee, “Finite Element Modelling of a Three-Component Force Balance for Hypersonic Flows,” *Comput. Struct.*, vol. 54, no. 1, pp. 35–48, 1995.

[25] A. L. Smith, D. J. Mee, W. J. T. Daniel, and T. Shimoda, “Design, Modelling and Analysis of a Six Component Force Balance for Hypervelocity Wind Tunnel Testing,” *Comput. Struct.*, vol. 79, no. 11, pp. 1077–1088, 2001.

[26] M. M. Abdel-Jawad, D. J. Mee, and R. G. Morgan, “New Calibration Technique for Multiple-Component Stress Wave Force Balances,” *Rev. Sci. Instrum.*, vol. 78, 2007.

[27] M. Carbonaro, “Aerodynamic Force Measurements in VKI Longshot Hypersonic Facility,” in *New Trends in Instrumentation for Hypersonic Research*, A. Boutier, Ed. Dordrecht, The Netherlands: Kluwer Academic Publishers, 1993, pp. 371–325.

[28] V. Storkmann, H. Olivier, and H. Gronig, “Force Measurements in Hypersonic Impulse Facilities,” *AIAA J.*, vol. 36, no. 3, pp. 342–348, 1998.

[29] I. I. Glassman and R. A. Yetter, *Combustion*, 4th Ed. San Diego, California: Academic, 2008.

[30] F. K. Lu, D. R. Wilson, R. J. Bakos, and J. I. Erdos, “Recent Advances in Detonation Techniques for High-Enthalpy Facilities,” *AIAA J.*, vol. 38, no. 9, pp. 1676–1684, 2000.

[31] P. Panicker, “The Development and Testing of Pulsed Detonation Engine Ground Demonstrators,” Ph.D. Dissertation, University of Texas at Arlington, 2008.

[32] D. L. Chapman, “On the Rate of Explosion in Gases,” *Philos. Mag. Ser. 5*, vol. 47, no. 284, pp. 90–104, 1889.

[33] E. Jouguet, “Sur la propagation des réactions chimiques dans les gaz,” *J. des Mathématiques Pures Appliquées*, vol. 1 and 2, pp. 347–425 and 5–86.

[34] Y. B. Zel’dovich, “Distribution of Pressure and Velocity in the Products of a Detonating Explosion and in Particular in the Case of a Spherical Propagation of the Detonation Waves,” *J. Exp. Theor. Phys.*, vol. 12, pp. 389–406, 1942.

[35] J. von Neumann, “Theory of Detonation Waves. Progress Report to the National Defense Research Committee Div. B, OSRD-549, (April 1, 1942. PB 31090),” in *John von Neumann: Collected Works, 1903-1957*, vol. 6, A. H. Taub, Ed. New York: Pergamon, 1963.

[36] W. Doering, “Uber den Detonationsvorgang in Gasen,” *Ann. Phys.*, vol. 43, pp. 421–436, 1943.

[37] J. H. S. Lee, *The Detonation Phenomenon*. New York: Cambridge, 2008.

[38] E. M. Braun, “New Detonation Concepts for Propulsion and Power Generation,” Ph.D. Dissertation, University of Texas at Arlington, 2012.

[39] B. J. McBride and S. Gordon, “Computer Program for Calculation of Complex Chemical Equilibrium Compositions and Applications Analysis,” NASA RP 1311, 1994.

[40] M. Roy, “Propulsion par statoreacteur a detonation,” *Comptes Rendus Hebd. des Séances l’ Académie des Sci.*, vol. 222, pp. 31–32, 1946.

[41] A. S. Nowick, “Internal Friction in Metals,” in *Progress in Metal Physics*, vol. 4, no. 1, New York: Wiley Interscience, p. 29, 1953.

[42] T. Endo, J. Kasahara, A. Matsuo, S. Sato, K. Inaba, and T. Fujiwara, “Pressure History at the Thrust Wall of a Simplified Pulse Detonation Engine,” *AIAA J.*, vol. 42, no. 9, pp. 1921–1930, 2004.

[43] E. Winterberger, J. Austin, M. Cooper, S. Jackson, and J. E. Shepherd, “Impulse of a Single-Pulse Detonation Tube,” GALCIT Rept. FM00-8, Aug. 2002.

[44] J. Bendat and A. Piersol, *Random Data*, 3rd ed. New York: Wiley, 2000.

[45] P. Vadassery, “Design, Calibration and Testing of a Force Balance for a Hypersonic Shock Tunnel,” Master's Thesis, University of Texas at Arlington, 2012.

[46] J. F. Doyle, *Wave Propagation in Structures*. New York: Springer-Verlag, 1989.

[47] A. A. Ortiz, “Development of Spectral and Wavelet Time-of-Flight Methods for Propagating Shock and Detonation Waves,” Master's Thesis, University of Texas at Arlington, 2008.

[48] H. W. Liepmann and A. Roshko, *Elements of Gasdynamics*. New York: Wiley, 1957.

[49] L. D. Landau and E. M. Lifshitz, "Fluid Dynamics of Combustion," in *Fluid Mechanics: Volume 6 of Course of Theoretical Physics*, Oxford: Pergamon Press, 1979, pp. 474–498.

[50] T. Endo and T. Fujiwara, "Analytical Estimation of Performance Parameters of an Ideal Pulse Detonation Engine," *Trans. Jpn. Soc. Aeronaut. Space Sci.*, vol. 45, no. 150, pp. 249–254, 2003.

[51] E. Wintenberger, J. M. Austin, M. Cooper, S. Jackson, and J. E. Shepherd, "Analytical Model for the Impulse of Single-Cycle Pulse Detonation Tube," *J. Propuls. Power*, vol. 19, no. 1, pp. 22–38, 2003.

[52] R. R. Craig and A. J. Kurdila, *Fundamentals of Structural Dynamics*. Hoboken, New Jersey: Wiley, 2006.

[53] R. D. Cook, *Finite Element Modeling for Stress Analysis*. New York: Wiley, 1995.

[54] H. H. Lee, *Finite Element Simulations with ANSYS Workbench 13*. Mission, Kansas: SDC Publications, 2011.

[55] C. M. Harris and C. E. Crede, Eds., *Shock and Vibration Handbook.* New York: McGraw-Hill, 1961.

[56] Anon.,"Gs Series Injector Installation Guide AFS Document No . 50-01199-01," 2008.

[57] Anon.,"LT1010 - Fast 150mA Power Buffer - Linear Technology." [Online]. Available: http://www.linear.com/product/LT1010. [Accessed: 04-Mar-2014].

[58] D. D. Joshi and F. K. Lu, "On the Unsteady Thrust Measurements for Pulse Detonation Engines," *AIAA Paper 2012–0324*, 2012.

[59] Y. Fujii, "Proposal for an Impulse Response Evaluation Method for Force Transducers," *Meas. Sci. Technol.*, vol. 10, no. 4, pp. N31–N33, 1999.

[60] Y. Fujii, "Proposal for a Step Response Evaluation Method for Force Transducers," *Meas. Sci. Technol.*, vol. 14, no. 10, pp. 1741–1746, 2003.

[61] Y. Fujii, "Measurement of the Electrical and Mechanical Responses of a Force Transducer against Impact Forces," *Rev. Sci. Instrum.*, vol. 77, no. 8, art. 055108–1–5, 2006.

[62] Y. Fujii, "Impact Force Measurement using an Inertial Mass and a Digitizer," *Meas. Sci. Technol.*, vol. 17, no. 4, pp. 863–868, 2006.

[63] Y. Fujii, “Method for Correcting the Effect of the Inertial Mass of Dynamic Force Measurements,” *Meas. Sci. Technol.*, vol. 18, no. 5, pp. N13–N20, 2007.

[64] R. B. Runyan, L. R. Deken, and J. T. Miller, “Structural Dynamics of a Small Rocket Thrust Stand,” *AIAA Paper 92–3787*, 1992.

[65] Z. Ren, B. Sun, J. Zhang, and M. Qian, “The Dynamic Model and Acceleration Compensation for the Thrust Measurement System of Attitude/Orbit Rocket,” *2008 Int. Workshop Model. Simul. Optim.*, pp. 30–33, 2008.

[66] J. L. Li, W. Fan, W. Chen, K. Wang, and C. J. Yan, “Propulsive Performance of a Liquid Kerosene/Oxygen Pulse Detonation Rocket Engine,” *Exp. Therm. Fluid Sci.*, vol. 35, no. 1, pp. 265–271, 2011.

[67] B. R. Munson, D. F. Young, and T. H. Okiishi, *Fundamentals of Fluid Mechanics*, 5th ed. Hoboken, New Jersey: Wiley, 2006.

[68] S. Sato, A. Matsuo, T. Endo, and J. Kasahara, “Numerical Studies on Specific Impulse of Partially Filled Pulse Detonation Rocket Engines,” *J. Propuls. Power*, vol. 22, no. 1, pp. 64–68, 2005.

[69] F. Schauer, J. Stutrud, and R. Bradley, “Detonation Initiation studies and Performance Results for Pulsed Detonation Applications,” *AIAA Paper 2001–1129*, 2001.

[70] M. Cooper and J. E. Shepherd, “The Effects of Nozzles and Extensions on Detonation Tube Performance,” *AIAA Paper 2002–3628*, 2002.

[71] C. Li and K. Kailasanath, “Partial Fuel Filling in Pulse Detonation Engines,” *J. Propuls. Power*, vol. 19, no. 5, pp. 908–916, 2003.

[72] N. Sahoo, D. R. Mahapatra, G. Jagadesh, S. Gopalakrishan, and K. P. J. Reddy, “Design and Analysis of a Flat Accelerometer-Based Force Balance System for Shock Tunnel Testing,” *Measurement*, vol. 40, no. 1, pp. 93–106, 2007.

[73] M. Robinson, “Simultaneous Lift , Moment and Thrust Measurements on a Scramjet in Hypervelocity Flow,” Ph.D. Dissertation, University of Queensland, Australia, 2003.

[74] E. C. Marineau, “Force Measurements in Hypervelocity Flows with an Acceleration Compensated Piezoelectric Balance,” *J. Spacecr. Rockets*, vol. 48, no. 4, pp. 697–700, 2011.

[75] F. K. Lu and D. R. Wilson, “Detonation Driver for Enhancing Shock Tube Performance,” *Shock Waves*, vol. 12, no. 6, pp. 457–468, 2003.

[76] R. Bello, “High-Enthalpy Characterization of the UTA Hypersonic Shock Tunnel,” Master's Thesis, University of Texas at Arlington, 2013.

[77] J. D. Anderson, *Fundamentals of Aerodynamics*. New York, NY: McGraw-Hill, 2001.

[78] J. J. Bertin, *Hypersonic Aerothermodynamics*. Washington, DC: AIAA, 1994.

[79] D. J. Mee, “Dynamic Calibration for Force Balances.” Centre for Hypersonics, The University of Queensland, Australia. Tech. Rep. 2002/6, 2003.

Biographical Information

Dibesh Joshi was born in Kathmandu, Nepal. He joined the University of Texas at Arlington(UTA) in the Spring Semester of 2007. He graduated with a B.S. degree in Aerospace Engineering in 2010. After the completion of his undergraduate degree, he continued his graduate studies as a BS to PhD student at UTA. He joined Aerodynamics Research Center as a undergraduate research assistant in 2009 due to his interest in the field of aerodynamics and propulsion. He was awarded with Dean's Undergraduate Research Assistantship (DURA) for his involvement in research activities as an undergraduate student. He was also a recipient of Enhanced Graduate Teaching Assistant. Dibesh has worked as a graduate research associate in several externally funded projects at the Aerodynamics Research Center and published his findings in form of numerous conference papers and journal articles.